

THEORETICAL AND NUMERICAL STUDIES ON THE  
TRANSPORT OF TRANSVERSE BEAM QUALITY IN  
PLASMA-BASED ACCELERATORS

Dissertation

Zur Erlangung der Würde des Doktors der Naturwissenschaften des Fachbereichs  
Physik, der Fakultät für Mathematik, Informatik und Naturwissenschaften, der  
Universität Hamburg

Vorgelegt von  
Timon Johannes Mehrling  
aus Unterseen (CH)

Hamburg, August 2014

BETREUER:

Dr. Jens Osterhoff  
Prof. Dr. Brian Foster

GUTACHTER DER DISSERTATION:

Dr. Jens Osterhoff  
Prof. Dr. Robi Banerjee

PRÜFUNGSKOMMISSION:

Prof. Dr. Dieter Horns  
Dr. Jens Osterhoff  
Prof. Dr. Jörg Roßbach  
PD Dr. Bernhard Schmidt  
Prof. Dr. Gudrid Moortgat-Pick

Datum der Disputation: 26. September 2014

Vors. der Prüfungskommission:	Prof. Dr. Dieter Horns
Vors. des Fach-Promotionsaussch.:	Prof. Dr. Daniela Pfannkuche
Fachbereichsleiter Physik:	Prof. Dr. Peter Hauschildt
Dekan der MIN Fakultät:	Prof. Dr. Heinrich Graener

Timon Johannes Mehrling: *Theoretical and numerical studies on the transport of transverse beam quality in plasma-based accelerators*, Dissertation - Zur Erlangung der Würde des Doktors der Naturwissenschaften des Fachbereichs Physik, der Fakultät für Mathematik, Informatik und Naturwissenschaften, der Universität Hamburg, © August 2014

TIMON JOHANNES MEHLING

THEORETICAL AND NUMERICAL STUDIES ON THE TRANSPORT OF  
TRANSVERSE BEAM QUALITY IN PLASMA-BASED ACCELERATORS

Hamburg, August 2014



"The sciences do not try to explain, they hardly even try to interpret, they mainly make models. By a model is meant a mathematical construct which, with the addition of certain verbal interpretations, describes observed phenomena. The justification of such a mathematical construct is solely and precisely that it is expected to work - that is correctly to describe phenomena from a reasonably wide area. Furthermore, it must satisfy certain aesthetic criteria - that is, in relation to how much it describes, it must be rather simple."

— John von Neumann

"Wahrlich es ist nicht das Wissen, sondern das Lernen, nicht das Besitzen sondern das Erwerben, nicht das Da-Seyn, sondern das Hinkommen, was den grössten Genuss gewährt."

— Carl Friedrich Gauß

Dedicated to the memory of Ernstfried Thiel, who once planted the seed of scientific curiosity into a boy's mind.

1920 – 2004



## ABSTRACT

---

This work examines effects, which impact the transverse quality of electron-beams in plasma-based accelerators, by means of theoretical and numerical methods.

Plasma-based acceleration is a promising candidate for future particle accelerator technologies. In plasma-based acceleration, highly intense laser beams or high-current relativistic particle beams are focused into a plasma to excite plasma-waves with extreme transverse and longitudinal electric fields. The amplitude of these fields exceed with 10 – 100 GV/m the ones in today's radio-frequency accelerators by several orders of magnitude, hence, in principle allowing for accordingly shorter and cheaper accelerators based on plasma. Despite the tremendous progress in the recent decade, beams from plasma accelerators are not yet achieving the quality as demanded for pivotal applications of relativistic electron-beams, e.g. free-electron lasers (FELs).

Studies within this work examine how the quality can be optimized in the production of the beams and preserved during the acceleration and transport to the interaction region. Such studies cannot be approached purely analytical but necessitate numerical methods, such as the Particle-In-Cell (PIC) method, which can model kinetic, electrodynamic and relativistic plasma phenomena. However, this method is computationally too expensive for parameter-scans in three-dimensional geometries. Hence, a quasi-static PIC code was developed in connection with this work, which is significantly more effective than the full PIC method for a class of problems in plasma-based acceleration.

The evolution of the emittance of beams which are injected into plasma modules was studied in this work by means of theoretical and the above numerical methods. It was shown that the beam parameters need to be matched accurately into the focusing plasma-channel in order to allow for beam-quality preservation. This suggested that new extraction and injection-techniques are required in staged plasma-acceleration concepts if the advantage of the short overall acceleration distance is to be sustained. Such a novel extraction method with tapered plasma-to-vacuum transitions was studied and found that it does not only facilitate the extraction but also is indispensable if beams need to be captured by beam-optics in order to be transported e.g. to some interaction region.





## ZUSAMMENFASSUNG

---

In dieser Arbeit werden mit Hilfe von theoretischen und numerischen Methoden Effekte untersucht, die in plasmabasierten Teilchenbeschleunigern die transversale Elektronenstrahlqualität beeinflussen.

Die plasmabasierte Teilchenbeschleunigung ist ein vielversprechender Kandidat für zukünftige Beschleunigertechnologien. Dabei werden entweder hochintensive Laserpulse oder relativistische Teilchenstrahlen mit hohen Strömen auf Plasmen fokussiert, um Plasmawellen mit extremen transversalen und longitudinalen Feldern zu treiben. Diese Felder können mit  $10 - 100 \text{ GV/m}$  um mehrere Größenordnungen jene übersteigen, die in heutigen Radiofrequenzbeschleunigern erzeugt werden, womit Plasmabeschleuniger prinzipiell entsprechend kürzer und günstiger sein können. Obwohl im letzten Jahrzehnt bemerkenswerte Fortschritte in der Plasmabeschleunigung erzielt wurden, ist die Strahlqualität noch nicht ausreichend für zentrale Anwendungen von relativistischen Elektronenstrahlen, z.B. FELs.

Im Zusammenhang mit dieser Arbeit wurde deshalb untersucht wie die Strahlqualität bei der Strahlerzeugung optimiert und während der Beschleunigung und des Transports zum Interaktionsbereich erhalten werden kann. Solche Studien können nicht rein analytisch durchgeführt werden und benötigen numerische Ansätze wie die PIC-Methode, die eine Beschreibung von kinetischen, elektrodynamischen und relativistischen Plasmaphänomenen erlaubt. Allerdings sind Simulationen mit dieser Methode zu rechenintensiv um z.B. Parameterstudien in dreidimensionalen Geometrien durchzuführen. Aus diesem Grund wurde in Verbindung mit dieser Arbeit ein quasi-statisches PIC-Simulationsprogramm entwickelt, das eine Klasse von Problemen der Plasmabeschleunigung deutlich effizienter modellieren kann.

In dieser Arbeit wird theoretisch und mit den o.g. numerischen Methoden erforscht wie sich die Emittanz von Elektronenstrahlen entwickelt, wenn diese extern in ein Plasmamodul eingekoppelt werden. Dabei wurde gezeigt, dass die Strahlparameter akkurat auf den fokussierenden Kanal im Plasmamodul angepasst sein müssen um die Strahlqualität zu erhalten. Dies erlaubt den Rückschluss auf modular aufgebaute Beschleunigerkonzepte, dass neuartige Extraktions- und Injektionsmethoden notwendig sind, wenn man den Vorteil der kürzeren Beschleunigungsstrecke erhalten will. Solch eine neuartige Extraktionsmethode mit speziell geformten Plasma-Vakuum-Übergängen wurde untersucht, und gezeigt, dass diese nicht nur das Auskoppeln erleichtert, sondern dass solche Methoden unerlässlich sind, wenn Strahlen in Strahloptiken eingekoppelt werden z.B. um zum Anwendungsbereich transportiert zu werden.



# CONTENTS

---

INTRODUCTION . . . . .	1
<b>I THEORY . . . . .</b>	<b>5</b>
<b>1 THEORETICAL BASIS . . . . .</b>	<b>7</b>
1.1 Basics of electrodynamics . . . . .	7
1.1.1 Basis of electromagnetism . . . . .	7
1.1.2 Electromagnetic waves . . . . .	9
1.1.3 Field energy and intensity . . . . .	13
1.1.4 Particle dynamics in electromagnetic fields . . . . .	15
1.2 Properties of plasmas . . . . .	20
1.2.1 Plasma definition . . . . .	20
1.2.2 Plasma classification . . . . .	24
1.3 Mathematical description of plasmas . . . . .	26
1.3.1 Model hierarchy . . . . .	26
1.3.2 Microscopic description . . . . .	27
1.3.3 Kinetic description . . . . .	29
1.3.4 Macroscopic or fluid description . . . . .	31
1.3.5 Plasma kinetic theory . . . . .	33
1.4 Beam-driven plasma waves . . . . .	34
1.4.1 Cold electron-fluid picture . . . . .	34
1.4.2 Ponderomotive force . . . . .	36
1.4.3 Quasi-static approximation . . . . .	37
1.4.4 Longitudinal plasma waves . . . . .	38
1.5 Plasma-based acceleration . . . . .	42
1.5.1 Methods of plasma acceleration . . . . .	43
1.5.2 Linear regime . . . . .	46
1.5.3 Mildly nonlinear regime . . . . .	48
1.5.4 Highly nonlinear or blow-out regime . . . . .	51
1.5.5 Wave-breaking . . . . .	54
1.5.6 Injection mechanisms . . . . .	55
1.5.7 Driver-energy depletion . . . . .	59
1.6 Transverse dynamics of charged particle-beams . . . . .	60
1.6.1 Emittance and Courant-Snyder parameters . . . . .	61
1.6.2 Luminosity and brightness . . . . .	63
1.6.3 Liouville's theorem . . . . .	65
1.6.4 Beam transport in ideal systems . . . . .	69
1.6.5 Emittance growth . . . . .	72
<b>II NUMERICAL METHODS . . . . .</b>	<b>75</b>
<b>2 PARTICLE-IN-CELL METHOD . . . . .</b>	<b>77</b>
2.1 Introduction . . . . .	77
2.2 Physical basis of the PIC method . . . . .	77

2.3	Numerical implementation and properties . . . . .	78
2.3.1	Current-density deposition . . . . .	79
2.3.2	Field solving . . . . .	80
2.3.3	Field interpolation and particle pushing . . . . .	82
2.3.4	Numerical sequence of a typical PIC cycle . . . . .	83
2.4	Relevant features of PIC simulations . . . . .	83
2.4.1	Numerical emittance growth from unphysical Cerenkov radiation . . . . .	84
2.4.2	Numerical scattering and heating . . . . .	84
3	DEVELOPMENT OF A QUASI-STATIC PIC CODE . . . . .	85
3.1	Introduction . . . . .	85
3.1.1	Motivation . . . . .	85
3.1.2	The quasi-static approach . . . . .	86
3.1.3	The quasi-static PIC code HiPACE . . . . .	86
3.2	Physical basis and mathematical model . . . . .	87
3.2.1	Physical basis and quasi-static approach . . . . .	87
3.2.2	Plasma formulation . . . . .	89
3.2.3	Beam equations . . . . .	91
3.2.4	Field equations . . . . .	91
3.3	Numerical implementation . . . . .	92
3.3.1	Beam current-density deposition . . . . .	92
3.3.2	Plasma and field routine . . . . .	93
3.3.3	Beam advance . . . . .	96
3.4	Comparison with explicit PIC simulations . . . . .	97
3.5	Parallelisation and scalings . . . . .	99
3.6	Discussion and conclusion . . . . .	103
III	PHYSICAL STUDIES . . . . .	107
4	BEAM MATCHING IN PLASMA ACCELERATION . . . . .	109
4.1	Introduction and motivation . . . . .	109
4.2	Matching of beams in plasma acceleration . . . . .	110
4.2.1	General matching considerations . . . . .	110
4.2.2	Matching in the linear regime . . . . .	112
4.2.3	Matching in the blowout regime . . . . .	113
4.3	Discussion and conclusion . . . . .	114
5	EMITTANCE GROWTH IN STAGED LWFA . . . . .	115
5.1	Introduction . . . . .	115
5.2	Analytical theory . . . . .	116
5.3	Comparison to PIC simulations . . . . .	118
5.4	Consequences for staged LWFA . . . . .	121
5.5	Summary and conclusion . . . . .	124
6	DENSITY-TAPERED BEAM EXTRACTION . . . . .	127
6.1	Introduction . . . . .	127
6.2	Density tapered extraction in ideal systems . . . . .	128
6.2.1	Numerical study . . . . .	128
6.2.2	Summary and conclusion . . . . .	134

6.3	Density tapered extraction in PWFA . . . . .	135
6.3.1	Introduction . . . . .	135
6.3.2	Physical scenario . . . . .	135
6.3.3	Numerical studies with PIC simulations . . . . .	137
6.3.4	Conclusion . . . . .	141
	SUMMARY, CONCLUSION AND OUTLOOK . . . . .	143
<b>IV</b>	<b>APPENDIX</b> . . . . .	147
<b>A</b>	<b>CALCULATIONS AND DERIVATIONS</b> . . . . .	149
A.1	Derivation of fluid momentum equation . . . . .	149
A.1.1	Momentum-divergence of Lorentz force . . . . .	149
A.1.2	Derivation of fluid momentum equation . . . . .	149
A.2	Relativistic particles in electromagnetic fields . . . . .	150
A.2.1	Direction of particle acceleration . . . . .	150
A.2.2	Azimuthally symmetric case . . . . .	151
A.2.3	Betatron equation of motion . . . . .	152
A.3	Linear wakefields - Gaussian drivers . . . . .	152
<b>B</b>	<b>DETAILS ON PERFORMED PIC SIMULATIONS</b> . . . . .	155
B.1	Simulation for display of blowout regime . . . . .	155
B.2	Simulation for HiPACE and OSIRIS comparison . . . . .	156
B.3	Simulations on emittance growth in staged LWFA . . . . .	157
B.4	Simulations on density tapered extraction . . . . .	158
<b>C</b>	<b>HIPACE - DETAILS AND CONSIDERATIONS</b> . . . . .	165
C.1	Basis of the fast Poisson solver . . . . .	165
C.1.1	Fast Poisson solver in one dimension . . . . .	165
C.1.2	Fast Poisson solver in two dimensions . . . . .	166
C.2	Details on the parallelization in HiPACE . . . . .	167
C.2.1	Halo cell method . . . . .	167
C.2.2	Parallelization of the fast Poisson solver . . . . .	169
C.2.3	Longitudinal parallelization . . . . .	169
C.2.4	Macro-particle exchange . . . . .	169
	LIST OF FIGURES . . . . .	171
	LIST OF TABLES . . . . .	173
	ACRONYMS . . . . .	174
	LIST OF SYMBOLS . . . . .	176
	BIBLIOGRAPHY . . . . .	179
	ACKNOWLEDGMENTS . . . . .	199
	CURRICULUM VITAE . . . . .	203
	LIST OF PUBLICATIONS . . . . .	205
	DECLARATION . . . . .	207



## INTRODUCTION

---

Advances in scientific understanding of nature rely on the construction of apparatuses which extend human perception in order to probe physical processes on a wide range of time and length scales. In this regard, synchrotron light sources are today's scientific slow-motion cameras and microscopes for the investigation of atomic and molecular processes in nature which occur on femtosecond time or nanometer length scales. Processes on even shorter time and length scales are analyzed by means of high-energy particle-colliders, which explore subatomic structures and the attributes of fundamental interactions.

Synchrotron light sources and colliders are driven by relativistic particle-beams which are provided by particle accelerators. Owing to the reciprocal time-energy and space-momentum relations, a finer resolution of features in time or space requires a higher energy or momentum of these particle beams, respectively. Modern conventional accelerators achieve gradients of more than 35 MV/m (see e.g. [Lilje et al., 2004]), but are ultimately limited by material breakdown to gradients of about 100 MV/m. Hence, pushing the frontiers of fundamental research forward involves the development of ever larger and more expensive accelerating machines when based on today's technology. The construction and funding of the latest generation of such machines, e.g. the European X-Ray Free-Electron Laser (XFEL), the Large Hadron Collider (LHC) or the International Linear Collider (ILC), breached the limit of ventures which can be carried by individual national economies. It may be inferred that the funding and realization of future endeavors in photon science and particle physics depends on the development of novel cheaper acceleration techniques.

Particle accelerators are indispensable for a variety of applications in modern medicine, industry and research. Low brilliance X-radiation is widely used e.g. in X-ray crystallography, mammography, medical computed tomography (CT) or airport security. High-brilliance X-ray radiation, which offers important advantages over low-brilliance radiation, is commonly produced in synchrotron light sources (such as FELs). Moreover, proton and ion accelerators are used for cancer treatments, accelerator driven subcritical reactors or nuclear transmutation reactors and spallation sources for research purposes.

A promising concept for cheap and affordable future electron accelerators is provided by the plasma-based acceleration approach [Esarey et al., 1996, 2009]. These methods exploit the extreme fields in plasma waves, excited by highly intense laser pulses or high current charged particle-beams, to transport and accelerate electron bunches to high energies within short distances. The longitudinal electric fields in

such plasma waves are on the order of 10-100 GV/m [Modena et al., 1995], hence in principle allowing for accelerating devices which can be by three orders of magnitude shorter than conventional accelerators. Concepts using short laser pulses as drivers of the plasma wave are called laser wakefield acceleration (LWFA) and methods employing short charged particle-beams as drivers are named plasma wakefield acceleration (PWFA). The field of plasma-based accelerator research has experienced a rapid development in the last decades, culminating in the experimental production of ultra-relativistic electron beams with a narrow spectrum [Geddes et al., 2004; Mangles et al., 2004; Faure et al., 2004] and of electron beams in the GeV range within centimeter-scale distances [Leemans et al., 2006; Kim et al., 2013; Wang et al., 2013] in LWFA. Energy gain of electrons by more than 40 GeV within distances shorter than a meter in PWFA was shown by Blumenfeld et al. [2007]. In addition, it was shown that beams from plasma-based acceleration can produce bright radiation during the acceleration process [Kneip et al., 2010] or can be used for the generation of brilliant X-ray radiation in undulators [Fuchs et al., 2009]. Not only will this development pave the way for the production of brilliant X-ray generation in small-scale labs but also allow for their application in hospitals, industry and university-scale photon research.

Although plasma-based accelerators are on the verge of providing beams suitable for some applications, electron beams, appropriate for the generation of FEL-radiation or for the use in particle colliders, have not been demonstrated yet. This is firstly owed to the high demands of these applications in terms of beam stability and quality but also due to the challenge to stage plasma acceleration modules, which becomes necessary when energies beyond the  $\sim 10$  GeV scale need to be obtained [Schroeder et al., 2010].

The beam-parameters primarily depend on the method of beam generation and a large number of methods for plasma-based accelerators have been proposed, showing the capability to enhance the stability and quality of the produced beams. A technique using the plasma-wakefields for ionization of a dopand gas as well as for trapping was proposed in correlation with the presented work [Martinez de la Ossa et al., 2013]. The emittance of a beam is a pivotal figure of merit for its quality. While the emittance is typically sufficiently small for FEL operation during the production in plasma-based accelerators with different injection techniques (see e.g. [Esarey et al., 2009]), the emittance-preserving transport of the beams from the plasma cell to the interaction point or to a subsequent plasma cell is highly challenging. Comprehensive theoretical, numerical and experimental studies are necessary to understand and improve the beam transport methods in plasma-based acceleration.



Progress in plasma accelerator research is vitally stimulated by the use of numerical methods, which were, similarly as in other scientific fields, established as a third pillar between theory and experiment. Numerical studies on plasma accelerators are primarily conducted using the Particle-In-Cell (PIC) technique, which enables a modeling of the kinetic, relativistic and electromagnetic interactions of intense laser beams or relativistic, high-current particle beams with plasmas. Highly parallel PIC codes allow for the fully three-dimensional emulation of plasma-based accelerators when running on modern supercomputers. However, the length-scales in such simulations show a large disparity, with smallest resolved length-scales on the order of micrometers and longest scales on the order of centimeters to meters. This renders full PIC simulations computationally very expensive and unsuitable for detailed studies or parameter scans in three-dimensional geometries.

A significant mitigation of the computational costs is possible by implementing a PIC scheme [Mora and Antonsen, 1996] based on the quasi-static approximation [Sprangle et al., 1990b]. Such a scheme is applicable, if the driver beam is evolving on much longer time-scales than the plasma, and allows for an order-of-magnitude speedup for a class of problems in PWFA, as demonstrated in the quasi-static PIC code HiPACE [Mehrling et al., 2014]. While quasi-static PIC codes cannot consistently simulate intrinsic injection methods in plasma-based accelerators, they feature the exceptional capability of consistently importing beams from full PIC codes during their propagation in plasmas.

Using the PIC method, the full variety of dynamics in plasma-based accelerators can be modeled. Recently, the topic of the transport of beam quality in plasma-based accelerators experienced an increasing interest in such numerical, and in theoretical investigations. This led to advances in the understanding and manipulation of the transport of the transverse beam quality, e.g. in staged LWFA [Mehrling et al., 2012], as discussed in the context of this dissertation. Such advances are vital for the field of plasma-based acceleration in order to realize the major leap forward into the domain of pivotal applications e.g. FELs or particle colliders.

This work discusses progress on the numerical modeling of plasma-based accelerators and reports on new insights into the transport and preservation of the transverse beam quality in plasma-based accelerators. It is structured as follows.

## PART I - THEORY

### 1. THEORETICAL BASIS

This chapter forms a comprehensive theoretical basis for the discussions and studies in the following chapters.

**PART II - NUMERICAL METHODS****2. PARTICLE-IN-CELL METHOD**

The principles of the particle-in-cell technique are outlined in this chapter. This serves as a footing for the understanding of the development of a derived code, described in the subsequent chapter and for numerical studies performed in chapter 5.

**3. DEVELOPMENT OF A QUASI-STATIC PIC CODE**

This chapter introduces a quasi-static **PIC** code for the efficient modeling of plasma-wakefield accelerators. The physical basis, numerical implementation, computational framework and parallel performance of this simulation code is discussed. It is of particular interest for studies on the beam dynamics in **PWFA**, such as performed in chapter 6.

AFFILIATED PUBLICATION: [Mehrling et al., 2014].

**PART III - PHYSICAL STUDIES****4. BEAM MATCHING IN PLASMA ACCELERATION**

This chapter introduces the general conditions for beam matching in plasma-based accelerators in the linear regime and in the blowout regime.

**5. EMITTANCE GROWTH IN STAGED LWFA**

New insights into the transverse dynamics of electron beams in staged **LWFA** are reported on in this chapter. It shows that matching of beams into plasma-based acceleration stages is indispensable for the preservation of the beam quality and predicts order-of-magnitude emittance growth in staged **LWFA**, if the beams are not appropriately extracted, transported and injected between the stages.

AFFILIATED PUBLICATION: [Mehrling et al., 2012].

**6. DENSITY-TAPERED BEAM EXTRACTION**

The studies in this chapter address the effect of density tapered plasma-to-vacuum transitions on the beam-quality transport during the extraction. It demonstrates that adequate density tapering facilitates the extraction of beams from a plasma stage. In addition, investigations on the emittance evolution during the extraction of realistic beams with significant energy spread from **PWFA** are performed by means of **PIC** simulations. Results indicate that an appropriate combination of plasma-to-vacuum transitions and a capturing optical lattice are crucial for the emittance preservation during the beam extraction.

**SUMMARY, CONCLUSION AND OUTLOOK**

The physical studies are summarized and concluded, and an outlook for anticipated progress on beam-quality preservation in plasma-based acceleration is presented.

## Part I

### THEORY

#### 1. THEORETICAL BASIS

*Content:* Basic definitions and equations of electrodynamics. Properties of electromagnetic waves. Energy density and intensity of electromagnetic waves. Dynamics of electrically charged particles in electromagnetic fields. Definition and classification of plasma. Plasma model hierarchy - from microscopic to macroscopic picture. Plasma waves excited by intense laser pulses and relativistic particle beams. Principles and attributes of plasma-based acceleration. Regimes of plasma-based acceleration. Relevant phenomena in plasma-based acceleration. Figure of merits for beam quality. Liouville's theorem. Transverse dynamics of beams in accelerators. Causes and mechanisms of emittance change.



## THEORETICAL BASIS

---

### 1.1 BASICS OF ELECTRODYNAMICS

Electrodynamics describes the interaction between electrically charged particles and electromagnetic fields. From the viewpoint of modern particle physics it constitutes the classical limit of quantum electrodynamics for low momentum- and energy-transfers and for a large number of virtual and real photons [Jackson, 1998]. Amongst all fundamental interactions, it is the strongest infinite-ranged interaction, which is the reason for the pervasiveness of electromagnetic phenomena in nature. These span from electrostatic attraction and repulsion of charged pieces of amber or the magnetostatic interaction between lodestones to the electromagnetic induction in generators, the generation of electromagnetic waves in antennas and the transport of light through different media. Observation of such phenomena eventually led to the mathematical formulation in form of the Maxwell equations, which define the basis of electromagnetism and the Lorentz force, which describes the dynamics of charged particles in the electromagnetic fields.

This work covers phenomena that are accurately described by, or founded on classical electrodynamics (an exception is the quantum-mechanical effect of ionization of atoms by virtue of external fields).

#### 1.1.1 Basis of electromagnetism

##### 1.1.1.1 Maxwell's equations

The basis of the formulation of electromagnetism is the *Maxwell's equations*, here in differential and microscopic formulation (see e. g. [Jackson, 1998]),

$$\nabla \cdot \mathbf{E} = 4\pi\rho, \quad (1.1a)$$

$$\nabla \cdot \mathbf{B} = 0, \quad (1.1b)$$

$$\nabla \times \mathbf{E} + \frac{\partial \mathbf{B}}{\partial ct} = 0, \quad (1.1c)$$

$$\nabla \times \mathbf{B} - \frac{\partial \mathbf{E}}{\partial ct} = \frac{4\pi \mathbf{J}}{c}, \quad (1.1d)$$

where  $c$  is the speed of light,  $\mathbf{E}$  and  $\mathbf{B}$  are the electric and magnetic field, respectively,  $\rho$  represents the charge density and  $\mathbf{J}$  the current density. Maxwell's equations are coupled, first-order partial differential equations (PDEs). Equations (1.1a) and (1.1b) are time-independent whereas Eqns. (1.1c) and (1.1d) are time-dependent. In

*The formulation of electrodynamics within this work is done in the Gaussian unit system. However, explicit values for electromagnetic quantities are given in Si units.*

general, equations (1.1a) and (1.1d) are inhomogeneous PDEs and Eqns. (1.1b) and (1.1c) are homogeneous PDEs.

For a more detailed discussion of Maxwell's equations, see e. g. Jackson [1998] or Nolting [2001].

Equation (1.1a) results from the *Gauss law* and expresses, the fact that electrical charge is a source of electrical field. The electrical field is considered to be the source of the *Coulomb force* between stationary charged particles. The fact that the magnetic field has no divergence and the non-existence of magnetic monopoles (sources of magnetic charge) is embodied in identity (1.1b). The third Maxwell's equation (1.1c) is a consequence of *Faraday's law of induction* and *Stokes' theorem*. *Ampère's law*, together with *Maxwell's displacement current* are expressed in Eq. (1.1d). The magnetic field is considered to be the source of *Ampère's force* between electrical currents.

Combining the time derivative of equation (1.1a) with the divergence of equation (1.1d) show, that the Maxwell's equations entail the *charge continuity equation*

$$\frac{\partial \rho}{\partial t} + \nabla \cdot \mathbf{J} = 0. \quad (1.2)$$

The charge continuity equation states, that the change of the amount of charge contained in a volume element must involve a corresponding charge current through the surface of this volume element and charge is therefore conserved in a closed system.

#### 1.1.1.2 Electromagnetic potentials

Maxwell's equations can also be expressed in terms of the *scalar potential*  $\Phi$  and the *vector potential*  $\mathbf{A}$ . These potentials are constructed to fulfil the homogeneous Maxwell's equations, while the inhomogeneous Maxwell's equations are transformed to second-order partial differential equations (see e. g. [Nolting, 2001]). The potentials are related to the electric field  $\mathbf{E}$  and magnetic field  $\mathbf{B}$  according to

$$\mathbf{E} = -\nabla\Phi - \frac{\partial\mathbf{A}}{\partial ct}, \quad (1.3a)$$

and

$$\mathbf{B} = \nabla \times \mathbf{A}. \quad (1.3b)$$

These identities contain degrees of freedom for the potentials, since the fields  $\mathbf{E}$ ,  $\mathbf{B}$  are invariant under the *gauge transformation*

$$\mathbf{A}' = \mathbf{A} + \nabla\chi, \quad (1.4a)$$

$$\Phi' = \Phi - \frac{\partial\chi}{\partial ct}, \quad (1.4b)$$

where  $\chi$  is an arbitrary scalar field. The relation between fields and potentials is confined by the choice of a *gauge* which removes these redundancies.

Popular gauge fixings are the *Coulomb gauge* and the *Lorenz gauge*. The Coulomb gauge

$$\nabla \cdot \mathbf{A} = 0, \quad (1.5)$$

transforms (1.1a) to the electrostatic *Poisson equation*

$$\nabla^2 \Phi = -4\pi\rho. \quad (1.6)$$

The Lorenz gauge,

$$\frac{\partial \Phi}{\partial ct} + \nabla \cdot \mathbf{A} = 0, \quad (1.7)$$

has the properties, among others, of decoupling the partial differential equations of scalar and vector potential and of being Lorentz invariant (cf. e.g. [Nolting, 2001]). The Lorenz gauge is not "complete" since it leaves a subset of gauge transformations which fulfill the three equations (1.3a), (1.3b) and (1.7), as shown in the following.

*This gauge is named after Ludvig Lorenz, but is often called Lorenz gauge due to its nature of being Lorentz invariant.*

### 1.1.2 Electromagnetic waves

#### 1.1.2.1 Governing equations of electromagnetic waves in vacuum

In vacuum, i.e. if no charge or current densities are present on relevant scales ( $\rho = 0$ ,  $\mathbf{J} = 0$ ), all Maxwell's equations are homogeneous. However, apart from the trivial solution  $\mathbf{E} = \mathbf{B} = 0$  of the homogeneous Maxwell's equations, non-zero solutions, called *electromagnetic waves*, can be found. The attributes of such electromagnetic waves are examined below.

After imposing the Lorenz gauge (1.7), the homogeneous Maxwell's equations become homogeneous *wave equations*

$$\square \Phi = 0, \quad (1.8a)$$

$$\square \mathbf{A} = 0, \quad (1.8b)$$

where the *d'Alembert operator*  $\square = \nabla^2 - \partial^2/\partial ct^2$  was introduced. The fact that the system has redundancies in addition to the gauge freedom is found by supposing the potentials  $\mathbf{A}'$  and  $\Phi'$  in Eqns. (1.4a) and (1.4b) not to fulfill the Lorenz gauge condition, such that  $\partial\Phi'/\partial ct + \nabla \cdot \mathbf{A}' = f(\mathbf{r}, t) \neq 0$ . This assumption yields with (1.7) the following inhomogeneous wave equation for the gauge function

$$\square \chi = f(\mathbf{r}, t), \quad (1.9)$$

The Lorenz gauge condition is hence fulfilled for any solution  $\chi$  of this equation. Furthermore, it is possible to add a solution  $\Lambda$  of the homogeneous wave equation  $\square \Lambda = 0$  to a chosen gauge function

*The explanations in this section follow Landau and Lifšic [1976, ch. VI], Nolting [2001] and Fließbach [2005, ch. VI].*

$\chi$  which is a particular solution of the inhomogeneous wave equation, without violating the Lorenz gauge condition (1.7). Without disrupting equations (1.3a), (1.3b) and (1.7) the potentials can thus be changed according to the special subset of gauge transformations,

$$\mathbf{A}'' = \mathbf{A} + \nabla\Lambda, \quad (1.10a)$$

$$\Phi'' = \Phi - \frac{\partial\Lambda}{\partial ct}, \quad (1.10b)$$

where  $\Lambda$  must be a solution of the homogeneous wave equation. Thus, to constrain these additional degrees of freedom, an additional gauge condition can be chosen. In the case of the homogeneous Maxwell's equations (1.8a) and (1.8b), it is possible to choose  $\partial\Lambda/\partial ct = -\Phi''$ , since  $\Phi''$  as well as  $\partial\Lambda/\partial ct$  satisfy the homogeneous wave equation. This results in the additional gauge condition  $\Phi = 0$ ; the equations, governing *electromagnetic waves* in vacuum in the Lorenz gauge are,

$$\square\mathbf{A} = 0, \quad (1.11a)$$

$$\nabla \cdot \mathbf{A} = 0, \quad (1.11b)$$

$$\Phi = 0. \quad (1.11c)$$

Equations (1.11a) and (1.11b) show, that two components of  $\mathbf{A}$  are independent with respect to each other, which is equivalent to two independent forms of polarization of an electromagnetic wave.

#### 1.1.2.2 Plane waves

The special case of electromagnetic waves which depend on one spatial coordinate  $z$  only, called *plane waves*, is studied in the following. The wave equation (1.11a) for the case of a plane wave then reduces for any component  $g$  of  $\mathbf{A}$  to

$$\left( \frac{\partial^2}{\partial z^2} - \frac{\partial^2}{\partial ct^2} \right) g(z, t) = 0. \quad (1.12)$$

The most general solution of this equation is given by [Landau and Lifšic, 1976]

$$g(z, t) = g_1(z - ct) + g_2(z + ct), \quad (1.13)$$

with  $g_1$  and  $g_2$  being arbitrary differentiable functions. The two functions can be interpreted as waves,  $g_1$  propagating with velocity  $c$  in the positive  $z$ -direction and  $g_2$  propagating in the negative  $z$ -direction. For plane waves in vacuum, areas with  $\pm z - ct = \text{const}$  have a constant *phase*. From equation (1.11b), the component  $A_z$  of a plane wave, propagating in positive or negative  $z$ -direction is constant and can be set to  $A_z = 0$ , considering that constant potential values do not contribute to the fields  $\mathbf{E}$  and  $\mathbf{B}$ . Such a wave with contributions of  $\mathbf{A}$  only in the plane transverse to the direction of propagation is called a *transverse wave*.



1.1.2.3 *Plane monochromatic waves*

A periodic electromagnetic wave with a single frequency  $\omega$  is called a *monochromatic wave*. For a monochromatic plane wave, equation (1.12) reduces to

$$\left(\frac{\partial^2}{\partial z^2} + \frac{\omega^2}{c^2}\right) \mathbf{A}(z, t) = 0, \tag{1.14}$$

and solutions are given by (compare e. g. [Landau and Lifšic, 1976])

$$\mathbf{A} = \text{Re} \left( \mathbf{A}_0 e^{i(kz - \omega t)} \right), \tag{1.15}$$

where  $k = \omega/c$  is the *wave number* in vacuum (the wave number in a medium is given by  $k = \omega/v_{ph}$ , where  $v_{ph}$  is the phase velocity). The factor  $\mathbf{A}_0$  is a constant complex vector with  $\mathbf{A}_0 \perp \mathbf{k}$  and  $\mathbf{k} = k \hat{\mathbf{e}}_z$ . The electric and magnetic field can be calculated by use of equations (1.3a) and (1.3b)

$$\mathbf{E} = \text{Re} \left( \mathbf{E}_0 e^{i(\mathbf{k} \cdot \mathbf{r} - \omega t)} \right), \tag{1.16a}$$

$$\mathbf{B} = \text{Re} \left( \mathbf{B}_0 e^{i(\mathbf{k} \cdot \mathbf{r} - \omega t)} \right), \tag{1.16b}$$

with  $\mathbf{E}_0 = ik\mathbf{A}_0$  and  $\mathbf{B}_0 = i\mathbf{k} \times \mathbf{A}_0$ . It can immediately be seen that the electric field in such a wave is always perpendicular to the magnetic field  $\mathbf{E} \perp \mathbf{B}$  and the electric and magnetic field are both perpendicular to the propagation direction of the wave  $\mathbf{E} \perp \mathbf{k}$ ,  $\mathbf{B} \perp \mathbf{k}$ , respectively. Furthermore, the magnitudes of the electric and magnetic fields are identical, such that

$$\mathbf{B} = \frac{\mathbf{k}}{k} \times \mathbf{E}. \tag{1.17}$$

The separation between two consecutive points with the same phase along a monochromatic wave in vacuum is given by the *wavelength*  $\lambda = 2\pi/k = 2\pi c/\omega$ .

1.1.2.4 *Polarization*

Electric and magnetic fields in plane waves are perpendicular to the propagation direction. The form in which the transverse field components oscillate is called *polarization*. The different types of polarization are addressed in the following.

The vector  $\mathbf{A}_0$  in equation (1.15) is, in general, complex and can be written as  $\mathbf{A}_0 = \mathbf{d} \exp(-i\alpha)$ , where  $\mathbf{d} = \mathbf{d}_1 + i\mathbf{d}_2$  is a complex vector with real square  $\mathbf{d}^2 = |\mathbf{A}_0|^2 = \mathbf{A}_0 \cdot \mathbf{A}_0^*$ , with  $\mathbf{A}_0^*$  connoting the complex conjugate of the vector  $\mathbf{A}_0$ . The square of  $\mathbf{d}$  is real and the real and imaginary part of this vector must hence be orthogonal  $\mathbf{d}_1 \cdot \mathbf{d}_2 = 0$ . The real part can be chosen to lie in  $x$ -direction  $\mathbf{d}_1 = d_1 \hat{\mathbf{e}}_x$ ,

*Solutions of Eq. (1.14) are in general complex-valued. However, since observable quantities are real-valued, it is convenient to use the real part of  $\mathbf{A}$  only.*

*The discussion of polarization here is analogous to Landau and Lifšic [1976].*

while the imaginary part is chosen to be in positive or negative  $y$ -direction  $\mathbf{d}_2 = \pm d_2 \hat{\mathbf{e}}_y$ . The components of the wave (1.15) are thus rewritten as

$$A_x = \operatorname{Re} \left( d_1 e^{i(\mathbf{k} \cdot \mathbf{r} - \omega t - \alpha)} \right) = d_1 \cos(\mathbf{k} \cdot \mathbf{r} - \omega t - \alpha), \quad (1.18a)$$

$$A_y = \operatorname{Re} \left( i d_2 e^{i(\mathbf{k} \cdot \mathbf{r} - \omega t - \alpha)} \right) = \mp d_2 \sin(\mathbf{k} \cdot \mathbf{r} - \omega t - \alpha), \quad (1.18b)$$

These equations specify possible field configurations in a plane electromagnetic wave, propagating in the positive  $z$ -direction and  $d_1$ ,  $d_2$  and  $\alpha$  are arbitrary real constants, where  $d_1$  and  $d_2$  span the types of polarization and  $\alpha$  specifies the phase. The wave is polarized in the  $x$ -direction for  $d_1 = A_0$ ,  $d_2 = 0$ , and in  $y$ -direction for  $d_1 = 0$ ,  $d_2 = A_0$ . These cases are referred to as *linear polarization* (LP), and can be specified as  $\mathbf{A}_0 = A_0 \hat{\mathbf{e}}_x$ , or  $\mathbf{A}_0 = A_0 \hat{\mathbf{e}}_y$ . The transverse components  $A_x$  and  $A_y$  are related with respect to each other through equations (1.18a) and (1.18b) by

$$\frac{A_x^2}{d_1^2} + \frac{A_y^2}{d_2^2} = 1. \quad (1.19)$$

Hence, allowed field configurations lie on an ellipse. The wave has an *elliptic polarization* for  $d_1 \neq d_2$  and  $d_1 \neq 0 \neq d_2$  and a *circular polarization* (CP) for  $d_1 = d_2 \neq 0$ . Elliptic and circular polarization can be regarded as a superposition of two linearly polarized waves, one polarized in the  $x$ -direction and the other polarized in the  $y$ -direction. A wave with circular polarization thus has an amplitude of  $\mathbf{A}_0 = A_0(\hat{\mathbf{e}}_x \pm i\hat{\mathbf{e}}_y)$ , where “+” stands for right- and “−” for left-circular polarization [Meyer-ter Vehn et al., 2001].

#### 1.1.2.5 Wave packets

The above discussion was treating monochromatic waves only. In reality, electromagnetic waves always have a finite spectral width, and can be viewed as a superposition of monochromatic waves. Waves containing a bandwidth of frequency components can form a *wave packet* of finite length. The length  $\Delta z$  and bandwidth of wavenumber components  $\Delta k$  thereby comply with the restriction  $\Delta z \Delta k \leq 1/2$  [Jackson, 1998, Ch. 7.8]. Hence, short wave packets contain a broad distribution of wavenumbers and long, sine-like waves are almost monochromatic.

The different frequency components of a wave packet travel at a different phase velocities in dispersive media which has the following implications for the wave packet. It propagates with the *group velocity* [Jackson, 1998, Ch. 7.8]

$$v_g = \left. \frac{d\omega}{dk} \right|_{k_0}, \quad (1.20)$$

The discussion here follows [Jackson, 1998, Ch. 7.8].

where  $k_0$  is the central wavenumber. The group velocity determines the speed at which the intensity envelope and the energy flux of the wave travel.

The phase velocity of the wave is determined through

$$v_{ph} = \frac{\omega(k)}{k}. \quad (1.21)$$

It can exceed the speed of light in dispersive media. The dispersion relation for electromagnetic waves in vacuum is given by

$$\omega = ck. \quad (1.22)$$

Hence, in vacuum, the speed of light is retrieved for both, the group velocity and phase velocity of a light wave.

### 1.1.3 Field energy and intensity

The energy contained and transported by electromagnetic fields in general and plane electromagnetic waves in particular is examined in this section.

*The argumentation in section 1.1.3 follows Nolting [2001, chapter 4.1.4].*

#### 1.1.3.1 Poynting's theorem

The energy conservation laws for electromagnetic fields are derived from the analysis of the work performed by fields on electric charges. The force from an electromagnetic field on a point particle with charge  $q$  and velocity  $\mathbf{V}$  is defined by the *Lorentz force* [Jackson, 1998]

$$\mathbf{F} = q \left( \mathbf{E} + \frac{\mathbf{V}}{c} \times \mathbf{B} \right). \quad (1.23)$$

For a continuous charge density  $\rho(\mathbf{r}, t)$  with velocity  $\mathbf{v}(\mathbf{r}, t)$ , the Lorentz force can be used to find the force density

$$\mathbf{f}(\mathbf{r}, t) = \rho(\mathbf{r}, t) \left[ \mathbf{E}(\mathbf{r}, t) + \frac{\mathbf{v}(\mathbf{r}, t)}{c} \times \mathbf{B}(\mathbf{r}, t) \right]. \quad (1.24)$$

When the field pushes the charge density by a distance  $d\mathbf{r}$  it performs the work  $\mathbf{f} \cdot d\mathbf{r}$ . The mechanical power density is thus given by

$$\mathbf{f}(\mathbf{r}, t) \cdot \frac{d\mathbf{r}}{dt} = \rho(\mathbf{r}, t) \mathbf{E}(\mathbf{r}, t) \cdot \mathbf{v}(\mathbf{r}, t) = \mathbf{J}(\mathbf{r}, t) \cdot \mathbf{E}(\mathbf{r}, t). \quad (1.25)$$

The magnetic field does not perform any work since it's force is always directed perpendicular to the velocity  $\mathbf{v}$ . The mechanical power deposited by the electrical field in a volume  $V$  is thus given by

$$\frac{dW}{dt} = \int_V d\mathbf{r} \mathbf{J} \cdot \mathbf{E}. \quad (1.26)$$

Maxwell's equations  
as well as derived  
equations like the  
Poynting theorem  
here are all  
expressed in terms of  
the "microscopic"  
field definitions.

Replacing  $\mathbf{J}$  according to the Maxwell's equation (1.1d) and applying the vector identity  $\nabla \cdot (\mathbf{E} \times \mathbf{B}) = \mathbf{B}(\nabla \times \mathbf{E}) - \mathbf{E}(\nabla \times \mathbf{B})$  with equation (1.1c) yields

$$\frac{dW}{dt} = -\frac{c}{4\pi} \int_V d\mathbf{r} \left[ \frac{\partial}{\partial ct} \left( \frac{\mathbf{E}^2 + \mathbf{B}^2}{2} \right) + \nabla \cdot (\mathbf{E} \times \mathbf{B}) \right]. \quad (1.27)$$

This equation is a continuity equation for the energy in the electromagnetic field. This becomes more clear after identifying the *energy density of the electromagnetic field*

$$w = \frac{1}{8\pi} (\mathbf{E}^2 + \mathbf{B}^2), \quad (1.28)$$

and the *Poynting-vector*

$$\mathbf{S} = \frac{c}{4\pi} \mathbf{E} \times \mathbf{B}. \quad (1.29)$$

Equation (1.27) can then be rewritten in the following differential form, representing the *Poynting's theorem* [Nolting, 2001]

$$\frac{\partial w}{\partial t} + \nabla \cdot \mathbf{S} = -\mathbf{J} \cdot \mathbf{E}. \quad (1.30)$$

Poynting's theorem states that the local energy density of the electromagnetic field  $w$  changes with time according to the mechanical power deposited into some charge density  $\mathbf{j} \cdot \mathbf{E}$  and according to the divergence of the energy flux density of electromagnetic field  $\mathbf{S}$ .

### 1.1.3.2 Energy transport in plane monochromatic waves

When calculating the energy flux of a plane monochromatic wave, only the time-averaged properties are relevant

$$\bar{C}(t) = \frac{1}{T} \int_t^{t+T} dt' C(t'), \quad (1.31)$$

For a more detailed  
discussion, see  
Nolting [2001].

where  $T = 2\pi/\omega$  is the time of one period. For the calculation of the energy density and the energy flux density, it can firstly be noted, that equation (1.16a) implies

$$\bar{\mathbf{E}}^2 = \text{Re}(\mathbf{E}_0)^2 \overline{\cos^2(\omega t)} + \text{Im}(\mathbf{E}_0)^2 \overline{\sin^2(\omega t)} = \frac{1}{2} |\mathbf{E}_0|^2, \quad (1.32)$$

The time-averaged energy density of a plane monochromatic wave in vacuum is thus with (1.28) and (1.17) given by

$$\bar{w} = \frac{1}{8\pi} (\bar{\mathbf{E}}^2 + \bar{\mathbf{B}}^2) = \frac{|\mathbf{E}_0|^2}{8\pi}, \quad (1.33)$$

and the time-averaged Poynting vector is obtained through (1.29)

$$\bar{\mathbf{S}} = \frac{c}{4\pi} \overline{\mathbf{E} \times \left( \frac{\mathbf{k}}{k} \times \mathbf{E} \right)} = \frac{c |\mathbf{E}_0|^2}{8\pi} \frac{\mathbf{k}}{k}. \quad (1.34)$$

The energy flux density of the electromagnetic wave is hence simply given by the energy density propagating with velocity  $c$  in  $\mathbf{k}$ -direction. The magnitude of  $\bar{\mathbf{S}}$  is the *intensity* of the electromagnetic wave (confer e. g. [Meyer-ter Vehn et al., 2001]),

$$I = |\bar{\mathbf{S}}| = \frac{c |\mathbf{E}_0|^2}{8\pi} = \frac{c\pi}{2} \frac{|\mathbf{A}_0|^2}{\lambda^2} = \frac{c\pi}{2} \frac{A_0^2}{\lambda^2} \times \begin{cases} 1 & \text{for LP,} \\ 2 & \text{for CP.} \end{cases} \quad (1.35)$$

A circularly polarized wave (CP) with amplitude  $A_0$  has twice the intensity of a linearly polarized (LP) wave with amplitude  $A_0$ . It is a measure for the mechanical power per unit area which can be transferred by the electromagnetic wave to some medium.

Modern laser systems using the chirped pulse amplification (CPA) technique [Strickland and Mourou, 1985] reach, by use of appropriate focusing optics, intensities of far more than  $10^{18} \text{ W cm}^{-2}$  [Yanovsky et al., 2008], which corresponds via equation (1.35) to electric field amplitudes of more than  $10^{10} \text{ V m}^{-1}$  in SI units.

*This would be the other way round if LP was defined as a superposition of two CPs in 1.1.2.4.*

#### 1.1.4 Particle dynamics in electromagnetic fields

The availability of lasers with ultra-high intensities and field amplitudes raises the question if these fields can be harnessed for the acceleration of electrons. The dynamics of electrons in highly-intense electromagnetic waves is studied in this context. Moreover, this topic is also crucial for a fundamental understanding of the dynamics of plasma-electrons in highly intense laser fields.

##### 1.1.4.1 General formalism of particle dynamics in electromagnetic fields

The *Lagrangian* function for a relativistic particle with charge  $q$ , mass  $m$ , position  $\mathbf{r}(t)$  and velocity  $\mathbf{v}(t) = d\mathbf{r}/dt = \dot{\mathbf{r}}$  in externally prescribed potentials  $\Phi$  and  $\mathbf{A}$  is given by [Jackson, 1998]

$$\mathcal{L}(\mathbf{r}, \mathbf{v}, t) = -mc^2 \sqrt{1 - \frac{\mathbf{v}(t)^2}{c^2}} + \frac{q}{c} \mathbf{v}(t) \cdot \mathbf{A}(\mathbf{r}, t) - q\Phi(\mathbf{r}, t). \quad (1.36)$$

Using the Euler-Lagrange equation [Arnold, 1989]

$$\frac{d}{dt} \frac{\partial \mathcal{L}}{\partial \mathbf{v}} - \frac{\partial \mathcal{L}}{\partial \mathbf{r}} = 0, \quad (1.37)$$

together with the definition of the potentials (1.3a) and (1.3b), yields the equation of motion

$$\frac{d\mathbf{p}}{dt} = q \left( \mathbf{E} + \frac{\mathbf{v}}{c} \times \mathbf{B} \right), \quad (1.38)$$

where  $\mathbf{p} = \gamma m \mathbf{v}$  is the particle's *momentum*, and  $\gamma = (1 - \mathbf{v}^2/c^2)^{-1/2}$  is the *Lorentz factor*. The *canonical momentum* is given by

$$\mathbf{p}_{can} = \frac{\partial \mathcal{L}}{\partial \mathbf{v}} = m\mathbf{v} \sqrt{1 - \frac{\mathbf{v}^2}{c^2}} + \frac{q}{c} \mathbf{A} = \mathbf{p} + \frac{q}{c} \mathbf{A}. \quad (1.39)$$

The *Hamiltonian*  $\mathcal{H} = \mathbf{v} \cdot \mathbf{P}_{can} - \mathcal{L}$  is the Legendre transform of the Lagrangian function [Arnold, 1989] and is constructed by expressing the velocity through the canonical momentum in equation (1.39) to find

$$\mathcal{H}(\mathbf{r}, \mathbf{P}_{can}, t) = c\sqrt{m^2c^2 + \left(\mathbf{P}_{can}(t) - \frac{q}{c}\mathbf{A}(\mathbf{r}, t)\right)^2} + q\Phi(\mathbf{r}, t). \quad (1.40)$$

For a more thorough discussion, see Arnold [1989].

The equations of motion are obtained from the Hamiltonian function by means of Hamilton's equations

$$\dot{\mathbf{P}}_{can} = -\frac{\partial \mathcal{H}}{\partial \mathbf{r}} \quad \text{and} \quad \dot{\mathbf{r}} = \frac{\partial \mathcal{H}}{\partial \mathbf{P}_{can}}. \quad (1.41)$$

Hamilton's (1.41) equations and the Euler-Lagrange equations (1.37) yield the same solutions for the particle's phase-space trajectories and are equivalent. The Euler-Lagrange equations are a set of  $n$  second-order differential equations and Hamilton's equations are a set of  $2n$  first-order differential equations, where  $n$  is the number of spatial dimensions considered.

#### 1.1.4.2 The relativistic threshold

The argumentation below follows Meyer-ter Vehn et al. [2001].

The magnitudes of magnetic and electric field in an electromagnetic wave in vacuum are identical  $|\mathbf{E}| = |\mathbf{B}|$  and the dynamics of an electron with charge  $q = -e$  in such a wave is according to the Lorentz force (1.38) dominated by the electric field as long as  $|\mathbf{v}| \ll c$  and the leading order dynamics in this case is defined by

$$\frac{d\mathbf{p}}{dt} = -e\mathbf{E}. \quad (1.42)$$

If the electron was at rest initially and the wave is either polarized in the  $x$ -direction or circularly polarized, equations (1.3a) and (1.15) yield for the electron momentum

$$\begin{aligned} \mathbf{u} &= \mathbf{a} & (1.43) \\ &= a_0 \times \begin{cases} \cos(\mathbf{k} \cdot \mathbf{r} - \omega t - \alpha) \hat{\mathbf{e}}_x & \text{for LP,} \\ \cos(\mathbf{k} \cdot \mathbf{r} - \omega t - \alpha) \hat{\mathbf{e}}_x \mp \sin(\mathbf{k} \cdot \mathbf{r} - \omega t - \alpha) \hat{\mathbf{e}}_y & \text{for CP.} \end{cases} \end{aligned}$$

where the *normalized vector potential* and *normalized electron momentum*

$$\mathbf{a} = \frac{e\mathbf{A}}{m_e c^2}, \quad a_0 = \frac{eA_0}{m_e c^2}, \quad (1.44)$$

$$\mathbf{u} = \frac{\mathbf{p}}{m_e c} = \boldsymbol{\beta} \gamma, \quad (1.45)$$

respectively, were introduced and  $\boldsymbol{\beta} = \mathbf{v}/c$  is the velocity normalized to the speed of light. Equation (1.43) simply describes a harmonic oscillation of the electron in the transverse plane, the *quiver motion*.

The quiver momentum in a linearly polarized electric light field is relativistic, when the amplitude of the light wave reaches  $a_0 \sim 1$ .

Intensity and normalized vector potential are through (1.35) related by the equality

$$I_0 = \frac{c\pi}{2} \left( \frac{a_0 m_e c^2}{e\lambda} \right)^2, \quad (1.46)$$

such that the relativistic threshold  $a_0 \simeq 1$  is associated with an intensity of  $I_0 \simeq 10^{18} \text{ W cm}^{-2}$  for  $\lambda \simeq 1 \mu\text{m}$  [Meyer-ter Vehn et al., 2001]. As mentioned before, intensities of today's laser systems readily exceed this value and can provide highly relativistic field amplitudes  $a_0 \gg 1$ . Of course, if  $a_0$  becomes comparable to 1, equation (1.42) does not hold anymore and the effect of the magnetic field has to be taken into account. This is done in the following.

### 1.1.4.3 Electron dynamics in plane electromagnetic waves

The relativistic dynamics of an electron acted upon by a plane electromagnetic wave can be derived analytically. It can first be noted, that the Lagrangian function for an electron acted upon by a plane electromagnetic wave which travels in  $z$ -direction does not have any dependence on transverse directions  $\partial\mathcal{L}/\partial\mathbf{r}_\perp = 0$ . Hence, the Euler-Lagrange equation (1.37) implies for the transverse canonical momentum to be invariant

$$\frac{d}{dt} \frac{\partial\mathcal{L}}{\partial\mathbf{v}_\perp} = \frac{d\mathbf{P}_{can,\perp}}{dt} = \frac{d}{dt} \left( \mathbf{p}_\perp - \frac{e}{c} \mathbf{A}_\perp \right) = 0 \quad (1.47)$$

for this problem. Furthermore, the vector potential of a plane wave in vacuum is invariant under a Gallilean transformation, i.e.  $\mathbf{A}(z, t) = \mathbf{A}(z - ct)$ . Hence, the following relation holds for the Lagrangian function,

$$-\frac{\partial\mathcal{L}}{\partial t} = c \frac{\partial\mathcal{L}}{\partial z} = c \frac{d}{dt} \frac{\partial\mathcal{L}}{\partial v_z} = c \frac{dP_{can,z}}{dt} = c \frac{dp_z}{dt}, \quad (1.48)$$

where the last equality is due to the fact that  $A_z = 0$  in a transverse wave. With

$$\frac{\partial\mathcal{L}}{\partial t} = -\frac{\partial\mathcal{H}}{\partial t} = m_e c^2 \frac{\partial\gamma}{\partial t}, \quad (1.49)$$

the invariant quantity  $m_e c^2 \gamma - cp_z = \text{const}$  is found. If the electron was at rest initially, the above equations together imply

$$cp_z = m_e c^2 (\gamma - 1), \quad \text{or equivalently} \quad u_z = \gamma - 1. \quad (1.50)$$

Hence, with the equalities  $\gamma = \sqrt{1 + \mathbf{u}_\perp^2 + u_z^2}$ , and  $\mathbf{a} = \mathbf{a}_\perp$  the equations of motion in normalized units give

$$\mathbf{u}_\perp = \gamma \frac{d\mathbf{r}_\perp}{dct} = \mathbf{a}, \quad (1.51a)$$

$$u_z = \gamma \frac{dz}{dct} = \frac{\mathbf{a}^2}{2}. \quad (1.51b)$$

*The derivation here follows Meyer-ter Vehn et al. [2001].*

*The general relationship between such symmetries and invariants is addressed by the Noether theorem [Arnold, 1989].*

For the solution of these equations of motion, it is convenient to introduce the variable  $\tau = t - z(t)/c$ , such that  $\mathbf{a}(z - ct) = \mathbf{a}(c\tau)$  for the plane wave. The derivatives in Eqns. (1.51a) and (1.51b) then transform according to [Meyer-ter Vehn et al., 2001]

$$\gamma \frac{d}{dt} = \gamma \frac{d\tau}{dt} \frac{d}{d\tau} = \left(\gamma - \frac{\mathbf{a}^2}{2}\right) \frac{d}{d\tau} = \frac{d}{d\tau}, \quad (1.52)$$

where  $\gamma = u_z + 1 = \mathbf{a}^2/2 + 1$  was used, and the equations of motion reduce to

$$\frac{d\mathbf{r}_\perp}{d\tau} = c\mathbf{a}, \quad (1.53a)$$

$$\frac{dz}{d\tau} = c \frac{\mathbf{a}^2}{2}. \quad (1.53b)$$

The light wave pulse is now assumed to be of linear polarization and to have a box-shaped envelope

$$\mathbf{a} = \begin{cases} a_0 \cos(\omega\tau) \hat{\mathbf{e}}_x & \text{for } 0 < \tau < 2\pi N/\omega, \\ 0 & \text{otherwise,} \end{cases} \quad (1.54)$$

where  $N$  is the number of wave-cycles in the pulse. If the electron is at position  $x(\tau \leq 0) = z(\tau \leq 0) = 0$  initially, the trajectory is given by [Meyer-ter Vehn et al., 2001]

$$x(\tau) = ca_0 \int_0^\tau \cos(\omega\tau') d\tau' = \frac{ca_0}{\omega} \sin(\omega\tau), \quad (1.55a)$$

$$z(\tau) = \frac{ca_0^2}{2} \int_0^\tau \cos^2(\omega\tau') d\tau' = \frac{ca_0^2}{8\omega} (2\omega\tau + \sin(2\omega\tau)), \quad (1.55b)$$

for  $0 < \tau < 2\pi N/\omega$ , and  $x(\tau) = 0$  and  $z(\tau) = ca_0^2\pi N/2\omega$  for  $\tau \geq 2\pi N/\omega$ . During the interaction, the electron experiences an average drift with velocity

$$\beta_{z,d} = \frac{v_{z,d}}{c} = \frac{\overline{dz}}{dct} = \frac{1}{c\gamma} \frac{dz}{d\tau} = \frac{\mathbf{a}^2}{2\gamma}, \quad (1.56)$$

such that, in the specific case of a box-shaped laser envelope,

$$\beta_{z,d} = 1 - \frac{1}{\sqrt{1 + a_0^2/2}}. \quad (1.57)$$

After the passage of such a light pulse with a box-shaped temporal envelope, the electron is at rest again, but shifted by a distance of  $ca_0^2\pi N/2\omega$  in the propagation direction of the light pulse. The trajectory of the electron is depicted in normalized units in Figure 1 for this case.

It can be noted, that the average motion is directed along the  $z$ -axis and scales with  $a_0^2$ . The transverse motion in the  $x$ -direction scales



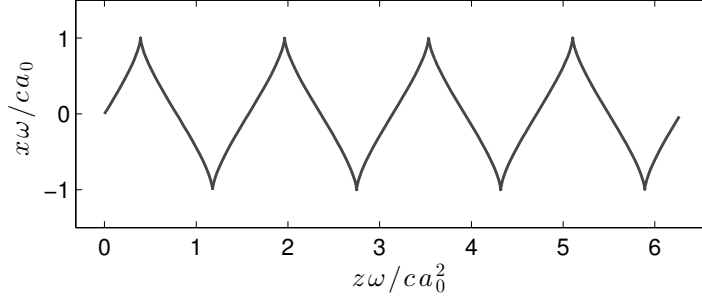


Figure 1: Trajectory of an electron interacting with a plane light-pulse of finite duration with  $N = 4$  in normalized amplitudes.

with  $a_0$ . Hence, for  $a_0 \ll 1$  the transverse motion dominates over the longitudinal motion and vice versa for  $a_0 \gg 1$ . This can be seen more clearly for a light pulse with a Gaussian envelope

$$\mathbf{a} = a_0 \exp\left(-\frac{\tau^2}{\tau_d^2}\right) \cos(\omega\tau) \hat{\mathbf{e}}_x, \quad (1.58)$$

which traverses an electron at rest. Here,  $\tau_d$  is the pulse duration. Figure 2 shows the numerical solution of Eqns. (1.53a) and (1.53b) for such a scenario. It can be seen that the electron predominantly oscillates in the transverse plane for small field amplitudes, whereas it is pushed in the propagation direction of the pulse as the amplitude increases. However, there is no net energy gain of the electron by virtue of this process and it is at rest after the pulse has passed.

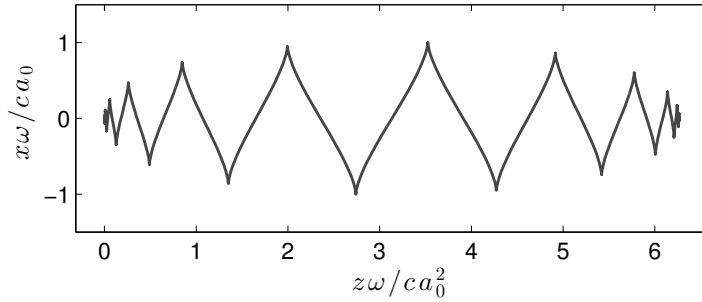


Figure 2: Trajectory of an electron interacting with a Gaussian light pulse for  $\omega\tau_d = 20$  in normalized amplitudes .

Plane electromagnetic waves cannot directly be used for the efficient acceleration of electrons. This fact is expressed in the Lawson-Woodward theorem [Lawson, 1979] [Palmer, 1982] which states, that electrons do not receive a net energy gain in plane electromagnetic waves under the following assumptions. (a) The interaction region is infinite, (b) the interaction occurs in vacuum with no boundaries present, (c) the electron is highly relativistic in the propagation direction of the light wave ( $v_z \simeq c$ ), (d) no external fields are present, (e) nonlinear effects can be neglected. Hence, at least one of these as-

assumptions must be violated to allow for efficient acceleration (see the discussion by [Esarey et al. \[2009, part I.B.\]](#)).

Instead of using the ultra-high electric fields in a highly intense laser-pulse to accelerate electrons directly, a more promising approach, as explicated within the scope of this work, focuses a highly intense laser-pulse into a plasma and excites large amplitude plasma waves. Electrons potentially get trapped in the plasma wave and gain high energies. This approach violates the assumptions (a), (b) and (e) in the Lawson-Woodward theorem and hence allows for efficient electron acceleration. The key idea is to first transfer the energy contained in the laser-pulse to the plasma wave, which in turn transfers the energy by means of the fields carried by the wave to a set of charged particles, which are placed in it.

## 1.2 PROPERTIES OF PLASMAS

Phenomena in plasma-based acceleration fundamentally depend on the unperturbed state of the plasma as well as on the characteristic length and time-scales and the type of the involved effects. Hence, a basic understanding of the attributes of plasmas is vital when studying plasma-based acceleration.

### 1.2.1 Plasma definition

The term plasma encompasses ionized matter with a wide range of temperatures and densities and associated physical effects. However, ionized matter is not automatically a plasma and an appropriate definition for a majority of the diverse manifestations of plasmas is given by the following criteria. A plasma is a *quasineutral* accumulation of charged (and neutral) particles which exhibits *collective effects* (cf. [[Chen, 2010](#)]). The interpretation of the properties of quasineutrality and exhibition of collective effects is given below.

#### 1.2.1.1 Debye shielding and collective effects

An important feature of a plasma is its ability to shield out the potential  $\Phi$  of a test particle with charge  $q$  which is inserted into the plasma. Pictorially, this is caused by the oppositely charged plasma particles which accumulate around the test charge. Instead of the Coulomb-type dependency of the electrostatic potential in vacuum  $\Phi \sim q/r$ , the potential in plasma decays asymptotically according to  $\Phi \sim q/r \exp(-r/\lambda_D)$ . The characteristic decay length  $\lambda_D$  is called *Debye length* and is defined by the following equations [[Spatschek, 1990](#)]

$$\frac{1}{\lambda_D^2} = \frac{1}{\lambda_{D,e}^2} + \frac{1}{\lambda_{D,i}^2}, \quad (1.59)$$

*Considerations here follow Spatschek [1990]. This reference is also recommended for further reading.*

where  $\lambda_{D,e}$  is the Debye length from the shielding by the plasma electrons and  $\lambda_{D,i}$  from the ions. These contributions to the Debye length for electrons ( $e$ ) or single-charged ions ( $i$ ) are given by

$$\lambda_{D,e,i}^2 = \frac{k_B T_{e,i}}{4\pi n_{e,i} e^2}, \quad (1.60)$$

where  $n$  is the particle density,  $T$  the temperature, and  $k_B$  the Boltzmann constant. The temperature plays a role in the shielding properties of the plasma, since a strong thermal motion qualitatively allows shielding particles to escape from the potential well, hence disrupting the shielding. A larger plasma density implies a shorter Debye length, since more plasma particles participate in the collective screening process. A plasma with spatial dimensions much larger than the Debye length  $L \gg \lambda_D$  is electrically neutral to an observer outside of the plasma. Moreover, internally the plasma is considered quasineutral on length-scales much larger than the Debye length.

Obviously, collective shielding can occur only, if the mean distance between plasma particles  $\sim n^{-1/3}$  is much smaller than the Debye length. This argument yields the condition [Spatschek, 1990]

$$\frac{k_B T_{e,i}}{n^{1/3} e^2} \gg 1, \quad (1.61)$$

for Debye shielding to take place. In other words, a Debye sphere  $\lambda_D^3 4\pi/3$  must contain a large number of charged particles to enable quasineutrality and to allow for collective effects to occur. Plasmas fulfilling this condition are called *ideal plasmas*, analogous to an ideal gas in which interactions between particles can be neglected compared to the thermal motion of the gas. The above requirement can also be expressed by means of the *plasma parameter*

$$\Lambda = \frac{4\pi}{3} n \lambda_D^3, \quad (1.62)$$

with the constraint  $\Lambda \gg 1$ . Furthermore, this condition can also be interpreted as the mean kinetic energy  $\sim k_B T$  dominating over the mean potential energy  $\sim n^{1/3} e^2$ , permitting collective effects [Spatschek, 1990]. The criterion of quasineutrality ( $L \gg \lambda_D$ ) is strongly related to the existence of collective effects ( $\Lambda \gg 1$ ). The characterization of a plasma is completed in the following by a condition which addresses the domination of collective over individual processes.

### 1.2.1.2 Time-scales of collective and individual processes

The considerations below aim at finding an estimation for the collision frequency of the plasma constituents and comparison of this frequency to characteristic frequencies in collective processes.

The characteristic collective response time of the plasma to a perturbation can be estimated in the following way (see [Spatschek, 1990]). The mean kinetic velocity of a plasma particle is given by

$$v_t = \sqrt{\frac{k_B T}{m}}, \quad (1.63)$$

and the time-scale for the passage of a distance equal to the Debye length is  $\tau = \omega^{-1} = \lambda_D / v_t$ . Characteristic response frequencies for the plasma electrons and single-charged plasma ions are hence (cf. [Tonks and Langmuir, 1929])

$$\omega_{pe} = \sqrt{\frac{4\pi n_e e^2}{m_e}} \quad \text{and} \quad \omega_{pi} = \sqrt{\frac{4\pi n_i e^2}{m_i}}, \quad (1.64)$$

respectively. Ions have a much greater mass than electrons, with a ratio of  $m_e / m_i \approx 5.49 \times 10^{-4}$  for a hydrogen plasma and less for ions with larger nucleon number. Plasma frequencies of ions and electrons therefore differ by at least two orders of magnitude. Hence, the total plasma wavelength  $\omega_p^2 = \omega_{pe}^2 + \omega_{pi}^2$  (see [Spatschek, 1990]) is generally dominated by the quicker plasma electron response time, such that

$$\omega_p \simeq \omega_{pe} = \sqrt{\frac{4\pi n_0 e^2}{m_e}} \quad (1.65)$$

where  $n_0$  here and henceforth denotes the ambient plasma electron density. This frequency defines the characteristic collective response-time of a plasma when perturbed out of the equilibrium state. Plasma electrons excited by an external force overshoot their initial position and collectively oscillate around it at the plasma frequency as described in 1.4.4.1.

Binary collisions between plasma constituents are typical examples of individual phenomena. In order to assess the dominance of collective over individual processes, the time-scales of the two need to be compared. For this reason, a collision frequency is derived. It first needs to be noted that elastic collisions between identical particles do not significantly contribute to relevant individual-event-driven effects like particle diffusion. This is due to the fact that identical particles only exchange trajectories during the collision process, so that the final state of the indistinguishable particles, long after the collision occurred, is identical to the final state without the collision taking place. However, the elastic collision of unlike particles with a large mass disparity causes diffusion, because the momentum transfer between the different particle species results in a blowup of the phase-space volume of the individual plasma constituents [Robson, 2006; Chen, 2010].

The following examines the Coulomb collisions between electrons with charge  $-e$  and single-charged ions with charge  $e$ , which, due

*For a more detailed derivation of the plasma frequency confer e. g. [Chen, 2010].*

*This approximation holds for all plasma phenomena regarded in this work.*

to their low temperature and large inertia, are assumed to be at rest. The differential scattering cross section of this process is given by the Rutherford formula [Povh et al., 2008]

$$\frac{d\sigma}{d\Omega} = \left( \frac{e^2}{4E_{kin} \sin^2 \frac{\theta}{2}} \right)^2, \quad (1.66)$$

where  $E_{kin}$  is the kinetic energy of the incident electron ( $E_{kin} \approx v^2 m_e / 2$  for nonrelativistic velocities) and  $\theta$  is the deflection angle. The average cross section for momentum transfer by virtue of this process, which is the relevant measure for diffusion effects, is given by [Robson, 2006]

$$\begin{aligned} \sigma_m &= \int (1 - \cos \theta) d\sigma \\ &= \int \left( \frac{d\sigma}{d\Omega} \right) (1 - \cos \theta) d\Omega \\ &= 2\pi \int_0^\pi \left( \frac{d\sigma}{d\Omega} \right) (1 - \cos \theta) \sin \theta d\theta. \end{aligned} \quad (1.67)$$

From equations (1.66) and (1.67) it can be seen that the momentum transfer cross section is dominated by small-angle ( $\theta \ll 1$ ) contributions. Although individual large-angle deflections result in greater momentum transfers, deflections by small angles are much more probable and therefore dominate the average momentum transfer. Expanding (1.67) in the small angle limit yields

$$\sigma_m \simeq \pi \left( \frac{2e^2}{v^2 m_e} \right)^2 \int_0^{\theta_{max}} \theta^{-1} d\theta. \quad (1.68)$$

The Rutherford scattering cross section used for the derivation for this formula assumes a Coulomb potential of the target ion. However, as discussed previously, the Coulomb potential in a plasma is shielded off exponentially at distances larger than the Debye length. Larger distances of the electron to the ion during the scattering process, or more accurately a larger impact parameter, implies smaller deflection angles. Hence, to account for Debye shielding, a lower cutoff for the deflection angles  $\theta_{min}$  can be introduced, such that

$$\sigma_m \simeq \pi \left( \frac{2e^2}{v^2 m_e} \right)^2 \log \left( \frac{\theta_{max}}{\theta_{min}} \right). \quad (1.69)$$

The last term in the above equation is called the *Coulomb logarithm* and is commonly approximated by  $\log(\theta_{max}/\theta_{min}) \approx \log(\Lambda)$  [Spatschek, 1990; Chen, 2010]. It expresses the domination of more probable events with small deflection angles over the rare large deflection angle events for the average momentum transfer.

The collision frequency for momentum transfer is given by the cross section multiplied by the target density and the average elec-

*This is the primal argumentation for the Fokker-Planck approach.*

tron velocity  $v_m = \sigma_m n_i v$ . Plugging the approximation (1.69) into this relation and given that  $n_i = n_0$  for single charged ions yields

$$v_m \approx \frac{4\pi n_0 e^4}{v^3 m_e^2} \log(\Lambda). \quad (1.70)$$

This collision frequency finally allows a comparison of frequencies of collective and individual processes [Spatschek, 1990]

$$\frac{\omega_p}{v_m} \approx \frac{\Lambda}{\log(\Lambda)} \approx \Lambda \gg 1. \quad (1.71)$$

The condition for a dominance of collective effects over individual (collisional) effects is thus also related to the plasma parameter being large compared to unity.

### 1.2.2 Plasma classification

#### 1.2.2.1 Ideal and non-ideal plasmas

Important plasma parameters, as the above introduced, depend on the temperature and density of the plasma. The plasma frequency scales according to  $\omega_p \sim n_0^{1/2}$ , the Debye length has the proportionality  $\lambda_D \sim (T_e/n_0)^{1/2}$  and the plasma parameter has the dependencies  $\Lambda \sim n_0(T_e/n_0)^{3/2}$ . Hence, the large variety of plasmas can be characterized by their densities and temperatures. Such a classification is depicted in Figure 3. The line, separating ideal and non-ideal plasma refers to the threshold when the left term in equation 1.61 is equal to one. The density of plasma used for the acceleration of

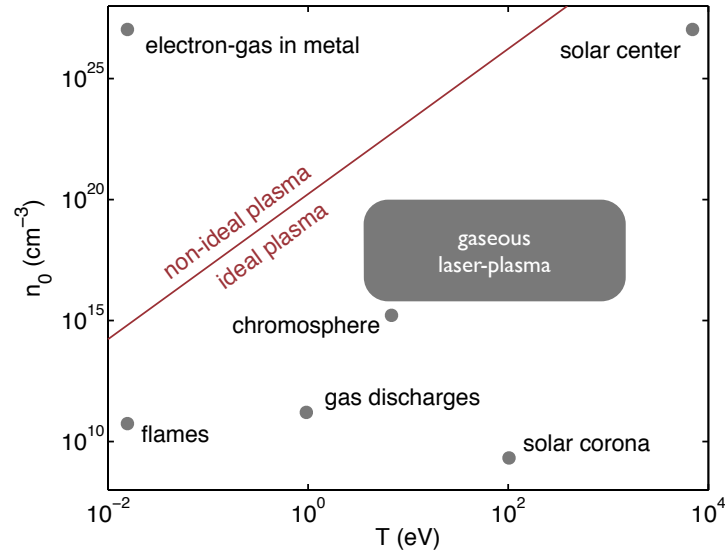


Figure 3: Plasma classification (compare [Gibbon, 2005]). The red line refers to the threshold when the left term in equation 1.61 is equal to one.

electrons ranges from  $10^{15}$  to  $10^{20} \text{ cm}^{-3}$ . The gas is photo-ionized by laser-pulses, which heat the plasma-electrons during and after the ionization process to temperatures of 10 to 1000 eV [Durfee et al., 1995]. Such photo-ionized laser-plasma is, as seen in Figure 3, an ideal plasma with a plasma parameter  $\Lambda$  spanning values from  $10^3 - 10^9$ . Collisions between the plasma species and related effects are negligible for plasmas regarded in this work and do not affect the collective phenomena e. g. the excitation of plasma waves.

#### 1.2.2.2 Electromagnetic waves in plasmas - underdense and overdense plasmas

Electromagnetic waves propagating in a plasma follow the dispersion relation [Chen, 2010]

$$\omega^2 = \omega_p^2 + c^2 k^2, \quad (1.72)$$

where  $\omega$  is the wavelength and  $k$  the wave number of the light pulse. The phase velocity, equation (1.21), of such a light wave in a plasma is greater than the speed of light in vacuum

$$v_{ph}^2 = \frac{\omega^2}{k^2} = c^2 + \frac{\omega_p^2}{k^2} > c^2. \quad (1.73)$$

The group velocity of the pulse in a plasma, defined by equation (1.20), is smaller than the speed of light, with

$$v_g = \frac{d\omega}{dk} = \frac{c^2}{\sqrt{\omega_p^2/k^2 + c^2}} = \frac{c^2}{v_{ph}}, \quad (1.74)$$

since the phase velocity is greater than  $c$ .

The dispersion relation (1.72) has several implications for the propagation of a light wave with frequency  $\omega$  in a plasma. Firstly, for a decreasing plasma density  $n_0$  with  $\omega_p \sim n_0^{1/2}$ , the expected dispersion relation of a light wave in vacuum is asymptotically recovered. However, when increasing the plasma frequency  $\omega_p$  towards  $\omega$ , the dispersion starts to differ from a vacuum-like dispersion. This can be seen when rearranging the dispersion relation, so that

$$k = \sqrt{\frac{\omega^2 - \omega_p^2}{c^2}}. \quad (1.75)$$

The wave number  $k$  decreases for increasing  $n_0$  and finally is zero for  $\omega_p = \omega$  at a *critical plasma density* of

$$n_c = \frac{\omega^2 m_e}{4\pi e^2}. \quad (1.76)$$

For even greater plasma densities, equation (1.72) cannot be fulfilled for a real value of  $k$ . Electromagnetic waves can therefore not propagate in a plasma with such densities. Plasma with densities above the

*The following considerations are in line with Chen [2010, Chapter 4.12].*

critical density are called *over-dense plasma* and plasma with densities well below  $n_c$  are called *under-dense plasma*. Light waves with frequencies of  $\omega \simeq 2 \times 10^{15}$  Hz (e. g. as produced in Ti-sapphire lasers) are associated to critical densities of  $n_c \simeq 2 \times 10^{21} \text{ cm}^{-3}$ . This work addresses only the physics of under-dense plasmas.

The group velocity of a light packet in an underdense plasma ( $\omega \gg \omega_p$ ), from equations (1.73), (1.74) and (1.75), is

$$v_g = c \sqrt{1 - \left(\frac{\omega_p}{\omega}\right)^2}. \quad (1.77)$$

As  $\omega_p$  increases, the group velocity of a light packet decreases. When the plasma density approaches zero, the group velocity approaches the speed of light, as expected.

For over-dense plasma, equation (1.75) can be written as  $k = i|\omega_p^2 - \omega^2|^{1/2}/c$ . The spatial dependence of the light wave is given by  $\exp(ikz)$  (see 1.15) and the imaginary wave number hence implies an exponential decay of the wave amplitude with the characteristic decay length, the *skin depth*,  $|k^{-1}| = c/(\omega_p^2 - \omega^2)^{1/2}$ . Although only having physical meaning as a characteristic attenuation length in an over-dense plasma, the term "skin-depth" will be used in the present work to define a characteristic length-scale in acceleration of electrons in underdense plasma with the asymptotic definition  $k_p^{-1} := c/\omega_p$ .

### 1.3 MATHEMATICAL DESCRIPTION OF PLASMAS

#### 1.3.1 Model hierarchy

After the discussion of the definition and general properties of a plasma, the focus now lies on the mathematical description of plasma. A plasma consists of a large number of charged particles and the elementary approach considers the motion of each single particle in the fields of all other particles. While being rigorous, this *microscopic picture* is in most cases of no practical interest although it serves as a starting point for the *kinetic picture*. As mentioned before, the plasma is dominated by collective effects and it is sufficient to regard the statistical averages of the ensemble of plasma particles. Furthermore, a large spectrum of plasma phenomena can be accurately described by the more simplified *macroscopic picture* which follows from the kinetic picture when only the (momentum) moments are relevant. The hierarchy of these models can be seen in Figure 4.

This work will make use of the kinetic and the fluid picture of plasmas. In order to understand which approximations these pictures involve and to make sure the model used is appropriate for the description of a given phenomenon, a short derivation from the microscopic to the kinetic picture and from the kinetic to the macroscopic picture will be presented in the following.

For a detailed discussion see [Decker and Mori, 1994].



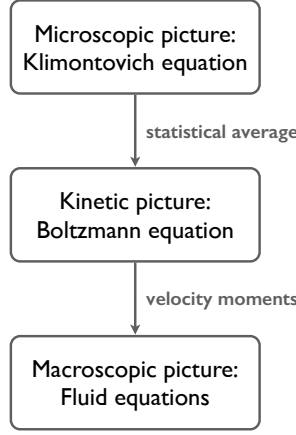


Figure 4: Plasma model hierarchy from microscopic to macroscopic picture (confer [Gibbon, 2005]).

1.3.2 Microscopic description

In 1.1.4, the dynamics of single particles in externally prescribed fields was addressed. This can be used as a footing for the description of the large number of charged point-like particles in a plasma. However, the place of external fields is now taken by *self-consistent* fields, whose sources are the charges and currents of the particles itself (and external fields).

*This derivation follows Nicholson [1983, ch. 3].*

The charge and current density of the plasma-electrons and all ion species in this microscopic picture is given by

$$\rho^m(\mathbf{r}, t) = \sum_s q_s \int d\mathbf{p} f_s^m(\mathbf{r}, \mathbf{p}, t), \tag{1.78a}$$

$$\mathbf{J}^m(\mathbf{r}, t) = \sum_s q_s \int d\mathbf{p} \mathbf{v} f_s^m(\mathbf{r}, \mathbf{p}, t), \tag{1.78b}$$

$$\mathbf{v} = \frac{\mathbf{p}}{m_s \sqrt{1 + (\mathbf{p}/m_s c)^2}}, \tag{1.78c}$$

where the subscript  $s$  denotes the species, and  $q_s$  and  $m_s$  are the charge and mass of the particle species, respectively. The quantity  $f_s^m$  here stands for the microscopic time-dependent density distribution in six-dimensional phase space of a given species with  $N_s$  particles

$$f_s^m(\mathbf{r}, \mathbf{p}, t) = \sum_{i=1}^{N_s} \delta(\mathbf{r} - \mathbf{R}_i(t)) \delta(\mathbf{p} - \mathbf{P}_i(t)), \tag{1.79}$$

with  $\delta$  denoting the Dirac delta function and  $\mathbf{R}_i$  and  $\mathbf{P}_i$  refer in this context to the single particle position and momentum. Within this derivation, the capitalised position and momentum are *Lagrangian* quantities which move with the particles, whereas  $\mathbf{r}$  and  $\mathbf{p}$  refer to the coordinates in 6D phase space. Fields, current or charge densities

*The differentiation between Lagrangian and Eulerian quantities also plays an integral role in the numerical PIC method.*

are on the other hand of *Eulerian* type. The microscopic field configurations  $\mathbf{E}^m(\mathbf{r}, t)$  and  $\mathbf{B}^m(\mathbf{r}, t)$  are then obtained by means of equations (1.1a)-(1.1d) and the equations of motion for the single particles read

$$\frac{d\mathbf{R}_i}{dt} = \mathbf{V}_i(t), \quad (1.80a)$$

$$\frac{d\mathbf{P}_i}{dt} = q_s \mathbf{E}(\mathbf{R}_i(t), t) + \frac{q_s}{c} \mathbf{V}_i(t) \times \mathbf{B}(\mathbf{R}_i(t), t), \quad (1.80b)$$

where

$$\mathbf{V}_i = \frac{\mathbf{P}_i}{m_s \sqrt{1 + (\mathbf{P}_i/m_s c)^2}}, \quad (1.81)$$

and the term on the right-hand side of equation (1.80b) expresses the Lorentz force (1.38), imposed on the particle.

### 1.3.2.1 Klimontovich equation

Equations (1.78a) to (1.80b) serve as a basis for the formulation of the exact evolution of the plasma. The time derivative of the particle density gives [Nicholson, 1983]

$$\begin{aligned} \frac{\partial f_s^m(\mathbf{r}, \mathbf{p}, t)}{\partial t} = & - \sum_{i=1}^{N_s} \frac{\partial \mathbf{R}_i}{\partial t} \frac{\partial}{\partial \mathbf{r}} \delta(\mathbf{r} - \mathbf{R}_i(t)) \delta(\mathbf{p} - \mathbf{P}_i(t)) \\ & - \sum_{i=1}^{N_s} \frac{\partial \mathbf{P}_i}{\partial t} \frac{\partial}{\partial \mathbf{p}} \delta(\mathbf{r} - \mathbf{R}_i(t)) \delta(\mathbf{p} - \mathbf{P}_i(t)). \end{aligned} \quad (1.82)$$

Partial and total temporal derivative of  $\mathbf{R}_i(t)$  or  $\mathbf{P}_i(t)$  are identical and equations (1.80a) and (1.80b) can be plugged into (1.82) to give

$$\begin{aligned} \frac{\partial f_s^m(\mathbf{r}, \mathbf{p}, t)}{\partial t} = & -\mathbf{v} \cdot \frac{\partial}{\partial \mathbf{r}} \sum_{i=1}^{N_s} \delta(\mathbf{r} - \mathbf{R}_i(t)) \delta(\mathbf{p} - \mathbf{P}_i(t)) \\ & - q_s \left[ \mathbf{E}^m(\mathbf{r}, t) + \frac{\mathbf{v}}{c} \times \mathbf{B}^m(\mathbf{r}, t) \right] \cdot \frac{\partial}{\partial \mathbf{p}} \sum_{i=1}^{N_s} \delta(\mathbf{r} - \mathbf{R}_i(t)) \delta(\mathbf{p} - \mathbf{P}_i(t)). \end{aligned} \quad (1.83)$$

The sums over the delta functions on the right hand side of (1.83) are identical to the particle density (1.79) and incorporation this finding yields the *Klimontovich equation* [Nicholson, 1983]

$$\begin{aligned} \frac{\partial f_s^m(\mathbf{r}, \mathbf{p}, t)}{\partial t} + \mathbf{v} \cdot \frac{\partial f_s^m(\mathbf{r}, \mathbf{p}, t)}{\partial \mathbf{r}} \\ + q_s \left( \mathbf{E}^m(\mathbf{r}, t) + \frac{\mathbf{v}}{c} \times \mathbf{B}^m(\mathbf{r}, t) \right) \cdot \frac{\partial f_s^m(\mathbf{r}, \mathbf{p}, t)}{\partial \mathbf{p}} = 0. \end{aligned} \quad (1.84)$$

This formula includes the equations of motion of all  $N_s$  particles and evolves the particle distribution along the single particle trajectories, which are the mathematical *characteristics* of the partial differential equation (1.84) [Callen, 2006]. The Klimontovich equation provides in combination with the Maxwell equation an exact classical

description of the evolution of the various plasma species (neglecting quantum-mechanical effects). From a known initial state  $f^m(\mathbf{r}, \mathbf{p}, t = 0) = \sum_s f_s^m(\mathbf{r}, \mathbf{p}, t = 0)$ , the system evolves completely deterministic according to (1.84). Discrete particle effects like classical radiation and elastic scattering are reproduced accurately by the Klimontovich-Maxwell system.

However, such an approach is usually impracticable and the individual particle information is often not of interest. A plasma is dominated by collective effects and a useful approach for a mathematical description of a plasma should reflect this by regarding only the average properties of the plasma. Consideration of only average properties of the plasma constitutes the transition from the microscopic to the kinetic picture, which is outlined in the following.

### 1.3.3 Kinetic description

#### 1.3.3.1 Statistical averaging

Instead of retaining the individual discrete particle information by use of the Klimontovich equation, a widely used and more practicable approach addresses the evolution of the statistical averages of the particle ensemble only. Although resulting from averaging of the microscopic particle description, it still features information and phenomena related to the motion of charged particles, and is hence also considered a *kinetic* description of the plasma. In the following, a heuristic interpretation of statistical averaging is illustrated (inspired by [Nicholson, 1983; Spatschek, 1990; Callen, 2006]).

When reviewing the latter considerations, it is noted that the Klimontovich equation (1.84) governs the evolution of the discrete particle distribution (1.79), which tells whether or not a particle populates a given position in phase-space at a given time. To obtain a smooth distribution function, the microscopic particle distribution is averaged over a small volume  $\Delta V = \Delta x \Delta y \Delta z \Delta p_x \Delta p_y \Delta p_z$  in six-dimensional phase space. The edge lengths should thereby be much larger than the average particle spacing in phase-space, i.e.  $\Delta x \gg n^{-1/3}$  in configuration space and  $\Delta p_x \gg m_s v_t n^{-1/3} \lambda_D^{-1}$  in momentum space [Callen, 2006]. This is in order to guarantee averaging over a large number of particles and a low fluctuation of average particle number in the volume. Moreover, the spatial edge length should be shorter than the Debye length  $\Delta x \ll \lambda_D$  to allow a description in terms of collective effects on or below the Debye scale. These constraints can always be fulfilled, since an edge length with  $n^{-1/3} \ll \Delta x \ll \lambda_D$  is easily found

*The radiation emitted by relativistic electrons in plasma-based acceleration is of interest.*

*A rigorous formulation of ensemble averaging is found e. g. in Spatschek [1990].*

in a plasma. The statistical average of the distribution function can now be defined by [Callen, 2006]

$$\begin{aligned} \langle f_s^m(\mathbf{r}, \mathbf{p}, t) \rangle &:= \lim_{n^{-1/3} \ll \Delta x \ll \lambda_D} \frac{1}{\Delta V} \int_{\Delta V} d\mathbf{r} d\mathbf{p} f_s^m(\mathbf{r}, \mathbf{p}, t) \\ &= \lim_{n^{-1/3} \ll \Delta x \ll \lambda_D} \frac{\int_{\Delta V} d\mathbf{r} d\mathbf{p} f_s^m(\mathbf{r}, \mathbf{p}, t)}{\int_{\Delta V} d\mathbf{r} d\mathbf{p}}. \end{aligned} \quad (1.85)$$

The averaged particle distribution so obtained has units of particles per phase-space volume and characterizes the smoothed attributes of the plasma species  $s$ . The error associated with performing this averaging is represented by  $\delta f_s^m = f_s^m - \langle f_s^m \rangle$  with vanishing average  $\langle \delta f_s^m \rangle = 0$ . In contrast to  $\langle f_s^m \rangle$ , the quantity  $\delta f_s^m$  incorporates the discrete particle nature of the plasma.

Not only the microscopic distribution function features the discrete particle nature but also the fields, and charge and current densities, respectively. For a consistent averaged description of the plasma these quantities also require averaging

$$\begin{aligned} \mathbf{E}^m &= \langle \mathbf{E}^m \rangle + \delta \mathbf{E}^m, & \mathbf{B}^m &= \langle \mathbf{B}^m \rangle + \delta \mathbf{B}^m, \\ \mathbf{J}^m &= \langle \mathbf{J}^m \rangle + \delta \mathbf{J}^m, & \rho^m &= \langle \rho^m \rangle + \delta \rho^m, \end{aligned} \quad (1.86)$$

with all averages of the errors also vanishing  $\langle \delta \mathbf{E}^m \rangle = \langle \delta \mathbf{B}^m \rangle = \langle \delta \mathbf{j}^m \rangle = \langle \delta \rho^m \rangle = 0$ . Plugging the above expressions (1.86) into the Klimontovich equation (1.84) and averaging of the complete equation yields [Callen, 2006]

$$\begin{aligned} \frac{\partial \langle f_s^m \rangle}{\partial t} + \mathbf{v} \cdot \frac{\partial \langle f_s^m \rangle}{\partial \mathbf{r}} + q_s \left( \langle \mathbf{E}^m \rangle + \frac{\mathbf{v}}{c} \times \langle \mathbf{B}^m \rangle \right) \cdot \frac{\partial \langle f_s^m \rangle}{\partial \mathbf{p}} \\ = -q_s \left\langle \left( \delta \mathbf{E}^m + \frac{\mathbf{v}}{c} \times \delta \mathbf{B}^m \right) \cdot \frac{\partial \delta f_s^m}{\partial \mathbf{p}} \right\rangle. \end{aligned} \quad (1.87)$$

The term on the right hand side persists, because the average of the product of the error quantities is in general not zero. It expresses effects caused by the graininess of the particle distributions and microscopic fields, such as elastic Coulomb collisions. The other terms represent the collective plasma behavior which will be studied in the following.

### 1.3.3.2 Vlasov equation

By identifying the fundamental particle distribution function with the average of the microscopic distribution function in (1.87),  $f_s(\mathbf{r}, \mathbf{p}, t) = \langle f_s^m(\mathbf{r}, \mathbf{p}, t) \rangle$ , and by identifying  $\mathbf{E} = \langle \mathbf{E}^m \rangle$  and  $\mathbf{B} = \langle \mathbf{B}^m \rangle$  as the smoothed fields, the plasma kinetic equation,

$$\frac{\partial f_s}{\partial t} + \mathbf{v} \cdot \frac{\partial f_s}{\partial \mathbf{r}} + q_s \left( \mathbf{E} + \frac{\mathbf{v}}{c} \times \mathbf{B} \right) \cdot \frac{\partial f_s}{\partial \mathbf{p}} = C(f_s), \quad (1.88)$$

is obtained from equation (1.87). The term  $C(f_s)$  represents the Coulomb collision term on the right side of (1.87).

*Equation (1.88) is not the Boltzmann equation since the right hand side is the Coulomb collision operator and not the Boltzmann collision operator (c.f. [Callen, 2006]).*

Large plasma parameters  $\Lambda \gg 1$  imply a domination of collective effects over collisional effects, as shown in 1.2.1.2. The left side of equation (1.88), accounting for collective plasma effects, can thus assumed to be  $\Lambda$  times greater than  $C(f_s)$ , representing discrete particle effects. Moreover, plasma phenomena regarded in this work occur on time-scales much quicker than the mean time between collisions, and the assumption of a collisionless plasma  $C(f_s) \simeq 0$  is thus a good approximation. The collisionless plasma kinetic equation is called the *Vlasov equation*

$$\frac{\partial f_s}{\partial t} + \mathbf{v} \cdot \frac{\partial f_s}{\partial \mathbf{r}} + q_s \left( \mathbf{E} + \frac{\mathbf{v}}{c} \times \mathbf{B} \right) \cdot \frac{\partial f_s}{\partial \mathbf{p}} = 0, \quad (1.89)$$

or equivalently, since  $\nabla_{\mathbf{p}} \cdot \mathbf{E} = \nabla_{\mathbf{p}} \cdot (\mathbf{v} \times \mathbf{B}) = 0$

$$\frac{\partial f_s}{\partial t} + \nabla_{\mathbf{r}} \cdot (\mathbf{v} f_s) + \nabla_{\mathbf{p}} \cdot \left[ q_s \left( \mathbf{E} + \frac{\mathbf{v}}{c} \times \mathbf{B} \right) f_s \right] = 0, \quad (1.90)$$

and is of fundamental importance in plasma physics and for the basis of this work. The Vlasov equation is also named the collisionless Boltzmann equation. It is connected with the Maxwell equations (1.1a)-(1.1d) through the charge and current density,

$$\rho(\mathbf{r}, t) = \sum_s q_s \int d\mathbf{p} f_s(\mathbf{r}, \mathbf{p}, t), \quad (1.91a)$$

$$\mathbf{J}(\mathbf{r}, t) = \sum_s q_s \int d\mathbf{p} \mathbf{v} f_s(\mathbf{r}, \mathbf{p}, t). \quad (1.91b)$$

The Maxwell-Vlasov system forms a closed set of equations. It should be noted that the Vlasov equation not only neglects the discrete particle effect of collisions, but also the classical discrete particle radiation, since (1.91b) constitutes only a smoothed current density. Due to the neglect of collisions, the Vlasov equation is time-reversible and its solutions follow the collisionless particle trajectories (characteristics) in phase-space. The time-reversibility of solutions of the Vlasov equation implies conservation of entropy and incompressibility of the phase space volume occupied by the particle distribution function [Callen, 2006].

#### 1.3.4 Macroscopic or fluid description

Many phenomena in plasmas can be analyzed by regarding the plasma as a fluid e.g. a composition of electron and ion fluid (two-fluid model). This assumption is particularly valid, if plasma particles in a given spatial region have only a small thermal velocity spread around a macroscopic velocity. Governing quantities in such a fluid picture are functions of three-dimensional configuration space and time only, and are obtained by forming momentum moments of the particle distribution function. This approach has the advantage of being more

*For more thorough discussion see [Nicholson, 1983; Spatschek, 1990; Callen, 2006].*

See A.1.1.

*For a more detailed discussion see [Nicholson, 1983; Callen, 2006].*

simple than the Vlasov method but neglects momentum-dependent effects.

The most important momentum moments are the spatial particle-density, fluid-momentum and fluid-velocity distributions

$$n_s(\mathbf{r}, t) = \int d\mathbf{p} f_s(\mathbf{r}, \mathbf{p}, t), \quad (1.92a)$$

$$\mathbf{p}_s(\mathbf{r}, t) = \frac{1}{n_s} \int d\mathbf{p} \mathbf{p} f_s(\mathbf{r}, \mathbf{p}, t), \quad (1.92b)$$

$$\mathbf{v}_s(\mathbf{r}, t) = \frac{1}{n_s} \int d\mathbf{p} \mathbf{v} f_s(\mathbf{r}, \mathbf{p}, t). \quad (1.92c)$$

In contrast to the Lagrangian particle velocity or momentum, the above velocity and momentum are Eulerian fluid quantities. When using these definitions and integrating the Vlasov equation (1.89) over all momentum space, the density continuity equation,

$$\frac{\partial}{\partial t} n_s + \nabla_{\mathbf{r}} \cdot (n_s \mathbf{v}_s) = 0, \quad (1.93)$$

is obtained. Here,  $f_s$  was assumed to decay to zero outside the region of interest. This is the first fundamental fluid equation and expresses the temporal change of  $n_s$ , assuming that  $n_s \mathbf{v}_s$  is known. A second fundamental fluid equation is found when multiplying the Vlasov equation with  $\mathbf{p}$  from the left and integrating (by parts) over all momentum space, yielding the fluid force equation for species  $s$  [Nicholson, 1983],

*See detailed calculation in A.1.*

$$\frac{\partial}{\partial t} (n_s \mathbf{p}_s) + \left[ \nabla_{\mathbf{r}} \cdot \left( \int d\mathbf{p} (\mathbf{v} \mathbf{p}^T f_s) \right) \right]^T = n_s q_s \left( \mathbf{E} + \frac{\mathbf{v}_s}{c} \times \mathbf{B} \right), \quad (1.94)$$

where  $\mathbf{a} \mathbf{b}^T$  is the outer product (in contrast to the inner product  $\mathbf{a}^T \mathbf{b} \equiv \mathbf{a} \cdot \mathbf{b}$ ) of the vectors  $\mathbf{a}$  and  $\mathbf{b}$  and the result is a  $3 \times 3$  matrix. It can be seen that the time-derivative of  $n_s \mathbf{p}_s$  depends on a higher-order moment.

When assuming the plasma to be cold, with  $f_s(\mathbf{r}, \mathbf{p}, t) = n_s(\mathbf{r}, t) \delta(\mathbf{p} - \mathbf{p}_s)$ , equation (1.94) can be rewritten as follows

$$\frac{\partial}{\partial t} (n_s \mathbf{p}_s) + [\nabla_{\mathbf{r}} \cdot (n_s \mathbf{v}_s \mathbf{p}_s^T)]^T = n_s q_s \left( \mathbf{E} + \frac{\mathbf{v}_s}{c} \times \mathbf{B} \right). \quad (1.95)$$

Application of the product rule for the first term on the left hand side and exploiting the identity  $(\nabla \cdot (\mathbf{a} \mathbf{b}^T))^T = \mathbf{b} (\nabla \cdot \mathbf{a}) + (\mathbf{a} \cdot \nabla) \mathbf{b}$  yields

$$\begin{aligned} n_s \frac{\partial \mathbf{p}_s}{\partial t} + \mathbf{p}_s \frac{\partial n_s}{\partial t} + \mathbf{p}_s (\nabla_{\mathbf{r}} \cdot (n_s \mathbf{v}_s)) + (n_s \mathbf{v}_s \cdot \nabla_{\mathbf{r}}) \mathbf{p}_s \\ = n_s q_s \left( \mathbf{E} + \frac{\mathbf{v}_s}{c} \times \mathbf{B} \right). \end{aligned} \quad (1.96)$$

Plugging the density continuity equation (1.93) times  $\mathbf{p}_s$  into equation (1.96) finally yields the fluid momentum equation

$$\frac{\partial \mathbf{p}_s}{\partial t} + (\mathbf{v}_s \cdot \nabla_{\mathbf{r}}) \mathbf{p}_s = q_s \left( \mathbf{E} + \frac{\mathbf{v}_s}{c} \times \mathbf{B} \right), \quad (1.97)$$

where the particle density  $n_s$  cancels out. The left hand side of equation (1.97) can also be interpreted from the viewpoint that the temporal change of the momentum of a fluid element  $d\mathbf{p}_s/dt$  is composed of the change of the fluid momentum at a fixed point in space  $\partial\mathbf{p}_s/\partial t$  and the change of the fluid momentum along the flux direction  $(\mathbf{v}_s \cdot \nabla)\mathbf{p}_s$ . Equations (1.93) and (1.97) will be used to study the behavior of plasma electrons when traversed by intense laser beams or relativistic charged particle beams.

The above method of deriving mean properties of the particle sets and their temporal evolution will be described in a more general context in the following.

### 1.3.5 Plasma kinetic theory

#### 1.3.5.1 Moment approach

Explicit solutions of the Vlasov equation (1.89) for non-trivial problems are in general difficult to find. However, often, e.g. in the above fluid description, the knowledge of a number of *moments* of the particle distribution function is sufficient. A method to obtain the time-dependence of such moments, called the *moment approach*, was already implicitly used in the derivation of the fluid equations. The following outlines the moment approach in a more general context.

If one is interested, for example, in the moment

$$\langle \Phi(\mathbf{r}, \mathbf{p}) \rangle = \frac{1}{N} \int d\mathbf{r} d\mathbf{p} \Phi(\mathbf{r}, \mathbf{p}) f(\mathbf{r}, \mathbf{p}, t), \quad (1.98)$$

with

$$N = \int d\mathbf{r} d\mathbf{p} f(\mathbf{r}, \mathbf{p}, t), \quad (1.99)$$

and its temporal evolution, the following procedure is performed. First, the Vlasov equation is multiplied with the quantity  $\Phi(\mathbf{r}, \mathbf{p})$  to obtain

$$\Phi(\mathbf{r}, \mathbf{p}) \frac{\partial f}{\partial t} + \Phi(\mathbf{r}, \mathbf{p}) \left( \mathbf{v} \cdot \frac{\partial f}{\partial \mathbf{r}} \right) + \Phi(\mathbf{r}, \mathbf{p}) \left[ q \left( \mathbf{E} + \frac{\mathbf{v}}{c} \times \mathbf{B} \right) \cdot \frac{\partial f}{\partial \mathbf{p}} \right] = 0. \quad (1.100)$$

Integration of the first term and integration of the other terms, under the assumption of  $f(\mathbf{r}, \mathbf{v}, t)$  being an integrable function, yields the moment equation

$$\frac{d \langle \Phi \rangle}{dt} = \left\langle \mathbf{v} \cdot \frac{\partial \Phi(\mathbf{r}, \mathbf{p})}{\partial \mathbf{r}} \right\rangle + q \left\langle \left( \mathbf{E} + \frac{\mathbf{v}}{c} \times \mathbf{B} \right) \cdot \frac{\partial \Phi(\mathbf{r}, \mathbf{p})}{\partial \mathbf{p}} \right\rangle. \quad (1.101)$$

It can be seen that the left hand side of (1.101) depends on other moments. Repetition of this procedure for the moments on the right hand side, yields, in general, an infinite chain of moment equations. This chain can only be truncated and closed by use of an appropriate Ansatz.

## 1.4 BEAM-DRIVEN PLASMA WAVES

In what follows, physical phenomena are investigated, which occur when a highly-intense laser pulse or relativistic charged particle beam is focused onto a plasma.

1.4.1 *Cold electron-fluid picture*1.4.1.1 *Motivation*

The mathematical formulation used here for the description of laser- or particle-beam driven plasma waves is based on a number of assumptions. (a) The gas target is ionized either by the front of the driver beam or by some pre-ionization technique. The main part of the laser- or particle beam hence encounters a fully ionized plasma. (b) The frequency of plasma electron-ion collisions is much smaller than the electron plasma frequency and can therefore be neglected. (c) Moreover, as explicated in 1.2.1.2, the characteristic time-scale of the collective electron response is much smaller than the one of the ions. Relevant phenomena in the interaction of laser- or particle-beams with underdense plasma are occurring on time-scales much shorter than the ion plasma frequency and are accurately described by assuming a static ion background. (d) Regions in velocity space where plasma electrons behave differently than thermal plasma electrons are not populated. (e) Furthermore, the thermal velocity spread is negligible compared to the mean velocity at a given spatial region and thermal effects are considered a small perturbation to the leading order fluid motion.

Analogous to the assumptions being made in 1.3.1 for the derivation of the fluid equations, the above points (a) and (b) justify the employment of the Vlasov equation and point (c) allows for the neglect of the ion dynamics and the introduction of a static ion background. Point (d) enables the employment of fluid moment equations with the assumption of a cold plasma (e) allowing for the truncation after the fluid momentum equation (1.97). The below discussion thus regards the plasma as a *cold electron fluid*.

1.4.1.2 *Fluid equations*

The governing equations of the cold electron fluid are the density continuity equation (1.93), the fluid momentum equation (1.97), and the Maxwell equations (1.1a)-(1.1d). The Maxwell equations are coupled to the fluid density and the fluid velocity via  $\rho = e(n_0 - n_e)$  and  $\mathbf{J} = -en_e\mathbf{v}_e$ . The continuity equation of the electron fluid is with (1.93) given by

$$\frac{\partial n_e}{\partial t} + \nabla \cdot (n_e \mathbf{v}_e) = 0. \quad (1.102)$$



Henceforth, the local electron density will simply be denoted by  $n \equiv n_e$ , the ambient, unperturbed electron density by  $n_0$  and the normalized electron fluid velocity will within the fluid picture be denoted by  $\boldsymbol{\beta} = \mathbf{v}_e/c$ , such that the density continuity equation reads

$$\frac{\partial n}{\partial ct} + \nabla \cdot (n\boldsymbol{\beta}) = 0. \quad (1.103)$$

The fluid momentum equation (1.97) can with (1.3a) and (1.3b) be written in terms of the potentials

$$\frac{\partial \mathbf{p}_e}{\partial t} + (\mathbf{v}_e \cdot \nabla) \mathbf{p}_e = -e \left( -\nabla\Phi - \frac{\partial \mathbf{A}}{\partial t} + \frac{\mathbf{v}_e}{c} \times (\nabla \times \mathbf{A}) \right). \quad (1.104)$$

where  $q_e = -e$  was used. Introducing the normalized scalar potential  $\phi = e\Phi/m_e c^2$  and normalized vector potential  $\mathbf{a} = e\mathbf{A}/m_e c^2$ , and the normalized electron fluid momentum  $\mathbf{u} \equiv \mathbf{p}_e/m_e c$ , this equation reads

$$\frac{\partial \mathbf{u}}{\partial ct} + \left( \frac{\mathbf{u}}{\gamma} \cdot \nabla \right) \mathbf{u} = \nabla\phi + \frac{\partial \mathbf{a}}{\partial ct} - \frac{\mathbf{u}}{\gamma} \times (\nabla \times \mathbf{a}). \quad (1.105)$$

Here, the second term on the left side can be rewritten by means of the vector identity  $(\mathbf{u} \cdot \nabla)\mathbf{u} = \nabla\mathbf{u}^2/2 - \mathbf{u} \times (\nabla \times \mathbf{u})$  to obtain the following equation (compare [Meyer-ter Vehn et al., 2001])

$$\frac{\partial}{\partial ct}(\mathbf{u} - \mathbf{a}) = \nabla(\phi - \gamma) + \frac{\mathbf{u}}{\gamma} \times (\nabla \times (\mathbf{u} - \mathbf{a})). \quad (1.106)$$

The curl of this equation,

$$\frac{\partial}{\partial ct}(\nabla \times (\mathbf{u} - \mathbf{a})) = \nabla \times \left( \frac{\mathbf{u}}{\gamma} \times (\nabla \times (\mathbf{u} - \mathbf{a})) \right), \quad (1.107)$$

shows that if  $\nabla \times (\mathbf{u} - \mathbf{a})$  is zero initially, it is zero for all times (see [Chen and Sudan, 1993]). For an unperturbed and cold plasma in the absence of a laser field  $\mathbf{u} = \mathbf{a} = 0$  holds initially. Hence the vorticity is zero for all times and Eq. (1.106) can be written (see [Esarey et al., 1993])

$$\frac{\partial}{\partial ct}(\mathbf{u} - \mathbf{a}) = \nabla(\phi - \gamma). \quad (1.108)$$

This *fluid momentum equation* describes the response of the electron fluid momentum to the potentials  $\phi$  and  $\mathbf{a}$  and is exact to the point, that the above vorticity was zero initially (compare [Esarey et al., 2009]).

As shown in 1.1.4.3 the interaction of plane light waves with electrons cannot not serve as effective acceleration mechanism under certain constraints, stated by the Lawson-Woodward theorem [Lawson, 1979]. Among others stipulated was the interaction to occur in vacuum with no external fields applied and the neglect of nonlinear effects, in order for the Lawson-Woodward theorem to hold. Similar

restrictions are also embodied in equation (1.108). In vacuum, and if external fields are absent,  $\nabla\phi = 0$  holds, if nonlinear effects are neglected,  $\nabla\gamma \approx 0$  is true, such that the momentum of the electron fluid  $\mathbf{u}$  follows exactly the vector-potential of the incoming light wave packet. After the light packet has passed, the fluid has zero momentum again.

However, if nonlinear effects are occurring and if the place of electrons in vacuum is now taken by a plasma, the co-action of the excitation of the plasma electrons via  $\nabla\gamma$  and the electrostatic fields carried by the generated plasma perturbations  $\nabla\phi$ , allows for the excitation of plasma waves and hence for an effective mechanism for the acceleration of charged particles in the waves, as shown in the following.

#### 1.4.2 Ponderomotive force

The nonlinear force term  $\nabla\gamma$  in equation (1.108) is called *general nonlinear ponderomotive force* [Esarey et al., 2009]

$$\mathbf{F}_{p,n} = -m_e c^2 \nabla\gamma. \quad (1.109)$$

To gain a better understanding of the ponderomotive action, equation (1.108) is regarded in the limit of a non-relativistic laser-field ( $|\mathbf{a}| \ll 1$ ) with no electrostatic force present ( $\nabla\phi = 0$ ). The leading order plasma fluid motion in this case is the *quiver momentum*  $\mathbf{u} = \mathbf{a}$  (compare [Esarey et al., 2009]). When assuming a small perturbation  $\delta\mathbf{u}$  with respect to the quiver momentum  $\mathbf{u} = \mathbf{a} + \delta\mathbf{u}$ , one finds with  $\gamma \simeq \sqrt{1 + \mathbf{a}^2}$ ,

$$\frac{\partial\delta\mathbf{u}}{\partial ct} = \frac{\nabla\mathbf{a}^2}{2\gamma}. \quad (1.110)$$

The ponderomotive force in the limit  $\mathbf{a}^2 \ll 1$  is hence given by [Esarey et al., 2009]

$$\mathbf{F}_p = -m_e c^2 \frac{\nabla\mathbf{a}^2}{2\gamma}, \quad (1.111)$$

and can be understood as a radiation pressure, pushing the electron fluid out of regions with high field magnitude, or through equation (1.46) out of high intensity regions.

For a plane electromagnetic wave, the ponderomotive force results in a fluid velocity, which is equivalent to the cycle-averaged single-electron drift velocity, calculated in equation (1.56). The fluid-electrons in such a plane wave are therefore displaced in longitudinal direction by a certain distance as described in 1.1.4.3, and create a fluid density accumulation near the rising edge of a finite duration plane wave and a density rarefaction near the falling edge.

For a more detailed discussion, see Kruer [1988, ch. 6].

However, for "slowly evolving" light pulses, which are, in addition, wide compared to the amplitude of the transverse electron quiver motion, neither (a) the leading order quiver motion nor (b) the ponderomotive force alone can effectively deposit energy into a set of electrons. Point (a) is due to the vanishing  $z$ - or time-integral over any finite duration, slowly evolving light pulse  $\mathbf{a}(\mathbf{r}, t)$ . Point (b) comes from the fact that for a slowly evolving light pulse, the  $z$ - or time-integral and the partial  $z$ -derivative of  $\mathbf{a}^2(\mathbf{r}, t)$  only imply an evaluation of the value of  $\mathbf{a}^2$  for times and positions ahead and behind of the pulse, which, for a finite duration light pulse, vanish. Only the electrostatic force  $\nabla\phi$ , which is generated through the excitation of the plasma via the ponderomotive force allows for a non-zero fluid momentum after the passage of the light pulse.

The above considerations show that the introduction co-moving variables and the discussion of the meaning of "slowly evolving" light pulses is needed.

*Even for quickly varying light pulses, (1.111) shows that the force is suppressed by  $\gamma$ .*

### 1.4.3 Quasi-static approximation

#### 1.4.3.1 Co-moving frame

The formulation of physics of plasma waves or plasma-based accelerators is often conducted in the *co-moving frame*

$$\zeta = z - vt, \quad (1.112a)$$

$$\tau = t. \quad (1.112b)$$

where  $v$  is usually chosen to be the velocity of the driver, propagating in positive  $z$ -direction. For the longitudinal and temporal partial derivatives of a dependent quantity  $Q = Q(\zeta, \tau)$  this Gallilean coordinate transformation implies

$$\frac{\partial}{\partial z} Q(\zeta, \tau) = \frac{\partial \tau}{\partial z} \frac{\partial Q}{\partial \tau} + \frac{\partial \zeta}{\partial z} \frac{\partial Q}{\partial \zeta} = \frac{\partial Q}{\partial \zeta}, \quad (1.113a)$$

$$\frac{\partial}{\partial t} Q(\zeta, \tau) = \frac{\partial \tau}{\partial t} \frac{\partial Q}{\partial \tau} + \frac{\partial \zeta}{\partial t} \frac{\partial Q}{\partial \zeta} = \frac{\partial Q}{\partial \tau} - v \frac{\partial Q}{\partial \zeta}. \quad (1.113b)$$

The *speed-of-light frame* in this work denotes the case when  $v \equiv c$ . The above transformation does not only provide the convenience of replacing dependencies on  $z - vt$  by dependencies on  $\zeta$ , but also permits a formulation in which a driver beam can be assumed rigid, or quasi-static in the co-moving frame, as described in the following.

#### 1.4.3.2 Quasi-static approximation

Dynamics in plasma-based accelerators span a large range of time-scales, and the characteristic time-scales for the driver and plasma evolution can differ by several orders of magnitude. The characteristic

time over which the plasma reacts to a perturbation is given by the inverse plasma frequency,  $\tau_p \sim \omega_p^{-1}$ .

A particle-beam in a plasma, on the contrary, evolves on time-scales on the order of the inverse betatron frequency  $\tau_b \sim \omega_\beta^{-1} \simeq \sqrt{2\gamma} \omega_p^{-1}$  (see e.g. [Esarey et al., 2001]), where  $\gamma$  is the Lorentz-factor of the beam. These time-scales differ by orders of magnitude  $\tau_b \gg \tau_p$  for highly relativistic ( $\gamma \gg 1$ ) particle-beams.

The evolution of the envelope of a laser-driver occurs transversely on the order of the pulse vacuum diffraction time  $\tau_{l,1} \sim z_R/c$ , where  $z_R \simeq \pi r_0^2/\lambda$  is the *Rayleigh-length* for Gaussian beams [Saleh and Teich, 2007],  $r_0$  is the spot size of the beam and  $\lambda$  denotes the central wavelength. The laser spot size denotes the  $\exp(-2)$  decay radius of the intensity. The longitudinal evolution of the laser-beam is given by the pulse dispersion time  $\tau_{l,2} \sim \omega/\omega_p^2$  (cf. [Sprangle et al., 1990a,b]). Laser beams with focal spot sizes which are much greater than their wavelengths  $r_0 \gg \lambda$  and on the order of the skin-depth  $r_0 \sim k_p^{-1}$  are modulated transversely on time-scales much longer than the plasma  $\tau_{l,1} \gg \tau_p$ . Additionally, the laser-frequency for laser-driven plasma acceleration is generally much greater than the plasma wavelength  $\omega \gg \omega_p$ , such that  $\tau_{l,2} \gg \tau_p$ .

This finding is used to formulate the quasi-static approximation (QSA) [Sprangle et al., 1990a,b; Ting et al., 1990]. Regarding a driver beam, traveling at velocity  $c$ , the temporal derivative of Eulerian quantities  $\mathcal{Q}$ , such as fluid quantities, charge and current densities, or electromagnetic fields, respectively, transform according to equation (1.113b) as  $\partial_t \mathcal{Q} = \partial_\tau \mathcal{Q} - c \partial_\zeta \mathcal{Q}$ . It can then be noted, that  $|\partial_\tau \mathcal{Q}| \sim \tau_d^{-1} |\mathcal{Q}|$  and  $c |\partial_\zeta \mathcal{Q}| \sim \tau_p^{-1} |\mathcal{Q}|$  (compare [Esarey et al., 1993]), where  $\tau_d$  stands for a characteristic time of the driver evolution ( $\tau_b, \tau_{l,1}$  or  $\tau_{l,2}$ ).

For driver beams with  $\tau_d \gg \tau_p$ , the time-variation of  $\mathcal{Q}$  is dominated by the dependency on the  $\zeta$ -variable. Fields and currents can then assumed to be frozen, or *quasi-static*, during plasma evolution in the speed-of-light frame

$$\frac{\partial \mathcal{Q}}{\partial t} \simeq -c \frac{\partial \mathcal{Q}}{\partial \zeta}. \quad (1.114)$$

The disparity of time-scales descriptively implies that the envelope of a laser-driver or the charge-distribution of a particle-beam does not change significantly during the characteristic time of the oscillatory plasma response to the excitation caused by the driver.

#### 1.4.4 Longitudinal plasma waves

##### 1.4.4.1 Longitudinal plasma waves in the linear and nonlinear regime

In the following, plane, longitudinal ( $\mathbf{k} \parallel \mathbf{E}$ ) plasma waves, excited by infinitely broad (i. e. no transverse dependency) laser- or charged

*Rayleigh length: see explanation in 1.5.1.2.*

*The QSA is used to derive the formulae describing the structure of the wakefields, but it is also the basis of quasi-static PIC codes (see chapter 3).*

particle-beams, are examined. This is done by means of the cold electron fluid theory in one spatial dimension with a three-component fluid momentum. The laser with polarization predominantly in the transverse plane  $\mathbf{a} = \mathbf{a}_\perp$  and the spatial distribution of the particle-beam  $n_b$  is assumed to be static during the plasma oscillation and hence are only functions of the co-moving variable  $\zeta$ . The drive-beam has a highly relativistic velocity  $\beta_{b,z} \rightarrow 1$ , such that field and fluid quantities are expressed in the speed-of-light frame, and are assumed quasi-static. The relativistic beam-particles have a negligible transverse momentum  $\mathbf{u}_{b,\perp} \simeq 0$  and conservation of canonical momentum, cf. Eq. (1.47), therefore implies [Esarey et al., 2009]

$$\mathbf{u}_\perp = \mathbf{a}_\perp = \mathbf{a}. \quad (1.115)$$

Here  $\mathbf{u}_\perp$  is the normalized plasma-electron fluid momentum. The charge density is a compound of the charge densities of plasma-electrons  $-en$ , immobile plasma-ions  $en_0$  and a rigid beam-electrons  $-en_b$  or -positrons  $en_b$ , resulting in  $\rho = -e(n - n_0 \pm n_b)$ . Hence, the electrostatic Maxwell equation (1.1a) is by means of equation (1.3a) and the QSA expressed as follows

$$\frac{\partial^2 \psi}{\partial \zeta^2} = -\frac{e4\pi}{m_e c^2} \rho = k_p^2 \left( \frac{n}{n_0} - 1 \pm \frac{n_b}{n_0} \right), \quad (1.116)$$

since transverse derivatives vanish identically. Here,  $n$  denotes the plasma electron density, and  $n_0$  is the ambient plasma electron density (or the ion density for a hydrogen plasma) and the beam-particle-density  $n_b$  contributes with a plus sign if the beam-particles are electrons and with a minus sign if the particles are positrons or protons. Applying the QSA to the continuity equation (1.103) yields

$$(1 - \beta_z)n = n_0, \quad (1.117)$$

where the fact was used that the electron density  $n$  before the interaction is identical to  $n_0$ . Hence for an initially unperturbed plasma the following equation is obtained

$$\frac{n}{n_0} = \frac{1}{1 - \beta_z}. \quad (1.118)$$

The z-component of the fluid momentum equation (1.108) in the QSA entails the invariant quantity  $\partial_\zeta(u_z + \psi - \gamma) = 0$ , where the *wakefield potential*

$$\psi = \phi - a_z \quad (1.119)$$

was introduced. For an initially cold and unperturbed plasma, this yields

$$u_z + \psi - \gamma = -1. \quad (1.120)$$

*This derivation of fluid properties in 1D linear and nonlinear plasma waves is inspired by Refs. [Sprangle et al., 1990a], [Esarey et al., 1993] and [Esarey et al., 2009].*

The latter equality is used to rewrite equation (1.118) as follows

$$\frac{n}{n_0} = \frac{\gamma}{1 + \psi}. \quad (1.121)$$

According to Eq. (1.115), the relativistic factor of the electron fluid can be expressed by  $\gamma = \sqrt{1 + u_z^2 + \mathbf{a}^2}$ , such that  $u_{e,z} = \sqrt{\gamma^2 - 1 - \mathbf{a}^2}$ . Plugging the latter identity into Eq. (1.120) yields after some algebra

$$\gamma = \frac{1 + \mathbf{a}^2 + (1 + \psi)^2}{2(1 + \psi)}. \quad (1.122)$$

Equations (1.116), (1.121) and (1.122) are combined to finally find the second-order ordinary differential equation

$$k_p^{-2} \frac{\partial^2 \psi(\zeta)}{\partial \zeta^2} = \frac{1 + \mathbf{a}^2(\zeta)}{2(1 + \psi)^2} \pm \frac{n_b(\zeta)}{n_0} - \frac{1}{2}, \quad (1.123)$$

describing the structure of the wakefield potential. The fluid quantities  $\gamma$ ,  $u_z$  and  $n/n_0$  are through  $\psi(\zeta)$  defined by Eq. (1.122) and through

$$\frac{n}{n_0} = \frac{1 + \mathbf{a}^2 + (1 + \psi)^2}{2(1 + \psi)^2}, \quad (1.124)$$

$$u_z = \frac{1 + \mathbf{a}^2 - (1 + \psi)^2}{2(1 + \psi)}. \quad (1.125)$$

Equations (1.122) - (1.125) describe linear ( $\mathbf{a}^2 \ll 1$  or  $n_b/n_0 \ll 1$ ) and nonlinear ( $\mathbf{a}^2 \sim 1$  or  $n_b/n_0 \sim 1$ ) longitudinal plasma waves in the cold fluid picture.

#### 1.4.4.2 Longitudinal plasma waves in the linear regime

Linear plasma waves (for  $\mathbf{a}^2 \ll 1$  or  $n_b/n_0 \ll 1$ ) and their attributes can be examined by expanding equation (1.123) for  $\psi \ll 1$  which implies  $(1 + \psi)^{-2} \simeq 1 - 2\psi$  and hence

$$\left( \frac{\partial^2}{\partial \zeta^2} + k_p^2 \right) \psi = k_p^2 \left( \frac{\mathbf{a}^2}{2} \pm \frac{n_b}{n_0} \right), \quad (1.126)$$

where  $\mathbf{a}^2 \psi \simeq 0$  was used. This is the differential equation of a forced harmonic oscillator with the Green's function  $G(\zeta) = \Theta(\zeta) k_p^{-1} \sin(k_p \zeta)$ , where  $\Theta$  is the Heaviside step function. The solution for the wakefield potential in the linear limit is hence given by

$$\psi(\zeta) = k_p \int_{-\infty}^{\zeta} \sin(k_p(\zeta - \zeta')) \left( \frac{\mathbf{a}^2(\zeta')}{2} \pm \frac{n_b(\zeta')}{n_0} \right) d\zeta'. \quad (1.127)$$

For finite-duration particle- or laser-beams the wakefield has a sinusoidal structure with wavelength  $\lambda_p = 2\pi k_p^{-1}$  after passage of the beams. Exploit of equation (1.116) and application of convolution differentiation algebra to Eq. (1.127) yields the density perturbation of

the plasma-electron density (compare [Gorbunov and Kirsanov, 1987] and [Esarey et al., 2009]) in the linear regime

$$\frac{n(\zeta) - n_0}{n_0} = k_p^{-1} \int_{-\infty}^{\zeta} \sin(k_p(\zeta - \zeta')) \frac{\partial^2}{\partial \zeta'^2} \left( \frac{\mathbf{a}^2(\zeta')}{2} \pm \frac{n_b(\zeta')}{n_0} \right) d\zeta' \mp \frac{n_b(\zeta)}{n_0}.$$

These longitudinal electron-density modulations impose the wake-field oscillations in  $\psi$  which are co-propagating with the driving beam.

#### 1.4.4.3 Length scales of laser or particle-beam driven plasma waves

The characteristic frequency for the collective response of a plasma to a small density perturbation is given by the plasma frequency

$$\omega_p = \sqrt{\frac{4\pi n_0 e^2}{m_e}}. \quad (1.128)$$

When a plasma slab is traversed by a laser- or charged particle-beam at velocity  $v_b$ , it locally oscillates at the plasma frequency. The phase of the local oscillation is given by the time elapsed since the passage of the driver beam and the plasma frequency. The phase velocity of the so created plasma wave is therefore (in a first order approximation) given by  $v_{ph} = v_b$ , so that a wave number can be assigned to the plasma wave

*For a more detailed discussion, see [Esarey et al., 2009, II. F].*

$$k_p^* = \frac{\omega_p}{v_b}. \quad (1.129)$$

And the corresponding wavelength in the linear regime is given by

$$\lambda_p^* = \frac{2\pi}{k_p^*} = \frac{2\pi v_b}{\omega_p}. \quad (1.130)$$

In this definition, the plasma frequency and the beam velocity determine the plasma wavelength. Since driver beams usually travel close to the speed of light, the following definitions for the plasma wave number and plasma wavelength

$$k_p \simeq \frac{\omega_p}{c}, \quad (1.131a)$$

$$\lambda_p \simeq \frac{2\pi c}{\omega_p}, \quad (1.131b)$$

are often used. The characteristic length scale of the skin depth  $k_p^{-1}$  is used in the present work e. g. for the normalization of length quantities.

## 1.4.4.4 Longitudinal plasma waves - Conclusion

The electrical field, carried by the above described longitudinal plasma waves is found by means of Eq. (1.3a), which implies with the QSA

$$E_z = -E_0 k_p^{-1} \frac{\partial \psi}{\partial \zeta}, \quad (1.132)$$

where  $E_0 = \omega_p m_e c / e$  is the cold non-relativistic wave-breaking field [Dawson, 1959].

If laser-beams with  $a_0 \ll 1$  or charged particle-beams with  $n_b/n_0 \ll 1$  and a longitudinal box profile with length  $L = \lambda_p/2$  of the envelope or charge distribution excite plasma waves, the resulting electrical fields can straightforwardly be calculated. Using Eq. (1.132) and Eq. (1.127) yields a peak longitudinal field of  $E_{z,max} = E_0 (a_0^2 + 2n_{b,0}/n_0)$ , where a circularly polarized laser was assumed. Using for instance  $a_0 = 0.1$  or  $n_b/n_0 = 0.005$  in a plasma density of  $n_0 = 10^{24} \text{ m}^{-3}$ , the longitudinal field is on the order of  $E_{z,max} \sim 1 \text{ GV/m}$ .

Today's Laser facilities readily attain intensities on target of far more than  $10^{18} \text{ W cm}^{-2}$  (see e. g. [Yanovsky et al., 2008; Leemans et al., 2010] and references therein). These intensities correspond through equation (1.35) for central wavelengths of  $\sim 1 \mu\text{m}$  to normalized vector potentials of  $a_0 \gtrsim 1$ . Particle accelerators can provide peak beam densities of  $n_b \sim 10^{24} \text{ m}^{-3}$  [Hogan et al., 2010]. When focussed into appropriate plasma targets, these laser- or particle-beams can create highly nonlinear plasma waves with fields of  $E_{z,max} \gtrsim E_0$ . Gradients of this magnitude are clearly beyond those provided by conventional accelerators ( $\sim 100 \text{ MV/m}$  [Linszen et al., 2012]). If harnessed for the acceleration of charged particles, such plasma waves offer the realization of highly compact acceleration devices.

## 1.5 PLASMA-BASED ACCELERATION

Accelerating gradients in conventional radio-frequency cavities are limited by material breakdown to accelerating gradients of  $\sim 100 \text{ MV/m}$ . Plasma-based accelerators are, due to their significantly enhanced gradients, considered one of the most promising technology candidates for future accelerators.

When analyzing Eq. (1.127) it can be seen that a light wave or particle distribution with only a small variation over a characteristic length  $\lambda_p$  does not efficiently excite a plasma wave. Efficient wave excitation either necessitates a driver with the same periodicity as the plasma wave or a short driver with a characteristic length  $L \sim \lambda_p/2$ . This work examines plasma-based acceleration with driver with a significant variation over short ( $L \lesssim \lambda_p$ ) distances. Plasma-based acceleration with short laser beams as drivers is called *laser-wakefield acceleration* (LWFA) whereas plasma-based acceleration using a short

An overview over plasma-based acceleration concepts, e.g. utilization of periodic drivers (e.g. plasma beat wave acceleration or self-modulated plasma-wakefield acceleration) is given in Esarey et al. [1996, 2009].



particle-beams is called *plasma-wakefield acceleration* (PWFA). The basis of these techniques is described in the following.

### 1.5.1 *Methods of plasma acceleration*

#### 1.5.1.1 *Plasma-wakefield acceleration*

Plasma-wakefield acceleration was proposed by Veksler [1956] and relies on the principle that relativistic charged particle beams expel plasma electrons by means of their space charge fields when propagating in a plasma target. If the beam is sufficiently short and has a significant amount of charge, this excitation leads to the generation of large amplitude plasma waves, co-propagating in the "wake" of the driver beam as described in 1.4.4.1. The fields carried by this plasma wave are called *wakefields*. The phase velocity of the plasma wave is approximately equal to the mean beam velocity, and for highly relativistic drive-beams close to the speed of light. Relativistic particles placed in a focusing and accelerating region of the plasma wave hence experience synchronous acceleration with no significant phase slippage. After firstly mentioned by Veksler, particle-beam driven plasma acceleration was reinvented by Chen et al. [1985] and analytically investigated e. g. by Keinigs and Jones [1987].

Modern accelerator facilities provide highly relativistic electron-beams with currents of more than 1 kA and longitudinal and transverse dimensions of  $\lesssim 100\mu\text{m}$ . Such beams are suitable to resonantly excite plasma waves at plasma densities of  $\sim 10^{17}\text{ cm}^{-3}$  in the nonlinear or blow-out regime. Plasma targets used or proposed to be used in PWFA are either alkali metal vapor ovens [Muggli et al., 1999] or steady-state-flow gas targets, (e. g. as used by Osterhoff et al. [2008]). The plasma is created by means of a pre-ionization laser [Muggli et al., 1999] or directly by the ionizing space-charge fields of the beam itself [Oz et al., 2007; Hogan et al., 2010].

The capability of such a technique to accelerate electrons to high energies in short distances was demonstrated by Blumenfeld et al. [2007], who focused a 42 GeV electron-beam with correlated energy spread of 1.5 GeV at the Stanford Linear Accelerator Center (SLAC) into a 85 cm long plasma target. Downstream of the plasma target, the beam showed a modulated energy spectrum with a small fraction of the electron distribution extending to energies of more than 80 GeV. Some electrons were thus accelerated by average gradients of up to  $\sim 50\text{ GV/m}$ . The injection and acceleration of spectrally distinct beams with significant charges and high quality is topic of current theoretical (e. g. [Oz et al., 2007; Hogan et al., 2010; Vieira et al., 2011; Hidding et al., 2012; Li et al., 2013] [Martinez de la Ossa et al., 2013, 2014]) and experimental (e. g. at FACET and FLASHForward) studies.

The ultimate limit for the possible energy gain of a single electron in the accelerating wakefields in PWFA is given by the transformer

*The emittance is explained in detail in 1.6*

ratio [Bane et al., 1985; Chen et al., 1986]. However, especially for large emittance drive beams, the effect of the *head-erosion* can be the limiting factor for the energy gain of the accelerated beam [Krall et al., 1989; Barov and Rosenzweig, 1994].

#### 1.5.1.2 Laser-wakefield acceleration

In contrast to PWFA, laser-wakefield acceleration (LWFA) [Esarey et al., 2009; Hooker, 2013] uses laser pulses to drive plasma waves and to accelerate electron beams. This method was proposed by Tajima and Dawson [1979] as an effective converter of the field energy in laser-pulses to kinetic energy of electron beams. Short ( $\lesssim 100$  fs) laser pulses with sufficient intensities ( $\gtrsim 10^{18}$  Wcm $^{-2}$ ) ionize the gas-target at the front of the pulse at intensities starting from  $\sim 10^{14}$  Wcm $^{-2}$ , such that the main pulse interacts with a fully ionized plasma and excites large amplitude plasma waves via the ponderomotive force (see 1.4.2). Charged particles, placed in the appropriate regions of this plasma wave are accelerated and transported via the longitudinal and transverse wakefields, respectively.

Above mentioned laser parameters are readily attained by modern laser systems. This is mostly contributed to the development of the chirped pulse amplification (CPA) technique, which stretches laser pulses temporally before amplifying them and compresses the amplified pulses again before using them for applications. The intensities are hence low enough to avoid nonlinear effects in the gain medium and air. Stretching and compression of the laser pulses is possible by the use of pairs of optical gratings. The frequency of the laser pulses has a time-dependence (chirp), and since the different frequency components have different path lengths between the grating pairs, the pulses are being compressed and stretched in an appropriate setup. If the bandwidth of the laser is sufficiently wide, a compression down to a few fs is possible using this technique. The advent of LWFA experiments is strongly related to the invention of CPA and the progress in laser technology still advances the frontiers of LWFA.

Laser pulses, in this work are assumed to be of fundamental Gaussian transverse mode with Gaussian temporal envelope. Moreover, the laser beams considered are paraxial wave packets and the slowly varying envelope approximation is assumed to hold [Saleh and Teich, 2007]. A radially symmetric Gaussian laser pulse is characterized by its energy content  $W$ , root mean square (RMS) pulse duration  $\sigma_t$  and

spot size at focus  $r_0$ . These attributes are related to the peak power  $P_0$  and the peak intensity  $I_0$  through the equation

$$\begin{aligned} W &= I_0 \int_0^\infty dr \int_0^{2\pi} d\varphi r \exp\left(-\frac{2r^2}{r_0^2}\right) \int_{-\infty}^\infty dt \exp\left(-\frac{t^2}{2\sigma_t^2}\right) \\ &= \frac{\pi r_0^2 I_0}{2} \int_{-\infty}^\infty dt \exp\left(-\frac{t^2}{2\sigma_t^2}\right) \\ &= P_0 \sigma_t \sqrt{2\pi}. \end{aligned} \quad (1.133)$$

With  $P_0 = \pi r_0^2 I_0 / 2$  and the **RMS** pulse duration is related to the intensity-**FWHM** duration through  $T = \sigma_t (2\sqrt{2\log(2)})$ . Such a transverse Gaussian mode laser beam diffracts in vacuum and the intensity depends on the position along the optical path according to [Saleh and Teich, 2007]

$$I(r, z) = I_0 \left(\frac{r_0}{r_s(z)}\right)^2 \exp\left(-\frac{2r^2}{r_s(z)^2}\right). \quad (1.134)$$

Here,  $r_s(z)$  denotes the spot size of the beam which is twice the radial intensity-**RMS** width  $r_s = 2\sigma_r$ ,

$$r_s(z) = r_0 \sqrt{1 + \left(\frac{z}{z_R}\right)^2}, \quad (1.135)$$

and  $z_R$  is the Rayleigh length

$$z_R = \frac{r_0^2 \pi}{\lambda}. \quad (1.136)$$

The Rayleigh-length denotes the characteristic length of vacuum diffraction of such a laser pulse. The intensity decays according to  $I \propto z^{-2}$  for  $z \gg z_R$  and is comparable to  $I_0$  only in distances within the Rayleigh-length to the position of the focal plane. Lasers in LWFA experiments need to be guided in order to extend the interaction region to lengths greater than  $z_R$  [Esarey et al., 2009].

Lasers propagate in a under-dense plasma with group velocity smaller than the speed of light (see 1.2.2.2). The plasma phase velocity is approximately equal to the group velocity of the laser (see 1.4.4.3), hence causing laser-wakefield accelerated electrons approaching the speed of light to outrun the plasma wave.

### 1.5.1.3 Physical formulation of plasma-based acceleration

The theoretical formulation in the following will make use of the **QSA** to describe the wakefield properties in different regimes of plasma waves.

Charges, moving at velocities close to the speed of light  $c$  in positive  $z$ -direction in a cylindrically symmetric field configuration, are subject to the fields  $E_z$  and  $E_r - B_\theta$  in terms of their longitudinal and

transverse dynamics, respectively (see A.2). A general relationship between the wakefield potential  $\psi$  and these fields in the quasi-static approximation is given by

$$\frac{E_z}{E_0} = -k_p^{-1} \frac{\partial \psi}{\partial \zeta} \quad (1.137a)$$

$$\frac{E_r - B_\theta}{E_0} = -k_p^{-1} \frac{\partial \psi}{\partial r}. \quad (1.137b)$$

These identities are found by means of equation (1.119) and the cylindrical representation of equations (1.3a) and (1.3b) and hold in general, if the drive-beam is radially symmetric, and if the QSA applies. A position in a plasma wakefield is accelerating for a particle propagating relativistically in the positive  $z$ -direction and with charge  $q$ , if  $qE_z > 0$  and focusing if  $q\partial_r(E_r - B_\theta) < 0$  at the given position (see A.2).

In plasma-based acceleration one usually distinguishes between the following different regimes. (a) The *linear regime* ( $\psi \ll 1$ ) which is accurately described by a 1D fluid theory extended to three dimensions. (b) The *nonlinear regime* with  $\psi \sim 1$  which generally requires a 3D fluid theory. (c) The *blowout* or *cavitated regime* ( $\psi \gg 1$ ) which requires a 3D kinetic description. These regimes are addressed in more detail within this section.

### 1.5.2 Linear regime

The linear regime in plasma-based acceleration refers to the case when  $a_0 \ll 1$  or  $n_b/n_0 \ll 1$  i.e.  $\psi \ll 1$ . The formulation of linear, longitudinal plasma waves in 1.4.4.2 can be extended to a 2D or 3D description of linear plasma waves [Esarey et al., 2009] as follows. Driver beams, particularly in LWFA, often have a radial extent which is greater than the longitudinal extent ( $\sigma_r \gg \sigma_\zeta$ ). The longitudinal component of the ponderomotive force (1.111) hence dominates the plasma dynamics ( $F_{p,r} \ll F_{p,\zeta}$ ). Exploiting this fact, it is straightforward to extend equation (1.127), which describes the wakefield, excited by a laser pulse or charged particle beam in one dimension, to three dimensions. Taking the radial dependence of the drive-beam distribution  $f$  into account, one finds (compare [Gorbunov and Kirsanov, 1987])

$$\psi(\zeta, r) = k_p \int_{-\infty}^{\zeta} \sin(k_p(\zeta - \zeta')) f(\zeta', r) d\zeta'. \quad (1.138)$$

The radial structure of the driver  $f(\zeta, r)$  now determines the radial wakefield amplitude and trough (1.137a) and (1.137b) also the radial dependence of the wakefields. The driver amplitude refers in the case of a laser pulse to

$$f(\zeta, r) = \frac{\mathbf{a}^2(\zeta, r)}{2}. \quad (1.139)$$

Or, for a single charged particle beam driver,

$$f(\zeta, r) = \pm \frac{n_b(\zeta, r)}{n_0}, \quad (1.140)$$

where the plus sign refers to electrons and minus sign to positrons or protons.

### 1.5.2.1 Gaussian drivers

Assuming temporal Gaussian drivers with radial Gaussian distributions of the form

$$f(\zeta, r) = f_0 \exp\left(-\frac{(\zeta - \zeta_c)^2}{2\sigma_\zeta^2}\right) \exp\left(-\frac{r^2}{2\sigma_r^2}\right), \quad (1.141)$$

the wakefield potential can with (1.127) be analytically calculated (see A.3). Using equation (A.31), the wakefield potential for positions far behind the driver  $(\zeta_c - \zeta)/\sigma_\zeta \gg 1$  is obtained

$$\begin{aligned} \psi(\zeta, r) = & -f_0 \sqrt{2\pi} k_p \sigma_\zeta \exp\left(-\frac{(k_p \sigma_\zeta)^2}{2}\right) \sin(k_p(\zeta - \zeta_c)) \\ & \times \exp\left(-\frac{r^2}{2\sigma_r^2}\right). \end{aligned} \quad (1.142)$$

The wakefield potential hence has a sinusoidal  $\zeta$ -dependency and a Gaussian radial dependency. The sinusoidal dependency of the wakefield for  $r = 0$  is shown for an example in Figure 5 with a comparison with the numerical solution of equation (1.126). It can be seen that the above equation (1.142) coincides well with the solution of (1.126) for positions behind the driver.

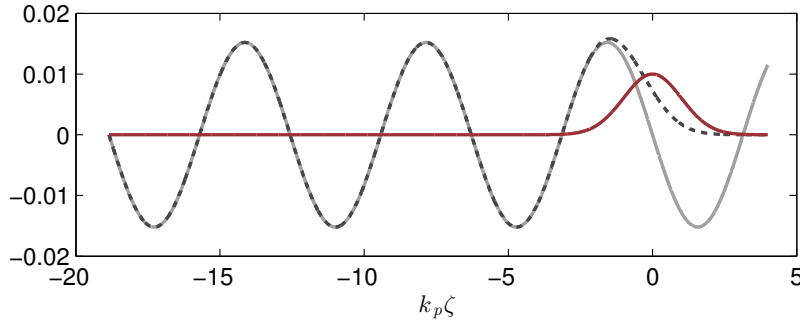


Figure 5: Driver beam profile and wakefield potential of a linear plasma wave with  $f_0 = 0.01$  and  $k_p \sigma_\zeta = 1$ . Wakefield potential  $\psi$  according to (1.142) for  $r = 0$  in light gray (—), numerical solution of equation (1.126) in dashed gray (- -) and the Gaussian driver profile  $f(\zeta, r = 0)$  in red (—).

When using equations (1.137a) and (1.137b), the field configuration in the case of a Gaussian driver results in (compare [Gorbunov and Kirsanov, 1987])

$$\frac{E_z}{E_0} = f_0 \sqrt{2\pi} k_p \sigma_\zeta \exp\left(-\frac{(k_p \sigma_\zeta)^2}{2}\right) \cos(k_p(\zeta - \zeta_c)) \times \exp\left(-\frac{r^2}{2\sigma_r^2}\right), \quad (1.143a)$$

$$\frac{E_r - B_\theta}{E_0} = -f_0 \sqrt{2\pi} k_p \sigma_\zeta \exp\left(-\frac{(k_p \sigma_\zeta)^2}{2}\right) \sin(k_p(\zeta - \zeta_c)) \times \frac{k_p r}{(k_p \sigma_r)^2} \exp\left(-\frac{r^2}{2\sigma_r^2}\right). \quad (1.143b)$$

Given  $f_0$  is fixed, it can be seen, that the field amplitudes are maximum if  $k_p \sigma_\zeta = 1$ . In this case, the equations for the longitudinal and transverse field reduce to

$$\frac{E_z}{E_0} = f_0 \sqrt{\frac{2\pi}{\exp(1)}} \cos(k_p(\zeta - \zeta_c)) \exp\left(-\frac{r^2}{2\sigma_r^2}\right), \quad (1.144a)$$

$$\frac{E_r - B_\theta}{E_0} = -f_0 \sqrt{\frac{2\pi}{\exp(1)}} \sin(k_p(\zeta - \zeta_c)) \frac{k_p r}{(k_p \sigma_r)^2} \exp\left(-\frac{r^2}{2\sigma_r^2}\right). \quad (1.144b)$$

These are the wakefields of a plasma wave, resonantly driven by a Gaussian driver. Nonetheless, it should be noted, that the resonance condition  $k_p \sigma_\zeta = 1$  only provides the most enhanced wakefields, if  $f_0$  is independent of  $\sigma_\zeta$ . In general, the invariant quantity is either the driver bunch charge for a particle beam driver or the pulse energy for a laser pulse. Hence, the current or intensity ( $\sim f_0$ ) is inversely proportional to the beam length  $f_0 \propto \sigma_\zeta^{-1}$ . For such driver beams, shortest beam duration gives most enhanced wakefields.

### 1.5.3 Mildly nonlinear regime

*The nonlinear regime in LWFA is reviewed in more detail by Esarey et al. [2009].*

Mildly nonlinear plasma waves are excited, if a laser pulse with  $a_0 \sim 1$  or a particle beam with  $n_b/n_0 \sim 1$  is propagating through a plasma. The response of the plasma then starts to significantly deviate from the above described linear behavior in terms of the plasma frequency, wavelength and shape of the wakefield potential. If electrons are gaining relativistic velocities, they are gaining relativistic mass. The plasma frequency, being inversely proportional to the electrons mass therefore decreases owing to this relativistic effect while the wavelength of driver beam induced oscillations increases. Such relativistic and nonlinear effects have several implications for the wakefield properties.

### 1.5.3.1 Transition from linear to nonlinear regime

In order to understand the transition from linear to nonlinear plasma waves, the example of a circular polarized Gaussian laser pulse with a pulse duration of  $k_p \sigma_\zeta = 1$  is studied for different amplitudes  $a_0$ . The spot size of the laser pulse is presumed much greater than the plasma skin depth and the pulse duration  $k_p r_s \gg 1 \sim \sigma_\zeta$ , which justifies the employment of the 1D longitudinal plasma wave picture 1.4.4.1 for the modeling of the plasma wave properties.

Starting point of the mathematical description for pure longitudinal nonlinear plasma wave picture is equation (1.123). This ordinary differential equation (ODE) can be solved analytically only for square pulse (see [Bulanov et al., 1989; Berezhiani and Murusidze, 1990, 1992]) and is here solved numerically for a Gaussian pulse. Numerical solutions for  $\psi$  are used for the calculation of derived quantities. The longitudinal field and plasma electron density are calculated by means of equations (1.137a) and (1.124). Figure 6 shows the laser intensity for the cases  $a_0 = 0.2$ ,  $a_0 = 1.0$  and  $a_0 = 4.0$  (top to bottom), and the resulting wakefield properties. It can be seen that the wakefield prop-

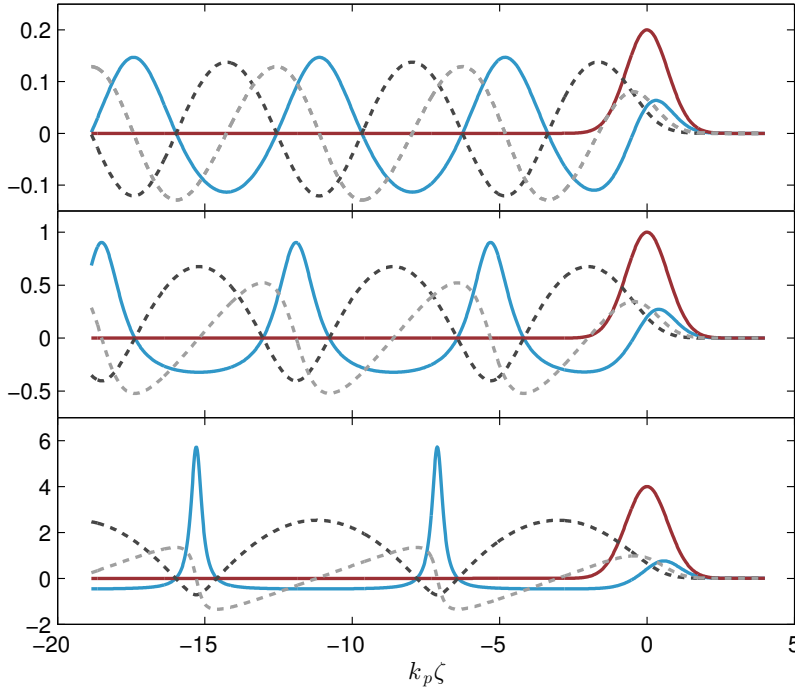


Figure 6: Transition from linear to nonlinear plasma waves for driver amplitudes of  $a_0 = 0.2$ ,  $a_0 = 1.0$  and  $a_0 = 4.0$  (top to bottom). The individual graphs show the normalized laser intensity of the circular polarized pulse  $a^2$  (—), wakefield potential  $\psi$  (- -), longitudinal electric field  $E_z/E_0$  (- -), and plasma electron density perturbation  $n/n_0 - 1$  (—).

erties in the case  $a_0 = 0.2$  are still close to the linear scenario with a sinusoidal-like dependency of  $\psi$  on the co-moving variable. Such

wakefields are often called *quasilinear*. However, when the laser amplitude is increased to  $a_0 = 1.0$ , several new features are observed. The plasma electron fluid density modulation becomes more peaked and the peaks are shifted to positions with larger distance with respect to the driver beam. This increase of the plasma wavelength for relativistic plasma waves was described e.g. by [Bulanov et al. \[1989\]](#) and [Berezhiani and Murusidze \[1990\]](#) (also confer [\[Esarey et al., 2009\]](#)). While the wakefield potential starts to deviate from a sinusoidal dependency and transits to a parabolic shape, the electric field becomes asymmetric. When finally going to a laser amplitude of  $a_0 = 4.0$ , the plasma electron density is highly peaked with a long trough in between the peaks. The wakefield potential has a parabolic shape and the electric field develops a sawtooth-like profile.

### 1.5.3.2 *Transverse properties of mildly nonlinear plasma waves*

Mildly nonlinear plasma waves, excited by broad drivers can be described by an extension of the 1D nonlinear longitudinal plasma wave description [1.4.4.1](#), analogous to the extension used for the 2D or 3D linear picture [1.5.2](#). When doing so, one finds that the dependency of the nonlinear plasma wavelength on the driver amplitude has the following transverse effect for drivers with a transverse amplitude gradient. The radial amplitude dependency of the driver results in a radial dependency of the nonlinear plasma wavelength, causing the plasma wave-fronts to be more and more curved with increasing wave period.

The validity of the assumption of pure longitudinal plasma waves for broad driver beams can be understood by the following considerations. An infinitely broad driver beam with transverse polarization  $\mathbf{a} = \mathbf{a}_\perp$  is assumed to interact with a plasma. Conservation of transverse canonical momentum,  $\mathbf{a}_\perp = \mathbf{u}_\perp$ , then implies for a plasma electron to finally being positioned at the transverse position at which it was located prior to the interaction. Only the longitudinal position, and, through the generated space charge fields, also the longitudinal component of the momentum have changed after the interaction.

However, for transversely limited drivers, the transverse canonical momentum is not conserved and electrons experience a transverse momentum carry. For [LWFA](#), this fact is incorporated in the expressions for the ponderomotive force [\(1.111\)](#) or [\(1.109\)](#). If the transverse gradient of the fluid quiver-energy is non-negligible, a transverse force acts on the electron fluid. In the case of [PWFA](#), the transverse momentum carry comes from the electrostatic field of the space-charge of a transversely limited beam, as seen from equations [\(1.108\)](#) or [\(1.116\)](#).

Hence, a rigorous study of nonlinear plasma waves with radially bounded drivers requires a 2D or 3D nonlinear plasma fluid model which needs to be solved numerically. Moreover, while the transverse



wakefield dependence in the linear regime is determined by the radial properties of the driver beam, the transverse dependency of the wakefields in the nonlinear regime does not necessarily follow the driver beam profile.

Drive-beams with large amplitudes  $a_0 \gg 1$  or  $n_b/n_0 \gg 1$  and large transverse gradients of the amplitudes create plasma waves which necessitate a 3D kinetic description. This regime is discussed below.

1.5.4 *Highly nonlinear or blow-out regime*

The plasma excitation by short ( $L < \lambda_p$ ) and highly intense ( $a_0^2 \gg 1$  or  $n_b/n_0 \gg 1$ ) beams with a transverse size on the order of the plasma wavelength leads to a scenario when practically all plasma electrons are radially expelled from the region near to the propagation axis of the driver beam. This stands in contrast to the linear regime, in which the excitation is purely longitudinal. In the highly nonlinear or *blow-out regime*, the electron-cavitation or bubble, formed by the radial expulsion of plasma electrons, co-propagates behind the driver beam. Plasma-based acceleration in this regime cannot be described

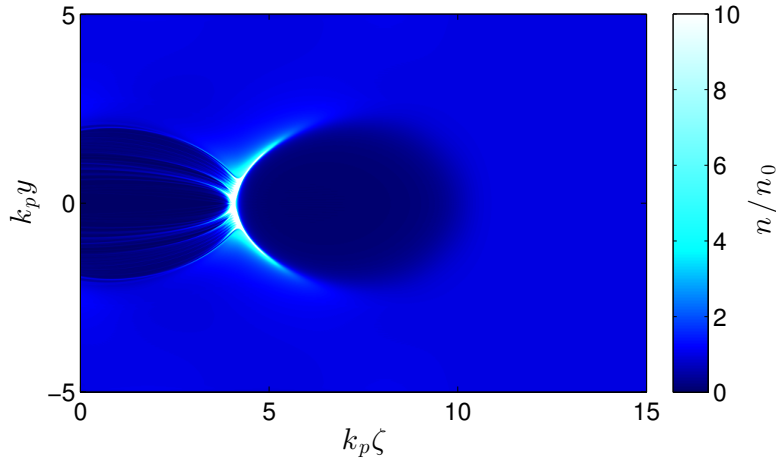


Figure 7: Simulation result obtained with HiPACE. Depicted is the plasma electron density, normalized to the ambient plasma density. The relevant simulation parameters are given in Table 2.

by means of a fluid theory. A fluid description demands that regions in momentum space where plasma electrons behave differently than thermal plasma electrons are not populated. This is not ensured in the blowout regime, since plasma-electrons populate spatial regions in the plasma wake behind the driver in which they feature non-thermal momentum spreads. The dynamics of individual electrons strongly depends on the populated momentum region especially in the crest region of the plasma wave at which it breaks, thus leading to highly kinetic effects, e.g. of electron self-trapping in the electron cavity.

*Confer 1.3.4 or point (d) in 1.4.1.1.*

An accurate description must hence account for kinetic effects and in general should be three-dimensional. The Maxwell-Vlasov system is therefore the appropriate physical basis for the description of plasma acceleration in the blowout regime. However, when regarding highly nonlinear plasma waves, the Maxwell-Vlasov equations cannot be solved analytically and numerical methods must be employed (see 2 or [Pukhov and Meyer-ter Vehn, 2002] and [Rosenzweig et al., 1991]). A popular numerical tool to study plasma-based acceleration in the blow-out regime is the Particle-In-Cell (PIC) technique which is illustrated in chapter 2. Figures 7, 8 and 9, depict some properties of an electron-beam driven plasma wave in the blowout regime as simulated by a 3D PIC code. The electron density in a central slice of the simulation is shown in Figure 7. Plasma electrons are expelled by virtue of the space charge fields of the driver beam (the driver beam is not depicted) and form a sheath around an electron-cavity before crossing at the back of the cavity. The thereby generated field configuration is presented in Figures 8 and 9. The longitudinal field has a linear dependence on the co-moving variable  $\zeta$  and no dependence on the transverse coordinate inside the cavity in regions with zero beam charge density. The transverse fields  $E_y + B_x$ , on the contrary, have a linear dependence on  $y$  and no dependence on the co-moving variable.

*The corresponding simulation parameters are given in Table 2.*

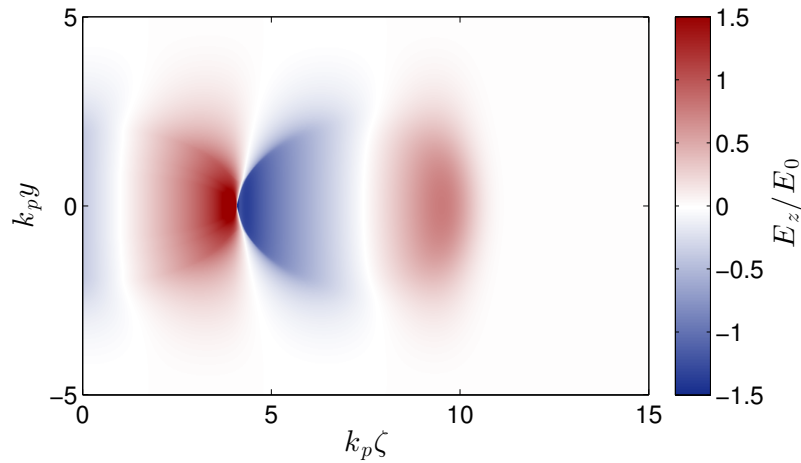


Figure 8: Result from a simulation with HiPACE. Depicted is the normalized longitudinal field  $E_z/E_0$ . The relevant simulation parameters are given in Table 2.

A number of phenomenological approaches for the description the blow-out regime have been proposed. The blow-out regime in PWFA has been investigated e. g. by Lu et al. [2006] and Lotov [2004], while the blow-out regime in LWFA has among others been addressed by Kostyukov et al. [2004], and Esarey et al. [2009]. For the deduction of the fields inside a cavity, it's shape can in first approximation be

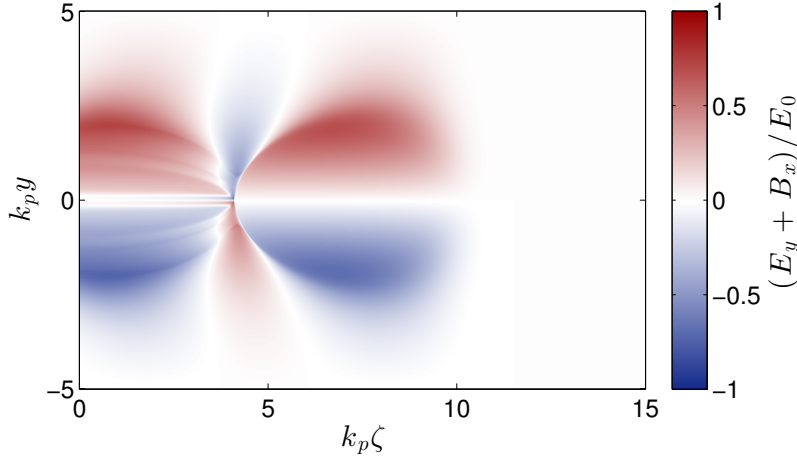


Figure 9: Result from a simulation with HiPACE. Depicted is the normalized transverse fields  $(E_y + B_x)/E_0$ . The relevant simulation parameters are given in Table 2.

assumed spherical with radius  $R$  and centered at  $\zeta = 0$  and  $r = 0$ , where  $r$  is the radius in a cylindrical geometry (compare [Esarey et al., 2009]). The cavity moves with the speed of light in positive  $z$ -direction.

Assuming the QSA holds, the wakefield potential inside such a cavity is given by (compare [Kostyukov et al., 2004; Lu et al., 2006])

$$\psi(\zeta, r) = \frac{(k_p R)^2}{4} - \frac{k_p^2 (\zeta^2 + r^2)}{4} - 1. \quad (1.145)$$

The field configuration follows with equations (1.137a) and (1.137b)

$$\frac{E_z}{E_0} = \frac{k_p \zeta}{2}, \quad (1.146a)$$

$$\frac{E_r - B_\theta}{E_0} = \frac{k_p r}{2}. \quad (1.146b)$$

The longitudinal force on an electron hence has a linear dependence on the co-moving variable and the transverse force has a linear dependence on the radius. While a spherical cavity was assumed for the derivation of the wakefield potential above, the fields inside the electron-cavity, in equations (1.146a) and (1.146b), hold for any shape of the electron-cavity, as long as a volume with complete electron blow-out exists. The shape of the plasma blow-out is, in general, not spherical and depends on the charge density or intensity profile of the driver beam [Lotov, 2004; Lu et al., 2006].

Albeit a phenomenological approach is accurately reproducing the fields inside the cavity, the dynamics of plasma electrons forming a sheath around the cavity and crossing at the back of the cavity is not sufficiently described by such an approach. The periodic structure as

*The linear dependence of the transverse force on the radius has a beneficial aspect for the beam transport, as discussed in 1.6 and 4.2.3.*

it exists for plasma waves in the linear regime or on-axis in the non-linear regime, is completely disrupted by the breaking of the waves in the blow-out regime due to the nonlinear transverse dynamics near to the crest of the wave. The occurrence of blow-out goes together with the phenomenon of wave-breaking.

### 1.5.5 Wave-breaking

The considerations here follow [Esarey et al., 2009].

Plasma waves, as created by laser- or particle-beam drivers, can support only limited electric field amplitudes. An estimation of this limit can be obtained when assuming a cold plasma, such that all electrons oscillate with the same wave number  $k_p = \omega_p/c$ . In the linear (or nonrelativistic) cold fluid case, the electric plasma wakefield behind the driver beam then follows  $E_z = E_{max} \cos(k_p \zeta)$  (compare e.g. equation (1.143a)). Using the Maxwell equation  $\nabla \cdot \mathbf{E} = 4\pi\rho$  (1.1a) with the charge density  $\rho = e(n_0 - n)$ , yields for pure longitudinal plasma waves the identity  $4\pi e(n_0 - n) = -E_{max} k_p \sin(k_p \zeta)$ . The electron plasma density  $n$  oscillates in this estimation harmonically around the ambient plasma density  $n_0$ , with minimum possible amplitude of  $n_{min} = 0$  and maximum possible amplitude  $n_{max} = 2n_0$ . The maximum amplitude refers to the value  $-E_{max} k_p$  on the right hand side of the above equation. The so obtained maximum field amplitude is  $E_{max} = E_0$ , where  $E_0$  the *cold nonrelativistic wave-breaking field* (see [Dawson, 1959])

$$E_0 = \frac{c\omega_p m_e}{e}. \quad (1.147)$$

The field amplitude in nonlinear plasma waves can easily surpass this limit. An expression for the *cold relativistic wave-breaking field* can be derived by means of cold nonlinear fluid equations [Esarey and Pilloff, 1995; Esarey et al., 2009]

$$E_{WB} = \sqrt{2(\gamma_{ph} - 1)} E_0, \quad (1.148)$$

where  $\gamma_{ph}$  is the gamma factor associated with the phase velocity of the plasma wave. If the phase velocity, which is approximately equal to the velocity of the driver, approaches the speed of light, the maximum plasma density and electric field amplitude become singular, indicating the breakdown of the cold fluid description [Esarey et al., 2009]. When assuming a thermalized electron plasma fluid with a nonrelativistic thermal energy  $k_b T_e \ll m_e c^2$ , the plasma density and the electric field amplitude remain finite for any plasma phase velocity [Schroeder et al., 2005].

All above considerations were assuming pure longitudinal plasma waves and were employing a 1D fluid picture. The wave-breaking field and the maximum plasma density in a three dimensional plasma wave can differ from the above expressions. Moreover, the transverse

structure of the plasma wave with increasing driver amplitude becomes more and more curved which eventually leads to transverse wave-breaking [Bulanov et al., 1997, 1998b, 2012a,b], when the curvature radius becomes on the order of the electron fluid displacement [Esarey et al., 2009]. Transverse wave-breaking disrupts the regular structure of the plasma wave and leads, due to the self-intersection of the electron trajectories to the injection of plasma electrons into the accelerating region of the plasma wave for phase velocities of the plasma wave significantly smaller than the speed of light [Bulanov et al., 1997].

Wave-breaking can also occur in the one-dimensional case [Bulanov et al., 1998b,a]. This longitudinal wave-breaking occurs especially, if the plasma has a inhomogeneous longitudinal density profile or if the driver amplitude fluctuates during the propagation in the plasma.

The injection of electrons into the plasma wave trough transverse wave-breaking is a highly nonlinear process and is not easily controllable. However, tailored plasma density gradients allow for the controlled injection of electrons through longitudinal wave-breaking.

#### 1.5.6 Injection mechanisms

Beam stability, quality and tunability in plasma-based acceleration strongly depends on the mechanism of the injection of electrons into the accelerating phase of the wakefields. Such an *injection mechanism* needs to occur localized in time and space in order to allow for the formation of a beam with low energy spread short duration. Moreover, the injected electrons must be well selected by their initial population of phase space so as to render possible beams with a well defined charge or finally occupied phase space region. The phase space distribution of a particle beam whose evolution is governed by the Vlasov equation cannot be compressed. This indicates that initial beam parameters are of fundamental importance for the best achievable final beam parameters. The injection mechanism should not rely on effects which translate fluctuations on initial conditions, such as variations of the initial driver beam properties or the plasma target attributes, in a nonlinear and enhanced fashion to the final beam parameters. Some injection techniques and their attributes are outlined below.

##### 1.5.6.1 Injection via wavebreaking

Wave-breaking was the dominating electron injection mechanism in many of the early experimental productions of electron beams in laser wakefield accelerators (see e.g. [Modena et al., 1995; Faure et al., 2004; Mangles et al., 2004; Geddes et al., 2004; Hidding et al., 2006; Osterhoff et al., 2008]). While electron injection through wave-breaking is inherent in many LWFA scenarios, experiments were showing that the injection process is unstable in terms of the final charge, energy dis-

tribution or pointing stability of the produced electron beams. This is mostly owed to the lack of shot to shot stability of today's laser systems and the nonlinear dependence of the wave-breaking process on laser parameters, such as the pointing, the transverse and longitudinal intensity distribution or the angular chirp.

Self-injection by means of wave-breaking in [PWFA](#) is suppressed by the highly relativistic phase velocity of the plasma wave. Electrons need to reach a velocity equal or greater than the phase velocity of the plasma phase in order to be trapped. This is elaborated in more detail below.

### 1.5.6.2 Density gradient injection

The explanations here follows [[Esarey et al., 2009, IV.D.](#)].

A plasma density transition can trigger localized injection of plasma electrons into the accelerating phase of the plasma wave [[Bulanov et al., 1998b,a](#)]. This injection technique can be regarded in the limit of a short, step-like transition compared to the plasma wavelength  $L_{tr} \lesssim \lambda_p$  or in the limit of a gradual negative density gradient with  $L_{tr} \gg \lambda_p$ .

Regarding e.g. the wakefield potential of a linear plasma wave,  $\psi = \psi_0 \cos(k_p \zeta)$ , it is noted that a certain phase position, located at  $N_{per} \lambda_{p,1}$  before a density transition is located at  $N_{per} \lambda_{p,2}$  after the transition, where  $N_{per}$  is the number of the wave period considered and  $\lambda_{p,1} < \lambda_{p,2}$  are the plasma wavelengths up- and downstream of the density transition, respectively. The phase position of interest changes by the distance  $\Delta \zeta = N_{per}(\lambda_{p,1} - \lambda_{p,2})$  during the density transition. In a short transition  $L_{tr} \lesssim \lambda_p$  plasma electrons are during their oscillation abruptly located in a different phase region and trapped, given they gain a sufficient longitudinal velocity. This is equivalent to a wave break of a wave at the sharp boundary between two media with different dispersive properties.

A gradual density transition has the following effect on a plasma wave. A phase position in a first order approximation is given by  $\phi(z) = k_p(z)(z - ct)$ , where a highly relativistic driver beam was assumed. The effective plasma frequency is given by  $\omega_{p,eff} = -\partial\phi/\partial t$  and the wave number by  $k_{p,eff} = \partial\phi/\partial z$ , so that the phase velocity of the plasma wave yields [[Esarey et al., 2009](#)]

$$\beta_{ph} = \frac{\omega_{p,eff}}{c k_{p,eff}} = \left[ 1 + k_p^{-1} \zeta \frac{dk_p(z)}{dz} \right]^{-1}. \quad (1.149)$$

Expanding this expression for small variations of the plasma wave number and for short distances behind the driver beam  $k_p^{-1} \zeta dk_p/dz \ll 1$ , gives

$$\beta_{ph} \simeq 1 - k_p^{-1} \zeta \frac{dk_p}{dz} = 1 - \frac{\zeta}{2n} \frac{dn}{dz}. \quad (1.150)$$

This suggests that a negative density gradient  $dn/dz < 0$  implies a decrease of the phase velocity for co-moving positions behind the

driver  $\zeta < 0$ . The criteria for trapping of an electron is given by  $\beta = \beta_{ph}$ , where  $\beta = v/c$  is the normalized electron velocity. The position behind the driver at which this equality is fulfilled is with the above equations given by [Esarey et al., 2009]

$$\zeta_{tr} = 2(\beta_e^{-1} - 1)n \left( \frac{dn}{dz} \right)^{-1}. \quad (1.151)$$

Theoretical and numerical investigation of gradual density gradient injection in LWFA were performed by Bulanov et al. [1998a]; Tomassini et al. [2003]; Kim et al. [2004]; Brantov et al. [2008].

Experimental realization of this technique is possible by tailoring of the longitudinal gas profile such that injection occurs in a localized region in a transition from high to low gas density ( $n_1 > n_2$ ) along the plasma target. The density transition can be generated by means of a laser prepulse, propagating perpendicular to the optical axis of the main laser pulse, thereby generating a localized thermal-expansion and hence a local plasma rarefaction [Chien et al., 2005]. An alternative method constitutes the insertion of a knife edge into a supersonic gas jet and the creation of a gas shock front [Schmid et al., 2010; Buck et al., 2013]. A longer, gradual density slope can be produced by means of a gas nozzle only. When a laser drive pulse is focused to the downstream edge of the gas profile, increasing laser amplitude and decreasing plasma density both induce a lowered plasma phase velocity in the nonlinear regime and trigger injection [Geddes et al., 2008]. Such a scheme can also be used to decouple injection and acceleration, if a gas flattop profile is employed after the gas jet, allowing for enhanced tunability [Gonsalves et al., 2011].

Injection in step-like transitions was studied theoretically and numerically for PWFA [Suk et al., 2001]. Density gradient injection in PWFA with transition lengths on the order of the plasma wavelength was studied by Grebenyuk et al. [2014].

### 1.5.6.3 Ionization injection

A widespread method for the injection and trapping of electrons exploits the localized field-ionization of a gas with high atomic number, the bulk plasma (typically hydrogen) is doped. A higher ionization potential of the bulk plasma or the dopand gas is chosen to be ionized by means of a laser-field, by the space-charge field of a particle beam or by the wakefield in the plasma. Important for these techniques is that the ionization of the electron from the higher ionization potential takes place in a plasma wave phase which allows trapping of the ionized electrons.

One method for the ionization and trapping in LWFA suggests the ionization of the electron in the higher ionization potential by the laser driver itself. Electrons are ionized from the dopand gas in this method only near to the peak intensity region of the driving laser

beam and hence follow different trajectories than plasma electrons which were ionized in the very front of the laser pulse. These orbits are trapped orbits for an appropriately chosen ionization potential and well controlled laser peak intensity and ambient plasma density. This technique was successfully demonstrated in a number of experiments [McGuffey et al., 2010; Pak et al., 2010; Clayton et al., 2010] and theoretically described by e.g. Chen et al. [2012]. However, the emittance values of beams generated by means of this technique are usually expected to be significantly greater than those from other techniques. This is a consequence of residual quiver motion and the non-canceling of the integrated ponderomotive force of an electron which is born inside of the laser pulse. This heats the generated electron bunch transversely.

The field ionization by lasers can also be used in PWFA to trigger injection [Hidding et al., 2012]. This is achieved by temporally and spatially aligning a laser beam with the particle beam driver, such that it co-propagates shortly behind it on axis. If the laser is tightly focused, it is capable of ionizing the dopand gas only during a short time-interval. Given the wakefield potential, excited by the particle beam, is capable of trapping the electrons from the phase-location at which the laser field-ionized electrons emerge at rest, injection occurs. The emittance of beams produced with this technique can be in the nanometer range, provided the laser-beam alignment is perfect [Hidding et al., 2012].

Similar techniques have been proposed for LWFA [Bourgeois et al., 2013; Yu et al., 2014]. The place of the particle beam driver is in LWFA taken by a laser beam which is followed by a second laser pulse. The challenge in LWFA is to avoid ionization of the dopand gas by the driver beam but to achieve ionization by the trailing beam without distortion of the wakefields. This can be achieved if the ionization laser is tightly focused such that it has a higher amplitude and short Rayleigh length [Bourgeois et al., 2013] or if the ionization laser has a significantly higher frequency, hence allowing for a lowered ionization threshold for a given laser intensity [Yu et al., 2014].

Injection in plasma wakefield acceleration in a doped plasma can also occur when the particle driver beam exhibits space charge fields which are sufficient to ionize a populated dopand gas ionization level [Oz et al., 2007]. Such an ionization mechanism depends on the transverse dynamics of the beam. When a particle beam generates a plasma wave, it is itself modulated by the transverse wakefields and beam particles undergo betatron oscillations. If the beam is not matched to the wakefields, these oscillations lead to the transverse modulation of the beam size which entails a modulation of the space charge fields. When these space charge fields reach the ionization threshold, localized ionization of the higher ionization potential takes place and the ionized electrons can be trapped. However, this



technique is not easily controllable, since the transverse dynamics of the beam are not easily steerable.

A novel method of ionization and trapping for the production of high-quality beams in PWFA was suggested by [Martinez de la Ossa et al. \[2013\]](#). It exploits the high magnitude of the wakefields to ionize the dopand gas. If the charge density of the driver beam is sufficiently high, a small overlap between the phase capable of trapping and the phase with field magnitudes high enough for ionization exists. Electrons are hence ionized and trapped from a well defined phase region, facilitating the generation of high quality beams while avoiding the dependence on the slice-properties of the driver beam.

#### 1.5.6.4 *External injection*

The injection of electrons provided by external sources constitutes an important and versatile injection mechanism. In this mechanism, an electron beam is propagating with a defined temporal and spatial offset with respect to a driver-beam. When the driver interacts with the plasma and creates a plasma wave, the trailing beam is positioned in a defined region within the plasma wave.

It is versatile in the sense that the provided electron bunch may have a tailored phase-space distribution as far as the source allows and the plasma wave can be populated in a high degree of freedom as far as the spatial and temporal offsets between driver and witness beam can be controlled. Moreover, it is important in the regard that it has to be mastered whenever plasma-based acceleration modules are staged.

Beams in external injection can be placed in a desired region which is focusing and accelerating. In addition, beams may be placed with a defined transverse offset to the driver propagation axis for the tailored generation of X-ray radiation. Moreover, low energy electron beams can be injected in a longitudinal phase, such that they are roated in phase space and longitudinally compressed [[Grebenyuk et al., 2012](#)].

In external injection methods, the trailing beam has to be matched to the focusing fields of the plasma wave in order to mitigate severe emittance growth [[Mehrling et al., 2012](#); [Grebenyuk et al., 2012](#)]. This poses a challenge as elaborated in chapter 5.

#### 1.5.7 *Driver-energy depletion*

The conservation of energy constitutes the ultimate limit for the energy gain of a witness beam in a single stage in plasma-based acceleration. Once the driver's energy was fully deposited into the generation of plasma waves, no further acceleration is possible. The energy-depletion mechanisms of laser- or particle-beam drivers are outlined below.

### 1.5.7.1 Laser-energy depletion in LWFA

A laser pulse deposits energy into the generated plasma wave and hence loses energy at a certain rate. This laser pump depletion was studied e.g. by [Bulanov et al. \[1992\]](#). Different scalings for the laser energy depletion dominate for different pulse lengths and amplitudes. A scaling for the laser pulse depletion length for the linear and non-linear case is given by [\[Esarey et al., 2004\]](#)

$$L_{pd} \simeq \frac{\lambda_p^3}{\lambda^2} \times \begin{cases} 2/a_0^2 & \text{for } a_0^2 \ll 1, \\ \sqrt{2} a_0 / \pi & \text{for } a_0^2 \gg 1. \end{cases} \quad (1.152)$$

This approximation is obtained when calculating the rate of energy transfer from the laser to the plasma wave, but does not only describe the rate of pump depletion but also the rate at which the pulse is redshifted and steepened [\[Esarey et al., 2009\]](#).

### 1.5.7.2 Beam-energy depletion in PWFA

A charged particle beam, driving a plasma wave is itself subject to the wakefields it produces and loses energy since inevitably being (partially) positioned in a decelerating phase of the plasma wave. The rate of energy loss is given by the longitudinal field magnitude at the driver beam position  $E_z^-$ . A simple approximation of the energy depletion length of an electron beam with initial energy  $m_e c^2 \gamma_b$  is thus

$$L_{ed} = \frac{m_e c^2 \gamma_b}{e E_z^-}. \quad (1.153)$$

The maximum possible energy gain of an individual witness beam particle for a given driver beam energy is determined by the ratio of the magnitudes of the decelerating longitudinal field at the driver beam position  $E_z^-$  to the accelerating longitudinal field at the witness beam position  $E_z^+$ . The number  $R = |E_z^+ / E_z^-|$  is called *transformer ratio*. Witness beam particles gain a maximum energy of  $R m_e c^2 \gamma_b$ .

It can be proven that the transformer ratio of a finite-length bunch with symmetric longitudinal charge distribution in the linear regime cannot exceed the value of two, i.e.  $R \leq 2$  [\[Bane et al., 1985; Chen et al., 1986\]](#). The transformer ratio can be optimized beyond this value by the use of triangular shaped beams in the linear regime [\[Chen et al., 1986; Katsouleas, 1986\]](#) and in the nonlinear regime [\[Lotov, 2005\]](#).

## 1.6 TRANSVERSE DYNAMICS OF CHARGED PARTICLE-BEAMS

Typical applications of relativistic particle beams are experiments in elementary particle physics, synchrotron radiation sources, nuclear

*A heavier beam species would enable a higher energy gain of a trailing electron beam [Caldwell et al., 2009].*

physics research, medical diagnoses and treatments or fusion reactor experiments [Edwards and Syphers, 2008]. Most of these applications require some sort of a high (6D) phase-space particle density at some interaction region. This is achieved firstly, by minimization of the phase-space volume while maximizing the total number of particles during the production, and secondly, through preservation of these beam attributes during the acceleration and transport of the beam to the interaction point. It will be shown (see 1.6.3) that the 6D phase-space volume occupied by the particles is constant if individual particle effects can be neglected.

A set of particles forms a *beam*, if the longitudinal momentum is much larger than the transverse momentum  $\langle p_z \rangle \gg \langle p_{x,y} \rangle$ . Due to the alternating accelerating fields in particle accelerators, beams are usually bunched, where a *bunch* denotes a beam or distinct part of a beam with a longitudinal extent comparable to the transverse extent ( $\sigma_z \sim \sigma_{x,y}$ ) [Reiser, 2008]. In order to measure the beam quality and to analyze its evolution during the acceleration and transport processes, some figure of merits for the beam quality are introduced and their properties studied.

### 1.6.1 Emittance and Courant-Snyder parameters

#### 1.6.1.1 Trace-space and trace-space emittance

In accelerator physics it is often convenient to use the concept of *trace-space* with the variables  $x-x'$ , and  $y-y'$ , where  $x' = dx/dz = \dot{x}/\dot{z} = p_x/p_z$ , and analogous for the  $y$ -direction, is the slope of a particle trajectory. The transverse properties of a beam are defined by its distribution in trace space, and the area occupied by the beam is closely related to the *transverse trace-space emittance* (see e. g. [Floettmann, 2003])

$$\hat{\epsilon} = \sqrt{\langle x_c^2 \rangle \langle x_c'^2 \rangle - \langle x_c x_c' \rangle^2}, \quad (1.154)$$

where  $x_c = x - \langle x \rangle$ , and  $x_c' = x' - \langle x' \rangle$ . Here, analogously to 1.3.5.1,

$$\langle \Phi(\mathbf{r}, \mathbf{p}) \rangle = \frac{1}{N} \int d\mathbf{r} d\mathbf{p} \Phi(\mathbf{r}, \mathbf{p}) f(\mathbf{r}, \mathbf{p}, t) \quad (1.155)$$

is the moment of a function  $\Phi(\mathbf{r}, \mathbf{p})$  and  $f$  is the beam particle distribution function. The term  $\sigma_x^2 = \langle x_c^2 \rangle$  resembles the beam size,  $\langle x_c'^2 \rangle$  expresses the transverse momentum spread and  $\langle x_c x_c' \rangle$  is the correlation between the trace space variables and conveys if a beam is converging or diverging. While the transverse beam properties are completely defined by the phase-space particle distribution  $f$ , the relevant or usable beam properties are given only by the moments  $\langle x_c^2 \rangle$ ,  $\langle x_c'^2 \rangle$ , and  $\langle x_c x_c' \rangle$  of the beam distribution  $f$ . Unless specified differently, the distribution is assumed centered around zero in transverse trace-space within the following considerations, such that  $x_c \equiv x$  and  $x_c' \equiv x'$ .

## 1.6.1.2 Courant-Snyder parameters

A beam, whose transverse properties are completely characterized by the above moments, takes the shape of an ellipse in trace-space [Reiser, 2008; Turner, 1994]

$$\hat{\gamma} x^2 + 2\hat{\alpha} xx' + \hat{\beta} x'^2 = \hat{\epsilon}. \quad (1.156)$$

Here, the Courant-Snyder parameters [Courant and Snyder, 1958]

$$\hat{\beta} = \frac{\langle x^2 \rangle}{\hat{\epsilon}}, \quad \hat{\gamma} = \frac{\langle x'^2 \rangle}{\hat{\epsilon}}, \quad \hat{\alpha} = -\frac{\langle xx' \rangle}{\hat{\epsilon}}, \quad (1.157)$$

were used. The parameters  $\hat{\beta}$ ,  $\hat{\alpha}$ , and  $\hat{\gamma}$  can be understood as normalized moments and define the orientation and shape of the beam-ellipse in trace-space while the emittance  $\hat{\epsilon}$  determines the extent of the ellipse. The characterization of the ellipse by the four parameters is redundant and the combination of eqns. (1.154) and (1.157) yields the relation  $\hat{\beta}\hat{\gamma} = 1 + \hat{\alpha}^2$ . Figure 10 depicts such an ellipse with specification of some relevant points on the circumference of the ellipse. The ellipse has the area  $F = \pi\hat{\epsilon}$  and the extent in  $x$ -direction is given by  $\sigma_x = \sqrt{\hat{\beta}\hat{\epsilon}}$ , and in  $x'$ -direction equivalently,  $\sigma_{x'} = \sqrt{\hat{\gamma}\hat{\epsilon}}$ , as specified by equations (1.157). The parameter  $\hat{\alpha}$  determines the inclination of the ellipse.

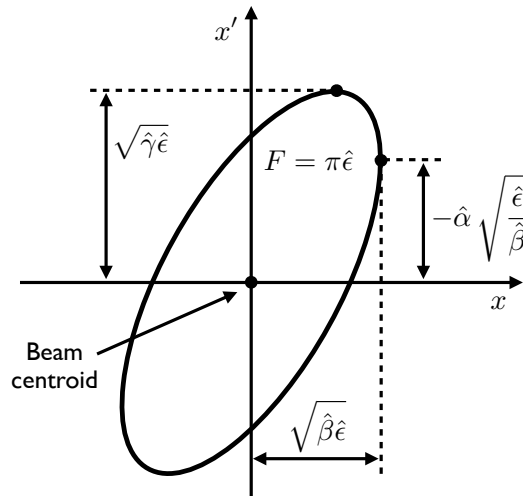


Figure 10: Trace-space ellipse, defined by equation (1.156) with relevant points on the circumference (compare [Turner, 1994; Reiser, 2008]).

While the emittance is a preserved quantity in a ideal system, the Courant-Snyder parameters generally depend on the position along the beam-propagation axis. As discussed later (see 1.6.4) the Courant-Snyder parameters may not only be seen as definitions of the beam

ellipse, but may also be interpreted from the viewpoint of the beam-line design, in which the *beta-function* or *betatron-function*  $\hat{\beta}(z)$  is a measure for the beam size and for the local betatron-oscillation length, and the alpha-function  $\hat{\alpha}(z)$  is proportional to the local change of the beta-function along the beam-path.

### 1.6.2 Luminosity and brightness

#### 1.6.2.1 Luminosity

High-energy colliders in particle physics require a large number of events to reach a signal-significance required to claim a discovery and to distinguish between signal and noise. The event rate in colliders is given by  $dN_{ev}/dt = \mathcal{L} \cdot \sigma_I$ , where  $\mathcal{L}$  is the *luminosity* and  $\sigma_I$  is the interaction cross section. While the interaction cross section is inherent in the examined physical process, the luminosity is a figure of merit for the collider and is proportional to the particle flux of two crossing bunches and to the frequency of these crossings. Furthermore, it depends on the transverse shape of the crossing bunches. The luminosity for colliding, identical Gaussian bunched beams is given by (see e. g. [Edwards and Syphers, 2008])

$$\mathcal{L} = \frac{N^2 f_{coll}}{4\pi\sigma_x\sigma_y} \quad (1.158)$$

where  $N$  is the number of particles in a bunch,  $f_{coll}$  is the bunch collision frequency and  $\sigma_{x,y}$  is the transverse RMS beam size. To optimize the event yield, one can increase the bunch collision frequency, increase the number of particles in a bunch, or decrease the beam sizes at the interaction point. The beam size at the interaction point is with the definition for the beta-function (1.157) determined by the beta-function at the interaction point  $\hat{\beta}^*$  and the beam emittance  $\sigma_{x,y} = \sqrt{\hat{\beta}_{x,y}^* \hat{\epsilon}_{x,y}}$ . The beta-function is a property of the beam-optics in the transport-beamline and the strength of the final focusing quadrupole-magnets in a collider defines the minimum beta function achievable at the interaction point. For a given  $\hat{\beta}^*$ , the luminosity hence is inversely proportional to the square root of the transverse emittance values of the beam,

$$\mathcal{L} = \frac{N^2 f}{4\pi \sqrt{\hat{\beta}_x^* \hat{\epsilon}_x \hat{\beta}_y^* \hat{\epsilon}_y}}. \quad (1.159)$$

Preservation of the transverse emittance (or minimization through radiative emittance damping) is therefore crucial for a high luminosity and thus for a high event rate in a collider.

1.6.2.2 *Brightness*

The figure of merit for the quality of a set of charged particles, used for the generation of synchrotron radiation, is the *brightness* [Reiser, 2008]

$$B = \frac{dI}{dS d\Omega}, \quad (1.160)$$

where  $I$  is the current, and  $S$  and  $\Omega$  the transverse area and the solid angle occupied by the particle set in phase-space, respectively. The brightness hence expresses the particle flux per unit area per unit solid angle and is a pivotal parameter for the use of the beam in an FEL. If the particle set is completely described by the second-order moments in trace-space only, and if the coordinate system was chosen such that correlations between the two directions vanish, it populates the hyperellipsoid

$$K = \left\{ (x, y) \in S, (x', y') \in \Omega \mid \frac{\hat{\gamma}_x x^2}{\hat{\epsilon}_x} + \frac{2\hat{\alpha}_x x x'}{\hat{\epsilon}_x} + \frac{\hat{\beta}_x x'^2}{\hat{\epsilon}_x} + \frac{\hat{\gamma}_y y^2}{\hat{\epsilon}_y} + \frac{2\hat{\alpha}_y y y'}{\hat{\epsilon}_y} + \frac{\hat{\beta}_y y'^2}{\hat{\epsilon}_y} \leq 1 \right\}. \quad (1.161)$$

The Courant-Snyder parameters and the transverse trace space emittance in both transverse directions define the size and shape of the hyperellipsoid. The volume  $V_4$ , occupied by the particles is thus given by

$$V_4 = \int_K dS d\Omega \simeq \int_K dx dy dx' dy' = \frac{\pi^2}{2} \hat{\epsilon}_x \hat{\epsilon}_y. \quad (1.162)$$

If the particle set under consideration forms a bunch with a box-shaped current profile with current  $I_0$ , one can directly find an expression for the Brightness of this bunch (compare [Reiser, 2008])

$$B = \frac{I_0}{V_4} = \frac{2I_0}{\pi^2 \hat{\epsilon}_x \hat{\epsilon}_y}. \quad (1.163)$$

Rigorously, the brightness is a property of a infinitely short-duration slice of a beam, but one may assess the average brightness of a beam with arbitrary current profile by integration of the occupied volume of the beam slices, weighted by the slice current. The beam-brightness only depends on the transverse trace-space emittance in the two transverse directions and the current profile of the beam.

1.6.2.3 *Longitudinal phase space*

Additionally, a well defined beam-energy with low spread

$$\Delta\gamma = \langle (\gamma - \langle \gamma \rangle)^2 \rangle, \quad (1.164)$$

with  $\gamma = \sqrt{1 + (p_x^2 + p_y^2 + p_z^2)/(m_e c)^2}$ , is crucial for the appropriate transport of the beams but also for their use in colliders or as synchrotron sources. Electrons in undulators, for example, radiate at specific energies, defined by the undulator strength and geometry and the energy of the electrons. A low energy spread together with a high brightness are vital for the gain in an FEL process [Röhrs, 2008]. Low energy spreads are also important for the analyses of data accumulated in colliders in order to allow for a precisely defined initial state of particles prior to the scattering processes which enables a deduction of the process from the particles in the final state.

Bunched beams also need to be short e.g. in order to allow for the pulsed generation of short X-ray flashes for the investigation of ultrafast processes in atomic or molecular science. The conservation of the longitudinal phase-space volume couples the requirement of short bunch duration and small energy spread.

In conclusion, a high phase-space density is indispensable for high-energy colliders and synchrotron sources. As explicated in the following, the phase space density of a beam is constant under if individual particle effects can be neglected.

### 1.6.3 Liouville's theorem

#### 1.6.3.1 Liouville equation

The Klimontovich equation, introduced in 1.3.2, provides an exact microscopic description of a set of individual particles and forms the basis of the plasma kinetic equation. The Liouville equation, formulated in the following is also exact, but describes the behavior of a system of particles instead of individual particles. If a system with  $N_0$  particles is regarded, a density of this system in  $6N_0$ -D can be defined

$$N(\mathbf{r}_1, \mathbf{p}_1, \mathbf{r}_2, \mathbf{p}_2, \dots, \mathbf{r}_{N_0}, \mathbf{p}_{N_0}, t) = \prod_{i=1}^{N_0} \delta(\mathbf{r}_i - \mathbf{R}_i(t)) \delta(\mathbf{p}_i - \mathbf{P}_i(t)), \quad (1.165)$$

where  $\mathbf{r}_i$  is the configuration space and  $\mathbf{p}_i$  is the momentum space for particle  $i$ , respectively and  $\mathbf{R}_i(t)$  is its position and  $\mathbf{P}_i(t)$  the momentum at time  $t$ , respectively. While  $N_0$  particles in the Klimontovich description occupy  $N_0$  positions in 6D phase space, a configuration of the system of  $N_0$  particles in the Liouville's description occupies one point in  $6N_0$ -D phase space. The time derivative of this system density is

$$\begin{aligned} \frac{\partial N}{\partial t} = & - \sum_{i=1}^{N_0} \mathbf{V}_i(t) \cdot \nabla_{\mathbf{r}_i} \prod_{j=1}^{N_0} \delta(\mathbf{r}_j - \mathbf{R}_j(t)) \delta(\mathbf{p}_j - \mathbf{P}_j(t)) \\ & - \sum_{i=1}^{N_0} \dot{\mathbf{P}}_i(t) \cdot \nabla_{\mathbf{p}_i} \prod_{j=1}^{N_0} \delta(\mathbf{r}_j - \mathbf{R}_j(t)) \delta(\mathbf{p}_j - \mathbf{P}_j(t)), \end{aligned} \quad (1.166)$$

The discussion here follows [Nicholson, 1983].

where  $\mathbf{V} = \mathbf{P}/m\sqrt{1 + (\mathbf{P}/mc)^2}$ , and  $m$  is the mass of the particle species. Here similar relations as in 1.3.2.1 for the derivation of the Klimontovich equation are used. From this equation one obtains the *Liouville equation* after some rearrangement

$$\frac{\partial N}{\partial t} + \sum_{i=1}^{N_0} \mathbf{v}_i(t) \cdot \nabla_{\mathbf{r}_i} N + \sum_{i=1}^{N_0} \dot{\mathbf{P}}_i(t) \cdot \nabla_{\mathbf{p}_i} N = 0. \quad (1.167)$$

The exact dynamical information of all  $N_0$  particles is contained in this equation which describes the evolution of the complete system of particles.

### 1.6.3.2 Liouville's theorem

With the introduction of a convective time derivative in the  $6N_0$ -D phase space,

$$\frac{D}{Dt} = \frac{\partial}{\partial t} + \sum_{i=1}^{N_0} \mathbf{v}_i(t) \cdot \nabla_{\mathbf{r}_i} + \sum_{i=1}^{N_0} \dot{\mathbf{P}}_i(t) \cdot \nabla_{\mathbf{p}_i}, \quad (1.168)$$

the Liouville equation can be written in the shape

$$\frac{D}{Dt} N(\mathbf{r}_1, \mathbf{p}_1, \mathbf{r}_2, \mathbf{p}_2, \dots, \mathbf{r}_{N_0}, \mathbf{p}_{N_0}, t) = 0. \quad (1.169)$$

This implies that the density of a system of particles in  $6N_0$ -D phase space is incompressible along the systems trajectory in  $6N_0$ -D phase space. When rewriting the Liouville equation by exploiting the independence of  $\mathbf{x}_i$  and  $\mathbf{p}_i$  and the vanishing momentum-divergence of the Lorentz force (see A.1.1), a continuity equation is obtained

For a more detailed discussion, confer [Nicholson, 1983].

$$\frac{\partial N}{\partial t} + \sum_{i=1}^{N_0} \nabla_{\mathbf{r}_i} \cdot (\mathbf{v}_i(t) N) + \sum_{i=1}^{N_0} \nabla_{\mathbf{p}_i} \cdot (\dot{\mathbf{P}}_i(t) N) = 0. \quad (1.170)$$

This equation expresses the conservation of systems  $6N_0$ -D phase space. The Liouville equation describes the propagation of the state of the system along a trajectory in  $6N_0$ -D phase space.

One usually does not know the exact state of the system at a time  $t$ . Hence, it is convenient to define a probability

$$f_{N_0}(\mathbf{r}_1, \mathbf{p}_1, \mathbf{r}_2, \mathbf{p}_2, \dots, \mathbf{r}_{N_0}, \mathbf{p}_{N_0}, t) d\mathbf{r}_1 d\mathbf{p}_1 d\mathbf{r}_2 d\mathbf{p}_2 \dots d\mathbf{r}_{N_0} d\mathbf{p}_{N_0}, \quad (1.171)$$

to find the system at the point  $(\mathbf{r}_1, \mathbf{p}_1, \mathbf{r}_2, \mathbf{p}_2, \dots, \mathbf{r}_{N_0}, \mathbf{p}_{N_0})$  in  $6N_0$ -D phase space. The function  $f_{N_0}$  then expresses the probability density and integration over the whole phase space must yield unity. The statements made above for  $N$  can now be made in a similar way for the smooth function  $f_{N_0}$ . One obtains the continuity equation for the probability

$$\frac{\partial f_{N_0}}{\partial t} + \sum_{i=1}^{N_0} \nabla_{\mathbf{r}_i} \cdot (\mathbf{v}_i(t) f_{N_0}) + \sum_{i=1}^{N_0} \nabla_{\mathbf{p}_i} \cdot (\dot{\mathbf{P}}_i(t) f_{N_0}) = 0, \quad (1.172)$$



and

$$\frac{D}{Dt} f_{N_0}(\mathbf{r}_1, \mathbf{p}_1, \mathbf{r}_2, \mathbf{p}_2, \dots, \mathbf{r}_{N_0}, \mathbf{p}_{N_0}, t) = 0, \quad (1.173)$$

which is the statement that the probability density is constant along the motion of systems. Regarding  $f_{N_0}$  as a fluid density in  $6N_0$ -D phase space, this equation implies for the fluid density to be constant along the fluid motion, and the fluid to be incompressible.

The Liouville equation can be transformed into a chain of equations, called the Bogoliubov, Born, Green, Kirkwood and Yvon (BBGKY) chain (see [Nicholson, 1983]). When regarding a set of individually non-interacting particles, the BBGKY hierarchy of equations can be truncated after the first term, which yields the Vlasov equation (1.89), which - given the force  $\mathbf{F}$  is  $\mathbf{p}$ -divergence free (see A.1.1) - may be written in the shape of a continuity equation expressing the conservation of particles in 6D phase space,

$$\frac{\partial f}{\partial t} + \nabla_{\mathbf{r}} \cdot (\mathbf{v}f) + \nabla_{\mathbf{p}} \cdot (\mathbf{F}f) = 0, \quad (1.174)$$

where  $f$  is the 6D phase space particle density. Moreover, the Vlasov equation (1.89) can also be written as a convective time derivative equation

$$\frac{\tilde{D}f(\mathbf{r}, \mathbf{p}, t)}{\tilde{D}t} = 0, \quad (1.175)$$

with the derivative

$$\frac{\tilde{D}}{\tilde{D}t} = \frac{\partial}{\partial t} + \nabla_{\mathbf{r}} \cdot \mathbf{v} + \nabla_{\mathbf{p}} \cdot \mathbf{F}. \quad (1.176)$$

The Vlasov equation is a special mathematical statement of *Liouville's theorem* and equation (1.175) expresses the invariance of the 6D phase-space density along the characteristics of the Vlasov equation. When regarding  $f$  as a fluid density in 6D phase space, equation (1.175) states that this fluid is incompressible.

The number of particles moving along with the phase space fluid must be conserved. Knowing this, and using the invariance of the particle density, a second statement of the Liouville's theorem can be formulated. The following regards the number of particles  $\delta N$  contained in a small 6D phase space volume

$$\delta V = \delta R_x(t) \delta R_y(t) \delta R_z(t) \delta P_x(t) \delta P_y(t) \delta P_z(t). \quad (1.177)$$

It is stipulated for the volume to move along the characteristics of the Vlasov equation, in order to contain the constant number of particles,

$$\delta N = f(\mathbf{R}(t), \mathbf{P}(t), t) \delta V, \quad (1.178)$$

*The argumentation is inspired by [Bradt, 2008].*

with

$$\frac{d\delta N}{dt} = \frac{d}{dt} [f(\mathbf{R}(t), \mathbf{P}(t), t) \delta V] = 0. \quad (1.179)$$

Hence, after applying the chain rule, one finds

$$\delta V \left. \frac{\tilde{D}f(\mathbf{r}, \mathbf{p}, t)}{\tilde{D}t} \right|_{\mathbf{r}=\mathbf{R}, \mathbf{p}=\mathbf{P}} + f(\mathbf{R}(t), \mathbf{P}(t), t) \frac{d\delta V}{dt} = 0. \quad (1.180)$$

The first term is zero by virtue of the Vlasov equation (1.175) and the particle density  $f$  in the second term is not zero for arbitrary  $\mathbf{R}$  and  $\mathbf{P}$ . This leads to the identity

$$\frac{d\delta V}{dt} = 0. \quad (1.181)$$

This equation expresses the conservation of the phase space volume along the characteristics of the Vlasov equation. This is the second statement of the Liouville's theorem, expressing that the phase space occupied by a set of particles may change its shape, but the volume is invariant during the motion of the set of particles.

In conclusion, the Liouville equation implies that the density of systems and the volume occupied by systems in  $6N_0$ -D phase space are constant along the trajectory of the systems. Moreover, for a particle set for which individual particle interactions (e.g. collisions) can be neglected, the Liouville's theorem states that the 6D particle density and the occupied volume is constant during the motion.

### 1.6.3.3 Emittance and phase-space

The beam-emittance fundamentally impacts pivotal parameters in an accelerator such as the luminosity or the brightness. It is closely related to the beam phase-space volume. However, equation (1.162) is only true in the special case of a beam whose particle distribution has vanishing higher order correlations between  $x$ ,  $x'$ ,  $y$  and  $y'$ . This is provided e.g. for a 4D Gaussian distribution, but is not generally the case. The emittance is related to the phase-space volume *and* its shape.

The 6D phase-space volume occupied by a beam is a conserved quantity during the motion if mutual particle interactions or radiation effects can be neglected. However, a conserved phase or trace space volume does not imply a conservation of the emittance since the shape of the populated phase space may change.

Beams, propagating in focusing fields with a linear transverse dependence, do not experience emittance growth (see 1.6.4.1). Non-linear transverse focusing fields, on the contrary, cause a beam filamentation (see [Reiser, 2008]), which implies an increase of the emittance while the phase or trace space volume is conserved. Furthermore, if linearly

*For a more detailed discussion, see [Reiser, 2008, Ch. 3].*

focusing fields vary along the beam axis, the beam emittance can increase while the phase-space volume is constant. Such effects will be elaborated in more detail within this work.

Another implication on the emittance of a beam is owed to its acceleration. The ratio  $x'$  of the transverse momentum  $p_x$  over the longitudinal momentum  $p_z$  is damped adiabatically when particles gain longitudinal momentum during the acceleration process. To compensate for this effect, the *normalized transverse trace-space emittance*,

$$\hat{\epsilon}_n = \frac{\langle p_z \rangle}{m_e c} \hat{\epsilon} = \frac{\langle p_z \rangle}{m_e c} \sqrt{\langle x^2 \rangle \langle x'^2 \rangle - \langle x x' \rangle^2}, \quad (1.182)$$

is introduced for convenience, with  $\langle p_z \rangle$  being the average longitudinal momentum.

An emittance definition which is frequently used and closely related to the above definition is the *normalized transverse phase-space emittance*

$$\epsilon_n = \frac{1}{m_e c} \sqrt{\langle x^2 \rangle \langle p_x^2 \rangle - \langle x p_x \rangle^2}, \quad (1.183)$$

While the two emittance definitions (1.182) and (1.183) yield the identical result for beams which are at waist  $\langle x x' \rangle = 0$ , there is a fundamental difference between the normalized trace-space and phase-space emittance of beams with significant energy spread which are highly divergent. The trace-space emittance is always constant during free drifts when neglecting space charge forces. This is in contrast to the transverse phase-space emittance, which can change during vacuum propagation when a correlation between the transverse position and the longitudinal momentum emerges in the beam phase-space distribution owed to a significant energy spread and a large divergence [Floettmann, 2003]. Considering this circumstance, this work will make use of both emittance definitions and present comparisons between the two when a different behavior is expected.

#### 1.6.4 Beam transport in ideal systems

##### 1.6.4.1 General Courant-Snyder theory

The following discusses the beam equations of motion in an ideal system. A system is considered ideal in the sense, that space charge effects do not play a role, the focusing forces are linear and depend only on the position along the propagation axis, the beam has negligible energy spread and the approximation of paraxial motion (see [Reiser, 2008, 3.3.2]) holds. The equation of motion for a single particle in a transverse direction (here  $x$ , analogously for  $y$ ) in such an ideal system is given by

$$x'' + K(z)x = 0, \quad (1.184)$$

*This discussion follows [Courant and Snyder, 1958], [Reiser, 2008, 3.8.2] and [Edwards and Syphers, 2008, 3.2].*

where  $x$  is the displacement from the beam axis,  $x'' = d^2x/dz^2$  and  $K = K(z)$  is a function on the axial coordinate only. Equation (1.184) has solutions of the form [Reiser, 2008]

$$x(z) = A w(z) \cos [\psi(z) + \phi] , \quad (1.185)$$

where the amplitude  $A$  and the phase  $\phi$  are constants and are determined by the initial conditions,  $\psi$  expresses the phase advance, and  $w$  is the amplitude function, depending on the position along the beam propagation axis. Equation (1.185) has an additional degree of freedom and one can choose the relation  $\psi' = w^{-2}$  to hold (see [Reiser, 2008]). Exploiting this equality and plugging (1.185) into (1.184) yields the differential equation for the amplitude function

$$w'' + Kw - \frac{1}{w^3} = 0 . \quad (1.186)$$

This equation describes the evolution of the beam-particle oscillation amplitudes.

The connection to the Courant-Snyder parameters (1.157) can be found as follows. By differentiation of equation (1.185),  $x'$  is obtained. The equation,

$$\frac{x^2}{w^2} + (wx' - w'x)^2 = A^2 , \quad (1.187)$$

can then be shown to hold for any position along the beam propagation axis. This equation describes the closed trajectories of particles in trace-space. One can now make a specific choice for the amplitude, e.g.

$$\hat{\beta} = w^2 , \quad (1.188a)$$

$$\hat{\alpha} = -ww' = -\frac{\hat{\beta}'}{2} , \quad (1.188b)$$

$$\hat{\gamma} = \frac{1}{w^2} + w'^2 = \frac{1 + \hat{\alpha}^2}{\hat{\beta}} . \quad (1.188c)$$

By doing so, one retrieves the known ellipse equation

$$\hat{\gamma}(z)x^2 + 2\hat{\alpha}(z)xx' + \hat{\beta}(z)x'^2 = \hat{\epsilon} , \quad (1.189)$$

where, in addition,  $A^2$  is identified with  $\hat{\epsilon}$ . This derivation proves that the emittance in ideal systems is conserved while the Courant-Snyder parameters are functions of the beam propagation axis.

With the above information, a description of the evolution of the parameter  $\hat{\beta}$  is possible. Combining the differential equation of the amplitude function (1.186) and the definition of the beta-function (1.188a) yields

$$\hat{\beta}\hat{\beta}'' - \frac{\hat{\beta}'^2}{2} + 2K\hat{\beta}^2 - 2 = 0 . \quad (1.190)$$

The envelope equation can alternatively, with equations (1.188b) and (1.188c), be expressed in terms of the Courant-Snyder parameters,

$$K\hat{\beta} = \hat{\gamma} + \hat{\alpha}' . \quad (1.191)$$

These differential equations express the evolution of the Courant-Snyder parameters in ideal systems with arbitrary functions  $K(z)$ .

#### 1.6.4.2 Betatron oscillations and matching in constant focusing channels

Equation (1.190) has analytic solutions for specific functions  $K(z)$  e.g. for  $K = \text{const}$ . In particular, during vacuum propagation ( $K = 0$ ), equations (1.190) or (1.191) feature the solution

$$\hat{\alpha}(z) = \frac{z_0 - z}{\hat{\beta}_0}, \quad \hat{\beta}(z) = \hat{\beta}_0 + \frac{(z - z_0)^2}{\hat{\beta}_0}, \quad \hat{\gamma}(z) = \frac{1}{\hat{\beta}_0}, \quad (1.192)$$

where  $z_0$  and  $\hat{\beta}_0$  are the initial (or focal) position and value of the beta function, respectively.

For positive, constant (or slowly varying)  $K > 0$ , equation (1.190) has the solution [Reiser, 2008]

$$\hat{\beta}(z) = \hat{\beta}_0 \cos^2(\sqrt{K}z) + \frac{1}{\hat{\beta}_0 K} \sin^2(\sqrt{K}z) . \quad (1.193)$$

Retrieval of the full set of Courant-Snyder parameters is possible by means of the relations (1.188b) and (1.188c). The beta function of a beam in a constant focusing channel oscillates between the two values  $\hat{\beta}_0$  and  $1/(\hat{\beta}_0 K)$ , while the alpha function oscillates around zero.

In a constant focusing channel, the individual particles in a beam oscillate according to equation (1.184) with constant  $K$ . In this case, this equation simply describes a harmonic oscillator with the known solutions. The particle orbits, in particular, are given by

$$x^2 + \frac{x'^2}{K} = \text{const} , \quad (1.194)$$

and hence follow ellipses in trace-space. The oscillation of the Courant-Snyder parameters implies a rotation of the beam trace-space ellipse, defined by (1.189). This is illustrated in Figure 11, which shows the example of a individual particle trajectory in trace-space (red) and a beam envelope ellipse (black). The ellipse rotates according to equation (1.193), while retaining its area.

A beam in a uniform focusing channel is called *matched*, if the beam envelop does not oscillate, i.e. if  $\hat{\beta}' = 0 = \hat{\alpha}$ . Equation (1.193) infers this being the case if  $\hat{\beta}_0 = \hat{\beta}_m = K^{-1/2}$ . The matched Courant-Snyder parameters in a constant focusing channel in an ideal system are thus

$$\hat{\alpha}_m = 0, \quad \hat{\beta}_m = \frac{1}{\sqrt{K}}, \quad \hat{\gamma}_m = \sqrt{K}. \quad (1.195)$$

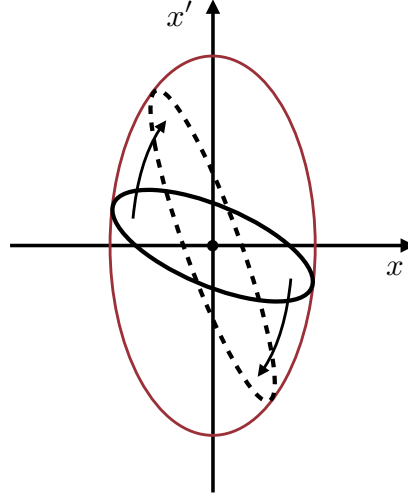


Figure 11: Illustration of trace-space ellipse rotation from betatron oscillation. The red ellipse represents a single-particle trajectory in trace-space defined by  $x^2 + x'^2/K = \hat{\epsilon}/\sqrt{K}$ . The black ellipse depicts the trace-space ellipse of a beam and the black-dashed ellipse illustrates the rotation from betatron oscillations.

The single particle orbits in trace-space (1.194) may be written in terms of the matched beta function

$$x^2/\hat{\beta}_m + \hat{\beta}_m x'^2 = \text{const.} \quad (1.196)$$

When a beam is matched to the focusing channel, the situation in Figure 11 is as follows. The beam trace-space ellipse (black) has the same shape as the individual electron trajectories (red). Hence, the trace-space ellipse does not rotate and betatron oscillations do not occur.

Changes of  $K$  on length-scales much longer than  $\hat{\beta}$  are imposing an *adiabatic change* of the transverse beam parameters and equation (1.193) locally holds for such changes.

### 1.6.5 Emittance growth

The beam-emittance is a pivotal parameter in accelerator physics. While the normalized emittance is preserved in an ideal system, it generally changes in realistic accelerator setups. This can be owing to a large number of mechanisms, resulting in different types of emittance change.

Some of the most relevant reasons of emittance growth in the context of plasma-based acceleration are listed below (compare [Reiser, 2008, Ch. 6]):

- (a) Off-axis injection of a beam into the accelerator, causing coherent (if correlated energy spread is negligible) oscillations around the optical axis.

- (b) Mismatch of beam parameters to the design transport parameters, resulting in a decoherence of the beam particle betatron oscillations,
- if the beam has a significant correlated or uncorrelated energy spread or
  - if the applied fields change along the longitudinal intra-bunch position.
- (c) Nonlinear transverse forces, leading to beam-filamentation.
- (d) Nonlinear coupling between transverse and longitudinal motion.
- (e) Intra-beam scattering or collisions between beam particles and background gas or ions.

The transverse normalized emittance can also decrease within the acceleration process. This can be owing to synchrotron radiation or effects which transforms transverse emittance to longitudinal emittance (see [Reiser, 2008]). Moreover, differential phase space rotation from point (b) can, in principle not only cause emittance growth but also an emittance decrease if the phase-space was already rotated initially. In a similar way, the application of appropriate nonlinear transverse forces on the beam can also in special cases reduce its emittance.

The emittance of a beam is related to the shape and volume of the phase space it populates. A change of the emittance must hence not necessarily be a result of a change of the occupied phase space volume but can be a cause of a change of the shape of the phase space volume. Among the above points, (a)-(d) are not changing the occupied 6D phase space volume, only point (e) can change the 6D phase space volume.

The emittance growth from scattering effects, point (e), will be neglected within this work for the following reasons. Firstly, the scattering processes between particles within in a beam (intra-beam scattering), which constitutes a coupling between longitudinal and transverse motion occur on time-scales much longer than the acceleration process for typical parameters used in plasma-based accelerators (see e.g. [Reiser, 2008; Kubo et al., 2005]). Secondly, as indicated by equation (1.66), the cross section of electrons scattering with (resting) background ions decreases quadratically with the electron energy. It can be estimated that an electron beam with an energy of  $\sim 1$  GeV, traversing a single-charged ion column with  $\sim 0.1$  m length and particle density of  $n_i \sim 10^{23} \text{ m}^{-3}$  does not gain any significant broadening of the transverse momentum distribution.

Moreover, some types of emittance growth are reversible while others are irreversible [Reiser, 2008; O'Shea, 1998]. It is often convenient to differentiate between two types of transverse emittance growth. One in which the emittance of a infinitely short slice of the beam is constant and one for which the emittance changes within one slice [O'Shea, 1998]. The emittance within a slice is constant for the above cases (a) and (b) under the assumption that the uncorrelated or slice

energy spread is negligible. The emittance change by virtue of (b) beam mismatch and betatron phase decoherence is discussed in chapter 4.



## Part II

### NUMERICAL METHODS

#### 2. PARTICLE-IN-CELL METHOD

*Content:* Introduction into the Particle-in-cell (PIC) technique. Physical basis of the PIC method. Numerical implementation and the PIC main cycle. Relevant features of PIC simulations.

#### 3. DEVELOPMENT OF A QUASI-STATIC PIC CODE

*Content:* Motivation for the need of improved computational efficiency and introduction of the quasi-static particle-in-cell approach. Physical basis and quasi-static framework. Numerical implementation in the quasi-static PIC code HiPACE. Comparison of results from HiPACE simulations with results from simulations with a fully explicit PIC code. Outline of the parallelization and assessment of parallel performance of HiPACE. Discussion and conclusion.



## 2.1 INTRODUCTION

Already with the first proposal of laser-driven plasma accelerators by Tajima and Dawson in 1979 [Tajima and Dawson, 1979], computational studies played an integral role for the comprehension of the physical basis of plasma-based accelerators [Esarey et al., 2009]. Today, numerical methods are a well established, and moreover, indispensable pillar in plasma-based accelerator research, not only interconnecting theory and experiment, but substantially driving innovations in this field. Experimental production of GeV-scale electron beams within few centimetre long plasma targets [Leemans et al., 2006; Wang et al., 2013; Kim et al., 2013], energy doubling of 40 GeV electrons within a distance of less than a meter [Blumenfeld et al., 2007] and advances such as demonstration of stable [Osterhoff et al., 2008] and tunable [Gonsalves et al., 2011] electron beams promoted plasma-based acceleration to a prime candidate for future accelerators. Along with the experimental progress, numerical techniques were becoming more versatile and efficient.

The most prevalent numerical method in plasma-based accelerator research is the Particle-In-Cell (PIC) technique [Hockney and Eastwood, 1981; Dawson, 1983; Birdsall and Langdon, 1985], which enables a modeling of complex kinetic and relativistic plasma phenomena. Extensive advances in computer technology during the past decades have laid the groundwork for scientific high-performance computing, with today's machines providing peak performances beyond  $10^{16}$  floating point operations per second [Meuer et al., 2014]. When executed on such machines, massively parallelised PIC codes allow for fully three-dimensional (3D) modeling of relativistic laser or charged particle-beam interactions with plasma by resolving small time- and length-scales. The basis of the PIC method is outlined below.

## 2.2 PHYSICAL BASIS OF THE PIC METHOD

The physical foundation of the PIC technique used in collisionless plasma physics is the Maxwell-Vlasov system (see 1.3.3.2). The PIC method is of Eulerian-Lagrangian type. More precisely, it processes the Eulerian information, namely the electric field  $\mathbf{E}(\mathbf{r}, t)$ , the magnetic field  $\mathbf{B}(\mathbf{r}, t)$ , and the charge- and current-density  $\rho(\mathbf{r}, t)$  and  $\mathbf{J}(\mathbf{r}, t)$ , respectively, on a spatial grid. The Lagrangian component of the PIC method comes from the introduction of *macro-particles* (also

called *numerical particles* or *quasi-particles*). These constitute the numerical discretization of the particle distribution function of a species  $s$ , associated with the Vlasov equation (1.89), via

$$f_s(\mathbf{r}, \mathbf{p}, t) \approx \sum_{\alpha=1}^{M_s} \tilde{n}_{s,\alpha}(\mathbf{r} - \mathbf{R}_{s,\alpha}(t)) \delta(\mathbf{p} - \mathbf{P}_{s,\alpha}(t)) \quad (2.1)$$

where  $\tilde{n}_{s,\alpha}$  is the spatial particle density shape function of individual macro-particles with positions  $\mathbf{R}_{s,\alpha}$  and momenta  $\mathbf{P}_{s,\alpha}$ . This particle density shape function is generally bounded, i.e. zero outside of some region. The number of the macro-particles used for the reproduction of the phase-space distribution of a plasma species  $s$  is here denoted by  $M_s$ . When rendering the particle distribution function in this way, an equation similar to the Klimontovich equation (confer 1.3.2.1) is obtained, which evolves the numerical particles along the characteristics of the Vlasov equation. These characteristics are the discrete particle trajectories, defined by (compare 1.3.2)

$$\frac{d\mathbf{R}_{s,\alpha}}{dt} = \mathbf{V}_{s,\alpha}, \quad (2.2a)$$

$$\frac{d\mathbf{P}_{s,\alpha}}{dt} = Q_{s,\alpha} \left( \mathbf{E} + \frac{\mathbf{V}_{s,\alpha}}{c} \times \mathbf{B} \right), \quad (2.2b)$$

where  $\mathbf{V}_{s,\alpha}$  is the macro-particle velocity and  $Q_{s,\alpha}$  is the integrated charge of a macro-particle. The partial differential Vlasov-equation is hence replaced with the ordinary differential Newton's equation of motion and the ordinary differential Lorentz-equation.

Charge and current densities in the Maxwell-Vlasov theory are computed by means of equations (1.91a) and (1.91b). These equations, together with the discretization (2.1) yield

$$\rho(\mathbf{r}, t) \approx \sum_s q_s \sum_{\alpha=1}^{M_s} \tilde{n}_{s,\alpha}(\mathbf{r} - \mathbf{R}_{s,\alpha}(t)), \quad (2.3a)$$

$$\mathbf{J}(\mathbf{r}, t) \approx \sum_s q_s \sum_{\alpha=1}^{M_s} \mathbf{V}_{s,\alpha} \tilde{n}_{s,\alpha}(\mathbf{r} - \mathbf{R}_{s,\alpha}(t)), \quad (2.3b)$$

where  $q_s$  denotes the charge of an elementary charge of the species. The system of equations is closed by virtue of the Maxwell equations (1.1a)-(1.1d). Such an approach allows for an efficient numerical investigation of kinetic and relativistic plasma phenomena while a full and direct Vlasov approach is impracticable for most problems in plasma-based acceleration. The numerical implementation of this approach is outlined below.

### 2.3 NUMERICAL IMPLEMENTATION AND PROPERTIES

The numerical implementation of the PIC technique is as follows. At the initialization of a PIC simulation, the charge-density and current-density on the grid are zero in order to fulfill the time-independent

Maxwell equations (1.1a) and (1.1b). These time-independent Maxwell equations are from that point on not anymore explicitly respected but are implicitly fulfilled, if the time-dependent Maxwell equations (1.1c) and (1.1d) and the charge continuity equation (1.2) are fulfilled.

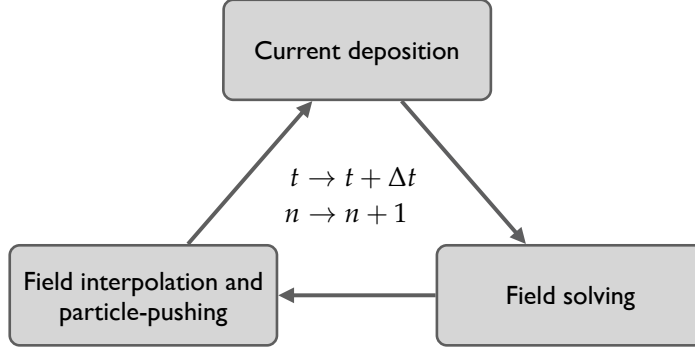


Figure 12: Main numerical time-integration cycle in PIC codes

The main time-integration cycle in a PIC simulation is then iterated until the maximum simulation run time is reached. It contains the substantial instances of current-density deposition, field solving, field interpolation and particle-pushing and is depicted in Figure 12. Here,  $n$  specifies the index of the time-step,  $\Delta t$  represents the time-step size which is usually constant in full PIC codes. The simulation time is then given by  $t = t_0 + n\Delta t$ .

### 2.3.1 Current-density deposition

The current-density in the PIC method is given by equation (2.3b). The function  $\tilde{n}(\mathbf{r} - \mathbf{R})$  in that equation specifies the particle density shape function of a numerical particle. These chunks of spatial particle density should be small enough to reproduce the expected spatial features of the particle density function  $f(\mathbf{r}, \mathbf{p}, t)$ . Moreover, since macro-particles have a point like shape in momentum space, a sufficient number of particles should be used to populate the momentum space to resolve the momentum distribution of  $f(\mathbf{r}, \mathbf{p}, t)$  appropriately.

The particle density shape function of macro-particle  $\alpha$  is for convenience decomposed into an individual magnitude  $\tilde{N}_\alpha$  and a general normalized shape-function  $S$ ,

$$\tilde{n}_\alpha(\mathbf{r} - \mathbf{R}_\alpha) = \tilde{N}_\alpha S(x - X_\alpha, y - Y_\alpha, z - Z_\alpha). \quad (2.4)$$

with

$$\int dx dy dz S(x - X_\alpha, y - Y_\alpha, z - Z_\alpha) = 1. \quad (2.5)$$

On a numerical lattice, the current-density is defined at the coordinates  $x_i, y_j, z_k$ , where  $i, j, k$  are the grid-point indices (see Yee mesh

*A reason, why non-point-like shapes in coordinate space are used is motivated in 2.4.*

2.3.2). A macro-particle, situated in this lattice deposits its current-density in the following charge conserving way.

In the example of a one-dimensional (1D) second-order polynomial shape-function, the fractions of the macro-particle current-density, deposited onto the nearest three grid-points, is given by (confer [Esirkepov, 2001])

$$S_i^{1D}(X_\alpha) = \frac{3}{4} - \left( \frac{x_i - X_\alpha}{\Delta x} \right)^2, \quad |x_i - X_\alpha| \leq \frac{\Delta x}{2}, \quad (2.6a)$$

$$S_{i\pm 1}^{1D}(X_\alpha) = \frac{1}{2} \left[ \frac{1}{2} \mp \left( \frac{x_i - X_\alpha}{\Delta x} \right) \right]^2, \quad (2.6b)$$

where  $\Delta x$  is the cell size. The density distribution of the macro-particles is a quadratic spline and bell-shaped with this definition. The three-dimensional (3D) shape-function is then given by

$$S_{i,j,k}^{3D}(X_\alpha, Y_\alpha, Z_\alpha) = S_i^{1D}(X_\alpha) S_j^{1D}(Y_\alpha) S_k^{1D}(Z_\alpha), \quad (2.7)$$

and accordingly for the other eight grid-points in the quadratic spline range. The current-density deposited by a macro-particle onto the nearest grid point is then given by

$$\mathbf{J}_{i,j,k} = Q_\alpha \mathbf{V}_\alpha S_{i,j,k}^{3D}(X_\alpha, Y_\alpha, Z_\alpha), \quad (2.8)$$

with  $Q_\alpha = q \tilde{N}_\alpha$ , and accordingly for the other eight grid-points in the quadratic spline range. The current-density deposited onto the grid by the individual macro-particles is added up.

### 2.3.2 Field solving

Particle-in-cell codes update the field values on the grid after macro-particle current-density deposition via the time-dependent Maxwell equations, namely

$$\frac{\partial \mathbf{B}}{\partial t} = -c \nabla \times \mathbf{E}, \quad (2.9a)$$

$$\frac{\partial \mathbf{E}}{\partial t} = c \nabla \times \mathbf{B} - 4\pi \mathbf{J}. \quad (2.9b)$$

These partial differential equations are discretized to enable a computation of the fields on the grid. To allow for a small error associated with the finite difference approximation of the time-derivative and the curls, the following time-centered and space-centered finite difference approach, called the Yee finite-difference time-domain (FDTD) method, was proposed [Yee, 1966]. It employs a spatially staggered mesh, depicted in Figure 13, to allow for a spatially centered finite difference with error  $\mathcal{O}(\Delta x^2)$ . The magnetic field values are thereby defined at the center of the faces of the cells whereas the electric field values are defined at the middle of the edges of the cells. The curls

*The charge conservation for deposition schemes with arbitrary form factor is studied by Esirkepov [2001].*

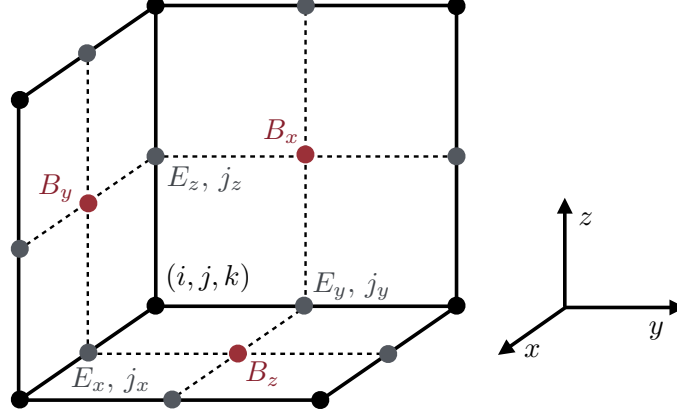


Figure 13: Spatially staggered Yee mesh. The electric field and current components are defined at the middle of the edges of the cells, respectively. The magnetic field components are defined at the middle of the faces of the cells.

can then be written in a space-centered finite difference scheme [Yee, 1966; Greenwood et al., 2004].

Moreover, the Yee FDTD scheme is also centered in time. The electric field values are computed at half-integer time steps whereas the magnetic field is computed at integer time steps (compare e.g. [Pritchett, 2003]),

$$\mathbf{E}^{n+1/2} = \mathbf{E}^{n-1/2} + \Delta t (c \nabla \times \mathbf{B}^n - 4\pi \mathbf{J}^n), \quad (2.10a)$$

$$\mathbf{B}^{n+1} = \mathbf{B}^n - c \Delta t \nabla \times \mathbf{E}^{n+1/2}, \quad (2.10b)$$

so that the error associated with the discrete time evaluation scales as  $\mathcal{O}(\Delta t^2)$ . Here, in addition, the quantity  $\mathbf{B}^{n+1/2} = (\mathbf{B}^n + \mathbf{B}^{n+1})/2$  is computed and stored for the use of particle pushing.

This is an explicit scheme for the numerical solution of partial differential equations. Explicit partial differential equation solvers are considered robust and stable. However, in order to guarantee for computational stability the following requirement must be fulfilled. The time step size must be limited by the Courant-Friedrichs-Lewy (CFL) condition [Courant et al., 1928; Yee, 1966],

$$\Delta t = C_{\text{CFL}} \frac{\sqrt{\Delta x^2 + \Delta y^2 + \Delta z^2}}{c}, \quad (2.11)$$

where  $C_{\text{CFL}}$  is the CFL number with the necessary requirement  $C_{\text{CFL}} < 1$  for stability of the numerical PDE solver. Moreover, to assure for light-like numerical dispersion along the diagonal of the cells, the CFL number must be close to one [Greenwood et al., 2004]. These conditions fundamentally couples the spatial and temporal resolutions in fully explicit PIC codes. PIC codes using a FDTD method with explicit PDE solvers are called "fully explicit PIC codes" within this work.

### 2.3.3 Field interpolation and particle pushing

Equations (2.2b) and (2.2a) define the macro-particle advance. A time-centered discretization of these equations is given by (compare [Vay, 2008])

$$\frac{\gamma_\alpha^{n+1} \mathbf{V}_\alpha^{n+1} - \gamma_\alpha^n \mathbf{V}_\alpha^n}{\Delta t} = \frac{q}{m} \left( \mathbf{E}_\alpha^{n+1/2} + \frac{\bar{\mathbf{V}}_\alpha^{n+1/2}}{c} \times \mathbf{B}_\alpha^{n+1/2} \right). \quad (2.12a)$$

$$\frac{\mathbf{R}_\alpha^{n+3/2} - \mathbf{R}_\alpha^{n+1/2}}{\Delta t} = \mathbf{V}_\alpha^{n+1}, \quad (2.12b)$$

Here, the indices of the particle species are dropped and  $\mathbf{E}_\alpha$  and  $\mathbf{B}_\alpha$  specify the field values at the position of macro-particle  $\alpha$ , and  $q/m$  denotes the charge mass ratio of the regarded species. These field values are obtained by means of an interpolation scheme, analogous to the current-density deposition scheme.

In the example of a quadratic spline interpolation scheme, the field values at the macro-particles position are obtained via

$$\mathbf{E}_\alpha = \sum_{\lambda, \mu, \nu = \{-1, 0, 1\}} \mathbf{E}_{i+\lambda, j+\mu, k+\nu} S_{i+\lambda}^{1D}(X_\alpha) S_{j+\mu}^{1D}(Y_\alpha) S_{k+\nu}^{1D}(Z_\alpha), \quad (2.13a)$$

$$\mathbf{B}_\alpha = \sum_{\lambda, \mu, \nu = \{-1, 0, 1\}} \mathbf{B}_{i+\lambda, j+\mu, k+\nu} S_{i+\lambda}^{1D}(X_\alpha) S_{j+\mu}^{1D}(Y_\alpha) S_{k+\nu}^{1D}(Z_\alpha), \quad (2.13b)$$

where the 1D shape functions (2.6a) and (2.6b) are used, bearing in mind that the various field components are defined at different locations within the cell.

Equation (2.12a) contains the macro-particle velocity at half-integer time step on the right hand side. This information is not explicitly known, but a method to compute it was proposed by Boris [1970]. The velocity at half-integer time step can firstly be written as (compare [Vay, 2008])

$$\bar{\mathbf{V}}_\alpha^{n+1/2} = \frac{\gamma_\alpha^n \mathbf{V}_\alpha^n + \gamma_\alpha^{n+1} \mathbf{V}_\alpha^{n+1}}{2 \bar{\gamma}_\alpha^{n+1/2}}. \quad (2.14)$$

Now, the advance by the electric field can be decoupled from the magnetic contribution by use of a relativistic factor of (see [Vay, 2008])

$$\bar{\gamma}_\alpha^{n+1/2} = \sqrt{1 + \left( \gamma_\alpha^n \mathbf{V}_\alpha^n + \frac{q \Delta t}{2m} \mathbf{E}_\alpha^{n+1/2} \right)^2}. \quad (2.15)$$

This is possible since the magnetic field does not change the kinetic energy of a particle. The resulting system is closed with the components of  $\gamma_\alpha^{n+1} \mathbf{V}_\alpha^{n+1}$  being the three unknowns and the components of (2.12a) being the determining equations. The macro-particle positions at integer time-steps are computed via  $\mathbf{R}_\alpha^{n+1} = (\mathbf{R}_\alpha^{n+1/2} + \mathbf{R}_\alpha^{n+3/2})/2 = \mathbf{R}_\alpha^{n+3/2} - \Delta t \mathbf{V}_\alpha^{n+1}/2$  during the next current deposition.

*Improved schemes  
are presented in  
[Vay, 2008].*



### 2.3.4 Numerical sequence of a typical PIC cycle

A typical numerical sequence in the example of a fully time-centered PIC cycle is illustrated below. The initially known quantities at time step  $n$  are:

$$\left\{ \mathbf{R}_\alpha^{n+1/2}, \mathbf{V}_\alpha^n, \mathbf{E}^{n-1/2}, \mathbf{B}^{n-1/2}, \mathbf{B}^n \right\} \quad (2.16)$$

The first step is the current density deposition:

$$\left\{ \mathbf{R}_\alpha^{n+1/2}, \mathbf{V}_\alpha^n \right\} \Rightarrow \mathbf{R}_\alpha^n, \quad (2.17a)$$

$$\left\{ \mathbf{R}_\alpha^n, \mathbf{V}_\alpha^n \right\} \Rightarrow \mathbf{J}^n. \quad (2.17b)$$

After current density deposition, the electric field and magnetic field can be computed:

$$\left\{ \mathbf{E}^{n-1/2}, \mathbf{B}^n, \mathbf{J}^n \right\} \Rightarrow \mathbf{E}^{n+1/2}, \quad (2.18a)$$

$$\left\{ \mathbf{B}^n, \mathbf{E}^{n+1/2} \right\} \Rightarrow \left\{ \mathbf{B}^{n+1}, \mathbf{B}^{n+1/2} \right\}. \quad (2.18b)$$

The field information is subsequently interpolated to the positions of the macro-particles:

$$\left\{ \mathbf{R}_\alpha^{n+1/2}, \mathbf{E}^{n+1/2}, \mathbf{B}^{n+1/2} \right\} \Rightarrow \left\{ \mathbf{E}_\alpha^{n+1/2}, \mathbf{B}_\alpha^{n+1/2} \right\}. \quad (2.19)$$

The field interpolation is followed by the macro-particle advance:

$$\left\{ \mathbf{V}_\alpha^n, \mathbf{E}_\alpha^{n+1/2}, \mathbf{B}_\alpha^{n+1/2} \right\} \Rightarrow \mathbf{V}_\alpha^{n+1}, \quad (2.20a)$$

$$\left\{ \mathbf{R}_\alpha^{n+1/2}, \mathbf{V}_\alpha^{n+1} \right\} \Rightarrow \mathbf{R}_\alpha^{n+3/2}. \quad (2.20b)$$

The quantities obtained at the end of the PIC cycle are:

$$\left\{ \mathbf{R}_\alpha^{n+3/2}, \mathbf{V}_\alpha^{n+1}, \mathbf{E}^{n+1/2}, \mathbf{B}^{n+1/2}, \mathbf{B}^{n+1} \right\}. \quad (2.21)$$

The computed information is now complete to start a new cycle with incremented time step.

## 2.4 RELEVANT FEATURES OF PIC SIMULATIONS

The following will summarize some features of PIC simulations which are relevant for the present work. A PIC code used in this work is OSIRIS [Fonseca et al., 2002, 2008, 2013]. It is a fully explicit electrodynamic and relativistic PIC code, which is massively parallelized and developed at the University of California Los Angeles (UCLA) and Instituto Superior Técnico Lisboa (IST).

#### 2.4.1 Numerical emittance growth from unphysical Cerenkov radiation

The standard Yee FDTD method, which is commonly used in PIC codes, has the following implications for the numerical dispersion. Electromagnetic waves at frequencies near to the cutoff frequency, which is the highest resolved mode on the grid  $\omega_c \sim \pi/\Delta t$ , travel slower than the speed of light along the axes [Godfrey, 1974; Greenwood et al., 2004]. This can effect high energy particles to emit numerical Cerenkov radiation and can lead to unphysical results when the radiation interacts with particles [Greenwood et al., 2004; Lehe et al., 2013]. In particular, such effects can cause unphysical numerical emittance growth of electron beams from numerical Cerenkov radiation [Lehe et al., 2013].

#### 2.4.2 Numerical scattering and heating

Simulations with the Particle-in-cell method can involve numerical scattering [Hockney, 1971] or heating [Lindman, 1970; Langdon, 1970] effects.

Despite being based on the collisionless kinetic Vlasov equation, PIC codes entail numerical particle collisions due to the use of discrete macro-particles instead of a smooth particle distribution function. Relative fluctuations of the macro-particle number in a cell during a simulation may therefore cause a change of the field values at the cell which causes macro-particles to experience an instantaneous force. Integrated over a long time period, these effects can add up and heat the particle ensemble. The effect of numerical scattering can be suppressed by increase of the number of macro-particles per cell or by use of higher-order particle shapes [Cormier-Michel et al., 2008].

Numerical heating occurs especially when the Debye length is not sufficiently resolved by the grid spacing. The dispersion relation of a warm plasma is then altered and aliasing of high-frequency modes results in unphysical heating [Langdon, 1970; Okuda, 1972; Birdsall and Maron, 1980]. Moreover, in problems of plasma-based acceleration, numerical heating can also be observed, if a cold plasma was initialized [Cormier-Michel et al., 2008]. Numerical heating can generally be suppressed by an increase of the spatial grid resolution or by higher-order particle shapes and field interpolation schemes [Birdsall and Maron, 1980; Cormier-Michel et al., 2008].

### 3.1 INTRODUCTION

#### 3.1.1 *Motivation*

The fully explicit particle-in-cell (PIC) method, outlined in the previous chapter, is the appropriate tool to study the relativistic interactions of highly-intense lasers or high-current particle-beams with plasmas. However, full, three-dimensional (3D) PIC simulations are possible only by means of substantial computational resources on modern supercomputers. A typical 3D simulation of a beam-driven plasma accelerator with centimetre-scale plasma target at a density of  $\sim 10^{17} \text{cm}^{-3}$ , and with an energy gain in the GeV regime, for instance, requires at least  $10^4 - 10^5$  core hours when simulated by means of a fully explicit PIC code, but can require substantially more resources, depending on the features to be resolved.

These extensive computational costs can be contributed to the disparity of smallest and greatest length and time scales which need to be resolved in simulations of plasma-based acceleration. The wavelength of lasers is on the order of sub-micrometers, particle beams have dimensions on the order of micrometers and plasma wavelengths are on the order of tens to hundreds of micrometers. Common plasma targets on the other hand are centimeters to meters long, resulting in a difference by five to seven orders of magnitude between a numerical cell size, which needs to resolve the small aforementioned features, and the total simulation distance. The CFL-stability condition for the PDE field solvers in fully explicit PIC codes limits the time-step by the cell size and hence fundamentally determines the minimum number of time-steps needed for a given cell size and propagation distance in a fully explicit PIC simulation. These restrictions constrain the usability of such codes for parameter scans, modeling of meter-scale propagation or comprehensive analyses of typical problems in plasma-based acceleration.

PIC codes can be written in an implicit scheme to avoid the time-step constraints of an explicit Particle-In-Cell code [Petrov and Davis, 2011]. Moreover, the computational costs of simulations of laser-driven plasma accelerators, in particular, can be reduced by utilization of a ponderomotive or laser envelope model, such that the laser wavelength (usually the shortest feature in the simulation) does not need to be resolved [Cowan et al., 2011; Benedetti et al., 2010, 2012a]. Another possibility to mitigate the affordable computational resources

for the simulation of typical LWFA scenarios is to Lorentz-transform the simulated problem into a boosted frame [Vay, 2007]. The disparity between laser- and plasma wavelength is reduced in this frame due to Lorentz-contraction which allows for a coarser grid spacing and reduces the number of time-steps required.

### 3.1.2 *The quasi-static approach*

A different method to render possible efficient PIC simulations of plasma accelerators was proposed by Mora and Antonsen [Mora and Antonsen, 1996] and Whittum [Whittum, 1997]. If the envelope of a laser pulse or the charge distribution of a particle-beam is not significantly evolving during the traversal of a plasma particle, the quasi-static approximation (QSA) [Sprangle et al., 1990a] is applicable. The QSA allows for a treatment of the plasma and particle- or laser-beams with decoupled time-advance. Such a decoupling in the quasi-static PIC scheme enables a time-step size which can be orders of magnitude greater than those in full PIC codes. This was successfully demonstrated in the relativistic and electrodynamic quasi-static PIC codes WAKE [Mora and Antonsen, 1996, 1997; Morshed et al., 2010], LCODE [Lotov, 2003, 2004] and QuickPIC [Huang et al., 2006; Feng et al., 2009; An et al., 2013]. WAKE is a 2D Cartesian or cylindrical quasi-static PIC code, emulating intense laser-propagation in plasmas and additionally capable of simulating particle-beam interaction with plasmas [Morshed et al., 2010]. The quasi-static PIC code LCODE is modelling highly relativistic particle beam interactions with plasmas in 2D Cartesian or cylindrical geometry. QuickPIC is a 3D PIC code using the QSA to efficiently simulate laser- or particle-beam interaction with plasmas [Huang et al., 2006]. It uses a pipelining algorithm to achieve high scalability [Feng et al., 2009] and since recently employs an advanced field solving routine to provide faster convergence of its predictor-corrector loop [An et al., 2013]. While being specialized on common plasma acceleration scenarios, quasi-static PIC codes provide considerably enhanced efficiency for these scenarios compared to full PIC codes.

### 3.1.3 *The quasi-static PIC code HiPACE*

This chapter discusses the electromagnetic, relativistic, three dimensional, and parallel quasi-static PIC code HiPACE. While retaining physical fidelity, the code shows orders of magnitude speedup compared to full 3D PIC codes for a variety of beam-driven plasma acceleration problems, enabling affordable meter-scale 3D plasma acceleration simulations. This is realised by the use of the above mentioned QSA, and by a computational efficiency and high degree of parallelisation.

*This code was developed at DESY in collaboration with the Lawrence Berkeley National Laboratory (LBNL).*

**HiPACE** is parallelised in all three dimensions and scales well for more than 64 processors. While fully explicit **PIC** codes use an **FDTD** method to update the field information in each time step, **HiPACE** recomputes the full self-consistent field information in each time step by means of fast Poisson-solvers. This feature allows for consistent initialisation of particle-beams within the plasma such that beams from full **PIC** codes can be imported into **HiPACE** during their propagation in a plasma target. Such a hybrid approach using a full **PIC** code and **HiPACE** enables the investigation of electron-injection techniques (self-injection is otherwise absent in codes using the **QSA**) and parameter scans in 3D geometry with centimetre to metre long propagation distances. In addition, beams with arbitrary phase-space distributions can be generated within **HiPACE** or can be imported from particle tracking codes, e.g. **ASTRA** or **ELEGANT**.

The development of a simulation program can be described in the following steps [**Hockney and Eastwood, 1981**]. (a) For a given physical phenomenon, (b) a mathematical model, describing this phenomenon is found. (c) The mathematical model is then to be discretized and (d) incorporated in numerical algorithms, which are finally (e) embedded in an appropriate simulation program.

The development of the quasi-static **PIC** code **HiPACE** is presented analogously. The physical scope of plasma-based acceleration, point (a), is reviewed in chapter 1. The physical basis and the mathematical model for the description of the relevant phenomena in plasma-based acceleration, posing point (b), are discussed in the present chapter in section 3.2. The discretizations, (c), and numerical algorithms, (d), are outlined in section 3.3. This is followed by a comparison between **HiPACE** and the full 3D particle-in-cell code (**OSIRIS**) in 3.4. The full exhibition of point (e) is beyond the scope of this work, but some conceptual approaches of the parallelization of the simulation program are discussed in section 3.5 and in Appendix C. The discussions and concluding remarks in 3.6 complete this chapter.

## 3.2 PHYSICAL BASIS AND MATHEMATICAL MODEL

### 3.2.1 *Physical basis and quasi-static approach*

Equivalently as full **PIC** codes, the present quasi-static **PIC** code is based on the Vlasov-Maxwell system. The Maxwell equations (1.1a)-(1.1d) are for convenience rewritten in terms of the normalized electric and magnetic field,  $\mathcal{E} = \mathbf{E}/E_0$  and  $\mathcal{B} = \mathbf{B}/E_0$ , respectively, where

$E_0 = \omega_p mc/e$  is the cold-nonrelativistic wavebreaking field [Dawson, 1959],

$$\tilde{\nabla} \cdot \boldsymbol{\mathcal{E}} = \varrho, \quad (3.1a)$$

$$\tilde{\nabla} \cdot \boldsymbol{\mathcal{B}} = 0, \quad (3.1b)$$

$$\tilde{\nabla} \times \boldsymbol{\mathcal{E}} + \frac{\partial \boldsymbol{\mathcal{B}}}{\partial \tilde{t}} = 0, \quad (3.1c)$$

$$\tilde{\nabla} \times \boldsymbol{\mathcal{B}} - \frac{\partial \boldsymbol{\mathcal{E}}}{\partial \tilde{t}} = \boldsymbol{\mathcal{J}}. \quad (3.1d)$$

Here, in addition, the normalized charge density  $\varrho = \rho/en_0$  and current density  $\boldsymbol{\mathcal{J}} = \mathbf{J}/ecn_0$  are introduced, where  $n_0$  is the reference plasma density. Independent time and length variables are normalized to the inverse plasma frequency,  $\tilde{t} = \omega_p t$ , and to the skin-depth,  $\tilde{x} = k_p x$ , where  $k_p = \omega_p/c$  and  $\omega_p = \sqrt{4\pi n_0 e^2/m_e}$ .

The particle phase-space distributions of beam-species and plasma-electrons are discretized by means of the macro-particle concept (see 2.2). These numerical particles are advanced along the characteristics of the Vlasov equation, given by the Newtonian equation of motion and the Lorentz force,

$$\frac{d\mathbf{X}}{d\tilde{t}} = \boldsymbol{\beta}, \quad (3.2a)$$

$$\frac{d\mathbf{U}}{d\tilde{t}} = \eta (\boldsymbol{\mathcal{E}} + \boldsymbol{\beta} \times \boldsymbol{\mathcal{B}}), \quad (3.2b)$$

where, within this chapter,  $\mathbf{X} = k_p \mathbf{R}$  is the normalized macro-particle position,  $\mathbf{U} = \mathbf{P}/Mc$  is the normalized macro-particle momentum,  $\boldsymbol{\beta} = \mathbf{V}/c = \mathbf{U}/\gamma$  is the macro-particle velocity, normalized to the speed of light and  $\eta = Qm_e/eM$  represents the charge-mass-ratio of a macro-particle relative to the positron charge mass ratio (i.e.  $\eta = -1$  for macro-particles representing an electron species).

The characteristic time scales for the beam and plasma evolution exhibit a significant disparity for highly relativistic beams. This is used to formulate the QSA, which is the basis of HiPACE. The QSA states (see 1.4.3.2) that Eulerian quantities evolve according to

$$\frac{\partial Q}{\partial \tilde{t}} \simeq -\frac{\partial Q}{\partial \tilde{\zeta}}, \quad (3.3)$$

in the speed of light frame  $\tilde{\zeta} = \tilde{z} - \tilde{t} = k_p z - \omega_p t$ ,  $\tilde{\tau} = \tilde{t}$ . Plasma macro-particle quantities  $\chi_p$ , which have a particle (Lagrangian) nature in the transverse direction and a fluid (Eulerian) nature in the co-moving direction, can be assumed quasi-static, such that the coordinate transformation yields

$$\frac{d\chi_p}{d\tilde{t}} = (\beta_{p,z} - 1) \frac{\partial \chi_p}{\partial \tilde{\zeta}} + \frac{\partial \chi_p}{\partial \tilde{\tau}} \simeq (\beta_{p,z} - 1) \frac{\partial \chi_p}{\partial \tilde{\zeta}}, \quad (3.4)$$

where  $\beta_{p,z} = V_{p,z}/c$  denotes the normalized particle velocity in  $z$ -direction. The beam, on the contrary, is considered to be highly relativistic  $\beta_{b,z} \simeq 1$ , such that the QSA does not apply for its dynamics,

and its properties are evolving in time  $\tilde{t}$ . This gives rise to the separated treatment of beam and plasma macro-particles (cf. [Morshed et al., 2010] and [Huang et al., 2006]). The basic scheme employed in HiPACE is therefore as follows. Particles of all beam species are static after their current was deposited, while plasma macro-particles are pushed and fields are computed. Plasma macro-particles and fields are advanced from the initial and unperturbed state, which exists prior to beam interaction. This implies, plasma and field integration must start from co-moving positions ahead of the beam and evolve in negative  $\tilde{\zeta}$ -direction. In a second step, the fields and the plasma are static while the beam is evolved in  $\tilde{t}$ . This time-staggered scheme is depicted in Figure 14.

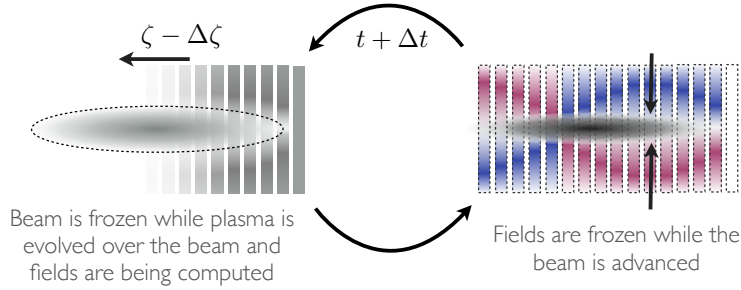


Figure 14: Basic staggered numerical scheme in HiPACE with separated treatment of beam and plasma macro-particles.

### 3.2.2 Plasma formulation

The quasi-static approximation induces a dynamical invariant of plasma motion, as will be shown in the following. The normalized Hamiltonian for a plasma electron in the normalized vector potential  $\mathbf{a} = e\mathbf{A}/m_e c^2$  and the normalized scalar potential  $\phi = e\Phi/m_e c^2$  is given by

$$\mathcal{H} = \sqrt{1 + |\mathbf{U}_{can} + \mathbf{a}|^2} - \phi = \gamma - \phi, \quad (3.5)$$

with the normalized canonical momentum  $\mathbf{U}_{can} = \mathbf{U} - \mathbf{a}$ . Using the QSA ( $\partial\mathcal{H}/\partial\tilde{t} \simeq -\partial\mathcal{H}/\partial\tilde{\zeta}$ ), one finds the following identity [Mora and Antonsen, 1996]

$$\frac{d\mathcal{H}}{d\tilde{t}} = \frac{\partial\mathcal{H}}{\partial\tilde{t}} \simeq -\frac{\partial\mathcal{H}}{\partial\tilde{\zeta}} = -\frac{\partial\mathcal{H}}{\partial\tilde{z}} = \frac{dU_{can,z}}{d\tilde{t}}, \quad (3.6)$$

such that  $d/dt(\gamma - \phi) = d/dt(U_z - a_z)$ . This suggests the quantity  $\gamma - \psi - U_z$  to be *invariant* during the advance of a plasma particle, with the wakefield-potential  $\psi = \phi - a_z$ . For an initially cold and unperturbed plasma, this entails the equality

$$\gamma - \psi - U_z = 1, \quad (3.7)$$

to be true for all times. It follows from Jean's theorem that the dynamical invariants are constant along the characteristics of the Vlasov equation. In the following,  $\psi_p = \psi$  will thus be interpreted as a Lagrangian quantity of the plasma macro-particles. Combination of equations (3.4) and (3.7) yield the change which plasma macro-particle quantities experience during integration in the co-moving variable

$$\frac{\partial \chi_p}{\partial \tilde{\zeta}} = -\frac{\gamma_p}{1 + \psi_p} \frac{d\chi_p}{d\tilde{t}}. \quad (3.8)$$

The factor  $-\gamma_p/(1 + \psi_p)$  can be interpreted as the weight with which the local temporal change contributes to the change along the co-moving variable. This results in the following equation of motion for the transverse plasma macro-particle position

$$\frac{\partial \mathbf{X}_{p,\perp}}{\partial \tilde{\zeta}} = \mathbf{F}_{X,\perp} = -\frac{\mathbf{U}_{p,\perp}}{1 + \psi_p}. \quad (3.9)$$

Equation (3.2b), together with the QSA, yields the evolution of the plasma macro-particle transverse momentum,

$$\frac{\partial \mathbf{U}_{p,\perp}}{\partial \tilde{\zeta}} = \mathbf{F}_{U,\perp} = \frac{\gamma_p}{1 + \psi_p} \begin{pmatrix} \mathcal{E}_x - \mathcal{B}_y \\ \mathcal{E}_y + \mathcal{B}_x \end{pmatrix} + \begin{pmatrix} \mathcal{B}_y \\ -\mathcal{B}_x \end{pmatrix}. \quad (3.10)$$

Here and henceforth within this chapter the axial magnetic field  $\mathcal{B}_z$  is assumed to be negligible for the dynamics and field evolution. This is justified, firstly, by the typically nonrelativistic transverse velocities of the beam  $\beta_{b,\perp} \ll 1$  which suppress the impact of the axial magnetic field to the beam evolution. Secondly, and most importantly, azimuthal currents, which may generate a field in axial direction, are generally by orders of magnitude less enhanced than axial and radial currents in problems of beam-driven plasma acceleration.

The wakefield potential is one initially ( $\psi_p(\zeta \rightarrow \infty) = 1$ ) for an cold plasma, and evolves according to

$$\frac{\partial \psi_p}{\partial \tilde{\zeta}} = F_\psi = \frac{\mathbf{U}_{p,\perp}}{1 + \psi_p} \cdot \begin{pmatrix} \mathcal{E}_x - \mathcal{B}_y \\ \mathcal{E}_y + \mathcal{B}_x \end{pmatrix} - \mathcal{E}_z. \quad (3.11)$$

Regarding  $\gamma_p = \sqrt{1 + \mathbf{U}_{p,\perp}^2 + U_{p,z}^2}$  together with equation (3.7), yields a definition for the Lorentz-factor,

$$\gamma_p = \frac{1 + \mathbf{U}_{p,\perp}^2 + (1 + \psi_p)^2}{2(1 + \psi_p)}. \quad (3.12)$$

which is independent of the longitudinal momentum. Equations (3.9), (3.10), (3.11) and (3.12) define the physical basis of the plasma macro-particle pusher whose numerical implementation will be explained in the subsequent section.



### 3.2.3 Beam equations

Beam macro-particles are highly relativistic  $\beta_{b,z} \simeq 1$ . The dynamics of beam macro-particles are thus with eqn. (3.2a) and (3.2b) given by the following set of equations

$$\frac{d\mathbf{X}_{b,\perp}}{d\tilde{t}} = \frac{\mathbf{U}_{b,\perp}}{\gamma_b}, \quad (3.13a)$$

$$\frac{d\mathbf{U}_{b,\perp}}{d\tilde{t}} = \eta \begin{pmatrix} \mathcal{E}_x - \mathcal{B}_y \\ \mathcal{E}_y + \mathcal{B}_x \end{pmatrix}, \quad (3.13b)$$

$$\frac{dU_{b,z}}{d\tilde{t}} = \eta \left( \mathcal{E}_z + \frac{U_{b,x}\mathcal{B}_y - U_{b,y}\mathcal{B}_x}{\gamma_b} \right), \quad (3.13c)$$

$$\gamma_b = \sqrt{1 + \mathbf{U}_{b,\perp}^2 + U_{b,z}^2}. \quad (3.13d)$$

The numerical scheme used for time integration of this set of equations will be illustrated in the following section.

### 3.2.4 Field equations

For a complete self-consistent description of beam and plasma, the field configuration as resulting from the current density needs to be calculated. This is done by use of the time-dependent Maxwell equations (3.1c) and (3.1d). Given the charge continuity equation is fulfilled, the time-independent Maxwell equations (3.1a) and (3.1b) are satisfied for all  $\tilde{\zeta}$  if they are satisfied at some initial co-moving position. Applying the QSA, to the transverse plane of eqn. (3.1d) yields the equality

$$\frac{\partial}{\partial \tilde{\zeta}} \begin{pmatrix} \mathcal{E}_x - \mathcal{B}_y \\ \mathcal{E}_y + \mathcal{B}_x \end{pmatrix} = \begin{pmatrix} \mathcal{J}_x \\ \mathcal{J}_y \end{pmatrix}. \quad (3.14)$$

The derivative of the transverse fields  $(\mathcal{E}_x - \mathcal{B}_y)$  and  $(\mathcal{E}_y + \mathcal{B}_x)$  with respect to the co-moving position is thus given by the transverse current density. This finding, together with the transverse plane of equation (3.1c) yields the equation

$$\tilde{\nabla}_{\perp}^2 \mathcal{E}_z = \tilde{\nabla}_{\perp} \cdot \mathcal{J}_{\perp}. \quad (3.15)$$

The field components left for the closure of the governing equations are the transverse components of the magnetic field, which are derived by use of the longitudinal component of equation (3.1d) and the identity  $\tilde{\nabla}_{\perp} \cdot \mathcal{B}_{\perp} = -\partial \mathcal{B}_z / \partial \tilde{\zeta} = 0$ , resulting in

$$\tilde{\nabla}_{\perp}^2 \mathcal{B}_x = -\frac{\partial}{\partial \tilde{y}} \left( \mathcal{J}_z - \frac{\partial \mathcal{E}_z}{\partial \tilde{\zeta}} \right), \quad (3.16a)$$

$$\tilde{\nabla}_{\perp}^2 \mathcal{B}_y = \frac{\partial}{\partial \tilde{x}} \left( \mathcal{J}_z - \frac{\partial \mathcal{E}_z}{\partial \tilde{\zeta}} \right). \quad (3.16b)$$

Equations (3.15), (3.16a) and (3.16b) are transverse Poisson equations, with the source terms being functions of the transverse coordinates only. The quasi-static approximation hence leads to transversely two-dimensional problems which can be solved by means of fast Poisson solvers as described in the next section. One notable aspect of the two latter equations is the dependency on the change of the longitudinal field  $\partial \mathcal{E}_z / \partial \tilde{\zeta}$ . Since plasma and fields are advanced in negative  $\tilde{\zeta}$  direction, equations (3.16a) and (3.16b) include the numerical challenge to know the longitudinal field  $\mathcal{E}_z$ , and hence the transverse currents  $\mathcal{J}_\perp$ , in the next  $\tilde{\zeta}$ -position in integration direction when using a central difference scheme (backward difference schemes are not stable in this context). This problem can only be solved by means of an iterative scheme which will be described below.

### 3.3 NUMERICAL IMPLEMENTATION

The **HiPACE** main loop consists of the following three steps (see Figure 15). In the first instance, beam currents are deposited onto the grid. The second step constitutes the advance of the plasma and fields in negative  $\tilde{\zeta}$ -direction. Field values are then interpolated to the beam macro-particles positions which are being pushed in the third step of the main loop. This section will outline the numerical implementation of **HiPACE** in the order of the numerical sequence.

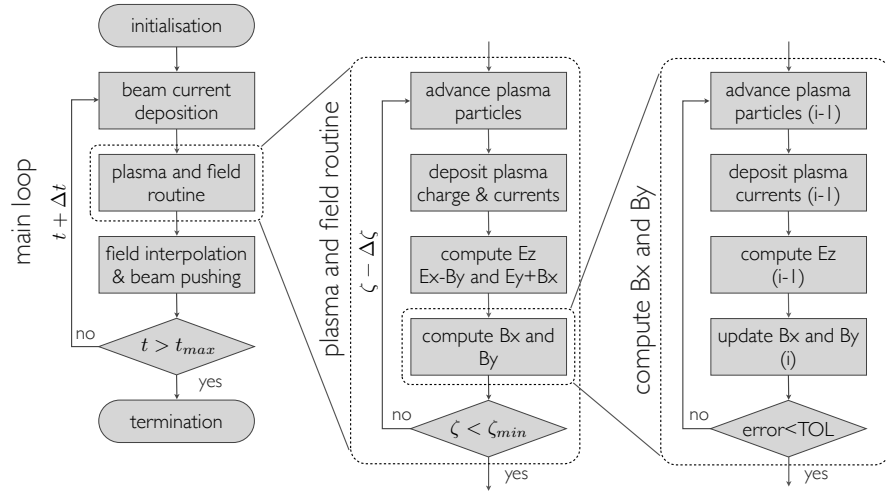


Figure 15: Schematic numerical flow in **HiPACE**.

#### 3.3.1 Beam current-density deposition

Deposition of beam current-densities onto the numerical lattice is conducted in the same fashion as in full **PIC** codes (see 2.3.1). The three-dimensional particle shape function is by default composed of

second-order transverse shape functions and a first-order longitudinal shape function,

$$S^{3D}(\tilde{\zeta}, \tilde{x}, \tilde{y}) = S_1^{1D}(\tilde{\zeta}) S_2^{1D}(\tilde{x}) S_2^{1D}(\tilde{y}), \quad (3.17)$$

where the subscript here denotes the order of the particle shape. The limitation of the longitudinal particle shape to a first order scheme is important for the parallel performance (more information in section 3.5). The current-density is then computed as usual (see 2.3.1).

### 3.3.2 Plasma and field routine

When compared to the typical main loop in full PIC codes (confer 2.3), the major distinction in the numerical implementation of HiPACE is the plasma and field solving subroutine which will be explained in the following.

#### 3.3.2.1 Plasma particle advance

The considered simulation domain contains a number of  $N_{\tilde{\zeta}}$  grid-points in longitudinal direction. The position of the grid-point with index  $i$  is given by  $\tilde{\zeta}^i = \tilde{\zeta}_{min} + i \times \Delta\tilde{\zeta}$ , where  $\tilde{\zeta}_{min}$  denotes the lower longitudinal simulation domain boundary. The unperturbed fields and plasma macro-particles are initialised within a transverse 2D sub-lattice at the upper longitudinal simulation box boundary, at position  $\tilde{\zeta}^{N_{\tilde{\zeta}}-1} = \tilde{\zeta}_{max}$ . The plasma routine decrements the index  $i$  and processes 2D sub-lattices starting from the upper longitudinal boundary to the lower boundary. In each 2D sub-lattice, the routine starts by pushing the plasma macro-particles according to eqns. (3.9), (3.10) and (3.11). This is done by means of a linear multistep method, assuming the right-hand sides  $F_{X,\perp}$ ,  $F_{U,\perp}$ ,  $F_{\psi}$  of equations (3.9), (3.10) and (3.11) to be known from the previously computed slices. The evolution of a plasma macro-particle quantity  $\chi$  is then given by

$$\chi^i = \chi^{i+1} - \Delta\tilde{\zeta} \left( b_1 F_{\chi}^{i+1} + b_2 F_{\chi}^{i+2} + b_3 F_{\chi}^{i+3} + b_4 F_{\chi}^{i+4} + b_5 F_{\chi}^{i+5} \right), \quad (3.18)$$

where  $b_{1,\dots,5}$  denote the coefficients for the fifth-order Adams-Bashforth method [Butcher, 2008]. It should be noted that co-moving positions of plasma macro-particles are advanced by  $-\Delta\tilde{\zeta}$ , independent of their longitudinal velocity, which enables the usage of the multistep method and assures that plasma macro-particles are always defined within the processed 2D slice.

### 3.3.2.2 Plasma current deposition

After particle pushing, the deposition of plasma currents onto the 2D slice is conducted. The plasma electron charge and current-densities are given by

$$\varrho = \sum_{\alpha} w_{\alpha} S^{2D}(\tilde{\mathbf{r}}_{\perp} - \mathbf{X}_{\alpha,\perp}(\tilde{\zeta})), \quad (3.19a)$$

$$\mathcal{J} = \sum_{\alpha} \beta_{\alpha} w_{\alpha} S^{2D}(\tilde{\mathbf{r}}_{\perp} - \mathbf{X}_{\alpha,\perp}(\tilde{\zeta})) \quad (3.19b)$$

where  $\alpha$  is the macro-particle index,  $w_{\alpha}$  is a to be determined macro-particle charge-weight and  $S^{2D}$  is the transverse shape function of the macro-particles with the normalization

$$\int S^{2D}(\tilde{\mathbf{r}}_{\perp} - \mathbf{X}_{\alpha,\perp}(\tilde{\zeta})) d\tilde{\mathbf{r}}_{\perp} = 1. \quad (3.20)$$

When applying the QSA to the charge continuity equation (1.2),

$$\frac{\partial}{\partial \tilde{t}} \varrho + \tilde{\nabla} \cdot \mathcal{J} = 0, \quad (3.21)$$

one finds (cf. [Huang et al., 2006])

$$-\frac{\partial}{\partial \tilde{\zeta}} \sum_{\alpha} w_{\alpha} S^{2D}(\tilde{\mathbf{r}}_{\perp} - \mathbf{X}_{\alpha,\perp}) + \tilde{\nabla} \cdot \sum_{\alpha} \beta_{\alpha} w_{\alpha} S^{2D}(\tilde{\mathbf{r}}_{\perp} - \mathbf{X}_{\alpha,\perp}) = 0. \quad (3.22)$$

Restructuring this equation yields

$$\begin{aligned} & \frac{\partial}{\partial \tilde{\zeta}} \sum_{\alpha} (1 - \beta_{\alpha,z}) w_{\alpha} S^{2D}(\tilde{\mathbf{r}}_{\perp} - \mathbf{X}_{\alpha,\perp}), \\ & = \tilde{\nabla}_{\perp} \cdot \sum_{\alpha} \beta_{\alpha,\perp} w_{\alpha} S^{2D}(\tilde{\mathbf{r}}_{\perp} - \mathbf{X}_{\alpha,\perp}), \\ & = \sum_{\alpha} w_{\alpha} \beta_{\alpha,\perp} \cdot \tilde{\nabla}_{\perp} S^{2D}(\tilde{\mathbf{r}}_{\perp} - \mathbf{X}_{\alpha,\perp}), \end{aligned} \quad (3.23)$$

and thus, after integration over the transverse plane

$$\frac{d}{d\tilde{\zeta}} \sum_{\alpha} (1 - \beta_{\alpha,z}) w_{\alpha} = 0. \quad (3.24)$$

The equation of continuity hence demands the quantity  $(1 - \beta_{\alpha,z})w_{\alpha} = Q_{\alpha}/e$  to be conserved for each numerical particle. The deposited weight for the charge-density and current-density deposition  $w_{\alpha}$  is therefore related to the conserved charge of a plasma macro-particle  $Q_{\alpha}$  through

$$w_{\alpha} = \frac{Q_{\alpha}}{e} \frac{\gamma_{p,\alpha}}{1 + \psi_{p,\alpha}}. \quad (3.25)$$

Descriptively, this factor accounts for the neglect of the role of longitudinal velocity to the time period during which a macro-particle contributes to the local charge and current densities. The current of the plasma macro-particles is deposited in the usual PIC-scheme (see 2.3.1) with a zeroth order deposition in longitudinal direction and higher order in transverse direction.

### 3.3.2.3 Field solving and iteration loop

After plasma current deposition, the fields  $(\mathcal{E}_x - \mathcal{B}_y)^i$ ,  $(\mathcal{E}_y + \mathcal{B}_x)^i$  and  $\mathcal{E}_z^i$  in the currently processed slice are calculated. Equation (3.14) is discretised to compute the transverse fields by using a third-order linear multistep scheme

$$\begin{aligned} \begin{pmatrix} \mathcal{E}_x - \mathcal{B}_y \\ \mathcal{E}_y + \mathcal{B}_x \end{pmatrix}^i &= \begin{pmatrix} \mathcal{E}_x - \mathcal{B}_y \\ \mathcal{E}_y + \mathcal{B}_x \end{pmatrix}^{i+1} \\ &\quad - \frac{\Delta\tilde{\zeta}}{12} \left( 23 \mathcal{J}_\perp^{i+1} - 16 \mathcal{J}_\perp^{i+2} + 5 \mathcal{J}_\perp^{i+3} \right). \end{aligned} \quad (3.26)$$

The longitudinal electric field is determined via the transverse Poisson equation (3.15). All fields are assumed to decay to zero at the boundaries, implying perfectly conducting walls (Dirichlet boundary conditions). An efficient method to solve elliptical partial differential equations similar to the Poisson equation, are *fast Poisson solvers* (see C.1). This technique utilises fast fourier transforms to achieve fast computation of the Poisson problem [Van Loan, 1992]. On a two-dimensional grid, equivalent to the discussed transverse slices, with a number of  $N_x \times N_y = N^2$  grid points, the fast Poisson solver requires  $\mathcal{O}(N^2 \log(N))$  operations to find a numerical solution, which is near to optimum speed ( $\mathcal{O}(N^2)$ ). Most direct methods (e.g. successive over-relaxation) need a significantly larger number of operations ( $\geq \mathcal{O}(N^3)$ ). However, fast fourier transforms (FFT)s are not straightforward to parallelise. The FFTs are being computed by use of the library FFTW<sub>3</sub> [Frigo and Johnson, 2005] which provides MPI-routines, allowing for the parallelisation in one spatial dimension.

*More detailed information on fast Poisson solvers can be found in Appendix C.*

The computation of the transverse magnetic fields  $\mathcal{B}_x^i$  and  $\mathcal{B}_y^i$  according to equations (3.16a) and (3.16b) can in principal also be performed by use of fast Poisson solvers. However, this presupposes the knowledge of  $\mathcal{E}_z^{i-1}$  for the calculation of the longitudinal derivative  $(\partial\mathcal{E}_z/\partial\tilde{\zeta})^i \simeq (\mathcal{E}_z^{i+1} - \mathcal{E}_z^{i-1})/2\Delta\tilde{\zeta}$  in the source terms. This problem can be solved by means of an iterative predictor-corrector method (cf. [Mora and Antonsen, 1997]) which uses an initial guess for the transverse fields to advance the plasma macro-particles to the next co-moving position  $\tilde{\zeta}^{i-1}$ . Then, plasma currents  $\mathcal{J}_\perp^{i-1}$  can be deposited and the field  $\mathcal{E}_z^{i-1}$  be computed. After deduction of  $(\partial\mathcal{E}_z/\partial\tilde{\zeta})^i$  by means of a central difference, the transverse magnetic fields  $\mathcal{B}_x^i$  and  $\mathcal{B}_y^i$  are updated to  $\mathcal{B}_{x,new}^i$  and  $\mathcal{B}_{y,new}^i$  by use of equations (3.16a) and (3.16b). This sequence is iterated (see Figure 15) until the following convergence criteria is met

$$\sup \left| \frac{\mathcal{B}_{new}^i - \mathcal{B}^i}{\sup |\mathcal{B}_{new}^i|} \right| < TOL, \quad (3.27)$$

where  $\sup |Y^i|$  denotes the supremum of the absolute value of quantity  $Y$  in the 2D slice  $i$  and  $TOL$  is a chosen tolerance. This method

terminates the predictor-corrector loop after a single iteration in regions in which the fields show negligible  $\tilde{\zeta}$ -dependence (e.g. ahead of the driver) and in the same time guarantees for accuracy in longitudinal regions with enhanced  $\tilde{\zeta}$ -dependence (e.g. near to the density spike in the blow out regime) by iterating several times. Fastest convergence was generally achieved in slice  $i$  when a composition of magnetic field configuration from slice  $i + 1$  and from the previous time step was used as an initial guess.

The above described scheme splits the 3D field and plasma problem into a set of 2D sub-problems and hence decreases the computing as well as the memory load when advancing the plasma and fields. Moreover, it should be noted that the plasma information and self-consistent field configuration in quasi-static PIC codes is re-computed in each time-step as described above, whereas fully explicit PIC codes only update the fields by means of a FDTD method and advance plasma information in each time-step.

### 3.3.3 Beam advance

After the fields in each two-dimensional sub-domain along  $\tilde{\zeta}$  were computed in the plasma and field routine, HiPACE returns to the main loop. The beam advance is performed in a second-order and symplectic scheme. The beam-macro-particles are spatially updated by half a time-step according to (3.13a),

$$\mathbf{x}_{b,\perp}^{n+1/2} = \mathbf{x}_{b,\perp}^n + \frac{\Delta\tilde{t}}{2} \frac{\mathbf{U}_{b,\perp}^n}{\gamma_b^n}. \quad (3.28)$$

Subsequently, the field values are interpolated to the positions of the macro-particles in the usual way (see 2.3.3), with the longitudinal interpolation scheme, for reasons related to parallel performance, being limited to first order (confer 3.5). The obtained field values at the particles positions are used to update the momenta according to equations (3.13b) and (3.29c),

$$\frac{\mathbf{U}_{b,\perp}^{n+1} - \mathbf{U}_{b,\perp}^n}{\Delta\tilde{t}} = \eta \begin{pmatrix} \mathcal{E}_x - \mathcal{B}_y \\ \mathcal{E}_y + \mathcal{B}_x \end{pmatrix}^{n+1/2}, \quad (3.29a)$$

$$\mathbf{U}_{b,\perp}^{n+1/2} = \frac{\mathbf{U}_{b,\perp}^{n+1} + \mathbf{U}_{b,\perp}^n}{2} \quad (3.29b)$$

$$\frac{U_{b,z}^{n+1} - U_{b,z}^n}{\Delta\tilde{t}} = \eta \left( \mathcal{E}_z^{n+1/2} + \frac{U_{b,x}^{n+1/2} \mathcal{B}_y^{n+1/2} - U_{b,y}^{n+1/2} \mathcal{B}_x^{n+1/2}}{\bar{\gamma}_b^{n+1/2}} \right). \quad (3.29c)$$

The half-integer relativistic factor does not change by virtue of the magnetic field and is hence computed via

$$\bar{\gamma}_b^{n+1/2} = \sqrt{1 + \left(\mathbf{U}_{b,\perp}^{n+1/2}\right)^2 + \left(U_{b,z}^n + \frac{\Delta\tilde{t}}{2}\eta \mathcal{E}_z^{n+1/2}\right)^2}. \quad (3.30)$$

After momentum update, the second half-step for the position advance can be performed

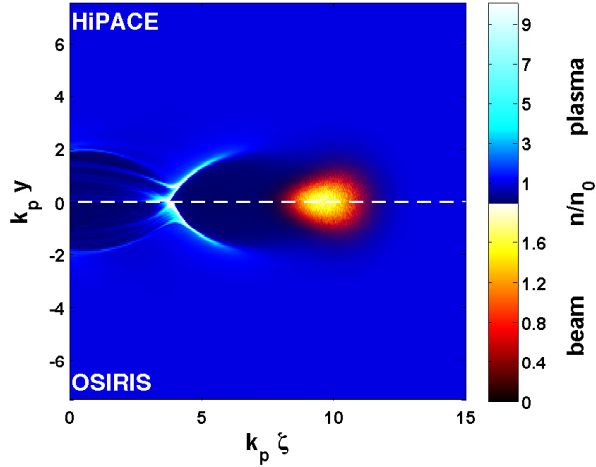
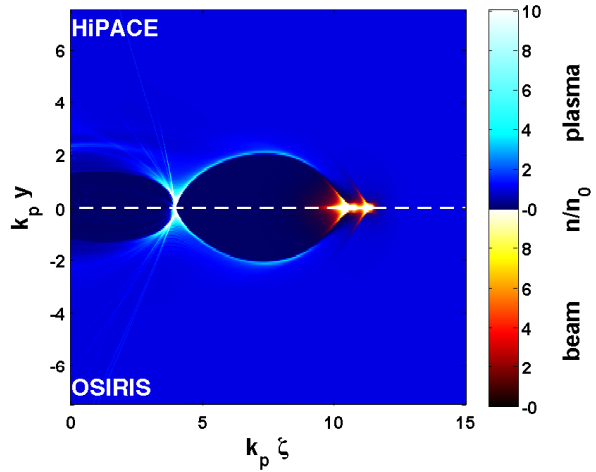
$$\mathbf{x}_{b,\perp}^{n+1} = \mathbf{x}_{b,\perp}^{n+1/2} + \frac{\Delta\tilde{t}}{2} \frac{\mathbf{U}_{b,\perp}^{n+1/2}}{\bar{\gamma}_b^{n+1/2}}. \quad (3.31)$$

The size of the time-step  $\Delta\tilde{t}$  is determined by the smallest beam energy which is to be resolved and the local plasma density. When the beam energy or the local plasma density changes, **HiPACE** dynamically adjusts  $\Delta\tilde{t}$  in order to guarantee optimum performance while rendering the beam dynamics consistently. The time-step is hence chosen according to  $\Delta\tilde{t} = \sqrt{2\gamma_c n_0/n_{loc}}/\Lambda_{res}$ , where  $\Lambda_{res}$  is the resolution of the inverse betatron wave-number (usually  $10 \leq \Lambda_{res} \leq 20$ ),  $n_0/n_{loc}$  is the ratio of reference over local plasma density and  $\gamma_c$  is a chosen minimal resolved beam energy. **HiPACE** chooses this minimal resolved energy by  $\gamma_c = \max(\gamma_{min}, \bar{\gamma} - 5\sigma_\gamma)$ , where  $\gamma_{min}$  is the minimum macro-particle energy and  $\langle\gamma\rangle$  and  $\sigma_\gamma$  are the mean and **RMS**-spread of energies of the beam-species in the simulation domain, respectively.

### 3.4 COMPARISON WITH EXPLICIT PIC SIMULATIONS

In order to assess the capability of **HiPACE** to consistently simulate common plasma acceleration problems, results from a **HiPACE** simulation and from a simulation with the full explicit **PIC** code **OSIRIS** [Fonseca et al., 2002, 2008, 2013] will be presented in the following. The considered problem consists of a highly relativistic ( $\langle\gamma_b\rangle = 2000$ ,  $\sigma_\gamma/\langle\gamma_b\rangle = 10^{-3}$ ), Gaussian ( $\tilde{\sigma}_{x,y,z} = 1.0$ ) electron beam with peak density  $n_b/n_0 = 1.0$  and normalised transverse emittance  $\tilde{\epsilon}_{x,y}^n = 0.5$ , propagating through a homogeneous plasma. The Gaussian beam distribution was truncated at a radius of  $3 \times \tilde{\sigma}_{x,y,z}$  (length-scales, including the emittance, are normalized to  $k_p^{-1}$ ). Physical and numerical simulation parameters were chosen identical for the **HiPACE** and **OSIRIS** simulations. The box dimensions are  $\tilde{L}_x \times \tilde{L}_y \times \tilde{L}_z = 15 \times 15 \times 15$ , the cell volume  $\Delta\tilde{x} \times \Delta\tilde{y} \times \Delta\tilde{z} = 0.0073 \times 0.0588 \times 0.0588$ , number of beam macro-particles per cell  $N_{b,ppc} = 2 \times 2 \times 2$  and plasma macro-particles per cell  $N_{p,ppc} = 2 \times 2 \times 1$ . The time-step in **OSIRIS** is constrained by the cell size and the **CFL** condition to  $\Delta\tilde{t} = 0.0072$ . The time step in **HiPACE** resolves the betatron motion of the beam (see explanation above) and is  $\Delta\tilde{t} = 4.21$ .

*Details on the simulation setup can also be found in B.2*

(a) Comparison after distance of  $\tilde{z} = 80$ .(b) Comparison after distance of  $\tilde{z} = 450$ .Figure 16: Densities of plasma and beam in **HiPACE** (top) and **OSIRIS** (bottom) simulations.

Figures 16, 17 and 18 show comparisons of simulation results from **HiPACE** and **OSIRIS**. Figure 16 depicts a qualitative comparison of a central slice of the plasma and beam densities after distances of  $\tilde{z} = 80$  and  $\tilde{z} = 450$  of beam propagation in the plasma. The beam density distributions and plasma wave structure are qualitatively close in the **HiPACE** and **OSIRIS** results. Subtle differences in the beam or plasma density distributions might originate from the fact that the **OSIRIS** beam was initialised before the plasma and the **HiPACE** beam in the plasma or from differences of the numerical approaches.

Figures 17 and 18 compare the field configurations, obtained from the **HiPACE** and **OSIRIS** simulations, quantitatively. Figure 17a depicts the longitudinal field values on the propagation axis. The curves are close to each other and the only significant deviation occurs at the



crest of the plasma wave, where a large amount of plasma macro-particle trajectories cross and generate a spike in the longitudinal field. This becomes more clear in Figure 17b which visualizes the absolute difference between the  $\mathcal{E}_z$ -curves in HiPACE and OSIRIS. The magnitude of the difference is at a significant level in the vicinity of the spikes of the longitudinal field curves. This can be attributed to the difference of the plasma advance and plasma current deposition scheme in OSIRIS and HiPACE. While plasma macro-particles with highly relativistic longitudinal velocities accumulate at the crest of the plasma wave in the full PIC code, the quasi-static PIC code only emulates this behaviour through the weighting factor in equation (3.19b). The discrepancy can be mitigated by adjusting the longitudinal resolution of the quasi-static simulation (cf. [Lotov, 2003]). Transverse beam dynamics crucially depend on the transverse fields in the plasma waves. These fields, obtained from simulations in OSIRIS and HiPACE are compared in Figure 18a at a co-moving position of  $\tilde{\zeta} = 7.33$ . The near-axis linear dependencies of the curves are close with respect to each other and differ on significant magnitude only at the high-density plasma electron sheath, surrounding the ion cavity, and in the details of the decay from plasma shielding as depicted in Fig. 18b.

Most importantly to note is the significant difference of the simulation runtimes. While OSIRIS needed 19968 core hrs to simulate this problem up to a distance of  $\tilde{z} = 450$ , HiPACE needed 474 core hrs only for the same propagation distance. This is equivalent to a speedup by a factor of 42. While the relevant measure for the propagation distance for OSIRIS is measured in units of  $k_p^{-1}$ , the measure in HiPACE is  $k_\beta^{-1}$ . As motivated before, for highly relativistic beams these measures can differ on orders of magnitude according to the beam energy  $k_\beta^{-1} = \sqrt{2\gamma} k_p^{-1}$ .

### 3.5 PARALLELISATION AND SCALINGS

Simulations of plasma acceleration in a 3D geometry with explicit PIC codes as well as with quasi-static PIC codes such as HiPACE are feasible only if the problem is parallelised and if the computing load is distributed amongst a number of processes. Thus, the degree of parallelisation also determines the computational efficiency of a code. This section describes the parallel implementation of the algorithms and the assessment of the parallel performance of HiPACE.

The code is parallelized using the Message Passing Interface [Message Passing Interface Forum, 2012] to run on distributed memory systems. The parallelisation is achieved by means of a spatial decomposition of the simulation domain in all three dimensions. However, in a quasi-static PIC code, parallelisation in the longitudinal direction and in the transverse plane is fundamentally different. This is

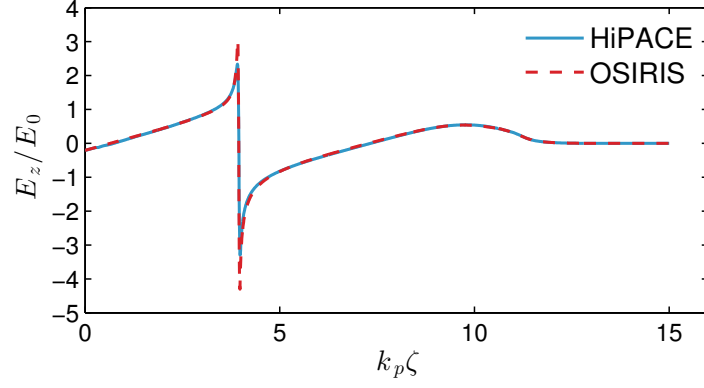
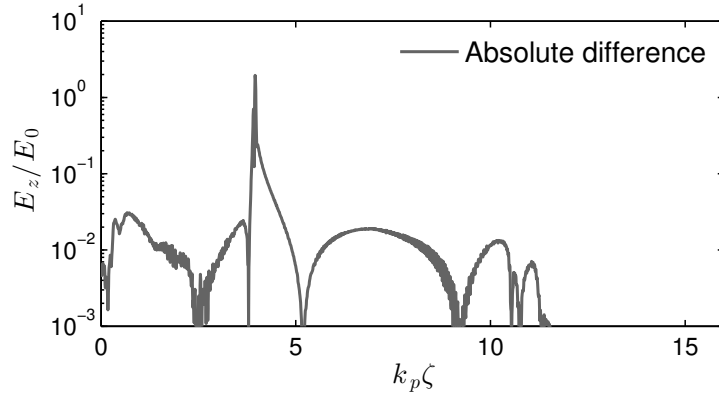
(a) Comparison of  $\mathcal{E}_z$ .(b) Absolute difference of  $\mathcal{E}_z$  curves.

Figure 17: Comparison of results obtained from [HiPACE](#) and [OSIRIS](#) after distance of  $\tilde{z} = 450$ . The on-axis longitudinal electric field  $\mathcal{E}_z$  is shown.

owed to the basic numerical scheme of quasi-static PIC codes which reduces a 3D problem to a set of 2D transverse plane problems. The transverse parallelisation is similar to the one in full explicit codes with beam- and plasma macro-particle exchange between neighbouring processors and exchange of values at the domain-boundaries by use of *halo-* or *ghost-cells* (see e.g. [[Wilkinson and Allen, 1999](#)]). However, the field solver in [HiPACE](#) is not based on a finite-difference time-domain (FDTD) method, but on fast Fourier transforms, which are, owed to their collective nature, not trivially parallelisable. The data, distributed amongst the memory of the processes within a transverse slice needs to be transposed during the fast Fourier transform. The library Fastest Fourier Transform in the West (FFTW) provides Message Passing Interface (MPI) subroutines to pass information between processors during the transposing process. However, transpositions cause a massive overhead because they require an all-to-all communication. In addition, the MPI FFTW libraries support only a 1D decomposition. The decomposition in the second transverse direction was hence implemented manually in [HiPACE](#).

Supplementary info  
on the fast Poisson  
solver and the  
parallelization, see  
Appendix C

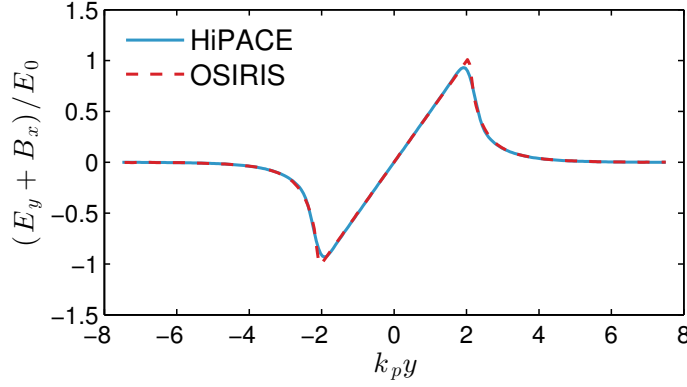
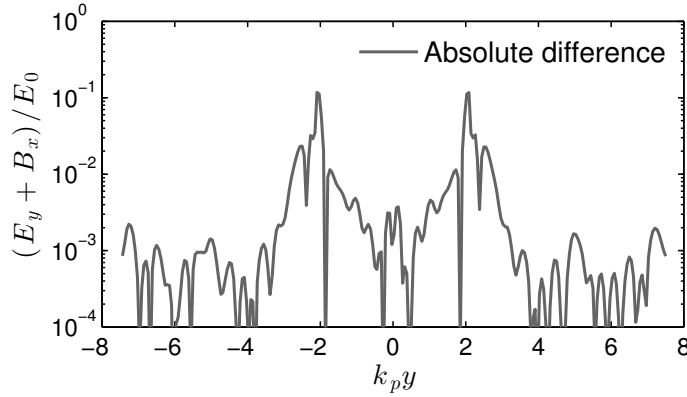
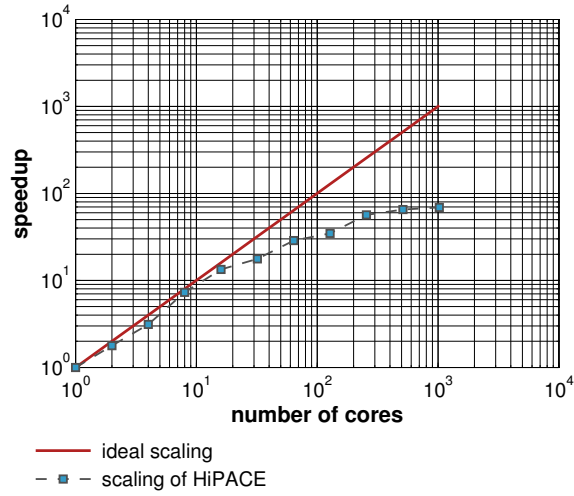
(a) Comparison of  $\mathcal{E}_y + \mathcal{B}_x$ .(b) Absolute difference of  $\mathcal{E}_y + \mathcal{B}_x$  curves.

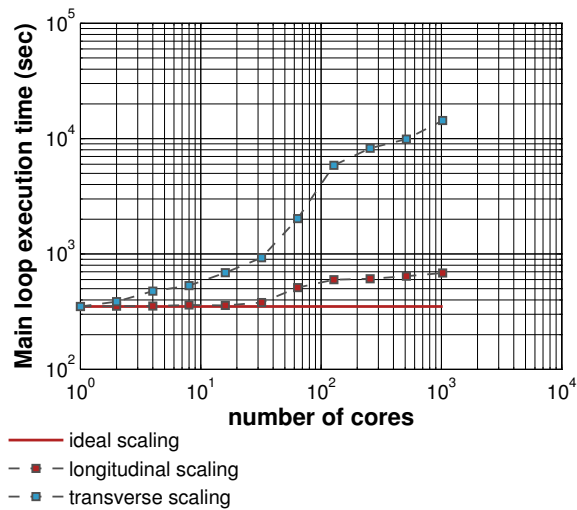
Figure 18: Comparison of results obtained from **HiPACE** and **OSIRIS** after distance of  $\tilde{z} = 450$ . The transverse fields  $\mathcal{E}_y + \mathcal{B}_x$  at co-moving position  $\tilde{\zeta} = 7.33$  is shown.

The parallelisation in the longitudinal direction essentially differs from the one in the transverse plane. Plasma and field information is advanced in the negative  $\tilde{\zeta}$ -direction. This implies that processes, responsible for a longitudinal domain  $k$ , are idle until processes, responsible for domain  $k + 1$ , pass the plasma macro-particle and field information. This causes massive idle times in a method which utilized synchronous advance in  $\tilde{t}$  and would thus strongly decrease the efficiency when running simulations with a large number of domains in longitudinal direction. This crucial issue can be overcome by allowing transverse process slabs  $k$  and  $k + 1$  to run asynchronously in such a way that process slab  $k + 1$  finishes with the plasma routine just when the plasma routine is called in process slab  $k$ . Message passing is then allowed only in the negative  $\tilde{\zeta}$ -direction, implying, that only zeroth order charge deposition and field interpolation along the longitudinal direction is permitted. This inhibits significant idle times. Load imbalances can still arise from a varying number of iterations for the calculation of the transverse magnetic fields at different longitudinal positions of the simulated problem. This load imbalance

can be mitigated in [HiPACE](#) by choosing a non-uniform longitudinal domain decomposition, such that domains, containing a field configuration with enhanced  $\tilde{\zeta}$ -dependence, have a smaller number of local grid-points.



(a) Strong scaling



(b) Weak scaling

Figure 19: Parallel scalings of [HiPACE](#).

To assess the parallel performance of [HiPACE](#), the *strong scaling* and the *weak scaling* are tested on a number of cores ranging from 1 to 1024. When performing a strong scaling benchmark the total problem size is constant, whereas for a weak scaling the problem size per core is kept constant. The strong scaling is therefore measuring the speedup of computing the same problem with an increasing number of processes. At larger number of processes, the communication overhead or the non-parallel part of the code generally starts to contribute to, and at some instance, dominate the simulation run time, hence

limiting the speedup. The weak scaling is not depending on the eventual memory boundedness of the problem. In addition, it reveals the communication overhead per additional process more clearly.

The physical problem simulated for the performance tests is a homogeneous distribution of beam-electrons and beam-positrons propagating through a plasma. The homogeneous distribution assures for a balanced load on the various cores while the overall charge neutrality assures for fulfillment of the boundary conditions. It should be noted, that this problem with plasma particles streaming through the simulation domain is closer to common problems in plasma acceleration than the case of a thermal plasma, which are usually used for parallel benchmarks. Figure 19a shows the strong scalability of the code, where speedup stands for the ratio of simulation run time on one core over the simulation run time on the considered number of cores. The red curve resembles the optimum scalability and blue boxes represent the measured scalability. As seen, the measured scalability starts deviating significantly from the optimum line when many more than 64 cores are used. The efficiency is at 15 % for 1024 cores.

The source of the overhead is investigated by use of a weak scaling. Since parallelisation differs in longitudinal and transverse directions, the scaling is performed by increasing the number of processing units in the longitudinal direction only (longitudinal scaling) or in the transverse directions only (transverse scaling). Figure 19b shows the result of this test. The data for the longitudinal scaling is near to the optimum, constant scaling, whereas the simulation run-time in the transverse scaling increases dramatically, especially when using more than 16 cores. This may be contributed to the overhead generated during the computation of the FFTs. The hardware used in this test had 16 cores in one CPU and 4 CPUs on one blade, such that the inter-CPU-communication and inter-blade communication were producing overhead when using more than 16 or 64 cores, respectively. As a result, the simulations run at best performance as long as the transverse plane in the 3D simulation geometry is decomposed in less than 16 cores. This test also suggests the necessity of employing FFT frameworks with better parallel performance (e.g., as described in [Pippig, 2013]).

### 3.6 DISCUSSION AND CONCLUSION

The following discussion summarizes the major strengths and drawbacks of HiPACE compared to full PIC codes. The most prominent feature of HiPACE is the enhanced efficiency when modelling interaction of highly relativistic particle-beams with plasma compared to conventional PIC codes. This is made possible by the separated treatment of the plasma. This also allows for a significantly reduced memory us-

age, since only plasma macro-particles within a transverse slice must be stored in the memory for momentary processing. In a simulation with a number of e.g. 1000 grid-points in longitudinal direction, the memory usage for the plasma species, which usually the dominating part, can be mitigated by this factor of 1000 (this memory needs to be reserved for each process-slab, if the simulation domain is decomposed into a number of processes in the longitudinal direction). While decoupling spatial and temporal resolutions, codes using the [QSA](#) are not restricted by the [CFL](#) condition but by an appropriate choice of the time-step, which must resolve the beam dynamics.

Quasi-static [PIC](#) codes are specialized on common plasma acceleration scenarios and hence, are not as versatile as full [PIC](#) codes. Particles must either be highly-relativistic (beam) or non- to mildly-relativistic (plasma) to satisfy the underlying approximations. This is the most evident drawback of [HiPACE](#) which also prevents modelling of self-injection processes. An approach of modelling the transit of plasma macro-particles to beam macro-particles in a quasi-static [PIC](#) code was presented by [Morshed et al. \[2010\]](#). However, this approach can only give a qualitative approximation of self-injection processes since it either violates equation (3.4) or does not resolve the beam evolution temporally during the process, yet both criteria are fundamental for a consistent quasi-static treatment. In simulations with [OSIRIS](#) and [HiPACE](#), a different method was used to circumvent this drawback. As discussed above, the self-consistent field configuration is computed at each time-step in [HiPACE](#). This feature enables a consistent import of beams from full [PIC](#) codes during their propagation in a plasma. Simulations using this hybrid approach have been performed by modeling the injection processes within the first few millimeters to centimeters within a plasma target with [OSIRIS](#) and using [HiPACE](#) to simulate the subsequent acceleration of imported driver- and witness-beam over centimeter- to meter-scale distances. However, fast Poisson solvers pose a challenge for the transverse parallelisation of [HiPACE](#).

Near future plans for further developments on [HiPACE](#) are described below. Improvements on the fast Poisson solver framework are foreseen to enhance the parallel efficiency. Also crucial for the efficiency is the convergence rate during the magnetic field iterations, which is planned to be increased. A method, to automatically adopt the local  $\Delta\tilde{\zeta}$  grid size according to the local  $\mathcal{E}_z$  field magnitude, as described in Ref. [[Lotov, 2003](#)], is foreseen to be implemented in [HiPACE](#) to improve accuracy as well as speed of the simulations. Beam particle slippage in the speed-of-light frame might become relevant in long-distance or moderate beam-energy simulations and the associated physics will be incorporated into [HiPACE](#). In order to address laser-driven plasma acceleration, a laser-envelope model with time-averaged ponderomotive force, to model the action on the plasma electrons, comparable

to the ones used in refs. [Cowan et al., 2011; Benedetti et al., 2010, 2012a], needs to be implemented into the code.

The PIC code `HiPACE` exploits the quasi-static approximation to apply a numerical scheme which decouples beam and plasma evolution in beam-driven plasma wakefield acceleration simulations. This enables time steps which can be orders of magnitudes larger than the ones in explicit PIC codes, making simulations of a variety of problems in beam-driven plasma acceleration highly efficient. Comparisons to results, obtained from the explicit PIC code `OSIRIS`, indicate the capability of `HiPACE` to simulate a variety of plasma acceleration problems with significantly lower computational costs while preserving the physical accuracy. This is achieved by an efficient quasi-static numerical scheme, a parallelisation in all three dimensions, and the use of fast Poisson solvers.





## Part III

### PHYSICAL STUDIES

#### 4. BEAM MATCHING IN PLASMA ACCELERATION

*Content:* Motivation of beam quality preservation. Relevance of beam matching. General considerations for matching of beams. Beam matching in linear regime plasma-based acceleration. Matching in the blowout regime. Discussion and conclusion.

#### 5. EMITTANCE GROWTH IN STAGED LWFA

*Content:* The necessity of staged LWFA. Theory describing the emittance growth in staged LWFA. Presentation of PIC simulation results for comparison. Quantitative discussion of the consequences for staged LWFA. Summary and conclusion.

#### 6. DENSITY-TAPERED BEAM EXTRACTION

*Content:* Formulation of the importance of the study on beam extraction techniques. Investigations on density tapered beam extraction in ideal systems. Study on density tapered beam extraction in realistic scenarios with beams with significant energy spread. Conclusion.

#### SUMMARY, CONCLUSION AND OUTLOOK

*Content:* Summary, conclusion and outlook on studies on transport of transverse beam quality in plasma-based accelerators.



#### 4.1 INTRODUCTION AND MOTIVATION

Plasma-based acceleration is a promising technology candidate for future particle colliders and FELs. Collider concepts based on laser wakefield acceleration (LWFA) [Leemans and Esarey, 2009; Schroeder et al., 2010] and on plasma wakefield acceleration (PWFA) [Seryi et al., 2009] have been proposed. The length of a plasma stage and hence the energy gain in one unit in these designs is fundamentally limited by energy depletion of the driving beam [Esarey et al., 2004; Lotov, 2005]. Laser-driven plasma acceleration of electron beams to energies beyond the 10 GeV level seems possible only by use of multiple stages in series, i.e. by staging (see 1.5.7 or confer [Schroeder et al., 2010]). Moreover, and most importantly, beams generated in any plasma-based accelerator scheme (single-stage or multi-stage) need to be extracted, transported and manipulated before being used for applications in photon science or particle physics.

As a consequence, pivotal beam parameters, such as the transverse emittance, must be conserved during the injection and extraction processes from conventional beam-optics to a plasma module and vice versa. Similarly as in conventional beam transport and accelerator systems, conservation of the beam emittance is possible only if the beam is matched into the transport structure of the accelerator. This means the beam parameters, such as the beta-function must be matched to the design beta-function of the accelerator.

This is highly challenging since beta-functions (see 1.6.4) in plasmas are typically by many orders of magnitude smaller than in conventional beam-optics, as shown in this chapter. This is owed to the high magnitude of the focusing force in a plasma wakefield, which is comparable to the magnitude of the accelerating force. In addition, beams produced in, or transported through a plasma accelerator often exhibit a significant energy spread on the percent level and chromatic effects can play a role in beam-quality degradation during the injection, acceleration or extraction processes.

This chapter serves as a basis for the subsequent chapters. It derives the matching conditions and the matched betatron-function in the linear and blowout regime in plasma-based acceleration and discusses the results.

## 4.2 MATCHING OF BEAMS IN PLASMA ACCELERATION

## 4.2.1 General matching considerations

The conservation of the beam-emittance in ideal systems has been shown in 1.6.4.1. However, in reality, often one or more of the assumptions for an ideal system do not hold. In the following, systems are regarded, which are ideal up to the point that the linear focusing fields are not only functions of the position along the propagation axis  $z$ , but also of time  $t$ . Moreover, the beam may now exhibit non-negligible energy spread. These assumptions are owed to the nature of the wakefields in plasma accelerators, which are generally functions of the time-variable in the co-moving frame  $\tau = t$  and the phase  $\zeta = z - ct$  behind the drive beam, where a highly relativistic driver velocity is assumed. The focusing and accelerating fields imposed onto an electron beam in a plasma wakefield are therefore depending on the beam-propagation coordinate  $z$  and the time  $t$ . In addition, electron beams in plasma-based accelerators often show an energy spread on the percent level, so that electrons with different Lorentz-factors are transported differently in the plasma module and in conventional beam optics used for the injection and extraction.

The equation of motion for an electron with energy  $\gamma m_e c^2$ , highly relativistic velocity in  $z$ -direction  $\beta_z \rightarrow 1$ , and nonrelativistic velocity in transverse direction  $\beta_x \ll 1$  in a setup with linear transverse force  $F_x = -\hat{k}_x(\zeta, \tau) x$  reads

Compare with the derivation in A.2.

$$x'' \simeq \frac{d^2 x}{dct^2} = -\frac{\hat{k}_x(\zeta, \tau)}{\gamma m_e c^2} x, \quad (4.1)$$

where (A.22) was used. The parameter  $K$  in equation (1.184) can hence be identified with the term

$$K = \frac{\hat{k}_x(\zeta, \tau)}{\gamma m_e c^2}, \quad (4.2)$$

where  $K$  here, unlike in the ideal case, is not only a function of the beam propagation axis  $z$  but on  $\zeta$  and  $\tau$  and on the relativistic factor of a particle  $\gamma$ .

If  $\hat{k}_x$  features a gradient with respect to the phase,  $\partial \hat{k}_x / \partial \zeta \neq 0$ , different slices of a finite length beam are associated to different values of  $K$ . The trace-space ellipse of each slice thus oscillates according to (1.193) at a different frequency. This causes a differential trace-space rotation along the beam which eventually leads to the configuration in which the slice ellipses are not overlapping but occupying a larger projected transverse trace-space volume. Significant beam-energy spread analogously results in betatron decoherence, where an uncorrelated energy spread generates a decoherence within the beam slices, i.e. an increase of the (non-projected) sliced trace space volume, and an energy spread which is correlated with the co-moving

position results in a differential trace-space rotation. The increase of projected or sliced trace space volume is equivalent to a growth of the *projected* and *sliced emittance*, respectively.

As discussed in 1.6.4.2, the envelope of beams which are matched into a focusing channel does not oscillate. Matching of a beam with respect to the mean  $K$  parameter thus mitigates betatron oscillations and associated emittance growth, whereas unmatched beams can experience severe emittance degradation. Projected emittance growth by virtue of differential trace-space rotation is theoretically reversible [O'Shea, 1998]. For beams with significant uncorrelated energy spread, the betatron decoherence occurs within the slices and the resulting emittance growth is irreversible

Emittance growth from betatron decoherence can only be efficiently mitigated by matching of the beams into the accelerating structures. In an accelerating structure with the radially symmetric, linear transverse force  $F_r = -e(E_r - B_\theta)$ , the matched Courant-Snyder parameters can be calculated as follows. The individual transverse electron trajectories in such a system are determined by the differential equation (see A.2)

$$\begin{aligned} \frac{d^2 r}{dz^2} &\simeq \frac{d^2 r}{dct^2} = \frac{F_r(\zeta, \tau)}{\gamma m_e c^2} \\ &= -\frac{\hat{k}_r(\zeta, \tau)}{\gamma m_e c^2} r \\ &= -K r \end{aligned} \quad (4.3)$$

In this context, the individual particle *betatron frequency*

$$\omega_\beta = c\sqrt{K}, \quad (4.4)$$

is introduced. In addition, a betatron wavenumber for highly relativistic particles  $k_\beta = \omega_\beta/c = \sqrt{K}$  can be assigned to the transverse particle oscillations.

The knowledge of the individual particle oscillations can be used to calculate a beam phase-space averaged parameter  $\bar{K} = \langle K \rangle$  for a given time  $\tau$ . The matched Courant-Snyder parameters for a beam with energy spread and finite duration are then with equation (4.5) given by

$$\hat{\alpha}_m = 0, \quad \hat{\beta}_m = \frac{1}{\sqrt{\bar{K}}} = \bar{k}_\beta^{-1}, \quad \hat{\gamma}_m = \sqrt{\bar{K}} = \bar{k}_\beta, \quad (4.5)$$

where  $\bar{k}_\beta$  is the average betatron wavenumber. The term "matching" in the following refers to the matching with respect to the mean parameter  $\bar{K}$ , where the approximation  $\bar{K} \approx K(\bar{\zeta}, \bar{\gamma}, \tau)$  is used, in order make the following argumentation approximately valid for arbitrary energy distributions or longitudinal charge distributions. The overlined quantities denote the beam average quantities, so that the

matching conditions are independent of the exact beam phase-space distribution.

Matching of beams in plasma-based acceleration in the linear regime differs from matching in the blowout regime owing to the different wakefield configurations in the different regimes. The focusing fields have a sinusoidal  $\zeta$ -dependence in the linear regime and a radial dependence which is imposed by the driver beam (compare 1.5.2). In the blowout regime, the focusing fields have no  $\zeta$ -dependence and always a linear radial dependence within the electron-cavity (see 1.5.4).

#### 4.2.2 Matching in the linear regime

It was shown in 1.6.4.1 that the emittance in ideal systems is a conserved quantity. If the beam transport is not ideal in the sense that the transverse fields are a nonlinear function on the particle displacement from the beam propagation axis, emittance growth generally occurs as discussed in 1.6.5 and as shown in [Reiser, 2008]. Hence, the transverse fields need to be linear in order not to deteriorate the emittance. To comply with the constraint of a linear focusing force in the linear plasma acceleration regime ( $a_0^2 \ll 1$  or  $n_b/n_0 \ll 1$ ), the driver beam distribution  $f(\zeta, r)$  in equation (1.138) must have a parabola-type radial profile,  $f \sim f_0(1 - r^2)$ .

Driver beams with a Gaussian radial intensity profile, as used in 1.5.2.1, excite plasma wakes with transverse fields of the following radial dependence

$$\frac{E_r - B_\theta}{E_0} \propto -\frac{k_p r}{(k_p \sigma_r)^2} \exp\left(-\frac{r^2}{2\sigma_r^2}\right) = -\frac{k_p r}{(k_p \sigma_r)^2} \left[1 - \mathcal{O}\left(\frac{r^2}{\sigma_r^2}\right)\right]. \quad (4.6)$$

For radial positions much smaller than the characteristic transverse size of the driver  $r \ll \sigma_r$ , these transverse fields satisfy the condition of linear transverse fields and hence have the capability to transport beams while conserving their emittance. The plasma wakefields, driven by a Gaussian beam with resonant duration are given by equations (1.144a) and (1.144b). The near-axis ( $r \ll \sigma_r$ ) expansion of these fields yield

$$\frac{E_z}{E_0} = f_0 \sqrt{\frac{2\pi}{e}} \cos(k_p(\zeta - \zeta_c)), \quad (4.7)$$

$$\frac{E_r - B_\theta}{E_0} = -f_0 \sqrt{\frac{2\pi}{e}} \frac{k_p r}{(k_p \sigma_r)^2} \sin(k_p(\zeta - \zeta_c)). \quad (4.8)$$

The aim in plasma-based acceleration is to place and transport electron bunches with a length much shorter than the plasma wavelength and a transverse extent much smaller than the transverse size of the driver into a co-moving region which is both focusing and accelerating (compare 1.5.1.3). In the linear regime such a region exists at co-moving positions  $(\zeta_c - \pi) < \zeta < (\zeta_c - \pi/2)$ . For simplicity  $k_p \zeta_c = \pi$

will be used in the following, such that maximum accelerating field and the zero-crossing of the focusing field are located at  $\zeta = 0$ .

The relevant parameters in the transverse focusing fields in the linear regime (4.8) are with equations (4.3) and (4.4) given by

$$K = \sqrt{\frac{2\pi}{e}} \frac{f_0}{\gamma \sigma_r^2} \sin(k_p \zeta), \quad (4.9a)$$

$$\omega_\beta^2 = \omega_p^2 \sqrt{\frac{2\pi}{e}} \frac{f_0 \sin(k_p \zeta)}{(k_p \sigma_r)^2 \gamma}. \quad (4.9b)$$

These parameters are only defined within the focusing region of the plasma wave, i.e. in regions with positive  $\sin(k_p \zeta)$ . The matched beta-function in the linear regime,

$$\hat{\beta}_m = \bar{K}^{-1/2} = \bar{k}_\beta^{-1} = \left(\frac{e}{2\pi}\right)^{1/4} \sqrt{\frac{\sigma_r^2 \bar{\gamma}}{f_0 \sin(k_p \bar{\zeta})}}, \quad (4.10)$$

depends on the phase  $k_p \bar{\zeta}$  in which the beam is located within the plasma wave, on the mean beam energy  $\bar{\gamma}$ , on the amplitude of the driver and the radial driver beam distribution.

#### 4.2.3 Matching in the blowout regime

The argumentation of beam matching in the blowout regime is analogous to the matching in the linear regime, discussed before. The transverse fields inside the ion cavity, given by (1.146a)

$$\frac{E_r - B_\theta}{E_0} = \frac{k_p r}{2}, \quad (4.11)$$

are independent of the co-moving variable  $\zeta$  and are linearly depending on the radius  $r$ , independent of the driver beam distribution. The force on an electron can is hence

$$F_r = -\frac{m_e c^2 k_p^2}{2} r = -\hat{k}_r r, \quad (4.12)$$

with  $\hat{k}_r = m_e c^2 k_p^2 / 2$  in the blowout regime. Hence, the equation of motion (4.3) of an electron in the fields (4.11) with utilization of equation (4.4) results in the parameters

$$K = \frac{k_p^2}{2\gamma}, \quad (4.13a)$$

$$\omega_\beta^2 = \frac{\omega_p^2}{2\gamma}. \quad (4.13b)$$

In the blow-out regime, the betatron frequency  $\omega_\beta$  (see also e. g. [Esarey et al., 2001]) and the parameter  $K$  only depend on the particle energy

and the ambient plasma density. The matched betatron function is now calculated via (4.5),

$$\hat{\beta}_m = \bar{K}^{-1/2} = \bar{k}_\beta^{-1} = k_p^{-1} \sqrt{2\bar{\gamma}}. \quad (4.14)$$

The matched beta-function in the blow-out regime is a function of the mean beam energy  $\bar{\gamma}$  and the ambient plasma density but is independent of the phase  $\bar{\zeta}$  of the beam within the electron cavity.

### 4.3 DISCUSSION AND CONCLUSION

The matching conditions and the matched beta-function in linear regime and blowout regime plasma-based accelerators have been derived. While the matched betatron function in the linear regime depends on the transverse driver profile and amplitude, and, in addition, on the phase in the plasma wave, the matched beta-function in the blowout regime is independent of these properties.

When comparing the matched betatron function for the two regimes, the following may be noted. The driver RMS radius for a transversely Gaussian driver is typically on the order of the plasma skindepth  $\sigma_r \sim k_p^{-1}$ , the driver amplitude is  $f_0 \lesssim 1$  and  $\sin(k_p \bar{\zeta}) \leq 1$ . Hence, from equation (4.10) follows  $\hat{\beta}_m^{\text{lin}} < k_p^{-1} \sqrt{2\bar{\gamma}} = \hat{\beta}_m^{\text{bo}}$ , where  $\hat{\beta}_m^{\text{lin}}$  is the matched beta function in the linear regime and  $\hat{\beta}_m^{\text{bo}}$  is the matched beta function in the blowout regime.

However, the betatron functions in plasma-based accelerators are generally very small compared to the betatron functions typically operated with in conventional beam optics. Considering a plasma at density of  $n_0 \sim 10^{17} \text{ cm}^{-3}$  and a beam at  $\sim 1 \text{ GeV}$ , equation (4.14) suggests a matched betatron function of  $\hat{\beta}_m^{\text{bo}} \sim 1 \text{ mm}$  in the blowout regime. When assuming a driver beam with  $\sigma_r \sim k_p^{-1}$ ,  $f_0 \sim 0.1$ , and a witness beam, placed in a focusing and accelerating region with  $\bar{\zeta} \sim \pi/4$ , a beta-function of  $\hat{\beta}_m^{\text{lin}} \sim 2.3 \text{ mm}$  is obtained with equation (4.10). The realization of the compatibility of beta-functions of this magnitude with conventional beam optics, which typically operate at betatron functions  $\sim 0.01 - 100 \text{ m}$  is technically challenging.

The betatron function can be reduced by usage of a lower plasma density in the linear and blowout regime. Moreover, in the linear regime, employment of transversely non-Gaussian shaped driver beams [Cormier-Michel et al., 2011] or near-hollow plasma channels [Schroeder et al., 2013b,a] can reduce the focusing fields.

*It is not preferable to place the beam near to  $\zeta \sim 0$ , for reasons which are discussed in chapter 5.*



## 5.1 INTRODUCTION

Current collider concepts, based on laser wakefield acceleration, stipulate the use of multiple plasma stages which are arranged as close with respect to each other as current laser focusing geometries allow in order to achieve the shortest possible overall length of the collider [Leemans and Esarey, 2009; Schroeder et al., 2010]. Electron beams in these concepts are ejected from one plasma stage and injected into a subsequent stage. However, as shown in this chapter, such schemes can result in significant emittance growth during the injection process, if beams are not matched into the plasma modules.

The catalyst for this beam emittance degradation is the decoherence of betatron oscillations of mismatched particle beams [Marsh et al., 2005; Khachatryan et al., 2007]. The betatron oscillations within a mismatched beam decohere, if the focusing fields vary along the beam or if the beam features a significant energy spread. It has been shown in earlier studies that matching of the bunch size reduces emittance growth from finite energy spread [Assmann and Yokoya, 1998; Michel et al., 2006], and mitigates energy loss and correlated growth of energy spread due to emission of synchrotron radiation [Michel et al., 2006].

This chapter investigates emittance growth due to varying focusing forces along a finite bunch length in the linear regime. Betatron-phase-mixing from varying forces along the beam appears very rapidly in plasma accelerators, which is related to the large magnitude of the focusing forces in a plasma accelerator and the small betatron function. The length over which the full emittance growth develops is found to be less than or comparable to the typical dimension of a single plasma module in current multistage designs. Matching of beams mitigates betatron-decoherence effects and can allow for beam-quality preservation during the transport of beams through plasma stages. This behavior is demonstrated by PIC simulations and supported by an analytic theory, reproducing the simulation results. In addition, an analytic theory enables the quantitative prediction of emittance degradation in two consecutive plasma acceleration modules, coupled by free-drift sections, excluding this scheme for the emittance preserving transport, and thus suggesting the necessity of yet to be developed electron-beam matching and extraction sections between acceleration stages.

*The here discussed topics also appeared in [Mehrling et al., 2012]*

## 5.2 ANALYTICAL THEORY

In this section, a general analytic expression for the final asymptotic emittance growth in LWFA, caused from betatron decoherence as expected by insufficient matching is derived.

In the following an electron-bunch, propagating collinear and with a defined temporal offset with respect to a laser pulse on the laser propagation axis is regarded. The laser pulse with normalized vector potential  $a_0$  is focused onto a gas target, ionizes the gas and simultaneously excites plasma waves that carry large amplitude wakefields. Experiments with externally injected electron bunches should be designed such that the laser drives linear ( $a_0 \ll 1$ ) or quasi-linear plasma waves ( $a_0 \lesssim 1$ ) to inhibit self-injection of plasma electrons [Modena et al., 1995]. The formulation within the scope of this chapter describes only this regime and is not valid for the nonlinear or blow-out regime.

Since the parameter  $K$  in equation (4.9a) depends on  $\zeta$  and on  $\gamma$ , beam-slices at different  $\zeta$ -positions and with different energies oscillate at different frequencies. This leads to a differential phase space rotation, and ultimately to complete decoherence during the acceleration process. This effect is illustrated in Figure 20, where the trace-space ellipses of longitudinal bunch slices from a PIC simulation are shown for different  $\zeta$ -positions. The interval  $[\bar{\zeta} - 3\sigma_{\zeta,e}, \bar{\zeta} + 3\sigma_{\zeta,e}]$ , where  $\sigma_{\zeta,e} = \sqrt{\langle (\zeta - \bar{\zeta})^2 \rangle}$  is the RMS electron-bunch length, was divided equidistantly into 10 slices and ellipse parameters for each slice particle subsets were calculated with eqns. (1.154) and (1.157). Slice ellipses develop a tilt with respect to each other which increases the projected area and hence causes growth of the projected emittance whereas the charge-weighted sum over the emittance of the slices, the sliced emittance, does not increase owing to this effect.

Emittance growth due to slice-ellipse rotation is theoretically reversible [O'Shea, 1998]. However, recovering the emittance by further rotation in a subsequent plasma stage requires a transformation  $(x, x') \rightarrow (\mp x, \pm x')$  in between stages which is not symplectic and hence not realizable by any combination of beam optics.

It should be noted, that the asymptotic emittance growth depends on the degree of mismatch only and is identical for any amount of finite energy spread or variance of the focusing forces along the beam. Only the *emittance growth-rate* depends on the latter properties. Emittance growth from uncorrelated energy spread emerges within the slices whereas an energy-phase correlation or a change of the focusing fields along the beam cause a differential phase-space rotation and projected emittance growth.

Nonetheless, emittance growth from any betatron decoherence can be suppressed by matching the transverse properties of the electron beam to the intrinsic electron-betatron motion in the plasma wake.

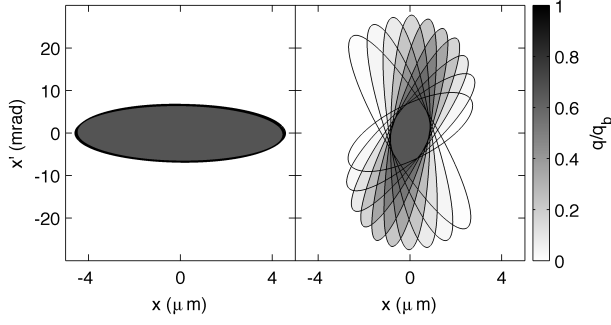


Figure 20: Ellipses representing bunch slices from the PIC simulation C2 (see below) at position  $z = -0.03$  mm (left) and  $z = 1.06$  mm (right). The gray-scale of the ellipse was chosen according to the ratio of the charge in a slice  $q$  and total bunch charge  $q_b$ .

The matching conditions in terms of the Courant-Snyder parameters in the relativistic limit are

$$\hat{\beta}_m = \bar{K}^{-1/2}, \quad \hat{\gamma}_m = \bar{K}^{1/2}, \quad \hat{\alpha}_m = 0, \quad (5.1)$$

with (see 4.2.2)

$$\bar{K} = \sqrt{\frac{2\pi}{e}} \frac{f_0}{\bar{\gamma} \sigma_f^2} \sin(k_p \bar{\zeta}). \quad (5.2)$$

Electron oscillations follow the ellipse defined by the Courant-Snyder parameters of matched beams. Once a bunch is matched, adiabatic changes of the betatron frequency, that is changes on time-scales  $T \gg \omega_\beta^{-1}$  or equivalently on length-scales  $L \gg k_\beta^{-1}$ , will not degenerate the beam quality.

The trace-space coordinate system is transformed such that particles have a circular trajectory in order to enable an estimation of the emittance growth caused by the decoherence of betatron oscillations

$$x^* = x / \sqrt{\hat{\beta}_m}, \quad x'^* = x' \sqrt{\hat{\beta}_m} \quad (5.3)$$

$$\hat{\gamma}^* = \hat{\gamma} \hat{\beta}_m, \quad \hat{\beta}^* = \hat{\beta} / \hat{\beta}_m, \quad \hat{\alpha}^* = \hat{\alpha}. \quad (5.4)$$

The emittance (eqn. 1.154) is invariant under this transformation. Total phase decoherence implies that the characteristic ellipse of the bunch evolves into a circle in transformed trace-space coordinates with a radius given by the initial standard deviations along the semi-major and semi-minor axes. The emittance after total phase mixing can therefore be estimated by

$$\hat{\epsilon}_{\text{fin}} = \langle x_{\text{rot}}^2 \rangle = \left\langle \frac{x_a^2 + x_b^2}{2} \right\rangle = \frac{a^2}{2} + \frac{b^2}{2}. \quad (5.5)$$

Here  $a$  and  $b$  are the semi-major and the semi-minor axes of the bunch ellipse in the transformed system prior to phase decoherence

$$a^2 = \frac{\hat{\epsilon}_{n,\text{init}}}{2} \left[ (\hat{\gamma}^* + \hat{\beta}^*) + \sqrt{(\hat{\gamma}^* + \hat{\beta}^*)^2 - 4} \right], \quad (5.6)$$

$$b^2 = \frac{\hat{\epsilon}_{n,\text{init}}}{2} \left[ (\hat{\gamma}^* + \hat{\beta}^*) - \sqrt{(\hat{\gamma}^* + \hat{\beta}^*)^2 - 4} \right]. \quad (5.7)$$

This yields the final normalized emittance for complete decoherence

$$\begin{aligned} \hat{\epsilon}_{n,\text{fin}} &= \frac{\hat{\epsilon}_{n,\text{init}}}{2} \left( \frac{1 + \hat{\alpha}^2}{\hat{\beta}^*} + \hat{\beta}^* \right), \\ &= \frac{\hat{\epsilon}_{n,\text{init}}}{2} \left( \frac{1 + \hat{\alpha}^2}{\hat{\beta}_0/\hat{\beta}_m} + \frac{\hat{\beta}_0}{\hat{\beta}_m} \right). \end{aligned} \quad (5.8)$$

This equation expresses the asymptotic emittance growth, which is expected if a beam with energy spread or with varying focusing fields along the bunch axis is not matched  $\hat{\alpha} \neq 0$  or  $\hat{\beta}_0/\hat{\beta}_m \neq 1$  into a plasma wakefield.

### 5.3 COMPARISON TO PIC SIMULATIONS

The above model is now compared to full 3D PIC simulations using the code **OSIRIS** [Fonseca et al., 2002]. Electron bunches with a low relative energy spread of  $\sigma_\gamma/\bar{\gamma} = 0.0065$  and an initial normalized emittance of  $\hat{\epsilon}_{n,\text{init}} = 0.3 \mu\text{m}$  propagate at a defined temporal offset collinear to a 5 J, 25 fs full width at half maximum (**FWHM**) length, 800 nm central wavelength,  $a_0 = 1.8$  linearly polarized laser pulse on the laser axis. The Rayleigh-length of the laser is long compared to the betatron length and the **FWHM** intensity waist of the pulse is  $50 \mu\text{m}$ , where the transverse profile is a Gaussian and the temporal profile is a symmetric polynomial. The dimensions of the co-propagating simulation box in the longitudinal and transverse directions are  $118 \times 336 \times 336 \mu\text{m}^3$ ,  $4620 \times 250 \times 250$  cells with 1 particle per cell for the plasma and a total number of  $\sim 5 \cdot 10^5$  beam particles. The charge was deposited using a quadratic interpolation scheme. Electron beams have a charge of 1 pC, mean energy of 5 MeV, and an **RMS** bunch length of  $\sigma_{z,e} = 3 \mu\text{m}$  resembling realistic parameters obtainable from conventional electron guns. The charge distribution of the bunch in focus is a Gaussian in space and momentum space. The charge is chosen sufficiently low to neglect space charge forces as well as beam loading, the energy low enough to see the betatron-phase mixing effect within the first few millimeters, and the bunch length much shorter than the plasma wavelength. The bunches are injected with a temporal offset of 120 fs with respect to the peak of the laser pulse envelope to allow for optimum acceleration in the focusing phase of the plasma wave. The plasma target has a flat-top

*Beam loading, see e.g. [Rechatin et al., 2010].*

longitudinal profile with an electron density of  $n_0 = 10^{17} \text{cm}^{-3}$ . The rising edge at position  $z_0 = 0$  was chosen short compared to the plasma wavelength to simplify the matching conditions. The falling edge is at position  $240 c/\omega_p \simeq 4.0 \text{ mm}$ .

Particle-in-cell simulations with different sets of Courant-Snyder parameters, resulting from different focusing geometries of the same electron beam are compared with respect to each other.

- Matched case (CM): Beam with matched Courant-Snyder parameters,  $\hat{\beta}_{CM}(z_0) = \hat{\beta}_m$ ,  $\hat{\alpha}_{CM}(z_0) = \hat{\alpha}_m = 0$ ;
- Mismatched case (C1): Beam with matched beta function at focus  $\hat{\beta}_{CM}(z_{f,C1}) = \hat{\beta}_m$  but with mismatched focal position  $z_{f,C1} \neq z_0 \rightarrow \hat{\alpha}_{C1}(z_0) \neq 0$ ;
- Mismatched case (C2): Beam with mismatched beta function  $\hat{\beta}_{C2}(z_0) \neq \hat{\beta}_m$  but matched focal position  $z_{f,C2} = z_0 \rightarrow \hat{\alpha}_{C2}(z_0) = 0$ .

For the matched case (CM), the focal position of the bunch  $z_{f,CM}$ , must be positioned at  $z_0$  to satisfy  $\hat{\alpha}_{CM}(z_0) = 0$  in the matching conditions (5.1). The slope of the transverse force  $\partial F_x/\partial x$  is analyzed at the position where the bunch is supposed to be injected and used eqns. (4.9b) and (4.10) to find the matching beta function  $\hat{\beta}_m = 0.126 \text{ mm}$ . This corresponds to an RMS beam size of  $1.97 \mu\text{m}$  for  $\hat{\epsilon}_{n,\text{init}} = 0.3 \mu\text{m}$ .

In simulation (C1), the focus is at  $z_{f,C1} = -20 c/\omega_p \simeq -0.33 \text{ mm}$ . During the initial vacuum propagation the Courant-Snyder parameters evolve according to the formulae for their evolution in a free drift, neglecting space charge forces,

$$\hat{\alpha}(z) = \frac{z_f - z}{\hat{\beta}_f}, \quad \hat{\beta}(z) = \hat{\beta}_f + \frac{(z - z_f)^2}{\hat{\beta}_f}, \quad \hat{\gamma}(z) = \frac{1}{\hat{\beta}_f}, \quad (5.9)$$

where  $\hat{\beta}_f$  is the beta function at focus  $z_f$ . The beta and gamma functions at  $z_0$  in the PIC simulation are  $\hat{\beta}_{C1,0} = 1.026 \text{ mm}$  and  $\hat{\gamma}_{C1,0} = 7.937 \text{ mm}^{-1}$ . For case (C2) the beta and gamma function at  $z_0$  are  $\hat{\beta}_{C2,0} = 0.678 \text{ mm}$ ,  $\hat{\gamma}_{C2,0} = 1.476 \text{ mm}^{-1}$ . Figure 21 depicts the evolution of the Courant-Snyder parameters during acceleration for the three mentioned cases. The evolution of the alpha parameter shows that bunches in simulations (CM) and (C2) are focused to position  $z_0$  whereas  $\hat{\alpha}_{C1}$  crosses zero before  $z_0$  and the bunch is defocused at position  $z_0$ . This is also indicated by the evolution of the beta parameter. Its parabola vertices (at focus) for cases (CM) and (C2) are situated at  $z_0$  in contrast to case (C1), for which the vertex is in front of the plasma rising edge. The gamma function of (C1) initially equals  $\hat{\gamma}_{CM}(z_0)$  whilst  $\hat{\gamma}_{C2}$  is not matched. If matched, the bunch ellipse will not oscillate after injection and  $\hat{\alpha}$  will remain zero during the acceleration process as observed for simulation (CM), whereas the alpha

*See derivation in 1.6.4.2 or confer [Courant and Snyder, 1958].*

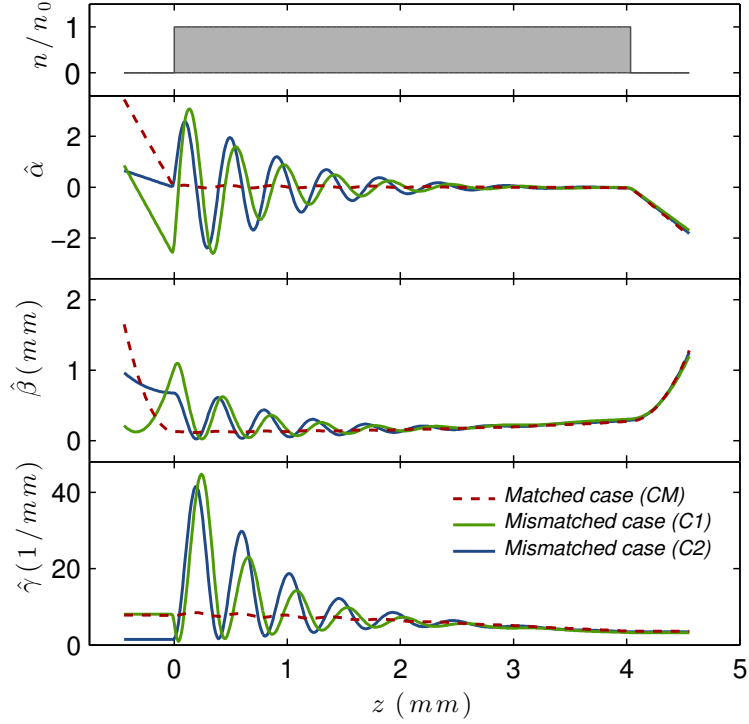


Figure 21: Plasma density profile and evolution of the Courant-Snyder parameters for the three considered cases in PIC simulations.

parameters in the cases (C1) and (C2) oscillate around zero. Owing to relativistic mass gain, the beta function increases adiabatically and the gamma function decreases accordingly. The  $\hat{\alpha}$ ,  $\hat{\beta}$ ,  $\hat{\gamma}$ -curves of (C1) and (C2) all approach the matched case (CM) by the cost of emittance growth during betatron-phase mixing as can be seen by comparison of Figures 21 and 22. It should be emphasized that the emittance in the matched case (CM) did not grow significantly despite the fact that the bunch slipped back substantially with respect to the plasma wave and despite the acceleration of the beam. This is because the phase slippage and energy gain occurs adiabatically and does not disrupt the matching conditions.

The betatron-phase is completely mixed at  $z \approx 2.5$  mm and emittance growth is saturated at that position in good agreement with expectations (confer eqn. (5.10) below). The emittance in the matched case (CM) grows marginally compared to the non-matched cases. After exiting the plasma target and the beam being at a waist ( $\hat{\alpha} = 0$ ), the Courant-Snyder parameters evolve again according to eqn. (5.9).

These numerical results on the emittance evolution are now compared with the above derived analytic theory. The normalized emittance at the plasma exit in the PIC simulation is  $\hat{\epsilon}_{n,C1} = 1.360 \mu\text{m}$  for case (C1) and  $\hat{\epsilon}_{n,C2} = 0.830 \mu\text{m}$  for case (C2). Using formula (5.8) the following asymptotic emittance values are found,  $\hat{\epsilon}_{n,\text{fin},C1} = 1.371 \mu\text{m}$  and  $\hat{\epsilon}_{n,\text{fin},C2} = 0.835 \mu\text{m}$ . Thus, the theory yields close estimates ac-

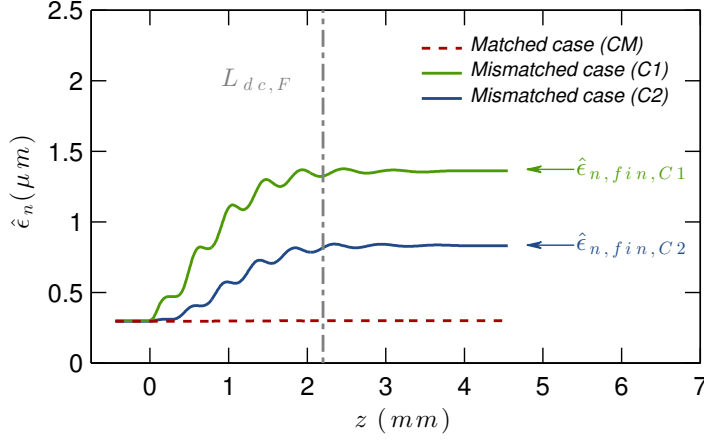


Figure 22: Evolution of the normalized emittance  $\hat{\epsilon}_n$  in PIC simulations for the three considered cases. Arrows show the analytic predictions of the emittance growth. The betatron-decoherence length for the injection phase in the simulations  $k_p \bar{\zeta} = 1.00$  relative to position  $z_0$  is indicated by the dash-dotted line.

curate to within one percent for emittance growth due to betatron-decoherence.

Emittance generation in the PIC calculations by insufficient spatial resolution or by numerical heating effects [Cormier-Michel et al., 2008] was shown to be negligible by comparison of the presented simulations to simulations with higher resolution and higher charge-interpolation schemes. The transverse bunch extent was small compared to the laser spot size such that the nonlinearity of the focusing fields at radii on the order of the laser spot size did not cause emittance growth. Comparison of transverse emittance in and perpendicular to the polarization plane ruled out laser heating as an emittance generator. Furthermore, bunch charge densities sufficiently low to neglect space-charge and beam loading effects were used.

#### 5.4 CONSEQUENCES FOR STAGED LWFA

The consequences of the presented calculations for staged acceleration are discussed in the following. Firstly, the propagation distance during which the betatron-phase of a bunch becomes mixed from finite bunch length is derived. An electron bunch with RMS length  $k_p \sigma_{\zeta,e} \ll 1$ , negligible energy spread and a charge well below the beam loading limit is considered in order to find an approximation for this distance. Assuming the bunch is injected and fixed to a phase  $\bar{\zeta}$  in a quasilinear plasma wave, an expression for the *complete decoherence length* caused by variation of focusing fields along the beam is found

$$L_{dc,F} \simeq \frac{2\pi}{k_\beta(\bar{\zeta}) k_p \sigma_{\zeta,e}} \tan(k_p \bar{\zeta}), \quad (5.10)$$

for  $0 < \bar{\zeta} < \lambda_p/2$ . The decoherence length from finite energy spread  $\sigma_\gamma$  is given by (c.f. [Michel et al., 2006])

$$L_{dc,E} \simeq \frac{2\pi\bar{\gamma}}{k_\beta(\bar{\zeta})\sigma_\gamma}. \quad (5.11)$$

Comparing this expression with eq. (5.10) suggests that finite bunch length as a generator of betatron decoherence is dominant over finite energy spread if  $k_p\sigma_{\zeta,e}/\tan(k_p\bar{\zeta}) > \sigma_\gamma/\bar{\gamma}$  holds and vice versa. To ensure for efficient acceleration, the bunch must be injected (and at best fixed e.g. as described in [Rittershofer et al., 2010]) close to the maximum accelerating field, i.e.  $k_p\bar{\zeta} \leq \pi/4$ , such that  $\tan(k_p\bar{\zeta}) \leq 1$ . Thus, for energy spreads as demanded for typical applications [Lee-mans and Esarey, 2009], the effect from finite length can generally be assumed to be dominant over the effect by finite energy spread. Nevertheless, energy spread and bunch length are strongly interrelated in wakefield- and vacuum-propagation and both need to be minimized to ensure for good beam quality.

The assumption  $k_p\bar{\zeta} < \pi/4$  simplifies equation (5.10) to  $k_pL_{dc,F} \leq 4.28\sqrt{\bar{\gamma}}k_pr_s/(a_0k_p\sigma_{\zeta,e})$ , where  $r_s = 2\sigma_r$  is the laser spot size. The maximum length of a plasma stage is given by the depletion length [Shadwick et al., 2009]  $k_pL_{pd} \simeq 17.4\lambda_p^2/(\lambda_l^2a_0^2)$ , where  $\lambda_l$  is the laser wavelength. The betatron-phase is thus completely mixed within the length of a stage, as long as

$$\frac{k_p\sigma_z\lambda_p^2}{\sqrt{\bar{\gamma}}k_pr_s a_0\lambda_l^2} > 0.25 \quad (5.12)$$

holds. Assuming  $k_p\sigma_{\zeta,e} = 0.1$ ,  $\lambda_p/\lambda_l = 100$ ,  $a_0 = 2$  and  $r_s = \lambda_p/2$ , parameters which are close to those proposed for a future plasma-based collider design [Schroeder et al., 2010], this is found to be the case for beam energies of  $< 250$  GeV. However, the effect of emittance growth by mismatch of the beta function and partial phase mixing is relevant as long as  $L_{dc,F}$  does not significantly exceed the length of an accelerating stage.

The above derived model is now applied to staged plasma acceleration concepts in which no electron beam optics are used in between stages to minimize the coupling distance  $L_c$ , which contributes critically to the total length of a multi-stage accelerator [Schroeder et al., 2010]. In the following, plasma stages longer than the betatron-decoherence length  $L_{dc,F}$  are regarded and beams thus having a matched beta function  $\hat{\beta}_m^i = \hat{\beta}_f^i$  and being at waist when exiting stage  $i$ , and subsequently performing a free drift with length  $L_c$  between stages  $i$  and  $i+1$ . Using an approximation for the betatron frequency  $\omega_\beta \simeq a_0\omega_p/(k_pr_s\sqrt{\bar{\gamma}})$  and assuming  $\hat{\beta}_f^i = \hat{\beta}_m^{i+1}$  together with eqns. (5.1), (5.4), (5.8), and (5.9) yields

$$\hat{\epsilon}_{n,\text{fin}} \simeq \hat{\epsilon}_{n,\text{init}} \left( 1 + \frac{\eta^2}{2\bar{\gamma}} \right) \quad (5.13)$$



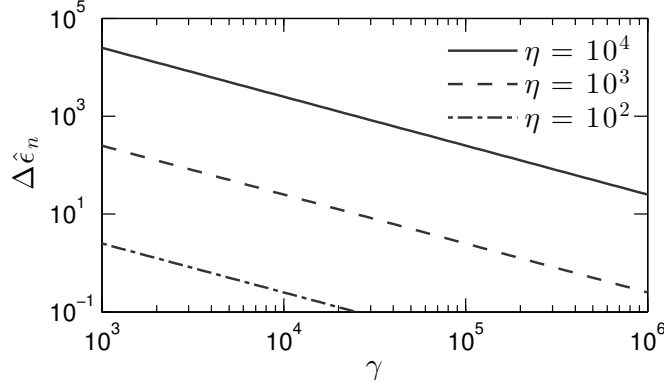


Figure 23: Relative per-stage emittance growth  $\Delta\hat{\epsilon}_n = \hat{\epsilon}_{n,\text{fin}}/\hat{\epsilon}_{n,\text{init}} - 1$  according to eq. (5.13) as a function of beam energy for different values of  $\eta = a_0 k_p L_c / (k_p r_s)$ .

after complete betatron-phase mixing with  $\hat{\epsilon}_{n,\text{init}}$  and  $\hat{\epsilon}_{n,\text{fin}}$  being the emittance values before and after transmission through stage  $i + 1$ , respectively and  $\eta = a_0 k_p L_c / (k_p r_s)$ . When assuming the use of plasma-based laser mirrors [Panasenko et al., 2010; Sokollik et al., 2010] to minimize  $k_p L_c$  to values of  $\sim 10^4$ , a per-stage emittance increase by a factor  $\geq 11$  is found for electron beams with energies  $\leq 500$  GeV, for  $a_0 = 2$  and  $r_s = \lambda_p/2$ , resulting in  $\eta \simeq 6.4 \cdot 10^3$ , rendering such beams unusable for applications after multiple stages. The per-stage emittance growth as a function of beam energy, depicted in Figure 23, suggests that the emittance growth per stage becomes insignificant for beam energies  $> 10$  GeV only if  $\eta < 10^2$ . With plasma-based and conventional laser-focusing technology this is attainable only if a low laser amplitude  $a_0 \ll 1$ , a large spot size  $k_p r_s \gg 1$ , or a non-fundamental transverse Gaussian mode with a low transverse intensity gradient are utilized. Since the accelerating field in the wake (4.7) is proportional to  $a_0^2$  and the required laser power increases with  $r_s^2$ , maintaining a value of  $\eta < 10^2$  would result in highly inefficient acceleration for pure Gaussian laser modes.

The assumption  $\hat{\beta}_f^i = \hat{\beta}_m^{i+1}$  for the derivation of equation (5.13) is contributed to the fact that sharp vacuum-plasma interfaces are considered in this study. Another option constitutes the investigation of tapered transitions, on the order of, or much longer than the local betatron frequency in order to match the electron beam (adiabatically) into the plasma wave by use of a tapered transition from the vacuum to the plasma, as proposed in earlier works [Assmann and Yokoya, 1998; Marsh et al., 2005]. This would imply the beta function of the bunch when emerging from stage  $i$  to be smaller than the beta function in the subsequent stage  $i + 1$  before being (adiabatically) matched,  $\hat{\beta}_f^i < \hat{\beta}_{m,\text{adj}}^{i+1}$ , thus reducing emittance growth after a free drift compared to the sharp interface case (cf. derivation of eq. 5.13). In addition to matching beams with this method, it may be

proposed to propose to expand beams transversely by employing tapered plasma to vacuum transitions with length on the order of, or much longer than the local betatron wavelength [Sears et al., 2010], hence (adiabatically) increasing the beam spot size  $\hat{\beta}_m^i < \hat{\beta}_{f,adj}^i$  immediately downstream of stage  $i$ . It should be noted that eq. (5.8) implies that density tapered matching or extraction without additional refocusing cannot inhibit emittance growth completely, since the beam is out of waist ( $\hat{\alpha} \neq 0$ ) before entering the subsequent stage. Bunches must thus be refocused to eliminate emittance growth, while adiabatic matching or extraction eases the focusing requirements by increasing the beta functions to which beams need to be matched. Another approach in this context can be the application of plasma lenses upstream or downstream of the plasma targets. Further research is necessary to prove the feasibility, stability and capability of emittance suppression by the aforementioned density tapered (adiabatic) matching or extraction techniques.

Moreover, the above considerations assumed a transversely homogeneous plasma profile. Schroeder et al. [2013b,a] proposed to use near-hollow plasma channels to control and reduce the focusing force on an electron beam independent from the longitudinal force. This method can moderate the stringent matching conditions in plasma-based acceleration and mitigate the emittance growth in staged LWFA.

## 5.5 SUMMARY AND CONCLUSION

The present study shows quantitatively that the emittance of an electron beam in an external-injection scheme, as necessary for staging, grows even for ideal laser-bunch alignment (stochastic errors on the alignment have been studied e.g. in [Cheshkov et al., 2000]), if the beam parameters are not matched to the intrinsic betatron length in the plasma wake. If matched, the emittance remains constant during the acceleration process within one percent whereas the emittance of non-matched beams may increase by orders of magnitude depending on the degree of mismatch.

As demonstrated in the discussed PIC simulations, matched beams stay matched if changes of the beam or wakefield properties occur adiabatically. Since the betatron frequency decreases for higher beam energies, changes of the wakefield amplitude e.g. laser spot size oscillations [Benedetti et al., 2012b] might eventually occur on time-scales on the order of the inverse betatron frequency, thus disrupting the matching conditions. This, however, is subject to further studies.

The challenge of matching electron beams into plasma waves arises from the fact that the generated focusing fields are comparable in their order of magnitude to the accelerating fields, and the corresponding matched beta function is therefore small. Assmann and Yokoya thus suggested [Assmann and Yokoya, 1998] to decouple the

amplitude of transverse and longitudinal fields by using transversely tailored drivers to increase the matched beta function. For laser drivers this can be achieved by combinations of higher order Laguerre-Gaussian modes [Cormier-Michel et al., 2011] which provide a focusing field with reduced linear radial dependence near axis and hence an increased matched beta function of the injected beam. Application of this technique is equivalent to utilization of an increased spot size  $r_s$  in eq. (5.13) and allows for a reduction, but not for a complete suppression of the emittance growth of unmatched beams after free drifts. In addition beating of the transverse modes needs to be mitigated to enable a stable focusing channel [Cormier-Michel et al., 2011].

An earlier analysis [Andreev et al., 1997] showed that the focusing phase of the wakefield in plasma channels shifts with respect to the accelerating phase such that the phases may entirely overlap in later wave periods and the maxima of transverse and longitudinal component thus being located at the same co-moving position. Given a high degree of control over absolute density and transverse density gradient in a plasma channel, this effect offers the possibility of reducing emittance growth from finite bunch length if electron bunches are being placed and fixed in this co-moving region and the decoherence length from finite bunch length eq. (5.10) hence tending to infinity. Albeit reducing emittance growth from finite bunch length, this method cannot mitigate emittance degradation by finite energy spread of unmatched electron bunches.

In conclusion, matching of electron beams is inevitable to efficiently suppress beam-quality degeneration due to betatron-phase decoherence. It may be inferred that this degeneration is relevant for electron energies up to the TeV-energy frontier. These findings can have an essential impact on the design and total length of multi-stage laser-wakefield accelerators since electron beam optics, significantly longer than each plasma stage, if based on today's technology, or yet to be developed plasma density tapered matching or extraction sections are necessary in between two stages in order to avoid substantial emittance aggregation.



DENSITY-TAPERED BEAM EXTRACTION

---

## 6.1 INTRODUCTION

The above explanations show that staged plasma acceleration necessitates a beam extraction technique with tapered plasma targets to mitigate severe quality degradation during the acceleration and transport of beams. Furthermore, such a technique is of relevance whenever beams need to be extracted from a plasma module and to be matched into a conventional transport beamline.

The concept of plasma density tapered matching or extraction makes use of the dependency of the transverse field amplitudes on the local plasma density. This can be used to focus and match beams from conventional beam optics into a plasma cell using an increasing plasma density profile as proposed in earlier works [Chen et al., 1990a,b; Assmann and Yokoya, 1998]. Equivalently, a decaying density profile from the plasma to vacuum can be used to match beams emerging from a plasma target into a capturing section with conventional beam optics. Such a method can form a beam-quality preserving transition from sub-millimeter to millimeter scale beta functions ( $\sim$ beam size) and accordingly large gamma functions ( $\sim$ divergence) in the plasma target to meter-scale beta functions and accordingly small gamma functions as required for the beam transport in conventional beam optics. Experimental measurements of the emittance and divergence of electron beams produced in LWFA by means of a pepper-pot method confirmed the reduction of beam divergence in long plasma vacuum transitions [Sears et al., 2010].

Adiabatic matching of mono-energetic beams into and from plasma cells was numerically studied in reference [Marsh et al., 2005]. A recent study by Floettmann [2014] investigated the transport of mono-energetic beams from the plasma to vacuum theoretically and optimized a particular functional dependence of the focusing parameter  $K$  on the beam propagation axis in order to mitigate emittance growth within the beam-capturing section. Moreover, the latter study showed in numerical examples that the transverse phase-space emittance of beams with large energy spread increases dramatically during the vacuum propagation (the trace-space emittance remains constant during the free drift but increases to the value of the phase-space emittance at the next focusing optic), if the beam is not adiabatically expanded and matched to the first capturing focusing optic.

While reference [Floettmann, 2014] serves as a basis for the general understanding of adiabatic beam matching and extraction, studies in-

cluding the effects of realistic plasma density profiles and realistic beam phase-space distributions on various aspects of the driver and witness-beam dynamics in plasma-based accelerators are necessary to draw conclusions which allow for the optimized design of experiments. Such studies on beam extraction from plasma-based accelerators by means of a density tapered extraction, with realistic density profiles and including the dynamics of the driver and witness beam in the plasma, are performed in the following.

Firstly, the density tapered beam-extraction of monoenergetic beams in ideal systems is investigated by means of an ODE, describing the transverse beam dynamics in such setups. Secondly, a study on beam-extraction is presented, which uses realistic setups with beams with significant energy spread, which are propagating through various plasma-vacuum transitions blow-out regime plasma-accelerators. This scenario is explored by means of 3D PIC simulations using the code HiPACE.

## 6.2 DENSITY TAPERED EXTRACTION IN IDEAL SYSTEMS

### 6.2.1 Numerical study

As a first approach to plasma density tapered beam-extraction, ideal systems are regarded. This implies (compare 1.6.4.1) space charge effects can be neglected, the approximation of paraxial motion holds, the focusing forces are linear and depend only on the position along the propagation axis and the beam has negligible energy spread. These are valid assumptions for a mono-energetic beam propagating in a blowout regime plasma wave with density variations on length scales longer than the plasma wavelength.

The single particle trajectories in such a system are governed by the differential equation  $x'' + Kx = 0$  and the betatron function is defined by the ODE (1.190)

$$\hat{\beta}\hat{\beta}'' - \frac{\hat{\beta}'^2}{2} + 2K\hat{\beta}^2 - 2 = 0, \quad (6.1)$$

where  $K = K(z)$  is a function of the beam propagation axis only.

The following study considers a mono-energetic beam which is transported by a blowout regime wakefield from a plasma to the vacuum with tapered plasma transitions. The aim is to reduce the divergence  $\sqrt{\hat{\epsilon}\hat{\gamma}}$  in the plasma-vacuum transitions. The conservation of the emittance in ideal systems implies that density tapered extraction converts beam divergence into beam size. However, since the divergence quickly starts to dominate the beam size evolution in the vacuum propagation of highly divergent and small beams such as produced in plasma-based acceleration, the ratio of the initial divergence over the final divergence  $\eta = \hat{\gamma}_0/\hat{\gamma}_e$  is the relevant measure for the divergence mitigation in the density tapered extraction mechanism. This

*For information about the paraxial approximation, confer [Reiser, 2008, 3.3.2].*

*Here and within this chapter only one transverse direction is regarded. Everything discussed also applies for the other transverse direction.*

ratio is thereby evaluated for a matched, i.e. non-oscillating, beam, which serves as a betatron phase-independent measure.

The parameter  $K$  in the blowout regime is given by (4.13a)

$$K = \frac{k_p^2}{2\gamma} = \frac{2\pi n e^2}{\gamma m_e c^2}, \quad (6.2)$$

with  $n = n(z)$  being a function of the position along the beam propagation axis. Density transitions regarded here are of exponential type with

$$n(z) = \begin{cases} n_0 & \text{for } z < 0, \\ n_0 \exp(-z/L) & \text{for } 0 < z < z_e, \\ 0 & \text{for } z > z_e, \end{cases} \quad (6.3)$$

where the exit of the plasma target is defined by  $z_e = 5 \times L$ . Transverse beam parameters subsequently evolve according to the free-drift equations (1.192).

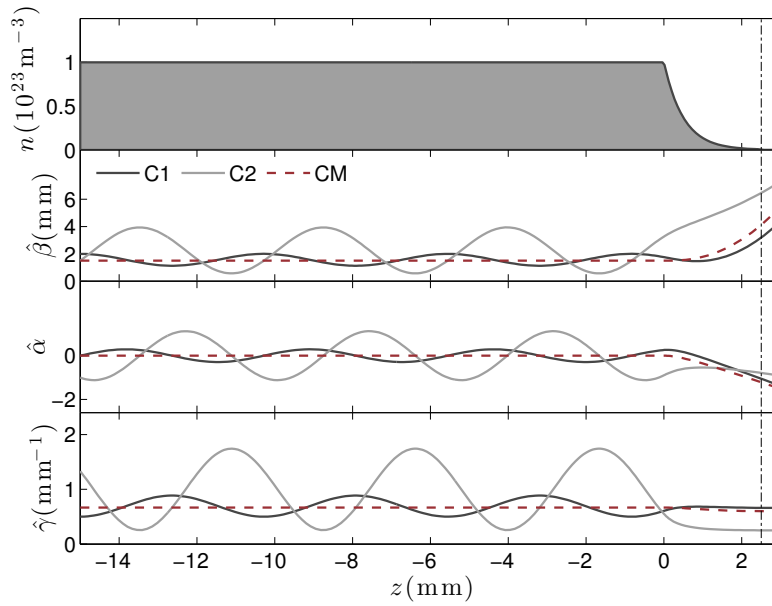


Figure 24: Exponential plasma-vacuum density transition according to eq. (6.2) with  $L = 0.5$  mm for three sets of initial conditions, C1, C2 and CM. The values of the Courant-Snyder parameters of the matched beam (CM) at the exit position  $z_e = 2.5$  mm are given by  $\hat{\beta}_{CM,e} = 4.16$  mm,  $\hat{\alpha}_{CM,e} = -1.23$  and  $\hat{\gamma}_{CM,e} = 0.601$  mm<sup>-1</sup>.

This information is now used to solve the ODE (6.1) numerically for some specific parameters. The plasma density chosen here is  $n_0 = 10^{23}$  m<sup>-3</sup> and the witness beam has an energy of  $\gamma = 4000$ , resulting in a matched betatron function in the constant channel of  $\hat{\beta}_m = \sqrt{2\gamma}k_p^{-1} = 1.5$  mm according to equation (4.14).

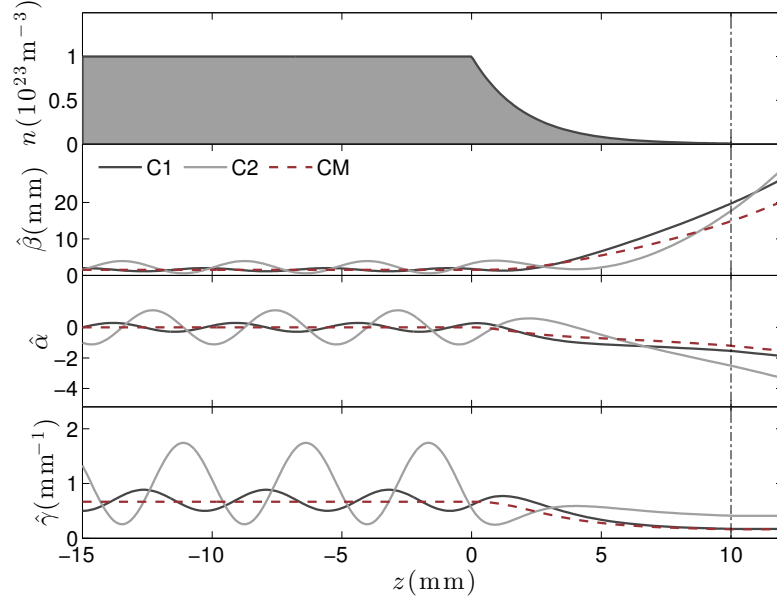


Figure 25: Exponential plasma-vacuum density transition according to eq. (6.2) with  $L = 2.0$  mm for three sets of initial conditions, C1, C2 and CM. The values of the Courant-Snyder parameters of the matched beam (CM) at the exit position  $z_e = 10.0$  mm are given by  $\hat{\beta}_{CM,e} = 15.0$  mm,  $\hat{\alpha}_{CM,e} = -1.21$  and  $\hat{\gamma}_{CM,e} = 0.165$  mm $^{-1}$ .

Three beams with different initial conditions at position  $z_0 = -15.0$  mm are studied. One beam (CM) is matched to the plasma plateau with  $\hat{\beta}_{CM,0} = \hat{\beta}_m = 1.5$  mm and  $\hat{\alpha}_{CM,0} = 0$  ( $\hat{\gamma}_{CM,0} = 0.667$  mm $^{-1}$ ). A second beam (C1) has a mismatched beta function  $\hat{\beta}_{C1,0} = 2.0$  mm and  $\hat{\alpha}_{C1,0} = 0$ , and a third beam (C2) has matched beta function with  $\hat{\beta}_{C2,0} = \hat{\beta}_m = 1.5$  mm but mismatched alpha function  $\hat{\alpha}_{C2,0} = -1.0$ .

Figures 24, 25, 26, and 28 depict the evolution of the Courant-Snyder parameters of these beams in exponential plasma-vacuum density transitions with varying characteristic decay lengths  $L$ . The uppermost part of the graphs shows the plasma density profile with the dash-dotted line indicating the exit position  $z_e$ . Below, the evolution of the Courant-Snyder beta, alpha and gamma functions are shown. During propagation in the plateau region of the plasma, the betatron functions of the cases C1 and C2 show the oscillations expected for unmatched beams in a constant focusing channel and described by equation (1.193). The matched beam envelope (CM), on the contrary, does not oscillate.

Figure 24 illustrates the evolution of the transverse beam parameters in a transition with characteristic decay length  $L = 0.5$  mm. This transition length is shorter than the local betatron functions of the three cases and acts on the beams as a sharp plasma-vacuum interface. The beam-divergence in this transition is only slightly reduced in the matched case with an initial gamma function of  $\hat{\gamma}_{CM,0} = 0.667$  mm $^{-1}$



and with  $\hat{\gamma}_{CM,e} = 0.601 \text{ mm}^{-1}$  at the exit position at  $z_e = 2.5 \text{ mm}$ . This results in a divergence mitigation by a factor of  $\eta = 1.11$ . The evolution of the alpha function also shows that the beam is not transported at waist until the exit position. It can also be seen from the evolution of the mismatched cases C1 and C2, that the Courant-Snyder parameters at the exit position are highly dependent on the local phase of the betatron oscillation at the onset of the plasma-vacuum transition.

*A transport at waist would imply a constant  $\alpha = 0$ .*

When applying a density transition with length  $L = 2 \text{ mm}$ , comparable to the local betatron wavelength, a significant damping of the divergence can be observed (see Figure 25). The gamma function at the exit in the matched case is damped to a value  $\hat{\gamma}_{CM,e} = 0.154 \text{ mm}^{-1}$ , which is significantly lower than the initial value  $\hat{\gamma}_{CM,0}$  and implies a divergence mitigation by a factor of  $\eta = 4.03$ . However, the beam expansion in this decay does not occur adiabatically, as indicated by the significant deviation of the alpha function from zero in the matched beam case.

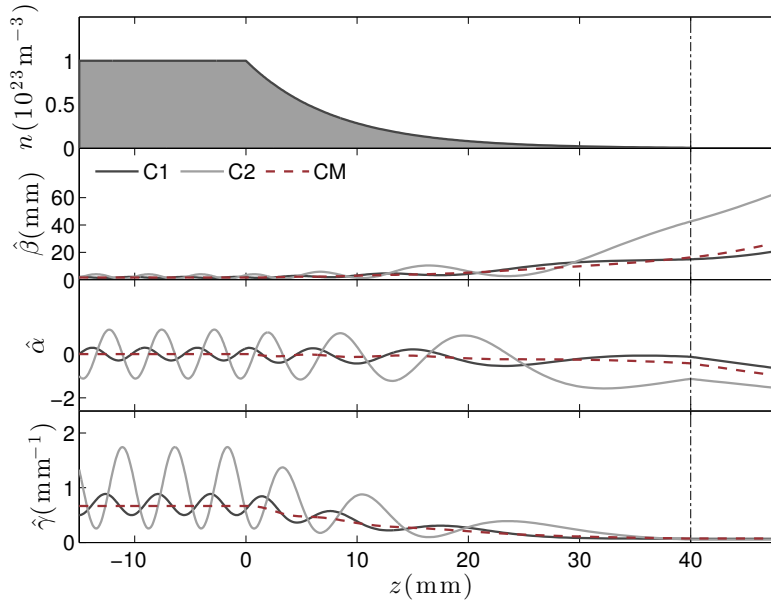


Figure 26: Exponential plasma-vacuum density transition according to eq. (6.2) with  $L = 8.0 \text{ mm}$  for three sets of initial conditions, C1, C2 and CM. The values of the Courant-Snyder parameters of the matched beam (CM) at the exit position  $z_e = 40.0 \text{ mm}$  are given by  $\hat{\beta}_{CM,e} = 16.2 \text{ mm}$ ,  $\hat{\alpha}_{CM,e} = -0.42$  and  $\hat{\gamma}_{CM,e} = 0.072 \text{ mm}^{-1}$ .

A density decay length of  $L = 8.0 \text{ mm}$ , depicted in Figure 26, exhibits a significant reduction of the betatron frequency. The divergence at the exit position, here  $z_e = 40.0 \text{ mm}$ , is reduced to a value of  $\hat{\gamma}_{CM,e} = 0.072 \text{ mm}^{-1}$  in the matched case, indicating a reduction of the divergence by a factor of  $\eta = 9.26$  to almost one order of magnitude lower than the initial value. The alpha function at the exit is  $\hat{\alpha}_{CM,e} = -0.42$ . The beam is transported close to waist until the exit.

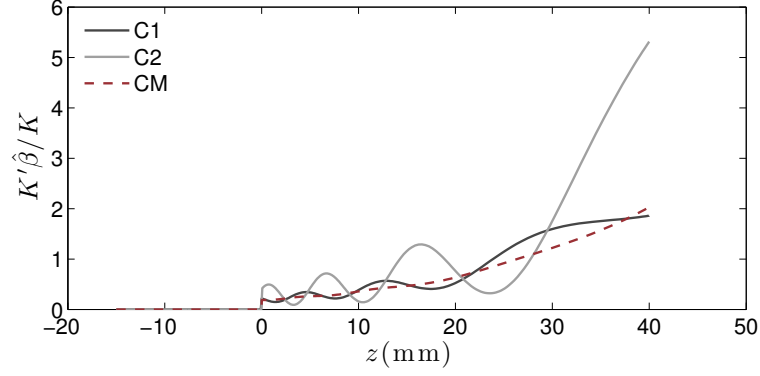


Figure 27: Adiabaticity for exponential plasma-vacuum density transition according to eq. (6.2) with  $L = 8.0$  mm.

In order to quantify if the transition occurred adiabatically, the quantity  $K'\hat{\beta}/K$ , expressing the adiabaticity is introduced and examined. If the adiabaticity is much smaller than one,  $K'\hat{\beta}/K \ll 1$  the transition occurs fully adiabatic. On the contrary, if  $K'\hat{\beta}/K \gtrsim 1$ , the transition does not act adiabatically on the beam evolution. The adiabaticity for the three cases C1, C2 and CM, for  $L = 8.0$  mm is depicted in Figure 27. It can be seen that the transition initially is adiabatic but becomes non-adiabatic towards the exit of the plasma cell.

The longest transition length regarded here is  $L = 32.0$  mm in Figure 28. This transition transports the matched beam at waist almost until the exit of the plasma target with  $\hat{\alpha}_{CM,e} = -0.15$  for the matched case. The divergence is damped by more than one order of magnitude compared to the initial divergence with a gamma function at the exit of  $\hat{\gamma}_{CM,e} = 0.057 \text{ mm}^{-1}$  for the matched case. The divergence is thus reduced by a factor of  $\eta = 11.70$ . Figure 29 shows the adiabaticity for this transition. Although the transition is fully adiabatic for all beams at the beginning of the decay, the adiabaticity approaches unity towards the end of the density taper. However, the transition exhibits a significant quasi-adiabatic reduction of the divergence. The exit beam parameters are less sensitive on the local betatron phase at the start of the density transition than for the shorter transitions, but depend on the local phase at the exit. The curves of the Courant-Snyder parameters for the matched case in Figure 28 indicate that the beam stays matched and the final parameters at the exit only depend on the plasma density value at the exit. This comes from the quasi-adiabaticity of the transition.

Figure 30 shows the ratio of the initial divergence over final divergence  $\eta = \hat{\gamma}_0/\hat{\gamma}_e$  of the matched case (CM) for different transition lengths  $L$ . For a fully adiabatic transition, the beam stays at waist and stays matched during the full transition. This means that the final divergence is given only by the final plasma density. The ratio  $\eta$  for such a fully adiabatic transition is indicated in Figure 30 by the dashed line.

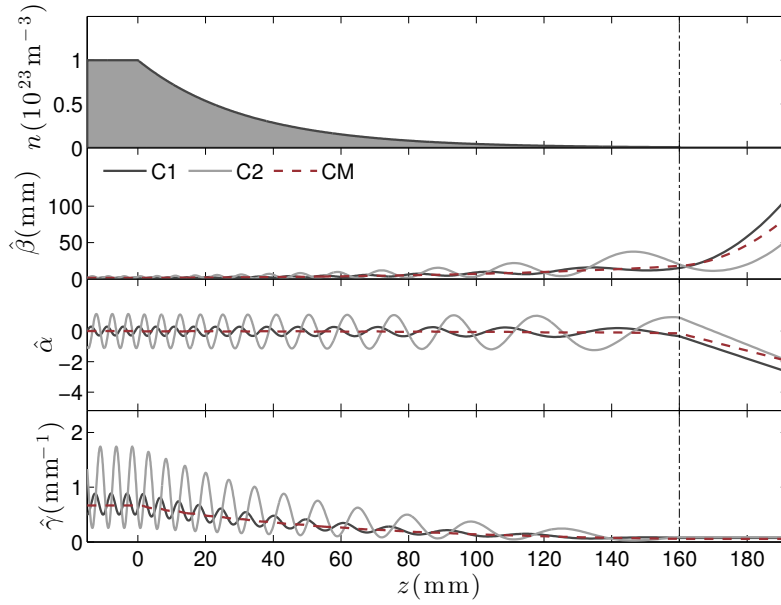


Figure 28: Exponential plasma-vacuum density transition according to eq. (6.2) with  $L = 32.0$  mm for three sets of initial conditions, C1, C2 and CM. The values of the Courant-Snyder parameters of the matched beam (CM) at the exit position  $z_e = 160.0$  mm are given by  $\hat{\beta}_{CM,e} = 18.1$  mm,  $\hat{\alpha}_{CM,e} = -0.15$  and  $\hat{\gamma}_{CM,e} = 0.057$  mm $^{-1}$ .

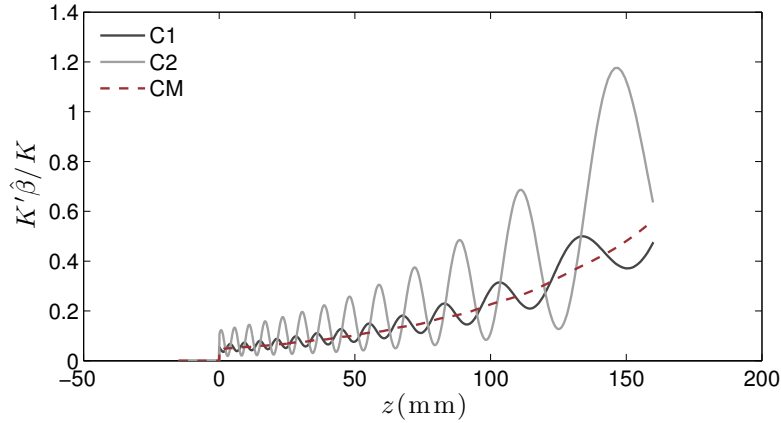


Figure 29: Adiabaticity for exponential plasma-vacuum density transition according to eq. (6.2) with  $L = 32.0$  mm.

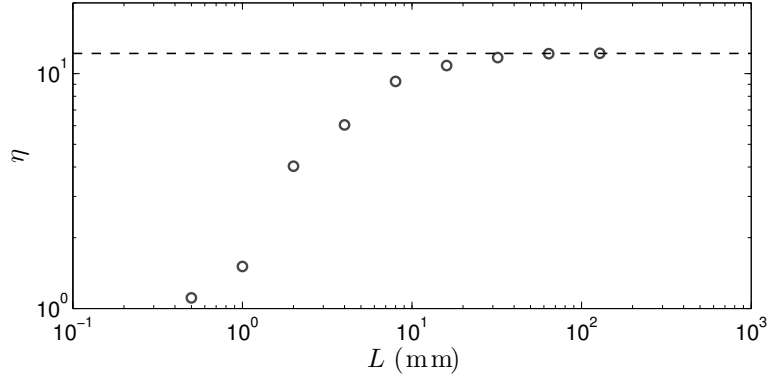


Figure 30: Ratio of initial divergence over final divergence  $\eta = \hat{\gamma}_0/\hat{\gamma}_e$  of the matched case (CM) for different transition lengths  $L$ . The dashed line indicates the divergence ratio for a beam which is transported at waist until the exit.

It can be seen that the divergence ratio approaches the fully adiabatic case for longer transition lengths and that the final gamma function of an initially matched beam is given only by the density at the exit position for fully adiabatic transitions.

### 6.2.2 Summary and conclusion

To conclude, the divergence and the betatron frequency of beams in ideal systems are significantly damped by plasma density transitions which are comparable to or longer than the local betatron oscillations. For short density transitions  $L \lesssim \hat{\beta}$ , the damping depends on the local phase of the betatron oscillations of the beams at the transition. If the betatron phase is well known and defined, this might be used to reduce the divergence. Longer transitions transport matched beams adiabatically near to or at waist and are less sensitive to the local phase of the oscillation at the onset of the density taper. This implies that the final beam parameters are expected to be less sensitive on fluctuations of the betatron phase when long transitions are used. For matched beams and fully adiabatic transitions, the final gamma function only depends on the plasma density at the exit (or on the density at positions after which the density drops off on length scales quicker than the local betatron function). The evolution of the adiabaticity in long transitions indicates that density tapers with a more gently decaying functional dependence than an exponential dependence may be more appropriate for fully adiabatic beam extraction.

### 6.3 DENSITY TAPERED EXTRACTION IN PWFA

#### 6.3.1 Introduction

Despite tremendous improvements in the last decade, electron beams produced in plasma-based accelerators still exhibit relative energy spreads in the percent range [Faure et al., 2004; Geddes et al., 2004; Mangles et al., 2004; Rechatin et al., 2009, 2010]. Conventional FELs usually require relative energy spreads in the per mil range. For this reason, concepts which allow for FEL-gain from beams generated in plasma-based accelerators have been proposed [Huang et al., 2012; Maier et al., 2012; Seggebrock et al., 2013].

Another challenging aspect of beams with significant energy spread as produced in plasma-based accelerators is the quality preserving transport from the plasma-target to the interaction region (e.g. an undulator). It has been pointed out by Floettmann [2003, 2014] that highly divergent beams with significant energy spread experience an increase of the emittance during the extraction and transport to some interaction region. While the trace-space emittance of the beams stays constant during the free drift downstream of the plasma target, the phase-space emittance increases in the drift. At the first divergence compensating optic, e.g. the first quadropole magnet, the trace-space emittance grows up to the value of the phase-space emittance [Floettmann, 2003]. The mitigation of the divergence by use of a slowly decaying  $K$ -parameter according to a particular functional dependence has been studied analytically and the growth of the phase-space emittance of beams with energy spread in the drifts downstream of such transitions has been studied numerically [Floettmann, 2014].

The following study investigates the extraction of beams in realistic plasma density profiles with realistic beam phase space distributions. Since the transport of beams with energy spread cannot be represented by an ideal system, the emittance may not be preserved and equation (6.1) does not apply. The numerical method used here is therefore the quasi-static PIC code HiPACE (see chapter 3) which takes into account the full dynamics of the driver and witness beam during their propagation in the plasma.

#### 6.3.2 Physical scenario

The following physical scenario is considered for the present study. A highly relativistic electron beam with an energy of 1 GeV, density of  $n_{db}/n_0 = 3.0$  and transverse dimensions of  $k_p\sigma_x = k_p\sigma_y = 0.7$ ,  $k_p\sigma_z = 1.0$  is focused into a plasma with density  $n_0 = 10^{17} \text{ cm}^{-3}$  and drives a plasma wave in the blowout regime. A witness beam with an energy of 1 GeV, initial relative energy spread of 0.5%, density of

$n_{wb}/n_0 = 15.0$  and size  $k_p\sigma_x = k_p\sigma_y = 0.05$ ,  $k_p\sigma_z = 0.2$  propagates with a well defined offset behind the driver in an accelerating phase of the plasma wave (see B.4). It is accelerated in a flat-top plasma target over 34 mm.

Subsequently, the beams are propagated through exponential plasma vacuum transitions with varying characteristic decay lengths  $L$  where the plasma density is given by

$$n(z) = \begin{cases} n_0 & \text{for } z < 0, \\ n_0 \exp(-z/L) & \text{for } 0 < z < z_e, \\ 0 & \text{for } z > z_e. \end{cases} \quad (6.4)$$

The plasma wavelength increases in this transition and the transverse field amplitudes decay. Beam particles with high transverse momentum may escape the focusing channel if the transition occurs on time scales shorter than the inverse particles betatron frequency. For the driver beam, which typically develops a large energy spread on the order of 10%, the individual electron betatron frequencies vary accordingly. This implies that a fraction of beam particles can escape during short transitions, thus changing the total beam charge and eventually the amplitude of the plasma wave. However, the focus of this study lies on the dynamics of the witness beam in the plasma-vacuum transition, which is expanded in the density transition while the divergence is damped. The plasma wavelength increases in the decaying density profile, and the witness beam is eventually located in a decelerating phase of the plasma wave.

The plasma-vacuum transition ends at position  $z_e$ , which constitutes the exit position of the plasma target. The Courant-Snyder beam parameters in the free drift evolve according to equation (1.192), where the trace-space emittance stays constant. The normalized trace-space emittance equals the normalized phase-space emittance, if the beam is at waist. However, during the beam-expansion in the free drift, the phase-space emittance is generally not constant, but evolves according to [Floettmann, 2003]

$$\epsilon_n^2 = \frac{1}{m^2 c^2} \left[ \left( \langle x'^2 \rangle_e \langle p_x^2 \rangle_e - \langle x' p_x \rangle_e^2 \right) (z - z_e)^2 + \left( \langle x x' \rangle_e \langle p_x^2 \rangle_e - \langle x p_x \rangle_e \langle x' p_x \rangle_e \right) 2(z - z_e) + \left( \langle x^2 \rangle_e \langle p_x^2 \rangle_e - \langle x p_x \rangle_e^2 \right) \right], \quad (6.5)$$

where  $\langle \Phi \rangle_e$  is the beam moment of the quantity  $\Phi$  at the exit position  $z_e$  and where  $\langle x \rangle_e = \langle p_x \rangle_e = \langle x' \rangle_e = 0$  was assumed. Equation

(6.5) implies that the phase-space emittance in the drift section is only constant, if

$$\langle x' p_x \rangle_e^2 = \langle x'^2 \rangle_e \langle p_x^2 \rangle_e \quad (6.6)$$

and

$$\langle x p_x \rangle_e \langle x' p_x \rangle_e = \langle x x' \rangle_e \langle p_x^2 \rangle_e . \quad (6.7)$$

Both identities hold, if the beam is monoenergetic, or, to be more precise, if all beam particles have the same longitudinal momentum. However, if the beam has a significant energy spread, equations (6.6) and (6.7) are not true and a correlation between energy and transverse position is generated during the vacuum propagation according to the motion of the individual particles  $x = x_e + x'_e \cdot (z - z_e)$  [Floettmann, 2003].

The relative growth of the phase space emittance in the free drift  $\delta_e$  has the following asymptotic dependence

$$\delta_e = \frac{\epsilon_n}{\epsilon_{n,e}} - 1 \simeq \frac{\kappa_e}{\epsilon_{n,e}} (z - z_e), \quad (6.8)$$

where

$$\kappa_e = \frac{\sqrt{\langle x'^2 \rangle_e \langle p_x^2 \rangle_e - \langle x' p_x \rangle_e^2}}{mc}. \quad (6.9)$$

A combination of a great divergence and large energy spread is reflected in the difference of the moments in this factor. When the beam is captured and transported by focusing optics, the beam is at waist again, which implies that the trace-space emittance grows up to the value of the phase-space emittance [Floettmann, 2003]. Equation (6.5) therefore allows for an estimation for the emittance growth for a given beam phase-space distribution after a certain propagation distance to the next divergence compensating element, e.g. the next quadrupole magnet. This emittance growth is theoretically reversible since it does not increase the volume of the occupied phase space, but only its shape [O'Shea, 1998; Floettmann, 2003].

### 6.3.3 Numerical studies with PIC simulations

The above described scenario is now examined by means of 3D PIC simulations with the code HiPACE. Driver and witness beam are propagated through the flattop plasma profile and the witness beam reaches an energy of 2.5 GeV with an energy spread of 7.7% immediately upstream of plasma-vacuum transition. It increases from the uncorrelated 0.5% energy spread due to the dependence of the longitudinal field on the co-moving position. The longitudinal phase-space distribution of the driver and witness beam at the onset of the plasma-vacuum transition, at  $z = 0.0$  mm, is depicted in Figure 35. The transverse phase space information prior to the density transition is shown

*Detailed information about the simulation setup and more results can be found in B.4.*

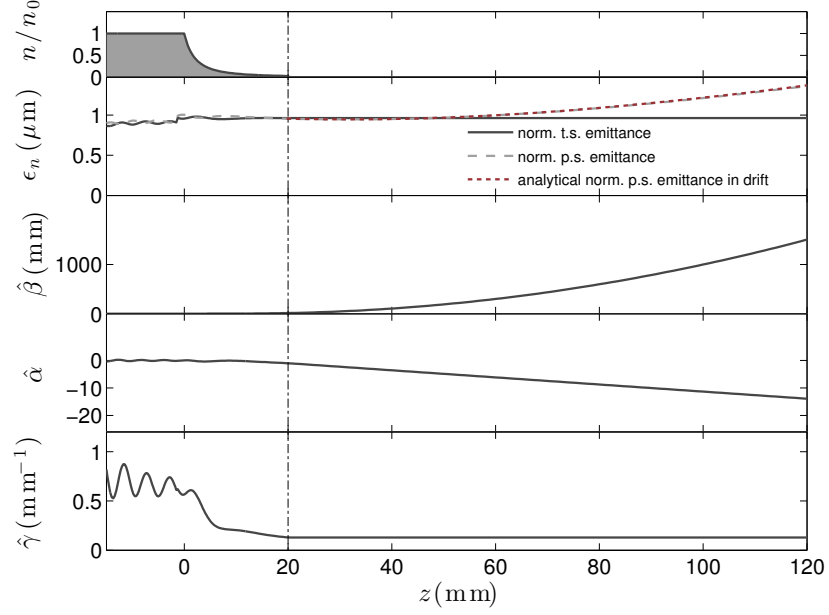


Figure 31: Evolution of the transverse beam properties in an exponential plasma-vacuum transition with length  $L = 4.0$  mm as simulated in a PIC simulation with HiPACE. The Courant-Snyder parameters at the exit position  $z_e = 20.0$  mm are  $\hat{\beta}_e = 14.87$  mm,  $\hat{\alpha}_e = -0.948$  and  $\hat{\gamma}_e = 0.128$  mm $^{-1}$ .

in B.4. Exponential plasma-vacuum transitions with lengths  $L$  of 0.5 mm, 1 mm, 2 mm, 4 mm and 8 mm are regarded in the following. The Courant-Snyder parameters immediately upstream of the density transitions are identical in all simulations with  $\hat{\beta}_0 = 1.64$  mm,  $\hat{\alpha}_0 = -0.006$  and  $\hat{\gamma}_0 = 0.609$  mm $^{-1}$ .

Figure 31 depicts the example of a density transition with  $L = 4$  mm and the evolution of some relevant beam parameters in this transition. Shown are the density profile along the beam propagation axis from  $z = -1.5$  mm to the vacuum, where position  $z_0 = 0$  defines the start of the density transition and the dash-dotted line indicates the end of the transition and the start of the vacuum drift. Below, the normalized trace-space emittance (solid dark gray) and the normalized phase-space emittance (dashed light gray) as retrieved from the PIC simulations in one plane are shown. These curves are accompanied with the analytic prediction according to equation (6.5) for the evolution of the phase-space emittance in the free drift, given the phase space distribution in the simulation at the exit position  $z_e$  (dashed red). The three bottom plots show the evolution of the Courant-Snyder beta-function, alpha-function and gamma-function in one plane in the density transition as calculated in the PIC simulations.

It can be seen from the  $\hat{\gamma}$ -curve that the beam performs betatron oscillations during the acceleration which are adiabatically damped



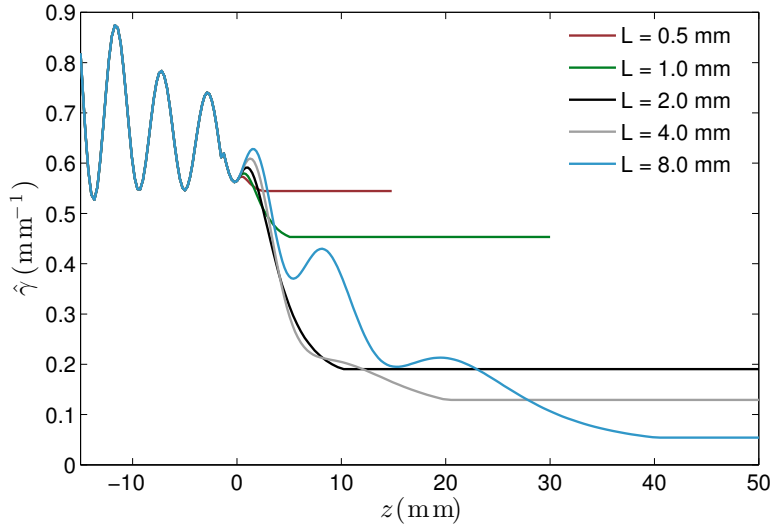


Figure 32: Evolution of  $\hat{\gamma}$  of the witness beam during the acceleration, propagation through the transitions with varying decay lengths  $L$  and free drift in the vacuum, retrieved from PIC simulations.

due to the energy gain of the particles. The alpha function oscillates around zero with small amplitude i.e. the beam is close to the waist. The gamma-function in the plasma channel has a high value compared to values used in conventional accelerators and the beta-function is accordingly small. The curves of the normalized phase-space and trace-space emittance are close with respect to each other and approximately constant during the propagation in the plasma target.

During the transition to vacuum, the gamma function is damped to a lower value while the phase-space and trace-space emittance stay approximately constant. The significant mitigation of the divergence is owed to the transition length  $L = 4$  mm in this case being longer than the betatron function prior to the transition  $\hat{\beta}_0 = 1.64$  mm. The betatron function expands in the transition and subsequently follows the known free drift dependence. The alpha function decreases in the transition, indicating that the beam is not transported at waist in the taper region, and subsequently decreases linearly. Important to note are the emittance curves, depicted in the second plot from the top. It can be seen that the trace-space emittance stays constant in the vacuum drift while the analytical and numerical curves of the phase-space emittance increase in the vacuum section during the beam expansion. Moreover, the analytical curve, calculated from equation (6.5), is close to the curve retrieved from the PIC simulation and can hence serve as a basis for analytical predictions on the emittance growth.

The energy spread is not significantly changed in the here considered density transitions. Thus, the emittance generating terms in

equation (6.5) can only be reduced by a reduction of the divergence. Figure 32 shows the evolution of  $\hat{\gamma}$  of the witness beam during the acceleration, propagation through the transitions with varying decay lengths  $L$  and free drift in the vacuum. The behavior is in qualitative agreement with the findings in 6.2. Transitions shorter than the local betatron wavelength reduce the divergence only slightly, depending on the local betatron phase, whereas transitions longer than the betatron wavelength significantly reduce the divergence. This is quantitatively shown in Table 1, where the values of  $\hat{\gamma}_e$  and  $\kappa_e$  at the exit positions for the different decay lengths  $L$  are given. The emittance generating term  $\kappa_e$  is reduced by more than one order of magnitude in longer transitions.

Using equation (6.5), the performed simulations allow for a quantitative prediction of the emittance growth during the extraction, depending on the distance to the first divergence compensating element  $d_{\text{quad}} = z_{\text{quad}} - z_e$  and depending on the decay length  $L$ . Such a quantitative prediction is depicted in Figure 33. It can be seen that the emittance growth can be greater than one order of magnitude for a transition length shorter than the betatron wavelength and for meter scale distances to the first focusing optic. On the contrary, the emittance growth is in the percent range only, if transition lengths much longer than the betatron function and centimeter distances to the first focusing element are used. This implies that longer taper lengths and shorter distances to the first focusing element in combination are crucial for a mitigation of the emittance growth during the beam extraction.

Moreover, the emittance growth predicted by equations (6.5) and (6.8) is investigated and compared in Figure 34. The solid curves show the emittance growth  $\delta_e$  according to the analytical prediction (6.5) and the dashed lines show the expected asymptotic linear behavior according to (6.8). The Figure suggests that the asymptotic linear behavior with slope  $\kappa_e$  is dominating the emittance growth. The reduction of the parameter  $\kappa_e$  in long density decays (see Table 1) is therefore one vital aspect of the emittance preservation in plasma-to-vacuum transitions. In addition, the dependence of the phase space emittance on the distance from the exit is asymptotically linear. This indicates the importance of placing the capturing lattice as near as

Table 1: Values of  $\hat{\gamma}_e$  and  $\kappa_e$  at the exit for different decay lengths  $L$ .

$L$ (mm)	0.5	1.0	2.0	4.0	8.0
$\hat{\gamma}_e$ (1/mm)	0.546	0.457	0.194	0.135	0.057
$\kappa_e \times 10^6$	47.3	40.6	12.7	11.2	3.83

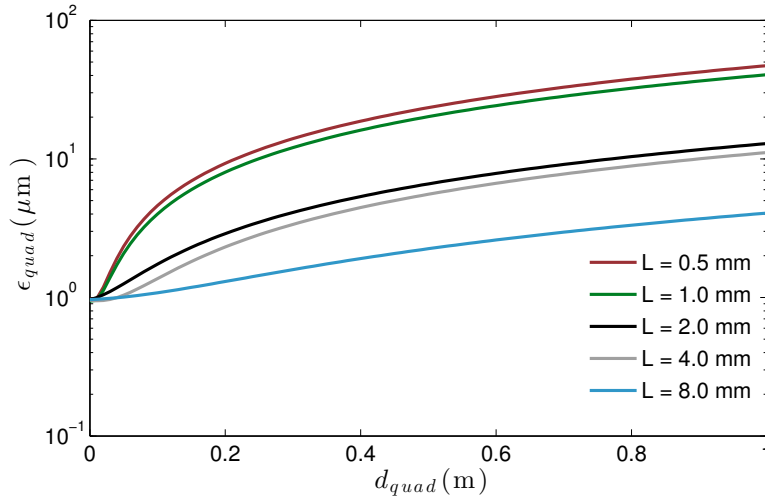


Figure 33: Analytical prediction for the emittance evolution according to equation (6.5), based on data from PIC simulations at various quadrupole positions for different transition lengths. Shown are the absolute values of the normalized phase-space emittance  $\epsilon_{n,quad}$  at the position of the focusing optic  $d_{quad}$  for different  $L$ .

possible to the exit of the plasma target. in order to preserve the emittance during the extraction process.

#### 6.3.4 Conclusion

Particle-in-cell simulations for the investigation of the dynamics of plasma accelerated beams in plasma-vacuum transitions of various lengths, have been performed in a 3D geometry, and were analyzed.

The results show a more significant divergence reduction for longer decay lengths and a betatron phase dependence of the divergence reduction for decay length shorter than or comparable to the betatron length. This is in qualitative agreement with the study of the dynamics of mono-energetic beams in plasma-to-vacuum transitions in ideal systems in 6.2. Hence, the length of transitions plays a major role for the beam expansion and divergence mitigation.

Moreover, quantitative investigations on the emittance growth of plasma accelerated beams with significant energy spread during the extraction have been presented. These predictions are possible through a modeling of realistic beam dynamics in a plasma-based accelerators, hence reproducing characteristic transverse phase space distributions of plasma-accelerated beams and their evolution in various plasma-to-vacuum transitions.

The present analysis shows an order of magnitude emittance growth for typical beams from plasma accelerators if the plasma-to-vacuum interface is shorter than the betatron function and if the first focusing optic is far compared to  $\epsilon_{n,e}/\kappa_e$  from the plasma cell. However,

*Divergence reduction is also vital to alleviate beam lengthening during the extraction [Khachatryan et al., 2007, IV].*

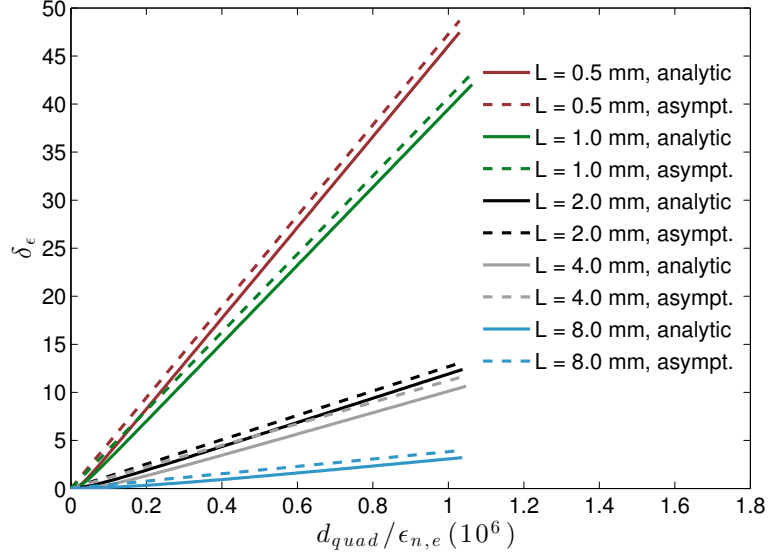


Figure 34: Analytical prediction for the emittance growth  $\delta_\epsilon$  according to equation (6.5) (solid curves), and equation (6.8) (dashed lines) for the various taper lengths  $L$ . The emittance growth  $\delta_\epsilon$  is plotted against the distance to the quadrupole, normalized to the phase space emittance  $d_{quad}/(\epsilon_{n,e} \times 10^6)$ .

it is also indicated that the combination of plasma-to-vacuum transitions longer than the betatron wavelength and the placement of the divergence compensating quadrupole near to the plasma cell allow for an emittance preservation up to a percent level. It should be noted that this requires permanent quadrupole magnets which typically have small diameters but can achieve comparably large magnetic field gradients ( $K \sim 100$  T/m, see e.g. [Mihara et al., 2006]). The minimum possible distance from the exit of the plasma target to the quadrupole  $d_{quad}$  is thereby limited by the technically achievable magnetic field gradient, in combination with the transverse beam size at the quadrupole.

Compare equation (1.184) or (1.186).

In conclusion, while most numerical studies on plasma-based accelerators so far analyzed the beam properties within the plasma and neglected the effects of plasma-vacuum transition and beam transport to the interaction region, this study sheds light on the importance of such considerations. The design of density tapered plasma-to-vacuum transitions, longer than the betatron wavelength in combination with the placement of permanent quadrupoles near to the plasma exit, can prove to be an indispensable method for the emittance preserving extraction of beams with energy spread from plasma-based accelerators.

## SUMMARY, CONCLUSION AND OUTLOOK

---

The following summarizes and concludes the physical studies and presents an outlook for anticipated progress on beam-quality preservation in plasma-based accelerators.

### SUMMARY

In chapter 4, the general conditions for matching, that is the conditions for a non-oscillating beam envelope, are derived for plasma-based acceleration in the linear regime and in the blowout regime. Matching requires a beam at waist ( $\hat{\alpha} = 0$ ) and a betatron function of the beam at a specific value ( $\hat{\beta} = \hat{\beta}_m$ ). The matched betatron function in the linear regime is a function of the beam energy, the phase-position in the plasma wave, the driver amplitude and transverse driver distribution. In the blowout regime, the matched betatron function is defined only by the beam energy and the ambient plasma density. The betatron function in the blowout regime is smaller than the betatron function in the linear regime and constitutes the lowest bound for a given beam energy. Values of the betatron function for plasma densities of  $n_0 \sim 10^{23} \text{ m}^{-3}$  and  $\sim 1 \text{ GeV}$  - scale beams are on the order  $\hat{\beta}_m \sim 1 \text{ mm}$ . Such small magnitudes of the betatron function pose a technical challenge, if attempted to be coupled with conventional beam optics.

Chapter 5 explores the emittance evolution of electron-beams which are accelerated in staged LWFA schemes in the linear regime in accordance with current plasma-based collider concepts (as proposed e.g. by Schroeder et al. [2010]). In order to achieve the minimum overall accelerator length, the drift sections between the stages are designed as short as possible and are given by the minimum laser coupling distance. The study presented in chapter 5 shows by means of an analytic theory and PIC simulations that the projected transverse emittance grows significantly in a single stage owed to differential phase space rotation and decoherence of the betatron oscillations, if the electron beam is not matched into the wakefields. The analytic theory is used to investigate what impact this effect has on beams which are ejected from one plasma module and injected into a subsequent module in staged LWFA with no electron beam optics in between the modules. The result shows order-of-magnitude per-stage emittance growth for currently proposed setups and parameters in staged LWFA. This finding indicates the necessity for the design of novel techniques for the external beam injection into plasma modules, for the transport in plasma accelerators and for the extraction from the modules.

Such a novel extraction method for PWFA is investigated in chapter 6. It is firstly shown that the density tapered plasma-to-vacuum extraction has the capability of reducing the beam divergence significantly if the transition length is longer than the local betatron wavelength. If the transition is shorter than the betatron wavelength, the divergence reduction is less substantial and sensitive on the local betatron phase. A large divergence and a significant energy spread at the plasma exit in combination can lead to a great phase-space emittance growth in the subsequent free drift, and the trace-space emittance matches up with the phase-space emittance in the transport lattice [Floettmann, 2003]. The mitigation of this effect by use of density tapered plasma roll-offs was studied by means of PIC simulations with the code HiPACE. The results suggest that an emittance preserving transport from the plasma cell is possible, if suitable (long) density tapered plasma-to-vacuum transitions are used in combination with a transport lattice starting with (permanent) quadrupole magnets which are placed near to the exit of the plasma target.

#### CONCLUSION

Studies in this work revealed challenges for the design and realization of staged plasma-based accelerators. Beams must be matched into the plasma-stages in order to prevent severe emittance deterioration. When based on today's technology, such matching sections would be significantly longer than the plasma modules and would therefore impede the realization of compact future accelerators based on plasma. Hence, novel methods for the compact matched injection and extraction of electron-beams into and from plasma modules have to be developed and mastered before staged plasma acceleration with a short overall acceleration distance can be achieved.

A novel method, investigated in this work, uses tapered plasma-to-vacuum transitions to facilitate the compact and quality preserving extraction of beams from plasma accelerators. It may be inferred that such methods are indispensable whenever beams are to be captured from a plasma cell and transported in a conventional optical lattice. The reason for this is the limited magnetic field gradient of the first quadrupole magnets, which gives a lower bound for the distance at which it can be placed downstream to the plasma exit. Only the combination of a divergence mitigation in the plasma, e.g. by means of density tapering and a focusing optic near to the exit of the plasma cell can guarantee for an emittance preserving extraction of beams. This is of fundamental importance to the field of plasma-based acceleration since such an extraction must be harnessed whenever plasma cells are staged or when beams are to be transported to some interaction region e.g. for the application of the produced beams (e.g. in colliders or FELs).

## OUTLOOK

The progress in the field of plasma-based acceleration in the past decades was occurring on a stunning speed. Since the first experimental demonstrations of LWFA in the mid 1990's [Modena et al., 1995] (about 16 years after the proposal by Tajima and Dawson [1979]), many experimental milestones followed, such as the generation of electron-beams with a narrow spectrum [Faure et al., 2004; Geddes et al., 2004; Mangles et al., 2004], improved stability [Osterhoff et al., 2008; Vargas et al., 2014], increased energy [Leemans et al., 2006; Kim et al., 2013; Wang et al., 2013], or enhanced tunability [Faure et al., 2006; Gonsalves et al., 2011]. Electrons in PWFA were accelerated by 40 GeV in a distance shorter than a meter [Blumenfeld et al., 2007].

This accelerated experimental development was rendered possible by an improved theoretical understanding of the relevant processes in the plasma. Current theoretical and numerical studies reveal the future experimental challenges but also offer solutions. The findings of studies, such as performed in this work, allow for an outlook into future development in experimental plasma accelerator research. If today's theoretical investigations find ways to master the quality preserving compact beam transport, there can be increasing confidence that tomorrow's experiments will do as well.

Taking the rapid experimental and technical development in the recent decade and the current theoretical progress as a basis and regarding the ever growing interest in the exciting field of plasma-based accelerators, it may be anticipated that a combined scientific effort will push the quality, stability, tunability and energy of beams from plasma-accelerators further in the next decades to eventually achieve stable and high-quality  $> 10$  GeV - scale beams which are suitable for the application in FELs or even in particle colliders.





Part IV

APPENDIX



## CALCULATIONS AND DERIVATIONS

---

### A.1 DERIVATION OF FLUID MOMENTUM EQUATION

#### A.1.1 Momentum-divergence of Lorentz force

This paragraph proves the identity of  $\mathbf{F} \cdot \nabla_{\mathbf{p}} f = \nabla_{\mathbf{p}} \cdot (\mathbf{F}f)$ , where  $\mathbf{F}$  is the Lorentz force

$$\mathbf{F} = q \left( \mathbf{E}(\mathbf{r}, t) + \frac{\mathbf{p}}{\gamma mc} \times \mathbf{B}(\mathbf{r}, t) \right). \quad (\text{A.1})$$

It can be quickly seen that

$$\nabla_{\mathbf{p}} \cdot (\mathbf{F}f) = \mathbf{F} \cdot \nabla_{\mathbf{p}} f + f \nabla_{\mathbf{p}} \cdot \mathbf{F}. \quad (\text{A.2})$$

The following shows that the Lorentz force is momentum-divergence free.

$$\begin{aligned} \nabla_{\mathbf{p}} \cdot \mathbf{F} &= q \nabla_{\mathbf{p}} \cdot \left( \frac{\mathbf{p}}{\gamma mc} \times \mathbf{B} \right), \\ &= \frac{q}{mc} \left( (\mathbf{p} \times \mathbf{B}) \cdot \nabla_{\mathbf{p}} \gamma^{-1} \right), \\ &= \frac{q}{(\gamma mc)^3} \left( (\mathbf{p} \times \mathbf{B}) \cdot \mathbf{p} \right), \\ &= 0. \end{aligned} \quad (\text{A.3})$$

Hence, the identity

$$\nabla_{\mathbf{p}} \cdot (\mathbf{F}f) = \mathbf{F} \cdot \nabla_{\mathbf{p}} f, \quad (\text{A.4})$$

is obtained.

#### A.1.2 Derivation of fluid momentum equation

The following outlines the derivation of the fluid momentum equation starting from the Vlasov equation (1.89),

$$\frac{\partial f_s}{\partial t} + \mathbf{v}^\top \nabla_{\mathbf{r}} f_s + \mathbf{F}^\top \nabla_{\mathbf{p}} f_s = 0, \quad (\text{A.5})$$

where  $\mathbf{F}$  represents the Lorentz force term and  $\mathbf{a}^\top \mathbf{b} \equiv \mathbf{a} \cdot \mathbf{b}$  is the inner product of two vectors  $\mathbf{a}$  and  $\mathbf{b}$ . Multiplication with  $\mathbf{p}$  from the left yields

$$\underbrace{\mathbf{p} \frac{\partial f_s}{\partial t}}_{T_1} + \underbrace{\mathbf{p} \mathbf{v}^\top \nabla_{\mathbf{r}} f_s}_{T_2} + \underbrace{\mathbf{p} \mathbf{F}^\top \nabla_{\mathbf{p}} f_s}_{T_3} = 0, \quad (\text{A.6})$$

The integration of the three terms over momentum space can now be evaluated individually. Integration of term  $T_1$  simply yields

$$\int d\mathbf{p} T_1 = \frac{\partial}{\partial t} (n_s \mathbf{p}_s). \quad (\text{A.7})$$

Before integration, the term  $T_2$  is transposed twice to obtain

$$\begin{aligned} T_2 &= [(\mathbf{p} \mathbf{v}^\top \nabla_{\mathbf{r}} f_s)^\top]^\top, \\ &= [(\mathbf{p} \mathbf{v}^\top \nabla_{\mathbf{r}})^\top f_s]^\top, \\ &= [\nabla_{\mathbf{r}}^\top \mathbf{v} \mathbf{p}^\top f_s]^\top. \end{aligned} \quad (\text{A.8})$$

This is possible, since  $\nabla_{\mathbf{r}}$  does not operate on  $\mathbf{v}$  or  $\mathbf{p}$ . Integration over momentum space yields

$$\int d\mathbf{p} T_2 = \left[ \nabla_{\mathbf{r}} \cdot \left( \int d\mathbf{p} (\mathbf{v} \mathbf{p}^\top f_s) \right) \right]^\top. \quad (\text{A.9})$$

The term  $\mathbf{v} \mathbf{p}^\top$  is an outer product and the result is a  $3 \times 3$  matrix. Before performing the integration of  $T_3$ , it can be noted from equation (A.3) that  $\mathbf{F}^\top \nabla_{\mathbf{p}} f_s = \nabla_{\mathbf{p}}^\top (\mathbf{F} f_s)$ . The integration of  $T_3$  over all momentum space therefor yields

$$\begin{aligned} \int d\mathbf{p} T_3 &= \int d\mathbf{p} \mathbf{p} \mathbf{F}^\top \nabla_{\mathbf{p}} f_s, \\ &= \int d\mathbf{p} \mathbf{p} \nabla_{\mathbf{p}}^\top (\mathbf{F} f_s), \\ &= [\mathbf{p}^\top (\mathbf{F} f_s)]_{\partial V} - \int d\mathbf{p} \mathbf{F} f_s, \\ &= -\mathbf{F}_s n_s. \end{aligned} \quad (\text{A.10})$$

Here, partial integration was used and assumed that  $f_s$  decays to zero towards the boundary  $\partial V$  of the regarded volume. Combining the three terms finally gives

$$\frac{\partial}{\partial t} (n_s \mathbf{p}_s) + \left[ \nabla_{\mathbf{r}} \cdot \left( \int d\mathbf{p} (\mathbf{v} \mathbf{p}^\top f_s) \right) \right]^\top = n_s q_s \left( \mathbf{E} + \frac{\mathbf{v}_s}{c} \times \mathbf{B} \right). \quad (\text{A.11})$$

## A.2 RELATIVISTIC PARTICLES IN ELECTROMAGNETIC FIELDS

This section discusses the forces imposed on a relativistic charged particle by external fields.

### A.2.1 Direction of particle acceleration

*This section follows Reiser [2008, ch. 2]*

Consider a particle with charge  $q$ , normalized velocity  $\boldsymbol{\beta} = \mathbf{v}/c$  and relativistic Lorentz factor

$$\gamma = \frac{1}{\sqrt{1 - \mathbf{v}^2/c^2}}. \quad (\text{A.12})$$

The Lorentz force on the particle is given by

$$\frac{d\mathbf{p}}{dt} = \mathbf{F} = q(\mathbf{E} + \boldsymbol{\beta} \times \mathbf{B}), \quad (\text{A.13})$$

where the particles momentum is defined by  $\mathbf{p} = m\gamma\mathbf{v}$ . Solving the Lorentz force for the acceleration  $\dot{\mathbf{v}}$  yields (cf. [Reiser, 2008, ch. 2])

$$\frac{d\mathbf{v}}{dt} = \frac{\mathbf{F} - (\mathbf{F} \cdot \boldsymbol{\beta})\boldsymbol{\beta}}{m\gamma}. \quad (\text{A.14})$$

This equation expresses that the acceleration in the non-relativistic case  $|\boldsymbol{\beta}| \ll 1$  is directed along the force  $\mathbf{F}$ , whereas in the relativistic case  $|\boldsymbol{\beta}| \rightarrow 1$ , this is in general not true. If  $\boldsymbol{\beta} \perp \mathbf{F}$ , it can be seen that

$$\frac{d\mathbf{v}_\perp}{dt} = \frac{\mathbf{F}_\perp}{m\gamma'}, \quad (\text{A.15})$$

and if  $\boldsymbol{\beta} \parallel \mathbf{F}$ , it is found that

$$\frac{d\mathbf{v}_\parallel}{dt} = \frac{\mathbf{F}_\parallel}{m\gamma^3}. \quad (\text{A.16})$$

The direction of the acceleration of a relativistic charged particle hence depends on the direction of the force and the direction of the momentary motion.

### A.2.2 Azimuthally symmetric case

In the following the equations of motion will be calculated from the Lorentz force A.13 in cylindrical coordinates with  $\mathbf{r} = r\hat{\mathbf{e}}_r + z\hat{\mathbf{e}}_z$ , where

$$\hat{\mathbf{e}}_r = \begin{pmatrix} \cos\theta \\ \sin\theta \\ 0 \end{pmatrix}, \quad \hat{\mathbf{e}}_\theta = \begin{pmatrix} -\sin\theta \\ \cos\theta \\ 0 \end{pmatrix}, \quad \hat{\mathbf{e}}_z = \begin{pmatrix} 0 \\ 0 \\ 1 \end{pmatrix}. \quad (\text{A.17a})$$

The velocity is then given by  $\mathbf{v} = \dot{\mathbf{r}} = \dot{r}\hat{\mathbf{e}}_r + r\dot{\theta}\hat{\mathbf{e}}_\theta + \dot{z}\hat{\mathbf{e}}_z$ . The equations of motion in cylindrical coordinates yield (compare [Reiser, 2008])

$$\frac{d}{dt}(\gamma m \dot{r}) - \gamma m r \dot{\theta}^2 = q(E_r + r\dot{\theta}B_z/c - \dot{z}B_\theta/c), \quad (\text{A.18a})$$

$$\frac{1}{r} \frac{d}{dt}(\gamma m r^2 \dot{\theta}) = q(E_\theta + \dot{z}B_r/c - \dot{r}B_z/c), \quad (\text{A.18b})$$

$$\frac{d}{dt}(\gamma m \dot{z}) = q(E_z + \dot{r}B_\theta/c - r\dot{\theta}B_r/c). \quad (\text{A.18c})$$

Problems under consideration in this work are often azimuthally symmetric, and in the following,  $\dot{\theta} = 0$ ,  $B_r = E_\theta = B_z = 0$  is assumed, such that the equations of motion can be written in the form

$$\frac{d}{dt}(\gamma m \dot{r}) = q(E_r - \beta_z B_\theta), \quad (\text{A.19a})$$

$$\frac{d}{dt}(\gamma m \dot{z}) = q(E_z + \beta_r B_\theta). \quad (\text{A.19b})$$

If the particle furthermore has a highly relativistic velocity in  $z$ -direction and a non-relativistic velocity in radial direction,  $\beta_r \ll \beta_z \rightarrow 1$ , the equations of motion reduce to

$$\frac{d}{dt}(\gamma m \dot{r}) = \frac{dp_r}{dt} = q(E_r - B_\theta), \quad (\text{A.20a})$$

$$\frac{d}{dt}(\gamma m \dot{z}) = \frac{dp_z}{dt} = qE_z. \quad (\text{A.20b})$$

These are the relevant equations of motion for a relativistic charged particle in externally prescribed, azimuthally symmetric fields.

### A.2.3 Betatron equation of motion

For problems of interest, the radial force is often on the same order of magnitude as the longitudinal force  $F_r \sim F_z$ . Hence, with  $\beta \simeq \beta_z \hat{e}_z$  neither (A.15) nor (A.16) applies. Nevertheless, the first order radial motion can be found by examining the radial component of equation (A.14)

$$\frac{d^2 r}{dt^2} = \frac{F_r - F_z \beta_z \beta_r - F_r \beta_r^2}{m\gamma}. \quad (\text{A.21})$$

When exploiting  $\beta_r \ll 1$ , it can quickly be seen that

$$\begin{aligned} \frac{d^2 r}{dt^2} &= \frac{F_r}{m\gamma} + \mathcal{O}(\beta_r), \\ &\simeq \frac{q(E_r - B_\theta)}{m\gamma} \end{aligned} \quad (\text{A.22})$$

This equality is used in this work for considerations on the betatron motion of relativistic charged particles in externally prescribed fields.

## A.3 LINEAR WAKEFIELDS - GAUSSIAN DRIVERS

This section evaluates the solution of the integral

$$I(x) = A \int_{-\infty}^x dx' \sin(x - x') \exp\left(-\frac{(x' - x_c)^2}{2\sigma^2}\right) \quad (\text{A.23})$$

Expanding the sinus yields

$$\begin{aligned} I(x) &= A \int_{-\infty}^x dx' \frac{\exp[i(x - x')]}{2i} \exp\left(-\frac{(x' - x_c)^2}{2\sigma^2}\right) \\ &\quad + c.c. \end{aligned} \quad (\text{A.24})$$

The exponentials can be rewritten, such that

$$\begin{aligned} I(x) &= \frac{A \exp[i(x - x_c) - \sigma^2/2]}{2i} \int_{-\infty}^x dx' \exp\left[-\left(\frac{x' - x_c}{\sqrt{2}\sigma} + \frac{i\sigma}{\sqrt{2}}\right)^2\right] \\ &\quad + c.c. \end{aligned} \quad (\text{A.25})$$

Now a integration by substitution can be performed, with

$$t = \varphi(x') = \frac{x' - x_c}{\sqrt{2}\sigma} + \frac{i\sigma}{\sqrt{2}} \quad \text{and} \quad dx' = \sqrt{2}\sigma dt \quad (\text{A.26})$$

The integral can then be written in the form

$$I(x) = \frac{A L \exp [i(x - x_c) - \sigma^2/2]}{2i} \int_{\varphi(\infty)}^{\varphi(x)} dt \exp(-t^2) + c.c. \quad (\text{A.27})$$

This can be written in terms of error functions

$$I(x) = \frac{A \sqrt{2\pi} \sigma \exp [i(x - x_c) - \sigma^2/2]}{4i} [\text{Erf}(\varphi(x)) - \text{Erf}(\varphi(\infty))] + c.c. \quad (\text{A.28})$$

Using  $\varphi(x) = (x - x_c)/(\sqrt{2}\sigma) - i\sigma/\sqrt{2}$  yields

$$I(x) = \frac{A \sqrt{2\pi} \sigma \exp [i(x - x_c) - \sigma^2/2]}{4i} \left[ \text{Erf} \left( \frac{x - x_c}{\sqrt{2}\sigma} + \frac{i\sigma}{\sqrt{2}} \right) - 1 \right] + c.c. \quad (\text{A.29})$$

Using the definition of the sine function gives

$$I(x) = -\frac{A \sqrt{2\pi} \sigma}{2} \exp \left( -\frac{\sigma^2}{2} \right) \sin(x - x_c) + \frac{A \sqrt{2\pi} \sigma}{2} \text{Im} \left[ \exp [i(x - x_c)] \text{Erf} \left( \frac{x - x_c}{\sqrt{2}\sigma} + \frac{i\sigma}{\sqrt{2}} \right) \right] \quad (\text{A.30})$$

For  $x \rightarrow -\infty$  the integral has the asymptotic solution

$$I(x) \simeq -A \sqrt{2\pi} \sigma \exp \left( -\frac{\sigma^2}{2} \right) \sin(x - x_c). \quad (\text{A.31})$$

This limit is also a valid approximation for positions  $(x_c - x)/\sigma^2 \gg 1$ .





## DETAILS ON PERFORMED PIC SIMULATIONS

---

This appendix contains details to performed simulations and supplementary information.

### B.1 SIMULATION FOR DISPLAY OF BLOWOUT REGIME

The relevant numerical parameters of the [HiPACE](#) simulation presented in [1.5.4](#) are listed below.

Table 2: Relevant parameters of blowout PIC simulation

Simulation setup		
Grid	Cell size ( $k_p^{-1}$ )	$\Delta x = \Delta y = 0.020; \Delta \zeta = 0.0073$
	Box size ( $k_p^{-1}$ )	$L_x = L_y = 10; L_\zeta = 15$
Beam	Peak density	$n_b/n_0 = 4.0$
	Beam centroid ( $k_p^{-1}$ )	$x_{b,0} = y_{b,0} = 0; \zeta_{b,0} = 10$
	Beam size ( $k_p^{-1}$ )	$\sigma_x = \sigma_y = 0.8; \sigma_\zeta = 0.5$
	Beam cutoff ( $k_p^{-1}$ )	$3 \times \sigma_x; 3 \times \sigma_y; 3 \times \sigma_\zeta$
	Particles per cell	$N_{p,x} \times N_{p,y} \times N_{p,\zeta} = 2 \times 2 \times 2$
Plasma	Plasma density	$1 \times n_0$
	Particles per cell	$N_{p,x} \times N_{p,y} \times N_{p,\zeta} = 2 \times 2 \times 1$

## B.2 SIMULATION FOR HIPACE AND OSIRIS COMPARISON

Listed below are the parameters for the simulations for the comparison between [HiPACE](#) and [OSIRIS](#) in 3.4.

Table 3: Relevant parameters of simulation for the comparison between [HiPACE](#) and [OSIRIS](#)

Simulation setup		
Grid	Cell size ( $k_p^{-1}$ )	$\Delta x = \Delta y = 0.0588; \Delta \zeta = 0.0073$
	Box size ( $k_p^{-1}$ )	$L_x = L_y = 15; L_\zeta = 15$
Beam	Peak density	$n_b/n_0 = 1.0$
	Beam centroid ( $k_p^{-1}$ )	$x_{b,0} = y_{b,0} = 0.0; \zeta_{b,0} = 10.0$
	Beam size ( $k_p^{-1}$ )	$\sigma_x = \sigma_y = \sigma_\zeta = 1.0$
	Beam cutoff ( $k_p^{-1}$ )	$3 \times \sigma_x; 3 \times \sigma_y; 3 \times \sigma_\zeta$
	Particles per cell	$N_{p,x} \times N_{p,y} \times N_{p,\zeta} = 2 \times 2 \times 2$
Plasma	Plasma density	$1 \times n_0$
	Particles per cell	$N_{p,x} \times N_{p,y} \times N_{p,\zeta} = 2 \times 2 \times 1$

## B.3 SIMULATIONS ON EMITTANCE GROWTH IN STAGED LWFA

Displayed here are detailed parameters used for simulations for the study on emittance growth in staged LWFA in 5.3.

Table 4: Parameters of PIC simulations on emittance growth in staged LWFA

Simulation setup		
Grid	Cell size ( $k_p^{-1}$ ) Box size ( $k_p^{-1}$ )	$\Delta x = \Delta y = 0.08; \Delta \zeta = 0.0015$ $L_x = L_y = 20.0; L_\zeta = 7.0$
Laser-beam	Amplitude Centroid ( $k_p^{-1}$ ) Size ( $k_p^{-1}$ ) Cutoff ( $k_p^{-1}$ ) Focal position ( $k_p^{-1}$ ) Central frequency	$a_0 = 1.8$ $x_{b,0} = y_{b,0} = 0.0; \zeta_{b,0} = 5.05$ $r_s = 0.7; \sigma_\zeta = 1.0$ $3 \times \sigma_x; 3 \times \sigma_y; 3 \times \sigma_\zeta$ $z_f = 127.0$ $\omega_0/\omega_p = 132.0$
Witness-beam	Peak density Centroid ( $k_p^{-1}$ ) Size ( $k_p^{-1}$ ) Cutoff ( $k_p^{-1}$ ) Emittance ( $k_p^{-1}$ ) Energy/-spread Particles per cell	$n_b/n_0 = 0.3427$ $x_{b,0} = y_{b,0} = 0; \zeta_{b,0} = 4.2$ $\sigma_x = \sigma_y = 0.05; \sigma_\zeta = 0.2$ $3 \times \sigma_x; 3 \times \sigma_y; 3 \times \sigma_\zeta$ $\epsilon_{x,n} = \epsilon_{y,n} = 0.0025$ $\gamma = 2000; \sigma_\gamma/\gamma = 2 \times 10^{-2}$ $N_{p,x} \times N_{p,y} \times N_{p,\zeta} = 2 \times 2 \times 2$
Plasma	Plasma density Particles per cell	$\begin{cases} n_0 & \text{if } -2000 < k_p z \leq 0 \\ 0 & \text{otherwise} \end{cases}$ $N_{p,x} \times N_{p,y} \times N_{p,\zeta} = 2 \times 2 \times 1$

## B.4 SIMULATIONS ON DENSITY TAPERED EXTRACTION

The relevant numerical parameters of the PIC simulation presented in 6.3 are listed below.

Table 5: Parameters of PIC simulations on density tapered matching

Simulation setup		
Grid	Cell size ( $k_p^{-1}$ ) Box size ( $k_p^{-1}$ )	$\Delta x = \Delta y = 0.047; \Delta \zeta = 0.015$ $L_x = L_y = 24; L_\zeta = 15$
Driver-beam	Peak density Centroid ( $k_p^{-1}$ ) Size ( $k_p^{-1}$ ) Cutoff ( $k_p^{-1}$ ) Emittance ( $k_p^{-1}$ ) Energy/-spread Particles per cell	$n_b/n_0 = 3.0$ $x_{b,0} = y_{b,0} = 0.0; \zeta_{b,0} = 10.0$ $\sigma_x = \sigma_y = 0.7; \sigma_\zeta = 1.0$ $3 \times \sigma_x; 3 \times \sigma_y; 3 \times \sigma_\zeta$ $\epsilon_{x,n} = \epsilon_{y,n} = 0.35$ $\gamma = 2000; \sigma_\gamma/\gamma = 10^{-3}$ $N_{p,x} \times N_{p,y} \times N_{p,\zeta} = 2 \times 1 \times 1$
Witness-beam	Peak density Centroid ( $k_p^{-1}$ ) Size ( $k_p^{-1}$ ) Cutoff ( $k_p^{-1}$ ) Emittance ( $k_p^{-1}$ ) Energy/-spread Number of particles	$n_b/n_0 = 15.0$ $x_{b,0} = y_{b,0} = 0; \zeta_{b,0} = 4.2$ $\sigma_x = \sigma_y = 0.05; \sigma_\zeta = 0.2$ $3 \times \sigma_x; 3 \times \sigma_y; 3 \times \sigma_\zeta$ $\epsilon_{x,n} = \epsilon_{y,n} = 0.0025$ $\gamma = 2000; \sigma_\gamma/\gamma = 5 \times 10^{-3}$ $N_{p,tot} = 10^5$
Plasma	Plasma density Particles per cell	$\begin{cases} n_0 & \text{if } -2e3 < k_p z \leq 0 \\ n_0 \exp(-\frac{z}{L}) & \text{if } 0 < k_p z \leq z_e \\ 0 & \text{otherwise} \end{cases}$ $N_{p,x} \times N_{p,y} \times N_{p,\zeta} = 2 \times 2 \times 1$

The following displays supplementary information on simulations performed in 6.3. Shown is the longitudinal phase space of driver and witness beam immediately upstream of the plasma-to-vacuum transitions in Figure 35. The driver lost energy while the witness beam is approximately energy-doubled. The witness beam has a significant energy spread, which comes from the slope of the longitudinal field.

Figures 36, 37 and 38 depict the phase space information in one transverse direction of the witness beam at position  $z_0$ , prior to the plasma-vacuum transitions. It can be seen that the  $x' - p_x$  phase space distribution is highly correlated, but has a certain finite width especially for greater  $x'$  or  $p_x$ . This width resembles the inequality

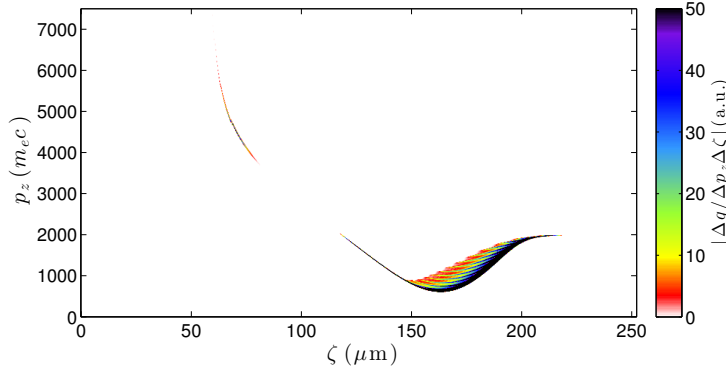


Figure 35: Longitudinal phase space of driver and witness beam in the study on density tapered extraction by means of a PIC simulation at position  $z_0$ .

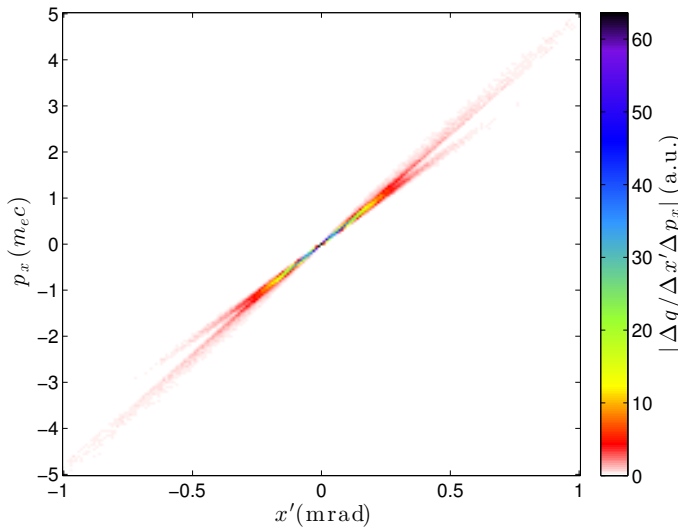


Figure 36: Transverse phase space  $x' - p_x$  of witness beam in a PIC simulation at position  $z_0$ .

$\langle x' p_x \rangle_0^2 \neq \langle x'^2 \rangle_0 \langle p_x^2 \rangle_0$ . The fork-structure comes from the tail of the beam which experienced defocusing forces for a short time. This can be also seen in Figures 37 and 38, where a subset of the beam can be seen at large transverse momenta. Moreover, these Figures indicate that the beam is near to waist prior to the density transition region.

Figures 39, 40 and 41 depict the phase space information in one transverse direction of the witness beam at the exit position  $z_e$  for a transition length  $L = 0.5$  mm. The  $x' - p_x$  phase space distribution, Figure 39, did not change significantly compared to the distribution in Figure 36. However, Figures 40 and 41, suggest that beam is diverging and was not transported near to waist during the transition.

Figures 42, 43 and 44 depict the phase space information in one transverse direction of the witness beam at the exit position  $z_e$  for a

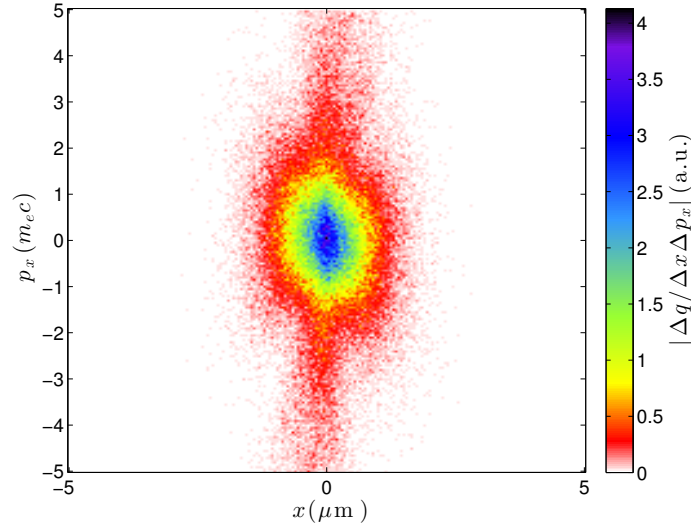


Figure 37: Transverse phase space  $x - p_x$  of witness beam in a PIC simulation at position  $z_0$ .

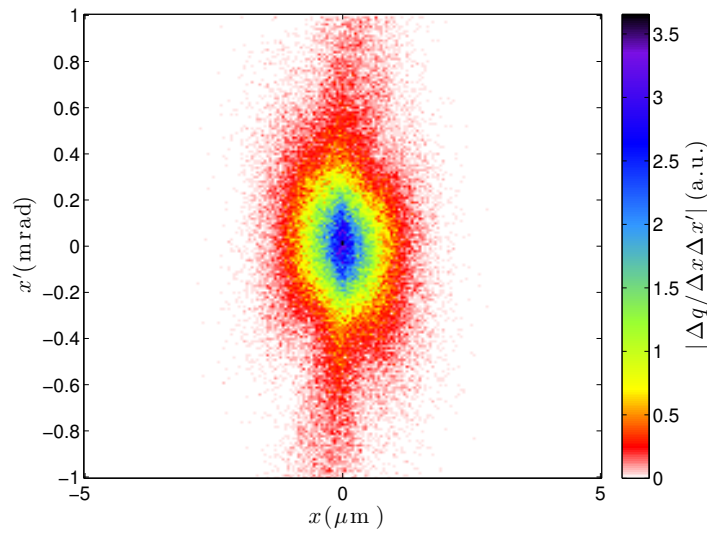


Figure 38: Transverse phase space  $x - x'$  of witness beam in a PIC simulation at position  $z_0$ .

transition length  $L = 8.0$  mm. The  $x' - p_x$  phase space distribution is significantly narrower in  $x'$  and  $p_x$  for this case than before the density transition and the divergence is accordingly reduced. Figures 43 and 44 show that the transverse phase space distribution was deformed such that the large beam divergence was transformed to a larger beam size. Moreover, it may be noted that the beam is near to waist.

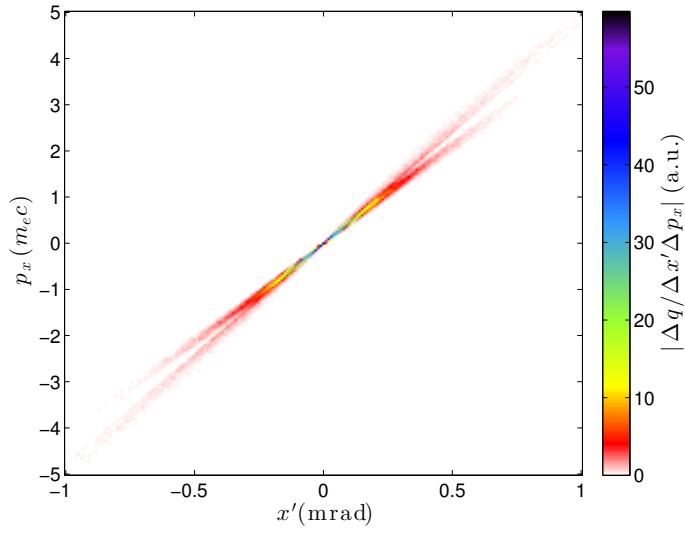


Figure 39: Transverse phase space  $x' - p_x$  of witness beam in a PIC simulation with transition length  $L = 0.5$  mm at position  $z_e$ .

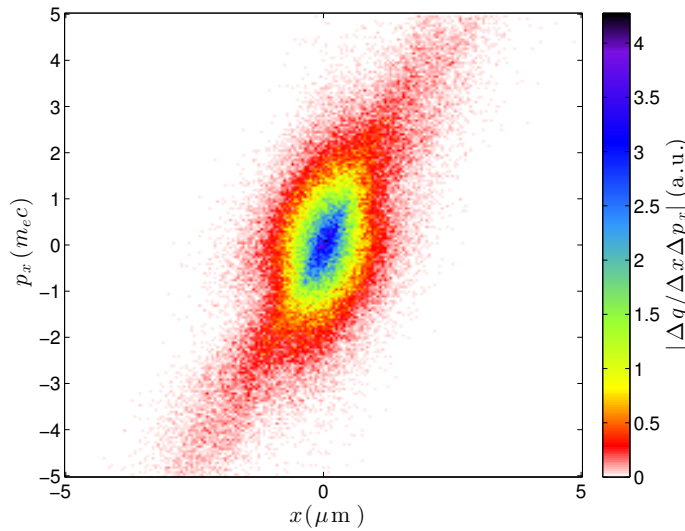


Figure 40: Transverse phase space  $x - p_x$  of witness beam in a PIC simulation with transition length  $L = 0.5$  mm at position  $z_e$ .

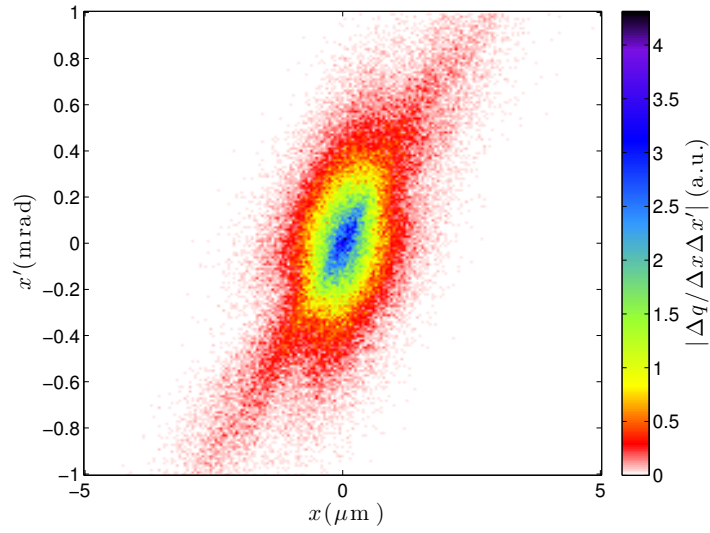


Figure 41: Transverse phase space  $x - x'$  of witness beam in a PIC simulation with transition length  $L = 0.5$  mm at position  $z_e$ .

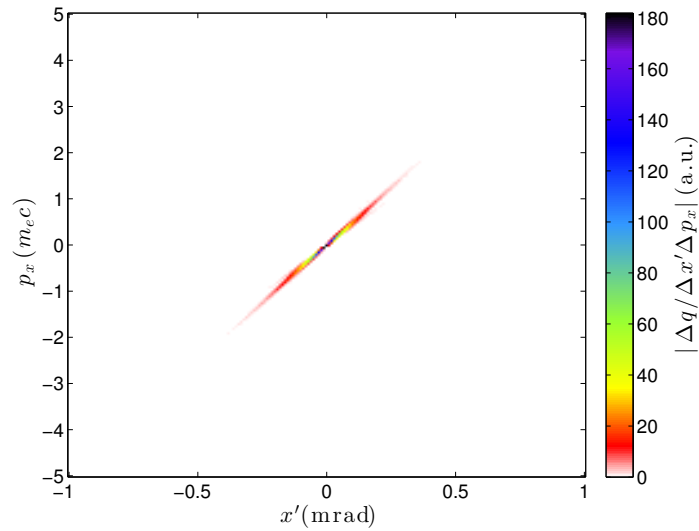


Figure 42: Transverse phase space  $x' - p_x$  of witness beam in a PIC simulation with transition length  $L = 8.0$  mm at position  $z_e$ .



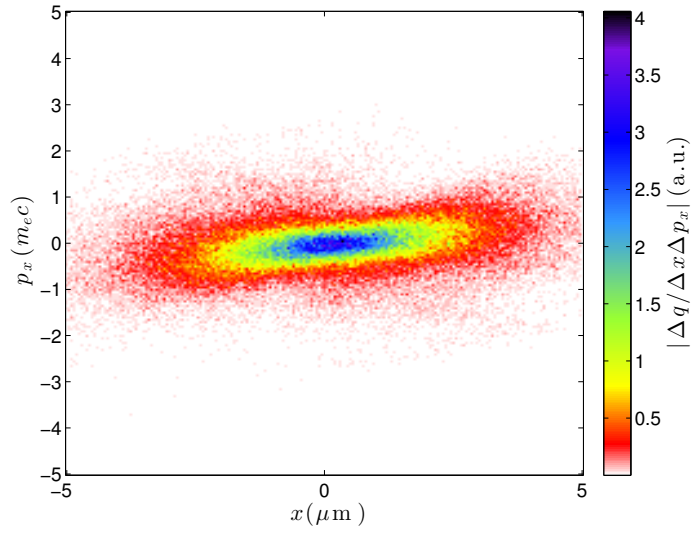


Figure 43: Transverse phase space  $x - p_x$  of witness beam in a PIC simulation with transition length  $L = 8.0$  mm at position  $z_e$ .

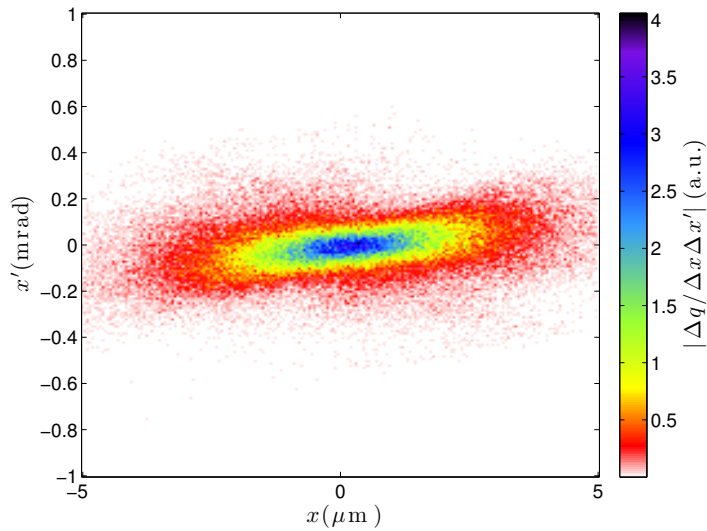


Figure 44: Transverse phase space  $x - x'$  of witness beam in a PIC simulation with transition length  $L = 8.0$  mm at position  $z_e$ .



## C.1 BASIS OF THE FAST POISSON SOLVER

## C.1.1 Fast Poisson solver in one dimension

The basis of the fast Poisson solver will be explained here in the example of the one-dimensional Poisson problem,

$$\frac{\partial^2 U}{\partial x^2} = F(x), \quad x_{min} < x < x_{max}. \quad (\text{C.1})$$

The boundary conditions considered here are Dirichlet at both borders, with  $U(x_{min}) = U(x_{max}) = 0$ .

The domain  $x_{min} < x < x_{max}$  is now discretized as follows,  $x_k = x_{min} + k \cdot \Delta x$  with  $k = 0, \dots, n$  and  $\Delta x = (x_{max} - x_{min})/n$ . The aim here is to approximate  $U$  on the interior grid points  $u_k = U(x_k)$  for  $k = 1, \dots, n-1$ , given the information  $f_k = F(x_k)$ . The values at the boundaries,  $u_0$  and  $u_n$ , are zero by stipulation of the above Dirichlet boundary conditions. The partial differential equation (C.1) can now be discretized in a second-order difference scheme according to

$$\frac{u_{k+1} - 2u_k + u_{k-1}}{\Delta x^2} \simeq f_k, \quad k \in \{1, \dots, n-1\}. \quad (\text{C.2})$$

When imposing Dirichlet boundary conditions, this equation reads in terms of a vector and matrix representation

$$\Delta x^{-2} T u \simeq f, \quad (\text{C.3})$$

where the  $(n-1) \times (n-1)$  matrix  $T$ , defined by

$$T = \begin{pmatrix} -2 & 1 & 0 & \cdots & 0 \\ 1 & -2 & \ddots & & \vdots \\ 0 & \ddots & \ddots & \ddots & 0 \\ \vdots & & \ddots & \ddots & 1 \\ 0 & \cdots & 0 & 1 & -2 \end{pmatrix}, \quad (\text{C.4})$$

acts as a central difference operator on  $u = (u_1, \dots, u_{n-1})$  and has a tridiagonal shape. The vector  $f = (f_1, \dots, f_{n-1})$  represents the function  $F$  on the discretized interior part domain.

Such a linear equation problem with a tridiagonal matrix is typically computationally efficiently solved by use of direct numerical methods, e.g. the Cholesky-discretization or the QR-discretization or

*The explanations here follow [Van Loan, 1992].*

by iterative methods, e.g. the Krylov-subspace method [Meister, 2011]. However, it can be shown that this particular problem can be solved by means of discrete sine-transforms, which are generally more efficient. This is possible since the matrix  $T$  can be factorized according to the following eigendecomposition (the proof is found in [Van Loan, 1992])

$$V^{-1}TV = \Lambda = \text{diag}(\lambda_1, \dots, \lambda_{n-1}), \quad (\text{C.5})$$

where the matrix  $V$  is the operator for a discrete sine transform

$$V_{jk} = \sin\left(\frac{jk\pi}{n}\right) \quad j, k \in \{1, \dots, n-1\}, \quad (\text{C.6})$$

and the eigenvalues  $\lambda_j$  of  $T$  are given by

$$\lambda_j = -4 \sin^2\left(\frac{j\pi}{2n}\right) \quad j \in \{1, \dots, n-1\}. \quad (\text{C.7})$$

Hence, equation (C.3) can be transformed as follows,

$$\Delta x^{-2} T u = f, \quad (\text{C.8})$$

$$\Rightarrow V^{-1}TVV^{-1}uV = \Delta x^2 V^{-1}fV, \quad (\text{C.9})$$

$$\Rightarrow \Lambda V^{-1}uV = \Delta x^2 V^{-1}fV, \quad (\text{C.10})$$

$$\Rightarrow u = \Delta x^2 V \Lambda^{-1} V^{-1} f. \quad (\text{C.11})$$

After noting that  $V^{-1} = 2V/n$  [Van Loan, 1992], this implies that  $u$  can be obtained by the following sequence of operations.

1. The data-array  $f$  is sine-transformed.
2. The resulting array is multiplied by  $2/n \Lambda^{-1}$ .
3. The resulting array is sine-transformed.

Computation of the vector  $u$  therefore requires two discrete sine-transforms and a multiplication by a matrix with the inverse of the eigenvalues of  $T$  on the diagonals.

### C.1.2 Fast Poisson solver in two dimensions

The Poisson problem for the computation of the fields in HiPACE is two-dimensional,

$$\frac{\partial^2 U}{\partial x^2} + \frac{\partial^2 U}{\partial y^2} = F(x, y), \quad x_{\min} < x < x_{\max}, \quad y_{\min} < y < y_{\max}. \quad (\text{C.12})$$

The 2D-domain is discretized analogously to the above discussed 1D case and the discretized 2D Poisson problem reads

$$\frac{u_{j+1,k} - 2u_{j,k} + u_{j-1,k}}{\Delta x^2} + \frac{u_{j,k+1} - 2u_{j,k} + u_{j,k-1}}{\Delta y^2} \simeq f_{j,k}, \quad (\text{C.13})$$

$$j \in \{1, \dots, n_x - 1\}, \quad k \in \{1, \dots, n_y - 1\},$$

with the Dirichlet boundary condition  $u_{0,k} = u_{n_x,k} = u_{j,0} = u_{j,n_y} = 0 \forall k, j$ . Equation (C.13) in matrix representation reads

$$\left( \Delta x^{-2} I_{n_y-1} T_{n_x-1} + \Delta y^{-2} T_{n_y-1} I_{n_x-1} \right) u = f, \quad (\text{C.14})$$

where  $I_m$  is the  $m \times m$  identity matrix and  $T_m$  is the tridiagonal matrix (C.4) with dimension  $m \times m$ . Analogously as for the 1D Poisson problem, the numerical solution is thus given by (see [Van Loan, 1992])

$$u = (V_B V_A) [I_\beta \Lambda_A / h_A^2 + \Lambda_B I_\alpha / h_B^2]^{-1} (V_B^{-1} V_A^{-1}) f, \quad (\text{C.15})$$

where  $V_A^{-1} A V_A = \Lambda_\alpha$  for  $A = T_\alpha \in \mathbb{R}^{\alpha \times \alpha}$  and  $V_B^{-1} B V_B = \Lambda_\beta$  for  $B = T_\beta \in \mathbb{R}^{\beta \times \beta}$ , and  $h_A = \Delta x$  and  $h_B = \Delta y$ . This implies that  $u$  in the 2D Dirichlet problem can be obtained by the following sequence of operations.

1. The 2D-array  $f$  is 2D sine-transformed.
2. The resulting 2D-array is multiplied by the matrix  $4 / (n_x n_y) [I_{n_y-1} \Lambda_{n_x-1} / \Delta x^2 + \Lambda_{n_y-1} I_{n_x-1} / \Delta y^2]^{-1}$ .
3. The resulting 2D-array is 2D sine-transformed.

A method based on this scheme is used in the code [HiPACE](#) for the computation of the fields during the plasma and field solving routine.

## C.2 DETAILS ON THE PARALLELIZATION IN HIPACE

The Cartesian three-dimensional simulation domain in [HiPACE](#) is decomposed in all three dimensions into subdomains which are computed by individual processes. This Cartesian virtual topology allows for an efficient distribution of the computational load on a large number of processes with the Message Passing Interface ([MPI](#)). The Eulerian information on the grid is exchanged in the transverse direction by use of the *halo cell method*. The fast Poisson solver computes transverse planes of Eulerian current information in the virtual topology and returns transverse planes of field information in the virtual topology, and hence, must be parallelized. The longitudinal parallelization in [HiPACE](#) differs from the transverse parallelization and uses a different scheme for the information exchange. Due to the virtual topology, particles crossing the boundaries of the subdomains in the [PIC](#) code need to be exchanged between the processes. All these methods and schemes will be outlined in the following.

### C.2.1 Halo cell method

Eulerian information in the simulation is stored on the grid. Each process in the virtual topology contains and computes a subgrid of

this information. Information exchange between the processes is necessary whenever a process needs to access information from a neighboring process or change information in the neighboring process. Examples for such actions in PIC codes are the field interpolation or the current deposition. Owing to the quasi-static scheme, an efficient parallelization in HiPACE demands for the current deposition and field interpolation to be performed with a first order scheme in the longitudinal direction whereas in the transverse plane the current deposition and field interpolation can be done with an arbitrary higher order scheme.

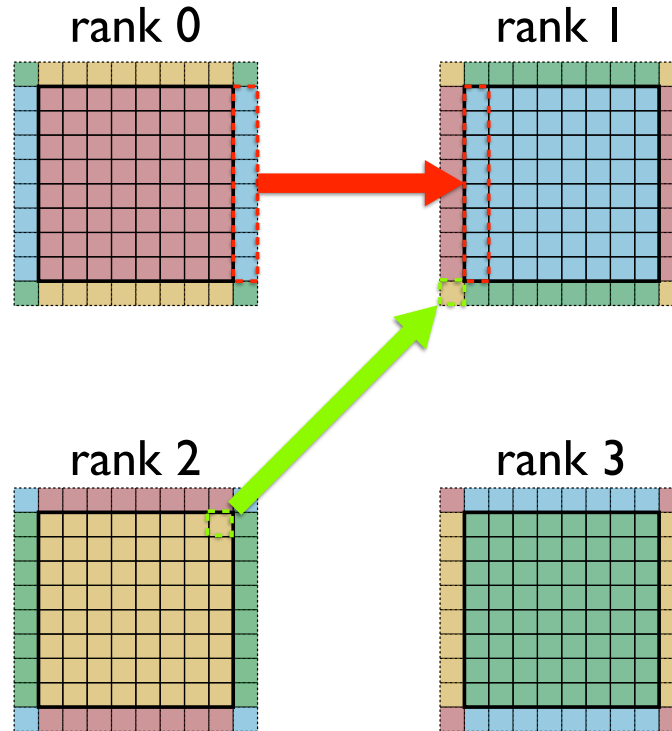


Figure 45: Illustration of MPI communication method using halo cells. Detailed explanation, see C.2.1.

The following describes the halo cell method (also called ghost or guard cell method) [Wilkinson and Allen, 1999] which is used for the parallelization in the 2D transverse plane. The halo cell scheme is illustrated in Figure 45 in the example of a 2D virtual topology with four processes (or ranks), with a halo cell width of one cell and periodic boundary conditions. The basic idea is that each process stores copies of the information from the neighboring process in the halo cells.

The red arrow in Figure 45 illustrates a communication from left to right in which information from the halo of rank 0 is copied and added to the inner area of rank 1. This is done e.g. after the current deposition. If the current of macro-particles near to the right border

in rank 0 is deposited in a higher order scheme, a fraction of the current is deposited in the halo area (marked blue). After the current deposition, this information is copied from the halo area of rank 0 and added to the inner area of rank 1.

The green arrow in Figure 45 depicts a diagonal communication in which information from the inner area of rank 2 is copied and written to the halo area of rank 1. This is done e.g. before the higher order transverse field interpolation, such that the field information in the vicinity of a macro-particle near to the border in rank 1 can be interpolated to this particle.

This halo information exchange [HiPACE](#) is done in a non-blocking way using [MPI](#) [[Message Passing Interface Forum, 2012](#)].

### *c.2.2 Parallelization of the fast Poisson solver*

The transverse Poisson solver routine in [HiPACE](#) requires the global transverse source (current) information for the computation of the fields and returns the global information. It must hence operate on the virtual topology in a parallel manner. The parallelization of the Poisson solver in [HiPACE](#) is as follows. The library used for the fast Fourier transforms, Fastest Fourier Transform in the West ([FFTW](#)), provides a 1D parallelization. For the parallel implementation in the second transverse dimension, the source information is gathered in the second direction in a 1D row of processes. The [FFT](#)s are performed in this row of processes and the resulting (field) information is scattered from the row of processes to the other processes.

### *c.2.3 Longitudinal parallelization*

The communication in the longitudinal direction is occurring only from the front to the back. This is to ensure a non-synchronous parallel computation of the information in the various transverse slabs of processes and hence to mitigate significant idle times during the plasma and field solving routine which computes information from the front of the simulation domain to the back. Information is hence only passed on from one slab of processes to the next slab of processes, which inherit this information to be able to start their plasma and field solving routine.

### *c.2.4 Macro-particle exchange*

The exchange of macro-particle information between the processes is done as follows. The macro-particle information of particles crossing the subdomain boundaries is stored in a buffer during the particle push and communicated to the appropriate neighboring process and after the particle advance. Boundary conditions are thereby periodic

for plasma macro-particles and optionally periodic, reflecting or open for the beam macro-particles.



## LIST OF FIGURES

---

Figure 1	Electron trajectory in plane light pulse . .	19
Figure 2	Electron trajectory in Gaussian light pulse	19
Figure 3	Plasma classification . . . . .	24
Figure 4	Gibbon - plasma model hierarchy . . . . .	27
Figure 5	Lin plasma wave . . . . .	47
Figure 6	Nonlin plasma wave . . . . .	49
Figure 7	Blowout regime - plasma and beam density	51
Figure 8	Blowout regime - $E_z$ . . . . .	52
Figure 9	Blowout regime - $E_y + B_x$ . . . . .	53
Figure 10	Trace-space ellipse . . . . .	62
Figure 11	T.s. ellipse rotation from betatron oscillation	72
Figure 12	PIC main cycle . . . . .	79
Figure 13	Yee mesh . . . . .	81
Figure 14	Basic numerical scheme in <a href="#">HiPACE</a> . . . . .	89
Figure 15	Schematic numerical flow in <a href="#">HiPACE</a> . . .	92
Figure 16	Densities in <a href="#">HiPACE</a> and <a href="#">OSIRIS</a> simulations	98
Figure 17	Longitudinal field in <a href="#">HiPACE</a> and <a href="#">OSIRIS</a> .	100
Figure 18	Transverse fields in <a href="#">HiPACE</a> and <a href="#">OSIRIS</a> . .	101
Figure 19	Parallel scalings of <a href="#">HiPACE</a> . . . . .	102
Figure 20	Trace-space ellipses in a PIC simulation .	117
Figure 21	Evolution of Courant-Snyder parameters	120
Figure 22	Emittance evolution . . . . .	121
Figure 23	Per-stage emittance growth . . . . .	123
Figure 24	Extraction in ideal systems, $L = 0.5$ mm .	129
Figure 25	Extraction in ideal systems, $L = 2.0$ mm .	130
Figure 26	Extraction in ideal systems, $L = 8.0$ mm .	131
Figure 27	Adiabaticity for $L = 8.0$ mm . . . . .	132
Figure 28	Extraction in ideal systems, $L = 32.0$ mm	133
Figure 29	Adiabaticity for $L = 32.0$ mm . . . . .	133
Figure 30	Divergence reduction . . . . .	134
Figure 31	Beam evolution in decay with $L = 4$ mm	138
Figure 32	Evolution of $\hat{\gamma}$ . . . . .	139
Figure 33	Emittance evolution in drift . . . . .	141
Figure 34	Emittance growth in drift . . . . .	142
Figure 35	Long. p.s. of driver and witness beam . .	159
Figure 36	Trans. p.s. $x' - p_x$ at $z_0$ . . . . .	159
Figure 37	Trans. p.s. $x - p_x$ at $z_0$ . . . . .	160
Figure 38	Trans. p.s. $x - x'$ at $z_0$ . . . . .	160
Figure 39	Trans. p.s. $x' - p_x$ at $z_e$ for $L = 0.5$ mm . .	161
Figure 40	Trans. p.s. $x - p_x$ at $z_e$ for $L = 0.5$ mm . .	161
Figure 41	Trans. p.s. $x - x'$ at $z_e$ for $L = 0.5$ mm . .	162

Figure 42	Trans. p.s. $x' - p_x$ at $z_e$ for $L = 8.0$ mm . .	162
Figure 43	Trans. p.s. $x - p_x$ at $z_e$ for $L = 8.0$ mm . .	163
Figure 44	Trans. p.s. $x - x'$ at $z_e$ for $L = 8.0$ mm . .	163
Figure 45	Illustration of halo method . . . . .	168

## LIST OF TABLES

---

Table 1	Exit values of $\hat{\gamma}_e$ and $\kappa_e$ . . . . .	140
Table 2	Parameters of PIC simulation in chapter 1	155
Table 3	Parameters of PIC simulations in chapter 3	156
Table 4	Parameters of PIC simulations in chapter 5	157
Table 5	Parameters of PIC simulations in chapter 6	158

## ACRONYMS

---

ASTRA	A Space Charge Tracking Algorithm <a href="http://www.desy.de/~mpyflo/">http://www.desy.de/~mpyflo/</a>
BBGKY	Bogoliubov, Born, Green, Kirkwood and Yvon
CFL	Courant-Friedrichs-Lewy [Courant et al., 1928]
CPA	chirped pulse amplification [Strickland and Mourou, 1985]
CT	computed tomography
DESY	Deutsches Elektronen-Synchrotron <a href="http://www.desy.de/">http://www.desy.de/</a>
ELEGANT	multi-purpose 3D particle tracking code <a href="#">URL</a>
FACET	Facilities for Accelerator science and Experimental Test beams at SLAC [Hogan et al., 2010]
FDTD	finite-difference time-domain [Yee, 1966]
FEL	free-electron laser
FFT	fast fourier transform
FFTW	Fastest Fourier Transform in the West [Frigo and Johnson, 2005]; <a href="http://www.fftw.org/">http://www.fftw.org/</a>
FLASH	Free-electron Laser in Hamburg <a href="http://flash.desy.de/">http://flash.desy.de/</a>
FLASHForward	Future-oriented wakefield-accelerator research and development at FLASH
FWHM	full width at half maximum
HiPACE	Highly efficient Plasma Accelerator Emulation (see chapter 3) or [Mehrling et al., 2014]
HPC	high-performance computing
ILC	International Linear Collider <a href="http://www.linearcollider.org/">http://www.linearcollider.org/</a> , [Behnke et al., 2013]
IST	Instituto Superior Técnico Lisboa <a href="http://tecnico.ulisboa.pt/">http://tecnico.ulisboa.pt/</a>
LAOLA	Laboratory for laser- and beam-driven plasma acceleration <a href="http://laola.desy.de/">http://laola.desy.de/</a>
LBNL	Lawrence Berkeley National Laboratory <a href="http://www.lbl.gov/">http://www.lbl.gov/</a>

LHC	Large Hadron Collider <a href="http://www.lhc-facts.ch/">http://www.lhc-facts.ch/</a>
LWFA	laser wakefield acceleration (see <a href="#">1.5.1.2</a> )
MPI	Message Passing Interface <a href="http://www.mpi-forum.org/">http://www.mpi-forum.org/</a>
ODE	ordinary differential equation
OSIRIS	full 3D particle-in-cell code [Fonseca et al., 2002, 2008, 2013]
PDE	partial differential equation
PWFA	plasma wakefield acceleration (see <a href="#">1.5.1.1</a> )
PIC	Particle-In-Cell (see chapter <a href="#">2</a> )
QSA	quasi-static approximation (see <a href="#">1.4.3.2</a> )
RMS	root mean square
SLAC	Stanford Linear Accelerator Center <a href="https://www6.slac.stanford.edu/">https://www6.slac.stanford.edu/</a>
UCLA	University of California Los Angeles <a href="http://www.ucla.edu/">http://www.ucla.edu/</a>
XFEL	X-Ray Free-Electron Laser <a href="http://www.xfel.eu/">http://www.xfel.eu/</a>

## LIST OF FREQUENTLY USED SYMBOLS

---

<b>A</b>	Vector potential
<b>a</b>	Normalized vector potential $\mathbf{a} = e\mathbf{A}/m_e c^2$
<b>B</b>	Magnetic field
<b><math>\mathcal{B}</math></b>	Normalized magnetic field $\mathcal{B} = \mathbf{B}/E_0$ , where $E_0$ is the wave-breaking field
<i>c</i>	Speed of light $c = 299792458$ m/s
<b>E</b>	Electric field
<b><math>\mathcal{E}</math></b>	Normalized electric field $\mathcal{E} = \mathbf{E}/E_0$ , where $E_0$ is the wave-breaking field
<i>e</i>	Absolute electron charge $e = 1.602 \times 10^{-19}$ Coulomb
$E_0$	Cold non-relativistic wave-breaking field $E_0 = m_e c \omega_p / e$
<i>I</i>	Intensity of a light wave or electric current
<b>J</b>	Current density $\mathbf{J} = \mathbf{J}(\mathbf{r}, t)$
$k_p$	Light-like plasma wave number or inverse skin depth $k_p = \omega_p / c$
<i>m</i>	Particle rest mass
$m_e$	Electron rest mass $m_e = 9.109 \times 10^{-31}$ kg
$n, n_e, n_0$	Particle density, electron particle density, reference particle density
<b>P</b>	Particle momentum
<b>p</b>	Momentum coordinate
$\mathbf{P}_{can}$	Canonical momentum $\mathbf{P}_{can} = \mathbf{p} + e\mathbf{A}$
<i>q</i>	Particle charge
<b>R</b>	Particle position in configuration space
<b>r</b>	Cartesian coordinate vector
<i>r</i>	Radius in a cylindrical coordinate system
$r_s$	Laser spot size, $r_s = 2\sigma_r$ , where $\sigma_r$ is the <a href="#">RMS</a> -intensity width

$\mathbf{U}$	Normalized particle momentum $\mathbf{U} = \mathbf{P}/mc = \beta\gamma$
$\mathbf{u}$	Normalized momentum $\mathbf{u} = \mathbf{p}/mc = \beta\gamma$
$\mathbf{v}$	Particle velocity
$v$	Velocity coordinate
$x$	Cartesian coordinate (perpendicular to beam propagation direction)
$y$	Cartesian coordinate (perpendicular to beam propagation direction)
$z$	Axial coordinate (in beam propagation direction)
$\hat{\alpha}, \hat{\beta}, \hat{\gamma}$	Courant-Snyder (Twiss) parameters
$\beta$	Velocity divided by the speed of light
$\gamma$	Lorentz factor, $\gamma = 1/\sqrt{1 - (\mathbf{v}/c)^2}$
$\epsilon$	Geometric phase-space emittance $\epsilon = \sqrt{\langle x^2 \rangle \langle p_x^2 \rangle - \langle xp_x \rangle^2} / \langle p_z \rangle$
$\epsilon_n$	Normalized phase-space emittance $\epsilon_n = \sqrt{\langle x^2 \rangle \langle p_x^2 \rangle - \langle xp_x \rangle^2} / m_e c$
$\hat{\epsilon}$	Trace-space-emittance $\hat{\epsilon} = \sqrt{\langle x^2 \rangle \langle x'^2 \rangle - \langle xx' \rangle^2}$
$\hat{\epsilon}_n$	Normalized trace-space emittance $\hat{\epsilon}_n = \hat{\epsilon} \langle p_z \rangle / m_e c$
$\lambda_p$	Plasma wavelength
$\zeta$	Co-moving space variable $\zeta = z - ct$
$\rho$	Charge density $\rho = \rho(\mathbf{r}, t)$
$\tau$	Co-moving time variable $\tau = t$
$\Phi$	Scalar potential
$\phi$	Normalized scalar potential $\phi = e\Phi/m_e c^2$
$\Psi$	Wake potential $\Psi = \Phi - A_z$
$\psi$	Normalized wake potential $\psi = e\Psi/m_e c^2$
$\omega$	Angular frequency/laser central frequency
$\omega_p$	Plasma frequency $\omega_p = \sqrt{4\pi n_e e^2/m_e}$





## BIBLIOGRAPHY

---

- An, W., Decyk, V. K., Mori, W. B., and Jr., T. M. A. An improved iteration loop for the three dimensional quasi-static particle-in-cell algorithm: QuickPIC. *Journal of Computational Physics*, 250(0):165 – 177, 2013. ISSN 0021-9991. doi: <http://dx.doi.org/10.1016/j.jcp.2013.05.020>. URL <http://www.sciencedirect.com/science/article/pii/S0021999113003525>.
- Andreev, N. E., Gorbunov, L. M., Kirsanov, V. I., Nakajima, K., and Ogata, A. Structure of the wake field in plasma channels. *Physics of Plasmas (1994-present)*, 4(4):1145–1153, 1997. doi: <http://dx.doi.org/10.1063/1.872186>. URL <http://scitation.aip.org/content/aip/journal/pop/4/4/10.1063/1.872186>.
- Arnold, V. I. *Mathematical Methods of Classical Mechanics*. Graduate Texts in Mathematics. Springer, 1989. ISBN 9780387968902.
- Assmann, R. and Yokoya, K. Transverse beam dynamics in plasma-based linacs. *Nuclear Instruments and Methods in Physics Research Section A: Accelerators, Spectrometers, Detectors and Associated Equipment*, 410(3):544 – 548, 1998. ISSN 0168-9002. doi: [http://dx.doi.org/10.1016/S0168-9002\(98\)00187-9](http://dx.doi.org/10.1016/S0168-9002(98)00187-9). URL <http://www.sciencedirect.com/science/article/pii/S0168900298001879>.
- Bane, K. L. F., Wilson, P. B., and Weiland, T. Wake fields and wake field acceleration. *AIP Conference Proceedings*, 127(1):875–928, 1985. doi: <http://dx.doi.org/10.1063/1.35182>. URL <http://scitation.aip.org/content/aip/proceeding/aipcp/10.1063/1.35182>.
- Barov, N. and Rosenzweig, J. B. Propagation of short electron pulses in underdense plasmas. *Phys. Rev. E*, 49:4407–4416, May 1994. doi: 10.1103/PhysRevE.49.4407. URL <http://link.aps.org/doi/10.1103/PhysRevE.49.4407>.
- Behnke, T., Brau, J. E., Foster, B., Fuster, J., Harrison, M., et al. The International Linear Collider Technical Design Report - Volume 1: Executive Summary. 2013.
- Benedetti, C., Schroeder, C. B., Esarey, E., Geddes, C. G. R., and Leemans, W. P. Efficient Modeling of Laser-Plasma Accelerators with INF&RNO. *AIP Conference Proceedings*, 1299(1):250–255, 2010. doi: <http://dx.doi.org/10.1063/1.3520323>. URL <http://scitation.aip.org/content/aip/proceeding/aipcp/10.1063/1.3520323>.
- Benedetti, C., Schroeder, C., Esarey, E., and Leemans, W. Efficient modeling of laser-plasma accelerators using the ponderomotive-based code inf&rno. *Proceedings of ICAP2012, Rostock-Warnemünde*,

- Germany, page THAAI2, 2012a. URL <http://accelconf.web.cern.ch/accelconf/icap2012/papers/thaa2.pdf>.
- Benedetti, C., Schroeder, C. B., Esarey, E., and Leemans, W. P. Quasi-matched propagation of ultra-short, intense laser pulses in plasma channels. *Physics of Plasmas (1994-present)*, 19(5):053101, 2012b. doi: <http://dx.doi.org/10.1063/1.4707393>. URL <http://scitation.aip.org/content/aip/journal/pop/19/5/10.1063/1.4707393>.
- Berezhiani, V. and Murusidze, I. Relativistic wake-field generation by an intense laser pulse in a plasma. *Physics Letters A*, 148(6-7):338 – 340, 1990. ISSN 0375-9601. doi: [http://dx.doi.org/10.1016/0375-9601\(90\)90813-4](http://dx.doi.org/10.1016/0375-9601(90)90813-4). URL <http://www.sciencedirect.com/science/article/pii/0375960190908134>.
- Berezhiani, V. I. and Murusidze, I. G. Interaction of highly relativistic short laser pulses with plasmas and nonlinear wake-field generation. *Physica Scripta*, 45(2):87, 1992. URL <http://stacks.iop.org/1402-4896/45/i=2/a=007>.
- Birdsall, C. and Langdon, A. *Plasma physics via computer simulation*. The Adam Hilger series on plasma physics. McGraw-Hill, 1985. ISBN 9780070053717.
- Birdsall, C. K. and Maron, N. Plasma self-heating and saturation due to numerical instabilities. *Journal of Computational Physics*, 36(1):1 – 19, 1980. ISSN 0021-9991. doi: [http://dx.doi.org/10.1016/0021-9991\(80\)90171-0](http://dx.doi.org/10.1016/0021-9991(80)90171-0). URL <http://www.sciencedirect.com/science/article/pii/0021999180901710>.
- Blumenfeld, I., Clayton, C. E., Decker, F.-J., Hogan, M. J., Huang, C., Ischebeck, R., Iverson, R., Joshi, C., Katsouleas, T., Kirby, N., Lu, W., Marsh, K. A., Mori, W. B., Muggli, P., Oz, E., Siemann, R. H., Walz, D., and Zhou, M. Energy doubling of 42 gev electrons in a metre-scale plasma wakefield accelerator. *Nature*, 445(7129):741–744, 02 2007. URL <http://dx.doi.org/10.1038/nature05538>.
- Boris, J. P. Relativistic plasma simulation-optimization of a hybrid code. In *Proceedings of the Fourth Conference on Numerical Simulation Plasmas*, pages 3–67, Washington, D.C., November 1970. Naval Research Laboratory.
- Bourgeois, N., Cowley, J., and Hooker, S. M. Two-pulse ionization injection into quasilinear laser wakefields. *Phys. Rev. Lett.*, 111:155004, Oct 2013. doi: [10.1103/PhysRevLett.111.155004](https://doi.org/10.1103/PhysRevLett.111.155004). URL <http://link.aps.org/doi/10.1103/PhysRevLett.111.155004>.
- Bradt, H. *Astrophysics Processes: The Physics of Astronomical Phenomena*. Cambridge University Press, 2008. ISBN 9781139469586. URL <http://www.cambridge.org/us/catalogue/catalogue.asp?isbn=9780521846561>.

- Brantov, A. V., Esirkepov, T. Z., Kando, M., Kotaki, H., Bychenkov, V. Y., and Bulanov, S. V. Controlled electron injection into the wake wave using plasma density inhomogeneity. *Physics of Plasmas (1994-present)*, 15(7):073111, 2008. doi: <http://dx.doi.org/10.1063/1.2956989>. URL <http://scitation.aip.org/content/aip/journal/pop/15/7/10.1063/1.2956989>.
- Buck, A., Wenz, J., Xu, J., Khrennikov, K., Schmid, K., Heigoldt, M., Mikhailova, J. M., Geissler, M., Shen, B., Krausz, F., Karsch, S., and Veisz, L. Shock-front injector for high-quality laser-plasma acceleration. *Phys. Rev. Lett.*, 110:185006, May 2013. doi: 10.1103/PhysRevLett.110.185006. URL <http://link.aps.org/doi/10.1103/PhysRevLett.110.185006>.
- Bulanov, S., Naumova, N., Pegoraro, F., and Sakai, J. Particle injection into the wave acceleration phase due to nonlinear wake wave breaking. *Phys. Rev. E*, 58:R5257–R5260, Nov 1998a. doi: 10.1103/PhysRevE.58.R5257. URL <http://link.aps.org/doi/10.1103/PhysRevE.58.R5257>.
- Bulanov, S., Pegoraro, F., and ichi Sakai, J. Variety of nonlinear wave-breaking. *Nuclear Instruments and Methods in Physics Research Section A: Accelerators, Spectrometers, Detectors and Associated Equipment*, 410(3):477 – 487, June 1998b. ISSN 0168-9002. doi: [http://dx.doi.org/10.1016/S0168-9002\(98\)00155-7](http://dx.doi.org/10.1016/S0168-9002(98)00155-7). URL <http://www.sciencedirect.com/science/article/pii/S0168900298001557>.
- Bulanov, S. V., Kirsanov, V. I., and Sakharov, A. S. Excitation of ultrarelativistic plasma waves by pulse of electromagnetic radiation. *JETP Lett.*, 50:198, 1989. URL [http://www.jetpletters.ac.ru/ps/1127/article\\_17078.shtml](http://www.jetpletters.ac.ru/ps/1127/article_17078.shtml).
- Bulanov, S. V., Inovenkov, I. N., Kirsanov, V. I., Naumova, N. M., and Sakharov, A. S. Nonlinear depletion of ultrashort and relativistically strong laser pulses in an underdense plasma. *Physics of Fluids B: Plasma Physics (1989-1993)*, 4(7):1935–1942, 1992. doi: <http://dx.doi.org/10.1063/1.860046>. URL <http://scitation.aip.org/content/aip/journal/pofb/4/7/10.1063/1.860046>.
- Bulanov, S. V., Pegoraro, F., Pukhov, A. M., and Sakharov, A. S. Transverse-wake wave breaking. *Phys. Rev. Lett.*, 78:4205–4208, Jun 1997. doi: 10.1103/PhysRevLett.78.4205. URL <http://link.aps.org/doi/10.1103/PhysRevLett.78.4205>.
- Bulanov, S. V., Esirkepov, T. Z., Kando, M., Koga, J. K., Pirozhkov, A. S., Nakamura, T., Bulanov, S. S., Schroeder, C. B., Esarey, E., Califano, F., and Pegoraro, F. On the breaking of a plasma wave in a thermal plasma. i. the structure of the density singularity. *Physics of Plasmas (1994-present)*, 19(11):113102, 2012a. doi: <http://dx.doi.org/>

- 10.1063/1.4764052. URL <http://scitation.aip.org/content/aip/journal/pop/19/11/10.1063/1.4764052>.
- Bulanov, S. V., Esirkepov, T. Z., Kando, M., Koga, J. K., Pirozhkov, A. S., Nakamura, T., Bulanov, S. S., Schroeder, C. B., Esarey, E., Califano, F., and Pegoraro, F. On the breaking of a plasma wave in a thermal plasma. ii. electromagnetic wave interaction with the breaking plasma wave. *Physics of Plasmas (1994-present)*, 19(11):113103, 2012b. doi: <http://dx.doi.org/10.1063/1.4764056>. URL <http://scitation.aip.org/content/aip/journal/pop/19/11/10.1063/1.4764056>.
- Butcher, J. *Numerical Methods for Ordinary Differential Equations*. Wiley, 2008. ISBN 9780470753750.
- Caldwell, A., Lotov, K., Pukhov, A., and Simon, F. Proton-driven plasma-wakefield acceleration. *Nat Phys*, 5(5):363–367, May 2009. ISSN 1745-2473. URL <http://dx.doi.org/10.1038/nphys1248>.
- Callen, J. D. Fundamentals of plasma physics. University of Wisconsin, Madison, June 2006. URL <http://homepages.cae.wisc.edu/~callen/book.html>. Draft Material for Fundamentals of Plasma Physics book.
- Chen, F. *Introduction to Plasma Physics and Controlled Fusion*. Number Bd. 1. Springer, 2010. ISBN 9781441932013.
- Chen, M., Esarey, E., Schroeder, C. B., Geddes, C. G. R., and Lee-mans, W. P. Theory of ionization-induced trapping in laser-plasma accelerators. *Physics of Plasmas (1994-present)*, 19(3):033101, 2012. doi: <http://dx.doi.org/10.1063/1.3689922>. URL <http://scitation.aip.org/content/aip/journal/pop/19/3/10.1063/1.3689922>.
- Chen, P., Dawson, J. M., Huff, R. W., and Katsouleas, T. Acceleration of electrons by the interaction of a bunched electron beam with a plasma. *Phys. Rev. Lett.*, 54:693–696, Feb 1985. doi: 10.1103/PhysRevLett.54.693. URL <http://link.aps.org/doi/10.1103/PhysRevLett.54.693>.
- Chen, P., Su, J. J., Dawson, J. M., Bane, K. L. F., and Wilson, P. B. Energy transfer in the plasma wake-field accelerator. *Phys. Rev. Lett.*, 56:1252–1255, Mar 1986. doi: 10.1103/PhysRevLett.56.1252. URL <http://link.aps.org/doi/10.1103/PhysRevLett.56.1252>.
- Chen, P., Oide, K., Sessler, A., and Yu, S. AN ADIABATIC FOCUSER. *Part.Accel.*, 31:7–20, 1990a. URL <http://www.slac.stanford.edu/pubs/slacpubs/5000/slac-pub-5060.html>.
- Chen, P., Oide, K., Sessler, A. M., and Yu, S. S. Plasma-based adiabatic focuser. *Phys. Rev. Lett.*, 64:1231–1234, Mar 1990b. doi:

- 10.1103/PhysRevLett.64.1231. URL <http://link.aps.org/doi/10.1103/PhysRevLett.64.1231>.
- Chen, X. L. and Sudan, R. N. Two-dimensional self-focusing of short intense laser pulse in underdense plasma. *Physics of Fluids B: Plasma Physics*, 5(4):1336–1348, 1993. doi: 10.1063/1.860923. URL <http://link.aip.org/link/?PFB/5/1336/1>.
- Cheshkov, S., Tajima, T., Horton, W., and Yokoya, K. Particle dynamics in multistage wakefield collider. *Phys. Rev. ST Accel. Beams*, 3:071301, Jul 2000. doi: 10.1103/PhysRevSTAB.3.071301. URL <http://link.aps.org/doi/10.1103/PhysRevSTAB.3.071301>.
- Chien, T.-Y., Chang, C.-L., Lee, C.-H., Lin, J.-Y., Wang, J., and Chen, S.-Y. Spatially localized self-injection of electrons in a self-modulated laser-wakefield accelerator by using a laser-induced transient density ramp. *Phys. Rev. Lett.*, 94:115003, Mar 2005. doi: 10.1103/PhysRevLett.94.115003. URL <http://link.aps.org/doi/10.1103/PhysRevLett.94.115003>.
- Clayton, C. E., Ralph, J. E., Albert, F., Fonseca, R. A., Glenzer, S. H., Joshi, C., Lu, W., Marsh, K. A., Martins, S. F., Mori, W. B., Pak, A., Tsung, F. S., Pollock, B. B., Ross, J. S., Silva, L. O., and Froula, D. H. Self-guided laser wakefield acceleration beyond 1 gev using ionization-induced injection. *Phys. Rev. Lett.*, 105:105003, Sep 2010. doi: 10.1103/PhysRevLett.105.105003. URL <http://link.aps.org/doi/10.1103/PhysRevLett.105.105003>.
- Cormier-Michel, E., Shadwick, B. A., Geddes, C. G. R., Esarey, E., Schroeder, C. B., and Leemans, W. P. Unphysical kinetic effects in particle-in-cell modeling of laser wakefield accelerators. *Phys. Rev. E*, 78:016404, Jul 2008. doi: 10.1103/PhysRevE.78.016404. URL <http://link.aps.org/doi/10.1103/PhysRevE.78.016404>.
- Cormier-Michel, E., Esarey, E., Geddes, C. G. R., Schroeder, C. B., Paul, K., Mullaney, P. J., Cary, J. R., and Leemans, W. P. Control of focusing fields in laser-plasma accelerators using higher-order modes. *Phys. Rev. ST Accel. Beams*, 14:031303, Mar 2011. doi: 10.1103/PhysRevSTAB.14.031303. URL <http://link.aps.org/doi/10.1103/PhysRevSTAB.14.031303>.
- Courant, E. and Snyder, H. Theory of the alternating-gradient synchrotron. *Annals of Physics*, 3(1):1 – 48, 1958. ISSN 0003-4916. doi: [http://dx.doi.org/10.1016/0003-4916\(58\)90012-5](http://dx.doi.org/10.1016/0003-4916(58)90012-5). URL <http://www.sciencedirect.com/science/article/pii/0003491658900125>.
- Courant, R., Friedrichs, K., and Lewy, H. über die partiellen differenzgleichungen der mathematischen physik. *Mathematische An-*

- nalen*, 100(1):32–74, 1928. ISSN 0025-5831. doi: 10.1007/BF01448839. URL <http://dx.doi.org/10.1007/BF01448839>.
- Cowan, B. M., Bruhwiler, D. L., Cormier-Michel, E., Esarey, E., Geddes, C. G., Messmer, P., and Paul, K. M. Characteristics of an envelope model for laser-plasma accelerator simulation. *Journal of Computational Physics*, 230(1):61 – 86, 2011. ISSN 0021-9991. doi: <http://dx.doi.org/10.1016/j.jcp.2010.09.009>. URL <http://www.sciencedirect.com/science/article/pii/S0021999110005036>.
- Dawson, J. M. Nonlinear electron oscillations in a cold plasma. *Phys. Rev.*, 113:383–387, Jan 1959. doi: 10.1103/PhysRev.113.383. URL <http://link.aps.org/doi/10.1103/PhysRev.113.383>.
- Dawson, J. M. Particle simulation of plasmas. *Rev. Mod. Phys.*, 55: 403–447, Apr 1983. doi: 10.1103/RevModPhys.55.403. URL <http://link.aps.org/doi/10.1103/RevModPhys.55.403>.
- Decker, C. D. and Mori, W. B. Group velocity of large amplitude electromagnetic waves in a plasma. *Phys. Rev. Lett.*, 72:490–493, Jan 1994. doi: 10.1103/PhysRevLett.72.490. URL <http://link.aps.org/doi/10.1103/PhysRevLett.72.490>.
- Durfee, C. G., Lynch, J., and Milchberg, H. M. Development of a plasma waveguide for high-intensity laser pulses. *Phys. Rev. E*, 51: 2368–2389, Mar 1995. doi: 10.1103/PhysRevE.51.2368. URL <http://link.aps.org/doi/10.1103/PhysRevE.51.2368>.
- Edwards, D. A. and Syphers, M. J. *An Introduction to the Physics of High Energy Accelerators*. Wiley Series in Beam Physics and Accelerator Technology. Wiley, 2008. ISBN 9783527617289.
- Esarey, E. and Pilloff, M. Trapping and acceleration in nonlinear plasma waves. *Physics of Plasmas (1994-present)*, 2 (5):1432–1436, 1995. doi: <http://dx.doi.org/10.1063/1.871358>. URL <http://scitation.aip.org/content/aip/journal/pop/2/5/10.1063/1.871358>.
- Esarey, E., Sprangle, P., Krall, J., Ting, A., and Joyce, G. Optically guided laser wake-field acceleration. *Physics of Fluids B: Plasma Physics*, 5(7):2690–2697, 1993. doi: 10.1063/1.860707. URL <http://link.aip.org/link/?PFB/5/2690/1>.
- Esarey, E., Sprangle, P., Krall, J., and Ting, A. Overview of plasma-based accelerator concepts. *Plasma Science, IEEE Transactions on*, 24(2):252–288, Apr 1996. ISSN 0093-3813. doi: 10.1109/27.509991. URL <http://dx.doi.org/10.1109/27.509991>.
- Esarey, E., Catravas, P., and Leemans, W. P. Betatron radiation from electron beams in plasma focusing channels. *AIP Conference Proceedings*, 569(1):473–486, 2001. doi: <http://dx.doi.org/10.1063/1.1361111>.

- 1063/1.1384377. URL <http://scitation.aip.org/content/aip/proceeding/aipcp/10.1063/1.1384377>.
- Esarey, E., Shadwick, B. A., Schroeder, C. B., and Leemans, W. P. Nonlinear pump depletion and electron dephasing in laser wake-field accelerators. *AIP Conference Proceedings*, 737(1):578–584, 2004. doi: <http://dx.doi.org/10.1063/1.1842594>. URL <http://scitation.aip.org/content/aip/proceeding/aipcp/10.1063/1.1842594>.
- Esarey, E., Schroeder, C. B., and Leemans, W. P. Physics of laser-driven plasma-based electron accelerators. *Rev. Mod. Phys.*, 81:1229–1285, Aug 2009. doi: [10.1103/RevModPhys.81.1229](https://doi.org/10.1103/RevModPhys.81.1229). URL <http://link.aps.org/doi/10.1103/RevModPhys.81.1229>.
- Esirkepov, T. Z. Exact charge conservation scheme for particle-in-cell simulation with an arbitrary form-factor. *Computer Physics Communications*, 135(2):144 – 153, 2001. ISSN 0010-4655. doi: [http://dx.doi.org/10.1016/S0010-4655\(00\)00228-9](http://dx.doi.org/10.1016/S0010-4655(00)00228-9). URL <http://www.sciencedirect.com/science/article/pii/S0010465500002289>.
- Faure, J., Glinec, Y., Pukhov, A., Kiselev, S., Gordienko, S., Lefebvre, E., Rousseau, J.-P., Burgy, F., and Malka, V. A laser-plasma accelerator producing monoenergetic electron beams. *Nature*, 431(7008):541–544, Sept. 2004. ISSN 0028-0836. URL <http://dx.doi.org/10.1038/nature02963>.
- Faure, J., Rechatin, C., Norlin, A., Lifschitz, A., Glinec, Y., and Malka, V. Controlled injection and acceleration of electrons in plasma wakefields by colliding laser pulses. *Nature*, 444(7120):737–739, 12 2006. URL <http://dx.doi.org/10.1038/nature05393>.
- Feng, B., Huang, C., Decyk, V., Mori, W., Muggli, P., and Katsouleas, T. Enhancing parallel quasi-static particle-in-cell simulations with a pipelining algorithm. *Journal of Computational Physics*, 228(15): 5340 – 5348, 2009. ISSN 0021-9991. doi: <http://dx.doi.org/10.1016/j.jcp.2009.04.019>. URL <http://www.sciencedirect.com/science/article/pii/S002199910900206X>.
- Fließbach, T. *Elektrodynamik*. Fließbach, Torsten: Lehrbuch zur theoretischen Physik. Spektrum Akademischer Verlag GmbH, 2005. ISBN 9783827415301.
- Floettmann, K. Some basic features of the beam emittance. *Phys. Rev. ST Accel. Beams*, 6:034202, Mar 2003. doi: [10.1103/PhysRevSTAB.6.034202](https://doi.org/10.1103/PhysRevSTAB.6.034202). URL <http://link.aps.org/doi/10.1103/PhysRevSTAB.6.034202>.
- Floettmann, K. Adiabatic matching section for plasma accelerated beams. *Phys. Rev. ST Accel. Beams*, 17:054402, May 2014. doi: [10.1103/PhysRevSTAB.17.054402](https://doi.org/10.1103/PhysRevSTAB.17.054402). URL <http://link.aps.org/doi/10.1103/PhysRevSTAB.17.054402>.

- Fonseca, R. A., Silva, L. O., Tsung, F. S., Decyk, V. K., Lu, W., Ren, C., Mori, W. B., Deng, S., Lee, S., Katsouleas, T., and Adam, J. C. OSIRIS: A three-dimensional, fully relativistic particle in cell code for modeling plasma based accelerators. In Sloot, P., Hoekstra, A., Tan, C., and Dongarra, J., editors, *Computational Science - ICCS 2002*, volume 2331 of *Lecture Notes in Computer Science*, pages 342–351. Springer Berlin Heidelberg, 2002. ISBN 978-3-540-43594-5. doi: 10.1007/3-540-47789-6\_36. URL [http://dx.doi.org/10.1007/3-540-47789-6\\_36](http://dx.doi.org/10.1007/3-540-47789-6_36).
- Fonseca, R. A., Martins, S. F., Silva, L. O., W., T. J., Tsung, F. S., and B., M. W. One-to-one direct modeling of experiments and astrophysical scenarios: pushing the envelope on kinetic plasma simulations. *Plasma Physics and Controlled Fusion*, 50(12):124034, 2008. URL <http://stacks.iop.org/0741-3335/50/i=12/a=124034>.
- Fonseca, R. A., Vieira, J., Fiuza, F., Davidson, A., Tsung, F. S., Mori, W. B., and Silva, L. O. Exploiting multi-scale parallelism for large scale numerical modelling of laser wakefield accelerators. *Plasma Physics and Controlled Fusion*, 55(12):124011, 2013. URL <http://stacks.iop.org/0741-3335/55/i=12/a=124011>.
- Frigo, M. and Johnson, S. The Design and Implementation of FFTW3. *Proceedings of the IEEE*, 93(2):216–231, 2005. ISSN 0018-9219. doi: 10.1109/JPROC.2004.840301. URL <http://dx.doi.org/10.1109/JPROC.2004.840301>.
- Fuchs, M., Weingartner, R., Popp, A., Major, Z., Becker, S., Osterhoff, J., Cortrie, I., Zeitler, B., Horlein, R., Tsakiris, G. D., Schramm, U., Rowlands-Rees, T. P., Hooker, S. M., Habs, D., Krausz, F., Karsch, S., and Gruner, F. Laser-driven soft-x-ray undulator source. *Nat Phys*, 5(11):826–829, Nov. 2009. ISSN 1745-2473. URL <http://dx.doi.org/10.1038/nphys1404>.
- Geddes, C. G. R., Toth, C., van Tilborg, J., Esarey, E., Schroeder, C. B., Bruhwiler, D., Nieter, C., Cary, J., and Leemans, W. P. High-quality electron beams from a laser wakefield accelerator using plasma-channel guiding. *Nature*, 431(7008):538–541, Sept. 2004. ISSN 0028-0836. URL <http://dx.doi.org/10.1038/nature02900>.
- Geddes, C. G. R., Nakamura, K., Plateau, G. R., Toth, C., Cormier-Michel, E., Esarey, E., Schroeder, C. B., Cary, J. R., and Leemans, W. P. Plasma-density-gradient injection of low absolute-momentum-spread electron bunches. *Phys. Rev. Lett.*, 100:215004, May 2008. doi: 10.1103/PhysRevLett.100.215004. URL <http://link.aps.org/doi/10.1103/PhysRevLett.100.215004>.
- Gibbon, P. *Short Pulse Laser Interactions with Matter : An Introduction*. London: Imperial College, 2005.



- Godfrey, B. B. Numerical Cherenkov instabilities in electromagnetic particle codes. *Journal of Computational Physics*, 15(4):504 – 521, 1974. ISSN 0021-9991. doi: [http://dx.doi.org/10.1016/0021-9991\(74\)90076-X](http://dx.doi.org/10.1016/0021-9991(74)90076-X). URL <http://www.sciencedirect.com/science/article/pii/002199917490076X>.
- Gonsalves, A. J., Nakamura, K., Lin, C., Panasenko, D., Shiraishi, S., Sokollik, T., Benedetti, C., Schroeder, C. B., Geddes, C. G. R., van Tilborg, J., Osterhoff, J., Esarey, E., Toth, C., and Leemans, W. P. Tunable laser plasma accelerator based on longitudinal density tailoring. *Nat Phys*, 7(11):862–866, Nov. 2011. ISSN 1745-2473. URL <http://dx.doi.org/10.1038/nphys2071>.
- Gorbunov, L. M. and Kirsanov, V. I. Excitation of plasma waves by an electromagnetic wave packet. *Sov. Phys. JETP*, 66:290, 1987. URL [http://www.jetp.ac.ru/cgi-bin/dn/e\\_066\\_02\\_0290.pdf](http://www.jetp.ac.ru/cgi-bin/dn/e_066_02_0290.pdf). [Zh. Eksp. Teor. Fiz. 93, 509 (1987)].
- Greenwood, A. D., Cartwright, K. L., Luginsland, J. W., and Baca, E. A. On the elimination of numerical Cerenkov radiation in PIC simulations. *Journal of Computational Physics*, 201(2):665 – 684, 2004. ISSN 0021-9991. doi: <http://dx.doi.org/10.1016/j.jcp.2004.06.021>. URL <http://www.sciencedirect.com/science/article/pii/S0021999104002608>.
- Hidding, B., Amthor, K.-U., Liesfeld, B., Schworer, H., Karsch, S., Geissler, M., Veisz, L., Schmid, K., Gallacher, J. G., Jamison, S. P., Jaroszynski, D., Pretzler, G., and Sauerbrey, R. Generation of quasi-monoenergetic electron bunches with 80-fs laser pulses. *Phys. Rev. Lett.*, 96:105004, Mar 2006. doi: 10.1103/PhysRevLett.96.105004. URL <http://link.aps.org/doi/10.1103/PhysRevLett.96.105004>.
- Hidding, B., Pretzler, G., Rosenzweig, J. B., Königstein, T., Schiller, D., and Bruhwiler, D. L. Ultracold electron bunch generation via plasma photocathode emission and acceleration in a beam-driven plasma blowout. *Phys. Rev. Lett.*, 108:035001, Jan 2012. doi: 10.1103/PhysRevLett.108.035001. URL <http://link.aps.org/doi/10.1103/PhysRevLett.108.035001>.
- Hockney, R. Measurements of collision and heating times in a two-dimensional thermal computer plasma. *Journal of Computational Physics*, 8(1):19 – 44, 1971. ISSN 0021-9991. doi: [http://dx.doi.org/10.1016/0021-9991\(71\)90032-5](http://dx.doi.org/10.1016/0021-9991(71)90032-5). URL <http://www.sciencedirect.com/science/article/pii/0021999171900325>.
- Hockney, R. and Eastwood, J. *Computer Simulation Using Particles*. Advanced book program: Addison-Wesley. McGraw-Hill, 1981. ISBN 9780070291089.

- Hogan, M. J., Raubenheimer, T. O., Seryi, A., Muggli, P., Katsouleas, T., Huang, C., Lu, W., An, W., Marsh, K. A., Mori, W. B., Clayton, C. E., and Joshi, C. Plasma wakefield acceleration experiments at facet. *New Journal of Physics*, 12(5):055030, 2010. URL <http://stacks.iop.org/1367-2630/12/i=5/a=055030>.
- Hooker, S. M. Developments in laser-driven plasma accelerators. *Nat Photon*, 7(10):775–782, Oct. 2013. ISSN 1749-4885. URL <http://dx.doi.org/10.1038/nphoton.2013.234>.
- Huang, C., Decyk, V., Ren, C., Zhou, M., Lu, W., Mori, W., Cooley, J., Jr., T. A., and Katsouleas, T. Quickpic: A highly efficient particle-in-cell code for modeling wakefield acceleration in plasmas. *Journal of Computational Physics*, 217(2):658 – 679, 2006. ISSN 0021-9991. doi: 10.1016/j.jcp.2006.01.039. URL <http://www.sciencedirect.com/science/article/pii/S0021999106000283>.
- Huang, Z., Ding, Y., and Schroeder, C. B. Compact x-ray free-electron laser from a laser-plasma accelerator using a transverse-gradient undulator. *Phys. Rev. Lett.*, 109:204801, Nov 2012. doi: 10.1103/PhysRevLett.109.204801. URL <http://link.aps.org/doi/10.1103/PhysRevLett.109.204801>.
- Jackson, J. D. *Classical Electrodynamics Third Edition*. Wiley, third edition, Aug. 1998. ISBN 047130932X.
- Katsouleas, T. Physical mechanisms in the plasma wake-field accelerator. *Phys. Rev. A*, 33:2056–2064, Mar 1986. doi: 10.1103/PhysRevA.33.2056. URL <http://link.aps.org/doi/10.1103/PhysRevA.33.2056>.
- Keinigs, R. and Jones, M. E. Two-dimensional dynamics of the plasma wakefield accelerator. *Physics of Fluids (1958-1988)*, 30(1):252–263, 1987. doi: <http://dx.doi.org/10.1063/1.866183>. URL <http://scitation.aip.org/content/aip/journal/pof1/30/1/10.1063/1.866183>.
- Khachatryan, A. G., Irman, A., van Goor, F. A., and Boller, K.-J. Femtosecond electron-bunch dynamics in laser wakefields and vacuum. *Phys. Rev. ST Accel. Beams*, 10:121301, Dec 2007. doi: 10.1103/PhysRevSTAB.10.121301. URL <http://link.aps.org/doi/10.1103/PhysRevSTAB.10.121301>.
- Kim, H. T., Pae, K. H., Cha, H. J., Kim, I. J., Yu, T. J., Sung, J. H., Lee, S. K., Jeong, T. M., and Lee, J. Enhancement of electron energy to the multi-gev regime by a dual-stage laser-wakefield accelerator pumped by petawatt laser pulses. *Phys. Rev. Lett.*, 111:165002, Oct 2013. doi: 10.1103/PhysRevLett.111.165002. URL <http://link.aps.org/doi/10.1103/PhysRevLett.111.165002>.

- Kim, J. U., Hafz, N., and Suk, H. Electron trapping and acceleration across a parabolic plasma density profile. *Phys. Rev. E*, 69: 026409, Feb 2004. doi: 10.1103/PhysRevE.69.026409. URL <http://link.aps.org/doi/10.1103/PhysRevE.69.026409>.
- Kneip, S., McGuffey, C., Martins, J. L., Martins, S. F., Bellei, C., Chvykov, V., Dollar, F., Fonseca, R., Huntington, C., Kalintchenko, G., Maksimchuk, A., Mangles, S. P. D., Matsuoka, T., Nagel, S. R., Palmer, C. A. J., Schreiber, J., Phuoc, K. T., Thomas, A. G. R., Yanovsky, V., Silva, L. O., Krushelnick, K., and Najmudin, Z. Bright spatially coherent synchrotron x-rays from a table-top source. *Nat Phys*, 6(12):980–983, Dec. 2010. ISSN 1745-2473. URL <http://dx.doi.org/10.1038/nphys1789>.
- Kostyukov, I., Pukhov, A., and Kiselev, S. Phenomenological theory of laser-plasma interaction in bubble regime. *Physics of Plasmas (1994-present)*, 11(11):5256–5264, 2004. doi: <http://dx.doi.org/10.1063/1.1799371>. URL <http://scitation.aip.org/content/aip/journal/pop/11/11/10.1063/1.1799371>.
- Krall, J., Nguyen, K., and Joyce, G. Numerical simulations of axisymmetric erosion processes in ion-focused regime-transported beams. *Physics of Fluids B: Plasma Physics (1989-1993)*, 1(10):2099–2105, 1989. doi: <http://dx.doi.org/10.1063/1.859074>. URL <http://scitation.aip.org/content/aip/journal/pofb/1/10/10.1063/1.859074>.
- Kruer, W. L. *The Physics of Laser Plasma Interactions*. Addison-Wesley, Redwood City, 1988.
- Kubo, K., Mtingwa, S. K., and Wolski, A. Intrabeam scattering formulas for high energy beams. *Phys. Rev. ST Accel. Beams*, 8: 081001, Aug 2005. doi: 10.1103/PhysRevSTAB.8.081001. URL <http://link.aps.org/doi/10.1103/PhysRevSTAB.8.081001>.
- Landau, L. and Lifšic, E. *Klassische Feldtheorie*. Lehrbuch der theoretischen Physik. Deutsch, 1976. ISBN 9783817113279.
- Langdon, A. Effects of the spatial grid in simulation plasmas. *Journal of Computational Physics*, 6(2):247 – 267, 1970. ISSN 0021-9991. doi: [http://dx.doi.org/10.1016/0021-9991\(70\)90024-0](http://dx.doi.org/10.1016/0021-9991(70)90024-0). URL <http://www.sciencedirect.com/science/article/pii/0021999170900240>.
- Lawson, J. D. Lasers and accelerators. *Nuclear Science, IEEE Transactions on*, 26(3):4217–4219, 1979. ISSN 0018-9499. doi: 10.1109/TNS.1979.4330749.
- Leemans, W. and Esarey, E. Laser-driven plasma-wave electron accelerators. *Physics Today*, 62(3):44, 2009. ISSN 00319228. doi: 10.1063/1.3099645. URL <http://link.aip.org/link/PHTOAD/v62/i3/p44/s1&Agg=doi>.

- Leemans, W. P., Nagler, B., Gonsalves, A. J., Toth, C., Nakamura, K., Geddes, C. G. R., Esarey, E., Schroeder, C. B., and Hooker, S. M. GeV electron beams from a centimetre-scale accelerator. *Nat Phys*, 2 (10):696–699, Oct. 2006. ISSN 1745-2473. URL <http://dx.doi.org/10.1038/nphys418>.
- Leemans, W. P., Duarte, R., Esarey, E., Fournier, S., Geddes, C. G. R., Lockhart, D., Schroeder, C. B., Toth, C., Vay, J.-L., and Zimmermann, S. The berkeley lab laser accelerator (bella): A 10 gev laser plasma accelerator. *AIP Conference Proceedings*, 1299(1):3–11, 2010. doi: <http://dx.doi.org/10.1063/1.3520352>. URL <http://scitation.aip.org/content/aip/proceeding/aipcp/10.1063/1.3520352>.
- Lehe, R., Lifschitz, A., Thaury, C., Malka, V., and Davoine, X. Numerical growth of emittance in simulations of laser-wakefield acceleration. *Phys. Rev. ST Accel. Beams*, 16:021301, Feb 2013. doi: [10.1103/PhysRevSTAB.16.021301](http://dx.doi.org/10.1103/PhysRevSTAB.16.021301). URL <http://link.aps.org/doi/10.1103/PhysRevSTAB.16.021301>.
- Li, F., Hua, J. F., Xu, X. L., Zhang, C. J., Yan, L. X., Du, Y. C., Huang, W. H., Chen, H. B., Tang, C. X., Lu, W., Joshi, C., Mori, W. B., and Gu, Y. Q. Generating high-brightness electron beams via ionization injection by transverse colliding lasers in a plasma-wakefield accelerator. *Phys. Rev. Lett.*, 111:015003, Jul 2013. doi: [10.1103/PhysRevLett.111.015003](http://dx.doi.org/10.1103/PhysRevLett.111.015003). URL <http://link.aps.org/doi/10.1103/PhysRevLett.111.015003>.
- Lilje, L., Kako, E., Kostin, D., Matheisen, A., Möller, W.-D., Proch, D., Reschke, D., Saito, K., Schmüser, P., Simrock, S., Suzuki, T., and Twarowski, K. Achievement of 35 mv/m in the superconducting nine-cell cavities for TESLA. *Nuclear Instruments and Methods in Physics Research Section A: Accelerators, Spectrometers, Detectors and Associated Equipment*, 524(1-3):1–12, 2004. ISSN 0168-9002. doi: <http://dx.doi.org/10.1016/j.nima.2004.01.045>. URL <http://www.sciencedirect.com/science/article/pii/S0168900204001391>.
- Lindman, E. Dispersion relation for computer-simulated plasmas. *Journal of Computational Physics*, 5(1):13 – 22, 1970. ISSN 0021-9991. doi: [http://dx.doi.org/10.1016/0021-9991\(70\)90049-5](http://dx.doi.org/10.1016/0021-9991(70)90049-5). URL <http://www.sciencedirect.com/science/article/pii/0021999170900495>.
- Linssen, L., Miyamoto, A., Stanitzki, M., and Weerts, H. Physics and Detectors at CLIC: CLIC Conceptual Design Report. *arXiv*, 2012. doi: [10.5170/CERN-2012-003](https://doi.org/10.5170/CERN-2012-003).
- Lotov, K. V. Fine wakefield structure in the blowout regime of plasma wakefield accelerators. *Phys. Rev. ST Accel. Beams*, 6:061301, Jun 2003. doi: [10.1103/PhysRevSTAB.6.061301](http://dx.doi.org/10.1103/PhysRevSTAB.6.061301). URL <http://link.aps.org/doi/10.1103/PhysRevSTAB.6.061301>.

- Lotov, K. V. Blowout regimes of plasma wakefield acceleration. *Phys. Rev. E*, 69:046405, Apr 2004. doi: 10.1103/PhysRevE.69.046405. URL <http://link.aps.org/doi/10.1103/PhysRevE.69.046405>.
- Lotov, K. V. Efficient operating mode of the plasma wakefield accelerator. *Physics of Plasmas (1994-present)*, 12(5):053105, 2005. doi: <http://dx.doi.org/10.1063/1.1889444>. URL <http://scitation.aip.org/content/aip/journal/pop/12/5/10.1063/1.1889444>.
- Lu, W., Huang, C., Zhou, M., Mori, W. B., and Katsouleas, T. Nonlinear theory for relativistic plasma wakefields in the blowout regime. *Phys. Rev. Lett.*, 96:165002, Apr 2006. doi: 10.1103/PhysRevLett.96.165002. URL <http://link.aps.org/doi/10.1103/PhysRevLett.96.165002>.
- Maier, A. R., Meseck, A., Reiche, S., Schroeder, C. B., Seggebrock, T., and Grüner, F. Demonstration scheme for a laser-plasma-driven free-electron laser. *Phys. Rev. X*, 2:031019, Sep 2012. doi: 10.1103/PhysRevX.2.031019. URL <http://link.aps.org/doi/10.1103/PhysRevX.2.031019>.
- Mangles, S. P. D., Murphy, C. D., Najmudin, Z., Thomas, A. G. R., Collier, J. L., Dangor, A. E., Divall, E. J., Foster, P. S., Gallacher, J. G., Hooker, C. J., Jaroszynski, D. A., Langley, A. J., Mori, W. B., Norreys, P. A., Tsung, F. S., Viskup, R., Walton, B. R., and Krushelnick, K. Monoenergetic beams of relativistic electrons from intense laser-plasma interactions. *Nature*, 431(7008):535–538, Sept. 2004. ISSN 0028-0836. URL <http://dx.doi.org/10.1038/nature02939>.
- Marsh, K., Clayton, C., Johnson, D., Huang, C., Joshi, C., Lu, W., Mori, W., Zhou, M., Barnes, C., Decker, F.-J., Hogan, M., Iverson, R., Krejcik, P., O'Connell, C., Siemann, R., Walz, D., Deng, S., Katsouleas, T. C., Muggli, P., and Oz, E. Beam matching to a plasma wake field accelerator using a ramped density profile at the plasma boundary. In *Particle Accelerator Conference, 2005. PAC 2005. Proceedings of the*, pages 2702–2704, 2005. doi: 10.1109/PAC.2005.1591234.
- McGuffey, C., Thomas, A. G. R., Schumaker, W., Matsuoka, T., Chvykov, V., Dollar, F. J., Kalintchenko, G., Yanovsky, V., Maksimchuk, A., Krushelnick, K., Bychenkov, V. Y., Glazyrin, I. V., and Karpeev, A. V. Ionization induced trapping in a laser wakefield accelerator. *Phys. Rev. Lett.*, 104:025004, Jan 2010. doi: 10.1103/PhysRevLett.104.025004. URL <http://link.aps.org/doi/10.1103/PhysRevLett.104.025004>.
- Meister, A. *Numerik linearer Gleichungssysteme*. Vieweg Verlag, Friedr. & Sohn Verlagsgesellschaft mbH, 2011. ISBN 9783834881007.

- Message Passing Interface Forum. MPI: A message-passing interface standard - version 3.0, September 2012. URL <http://www.mpi-forum.org/docs/mpi-3.0/mpi30-report.pdf>.
- Meuer, H., Strohmaier, E., Dongarra, J., and Simon, H. Top 500 supercomputers, 2014. URL <http://www.top500.org/lists/2014/06/>.
- Meyer-ter Vehn, J., Pukhov, A., and Sheng, Z.-M. Relativistic laser plasma interaction. In *Atoms, Solids, and Plasmas in Super-Intense Laser Fields*, pages 167–192. Springer US, 2001. ISBN 978-1-4613-5511-3. doi: 10.1007/978-1-4615-1351-3\_9. URL [http://dx.doi.org/10.1007/978-1-4615-1351-3\\_9](http://dx.doi.org/10.1007/978-1-4615-1351-3_9).
- Michel, P., Schroeder, C. B., Shadwick, B. A., Esarey, E., and Lee-mans, W. P. Radiative damping and electron beam dynamics in plasma-based accelerators. *Phys. Rev. E*, 74:026501, Aug 2006. doi: 10.1103/PhysRevE.74.026501. URL <http://link.aps.org/doi/10.1103/PhysRevE.74.026501>.
- Mihara, T., Iwashita, Y., Kumada, M., and Spencer, C. Variable permanent magnet quadrupole. *Applied Superconductivity, IEEE Transactions on*, 16(2):224–227, June 2006. ISSN 1051-8223. doi: 10.1109/TASC.2006.873248. URL <http://dx.doi.org/10.1109/TASC.2006.873248>.
- Modena, A., Najmudin, Z., Dangor, A., Clayton, C., Marsh, K. A., Joshi, C., Malka, V., Darrow, C., Danson, C., and Neely, D. and Walsh, F. Electron acceleration from the breaking of relativistic plasma waves. *Nature*, 377(6550):606–608, Oct. 1995. URL <http://dx.doi.org/10.1038/377606a0>.
- Mora, P. and Antonsen, J. T. M. Kinetic modeling of intense, short laser pulses propagating in tenuous plasmas. *Physics of Plasmas*, 4(1):217–229, 1997. doi: 10.1063/1.872134. URL <http://link.aip.org/link/?PHP/4/217/1>.
- Mora, P. and Antonsen, T. M. Electron cavitation and acceleration in the wake of an ultraintense, self-focused laser pulse. *Phys. Rev. E*, 53:R2068–R2071, Mar 1996. doi: 10.1103/PhysRevE.53.R2068. URL <http://link.aps.org/doi/10.1103/PhysRevE.53.R2068>.
- Morshed, S., Antonsen, T. M., and Palastro, J. P. Efficient simulation of electron trapping in laser and plasma wakefield acceleration. *Physics of Plasmas*, 17(6):063106, 2010. doi: 10.1063/1.3432685. URL <http://link.aip.org/link/?PHP/17/063106/1>.
- Muggli, P., Marsh, K., Wang, S., Clayton, C., Lee, S., Katsouleas, T., and Joshi, C. Photo-ionized lithium source for plasma accelerator applications. *Plasma Science, IEEE Transactions on*, 27(3):791–799, Jun 1999. ISSN 0093-3813. doi: 10.1109/27.774685. URL <http://dx.doi.org/10.1109/27.774685>.

- Nicholson, D. R. *Introduction to plasma theory*. Wiley series in plasma physics. Wiley, 1983. ISBN 9780471090458.
- Nolting, W. *Grundkurs Theoretische Physik 3*: Grundkurs Theoretische Physik / Wolfgang Nolting. Springer, 2001. ISBN 9783540205098.
- Okuda, H. Nonphysical noises and instabilities in plasma simulation due to a spatial grid. *Journal of Computational Physics*, 10(3):475 – 486, 1972. ISSN 0021-9991. doi: [http://dx.doi.org/10.1016/0021-9991\(72\)90048-4](http://dx.doi.org/10.1016/0021-9991(72)90048-4). URL <http://www.sciencedirect.com/science/article/pii/0021999172900484>.
- O'Shea, P. G. Reversible and irreversible emittance growth. *Phys. Rev. E*, 57:1081–1087, Jan 1998. doi: 10.1103/PhysRevE.57.1081. URL <http://link.aps.org/doi/10.1103/PhysRevE.57.1081>.
- Osterhoff, J., Popp, A., Major, Z., Marx, B., Rowlands-Rees, T. P., Fuchs, M., Geissler, M., Hörlein, R., Hidding, B., Becker, S., Peralta, E. A., Schramm, U., Grüner, F., Habs, D., Krausz, F., Hooker, S. M., and Karsch, S. Generation of stable, low-divergence electron beams by laser-wakefield acceleration in a steady-state-flow gas cell. *Phys. Rev. Lett.*, 101:085002, Aug 2008. doi: 10.1103/PhysRevLett.101.085002. URL <http://link.aps.org/doi/10.1103/PhysRevLett.101.085002>.
- Oz, E., Deng, S., Katsouleas, T., Muggli, P., Barnes, C. D., Blumenfeld, I., Decker, F. J., Emma, P., Hogan, M. J., Ischebeck, R., Iverson, R. H., Kirby, N., Krejcik, P., O'Connell, C., Siemann, R. H., Walz, D., Auerbach, D., Clayton, C. E., Huang, C., Johnson, D. K., Joshi, C., Lu, W., Marsh, K. A., Mori, W. B., and Zhou, M. Ionization-induced electron trapping in ultrarelativistic plasma wakes. *Phys. Rev. Lett.*, 98:084801, Feb 2007. doi: 10.1103/PhysRevLett.98.084801. URL <http://link.aps.org/doi/10.1103/PhysRevLett.98.084801>.
- Pak, A., Marsh, K. A., Martins, S. F., Lu, W., Mori, W. B., and Joshi, C. Injection and trapping of tunnel-ionized electrons into laser-produced wakes. *Phys. Rev. Lett.*, 104:025003, Jan 2010. doi: 10.1103/PhysRevLett.104.025003. URL <http://link.aps.org/doi/10.1103/PhysRevLett.104.025003>.
- Palmer, R. B. A Laser Driven Grating Linac. *eConf*, C8209271:267, 1982. URL <http://lss.fnal.gov/conf/C8209271/p267.pdf>.
- Panasenko, D., Shu, A. J., Gonsalves, A., Nakamura, K., Matlis, N. H., Toth, C., and Leemans, W. P. Demonstration of a plasma mirror based on a laminar flow water film. *Journal of Applied Physics*, 108(4):044913, 2010. doi: <http://dx.doi.org/10.1063/1.3460627>. URL <http://scitation.aip.org/content/aip/journal/jap/108/4/10.1063/1.3460627>.

- Petrov, G. M. and Davis, J. A generalized implicit algorithm for multi-dimensional particle-in-cell simulations in cartesian geometry. *Physics of Plasmas (1994-present)*, 18(7):073102, 2011. doi: <http://dx.doi.org/10.1063/1.3603837>. URL <http://scitation.aip.org/content/aip/journal/pop/18/7/10.1063/1.3603837>.
- Pippig, M. PFFT: An Extension of FFTW to Massively Parallel Architectures. *SIAM Journal on Scientific Computing*, 35(3):C213–C236, 2013. doi: [10.1137/120885887](https://doi.org/10.1137/120885887). URL <http://epubs.siam.org/doi/abs/10.1137/120885887>.
- Povh, B., Lavelle, M., Rith, K., Scholz, C., and Zetsche, F. *Particles and Nuclei: An Introduction to the Physical Concepts*. Springer, 2008. ISBN 9783540793687.
- Pritchett, P. L. Particle-in-cell simulation of plasmas - a tutorial. In Büchner, J., Scholer, M., and Dum, C. T., editors, *Space Plasma Simulation*, volume 615 of *Lecture Notes in Physics*, pages 1–24. Springer Berlin Heidelberg, 2003. ISBN 978-3-540-00698-5. doi: [10.1007/3-540-36530-3\\_1](https://doi.org/10.1007/3-540-36530-3_1). URL [http://dx.doi.org/10.1007/3-540-36530-3\\_1](http://dx.doi.org/10.1007/3-540-36530-3_1).
- Pukhov, A. and Meyer-ter Vehn, J. Laser wake field acceleration: the highly non-linear broken-wave regime. *Applied Physics B*, 74(4-5): 355–361, 2002. ISSN 0946-2171. doi: [10.1007/s003400200795](https://doi.org/10.1007/s003400200795). URL <http://dx.doi.org/10.1007/s003400200795>.
- Rechatin, C., Faure, J., Ben-Ismaïl, A., Lim, J., Fitour, R., Specka, A., Videau, H., Tafzi, A., Burgy, F., and Malka, V. Controlling the phase-space volume of injected electrons in a laser-plasma accelerator. *Phys. Rev. Lett.*, 102:164801, Apr 2009. doi: [10.1103/PhysRevLett.102.164801](https://doi.org/10.1103/PhysRevLett.102.164801). URL <http://link.aps.org/doi/10.1103/PhysRevLett.102.164801>.
- Rechatin, C., Faure, J., Davoine, X., Lundh, O., Lim, J., Ben-Ismaïl, A., Burgy, F., Tafzi, A., Lifschitz, A., Lefebvre, E., and Malka, V. Characterization of the beam loading effects in a laser plasma accelerator. *New Journal of Physics*, 12(4):045023, 2010. URL <http://stacks.iop.org/1367-2630/12/i=4/a=045023>.
- Reiser, M. *Theory and Design of Charged Particle Beams*. Wiley series in beam physics and accelerator technology. John Wiley & Sons, New York, 2008. ISBN 978-3-527-40741-5.
- Rittershofer, W., Schroeder, C. B., Esarey, E., Grüner, F. J., and Lee-mans, W. P. Tapered plasma channels to phase-lock accelerating and focusing forces in laser-plasma accelerators. *Physics of Plasmas (1994-present)*, 17(6):063104, 2010. doi: <http://dx.doi.org/10.1063/1.3430638>. URL <http://scitation.aip.org/content/aip/journal/pop/17/6/10.1063/1.3430638>.



- Robson, R. *Introductory Transport Theory for Charged Particles in Gases*. World Scientific, 2006. ISBN 9789812700117.
- Röhrs, M. *Investigation of the Phase Space Distribution of Electron Bunches at the FLASH-Linac Using a Transverse Deflecting Structure*. PhD thesis, Univ. Hamburg, 2008. URL <http://www-library.desy.de/cgi-bin/showprep.pl?desy-thesis-08-012>.
- Rosenzweig, J. B., Breizman, B., Katsouleas, T., and Su, J. J. Acceleration and focusing of electrons in two-dimensional nonlinear plasma wake fields. *Phys. Rev. A*, 44:R6189–R6192, Nov 1991. doi: 10.1103/PhysRevA.44.R6189. URL <http://link.aps.org/doi/10.1103/PhysRevA.44.R6189>.
- Saleh, B. E. A. and Teich, M. C. *Fundamentals of Photonics*. Wiley Series in Pure and Applied Optics. Wiley, 2007. ISBN 9780471358329.
- Schmid, K., Buck, A., Sears, C. M. S., Mikhailova, J. M., Tautz, R., Herrmann, D., Geissler, M., Krausz, F., and Veisz, L. Density-transition based electron injector for laser driven wakefield accelerators. *Phys. Rev. ST Accel. Beams*, 13:091301, Sep 2010. doi: 10.1103/PhysRevSTAB.13.091301. URL <http://link.aps.org/doi/10.1103/PhysRevSTAB.13.091301>.
- Schroeder, C. B., Esarey, E., and Shadwick, B. A. Warm wave breaking of nonlinear plasma waves with arbitrary phase velocities. *Phys. Rev. E*, 72:055401, Nov 2005. doi: 10.1103/PhysRevE.72.055401. URL <http://link.aps.org/doi/10.1103/PhysRevE.72.055401>.
- Schroeder, C. B., Esarey, E., Geddes, C. G. R., Benedetti, C., and Leemans, W. P. Physics considerations for laser-plasma linear colliders. *Phys. Rev. ST Accel. Beams*, 13:101301, Oct 2010. doi: 10.1103/PhysRevSTAB.13.101301. URL <http://link.aps.org/doi/10.1103/PhysRevSTAB.13.101301>.
- Schroeder, C. B., Benedetti, C., Esarey, E., and Leemans, W. P. Beam loading in a laser-plasma accelerator using a near-hollow plasma channel. *Physics of Plasmas (1994-present)*, 20(12):123115, 2013a. doi: <http://dx.doi.org/10.1063/1.4849456>. URL <http://scitation.aip.org/content/aip/journal/pop/20/12/10.1063/1.4849456>.
- Schroeder, C. B., Esarey, E., Benedetti, C., and Leemans, W. P. Control of focusing forces and emittances in plasma-based accelerators using near-hollow plasma channels. *Physics of Plasmas (1994-present)*, 20(8):080701, 2013b. doi: <http://dx.doi.org/10.1063/1.4817799>. URL <http://scitation.aip.org/content/aip/journal/pop/20/8/10.1063/1.4817799>.
- Sears, C. M. S., Buck, A., Schmid, K., Mikhailova, J., Krausz, F., and Veisz, L. Emittance and divergence of laser wakefield accelerated

- electrons. *Phys. Rev. ST Accel. Beams*, 13:092803, Sep 2010. doi: 10.1103/PhysRevSTAB.13.092803. URL <http://link.aps.org/doi/10.1103/PhysRevSTAB.13.092803>.
- Seggebrock, T., Maier, A. R., Dornmair, I., and Grüner, F. Bunch de-compression for laser-plasma driven free-electron laser demonstration schemes. *Phys. Rev. ST Accel. Beams*, 16:070703, Jul 2013. doi: 10.1103/PhysRevSTAB.16.070703. URL <http://link.aps.org/doi/10.1103/PhysRevSTAB.16.070703>.
- Seryi, A., Hogan, M., Pei, S., Raubenheimer, T., Tenenbaum, P., et al. A concept of plasma wake field acceleration linear collider (pwfac). 2009. URL <http://www.slac.stanford.edu/cgi-wrap/getdoc/slac-pub-13766.pdf>.
- Shadwick, B. A., Schroeder, C. B., and Esarey, E. Nonlinear laser energy depletion in laser-plasma accelerators. *Physics of Plasmas (1994-present)*, 16(5):056704, 2009. doi: <http://dx.doi.org/10.1063/1.3124185>. URL <http://scitation.aip.org/content/aip/journal/pop/16/5/10.1063/1.3124185>.
- Sokollik, T., Shiraishi, S., Osterhoff, J., Evans, E., Gonsalves, A. J., Nakamura, K., van Tilborg, J., Lin, C., Toth, C., and Lee-mans, W. P. Tape-drive based plasma mirror. *AIP Conference Proceedings*, 1299(1):233–237, 2010. doi: <http://dx.doi.org/10.1063/1.3520320>. URL <http://scitation.aip.org/content/aip/proceeding/aipcp/10.1063/1.3520320>.
- Spatschek, K. H. *Theoretische Plasmaphysik: Eine Einführung*. Teubner Studienbücher: Physik. Vieweg+Teubner Verlag, 1990. ISBN 9783519030416.
- Sprangle, P., Esarey, E., and Ting, A. Nonlinear interaction of intense laser pulses in plasmas. *Phys. Rev. A*, 41:4463–4469, Apr 1990a. doi: 10.1103/PhysRevA.41.4463. URL <http://link.aps.org/doi/10.1103/PhysRevA.41.4463>.
- Sprangle, P., Esarey, E., and Ting, A. Nonlinear theory of intense laser-plasma interactions. *Phys. Rev. Lett.*, 64:2011–2014, Apr 1990b. doi: 10.1103/PhysRevLett.64.2011. URL <http://link.aps.org/doi/10.1103/PhysRevLett.64.2011>.
- Strickland, D. and Mourou, G. Compression of amplified chirped optical pulses. *Optics Communications*, 56(3):219 – 221, 1985. ISSN 0030-4018. doi: [http://dx.doi.org/10.1016/0030-4018\(85\)90120-8](http://dx.doi.org/10.1016/0030-4018(85)90120-8). URL <http://www.sciencedirect.com/science/article/pii/0030401885901208>.
- Suk, H., Barov, N., Rosenzweig, J. B., and Esarey, E. Plasma electron trapping and acceleration in a plasma wake field using a

- density transition. *Phys. Rev. Lett.*, 86:1011–1014, Feb 2001. doi: 10.1103/PhysRevLett.86.1011. URL <http://link.aps.org/doi/10.1103/PhysRevLett.86.1011>.
- Tajima, T. and Dawson, J. M. Laser electron accelerator. *Phys. Rev. Lett.*, 43:267–270, Jul 1979. doi: 10.1103/PhysRevLett.43.267. URL <http://link.aps.org/doi/10.1103/PhysRevLett.43.267>.
- Ting, A., Esarey, E., and Sprangle, P. Nonlinear wake-field generation and relativistic focusing of intense laser pulses in plasmas. *Physics of Fluids B: Plasma Physics*, 2(6):1390–1394, 1990. doi: 10.1063/1.859561. URL <http://link.aip.org/link/?PFB/2/1390/1>.
- Tomassini, P., Galimberti, M., Giulietti, A., Giulietti, D., Gizzi, L. A., Labate, L., and Pegoraro, F. Production of high-quality electron beams in numerical experiments of laser wakefield acceleration with longitudinal wave breaking. *Phys. Rev. ST Accel. Beams*, 6:121301, Dec 2003. doi: 10.1103/PhysRevSTAB.6.121301. URL <http://link.aps.org/doi/10.1103/PhysRevSTAB.6.121301>.
- Tonks, L. and Langmuir, I. Oscillations in ionized gases. *Phys. Rev.*, 33:195–210, Feb 1929. doi: 10.1103/PhysRev.33.195. URL <http://link.aps.org/doi/10.1103/PhysRev.33.195>.
- Turner, S. CAS-CERN Accelerator School: 5th General accelerator physics course, Jyväskylä, Finland, 7-18 Sep 1992: Proceedings. 2., 1994. doi: 10.5170/CERN-1994-001. URL <http://dx.doi.org/10.5170/CERN-1994-001>.
- Van Loan, C. *Computational Frameworks for the Fast Fourier Transform*. Frontiers in Applied Mathematics. Society for Industrial and Applied Mathematics, 1992. ISBN 9780898712858.
- Vargas, M., Schumaker, W., He, Z.-H., Zhao, Z., Behm, K., Chvykov, V., Hou, B., Krushelnick, K., Maksimchuk, A., Yanovsky, V., and Thomas, A. G. R. Improvements to laser wakefield accelerated electron beam stability, divergence, and energy spread using three-dimensional printed two-stage gas cell targets. *Applied Physics Letters*, 104(17):174103, 2014. doi: <http://dx.doi.org/10.1063/1.4874981>. URL <http://scitation.aip.org/content/aip/journal/apl/104/17/10.1063/1.4874981>.
- Vay, J.-L. Noninvariance of space- and time-scale ranges under a lorentz transformation and the implications for the study of relativistic interactions. *Phys. Rev. Lett.*, 98:130405, Mar 2007. doi: 10.1103/PhysRevLett.98.130405. URL <http://link.aps.org/doi/10.1103/PhysRevLett.98.130405>.
- Vay, J.-L. Simulation of beams or plasmas crossing at relativistic velocity). *Physics of Plasmas (1994-present)*, 15(5):056701, 2008.

- doi: <http://dx.doi.org/10.1063/1.2837054>. URL <http://scitation.aip.org/content/aip/journal/pop/15/5/10.1063/1.2837054>.
- Veksler, V. I. Coherent Principle Of Acceleration Of Charged Particles. *Proceedings of the CERN Symposium On High-Energy Accelerators And Pion Physics*, pages 80–83, 1956. URL <http://inspirehep.net/record/921325?ln=en>.
- Vieira, J., Martins, S. F., Pathak, V. B., Fonseca, R. A., Mori, W. B., and Silva, L. O. Magnetic control of particle injection in plasma based accelerators. *Phys. Rev. Lett.*, 106:225001, May 2011. doi: 10.1103/PhysRevLett.106.225001. URL <http://link.aps.org/doi/10.1103/PhysRevLett.106.225001>.
- Wang, X., Zgadzaj, R., Fazel, N., Li, Z., Yi, S. A., Zhang, X., Henderson, W., Chang, Y. Y., Korzekwa, R., Tsai, H. E., Pai, C. H., Quevedo, H., Dyer, G., Gaul, E., Martinez, M., Bernstein, A. C., Borger, T., Spinks, M., Donovan, M., Khudik, V., Shvets, G., Ditmire, T., and Downer, M. C. Quasi-monoenergetic laser-plasma acceleration of electrons to 2 GeV. *Nat Commun*, 4:1988, 06 2013. URL <http://dx.doi.org/10.1038/ncomms2988>.
- Whittum, D. H. Transverse two-stream instability of a beam with a bennett profile. *Physics of Plasmas (1994-present)*, 4 (4):1154–1159, 1997. doi: <http://dx.doi.org/10.1063/1.872202>. URL <http://scitation.aip.org/content/aip/journal/pop/4/4/10.1063/1.872202>.
- Wilkinson, B. and Allen, C. *Parallel Programming: Techniques and Applications Using Networked Workstations and Parallel Computers*. An Alan R. Apt book. Prentice Hall PTR, 1999. ISBN 9780136717102.
- Yanovsky, V., Chvykov, V., Kalinchenko, G., Rousseau, P., Planchon, T., Matsuoka, T., Maksimchuk, A., Nees, J., Cheriaux, G., Mourou, G., and Krushelnick, K. Ultra-high intensity- 300-tw laser at 0.1 hz repetition rate. *Opt. Express*, 16(3):2109–2114, Feb 2008. doi: 10.1364/OE.16.002109. URL <http://www.opticsexpress.org/abstract.cfm?URI=oe-16-3-2109>.
- Yee, K. Numerical solution of initial boundary value problems involving maxwell's equations in isotropic media. *Antennas and Propagation, IEEE Transactions on*, 14(3):302–307, 1966. ISSN 0018-926X. doi: 10.1109/TAP.1966.1138693. URL <http://dx.doi.org/10.1109/TAP.1966.1138693>.
- Yu, L.-L., Esarey, E., Schroeder, C. B., Vay, J.-L., Benedetti, C., Geddes, C. G. R., Chen, M., and Leemans, W. P. Two-color laser-ionization injection. *Phys. Rev. Lett.*, 112:125001, Mar 2014. doi: 10.1103/PhysRevLett.112.125001. URL <http://link.aps.org/doi/10.1103/PhysRevLett.112.125001>.

*Das gute Beispiel ist nicht nur eine Möglichkeit, andere Menschen zu beeinflussen. Es ist die einzige.*

— Albert Schweitzer

## ACKNOWLEDGMENTS

---

This thesis is not only a result of my scientific work but also a result of the support and impact of people I worked together and spent three fantastic years with in Hamburg and at DESY. I'd like to (not exclusively) thank the persons listed below.

### DR. JENS OSTERHOFF

Jens was my doctoral supervisor and adviser. He was not only a great supporter and a driving force of my work but in the same time always managed to keep his supervision informal and personable. I am grateful for his scientific guidance, for his inspiration and for his encouragement for my career. I have deepest respect for his capability to organize numerous issues in no time and to quickly apprehend the pivotal point of physical problems. Until family responsibilities kicked in, Jens used to be available for any kind of leisure time activities and also was a fun person to spend after office closing time with.

### PROF. DR. BRIAN FOSTER

Brian accepted to be my doctoral supervisor and I would like to express my gratitude for his interest in my work, the revision of this thesis and for all his support.

### PROF. DR. ROBI BANERJEE

Prof. Banerjee kindly accepted to examine this thesis although there was only very limited time for him to do so.

### DR. BERNHARD SCHMIDT

As the head of the FLA department, Bernhard always knew how to bring good atmosphere to the group. When I had the chance to go for lunch or to have a coffee with him, he certainly would tell one of his thousands enjoyable anecdotes on absurd incidents in his (or other people's) life. I always appreciated his honest and forthright opinion on various topics and profited from his hints and comments on physical problems.

### DR. JULIA GREBENYUK

Julia was my direct adviser in the first PhD year and substantially supported me in the everyday work at DESY. She is a person I could always rely on, a great colleague and wonderful person. Moreover I'd say she is the best (bar) tour guide for newcomers in Hamburg. Thank you, Julia!

## DR. CARL B. SCHROEDER

Carl gave me the excellent chance to visit [LBNL](#) for some months which was great experience and inspiration for me. I would like to express my gratitude for the hospitality I experienced during that time, and for the scientific advice I got from Carl within and beyond the period of the visit.

## DR. CARLO BENEDETTI

Special thanks go to Carlo who did not only keep me awake during working times at [LBNL](#) with his singing in the office and playing of the cornett, but also greatly guided and supported me with the foundations of [HiPACE](#). Without Carlos navigation, there would not be any working [HiPACE](#) code.

## PROF. DR. ROBERT ROBSON

At this point I would like to express my gratitude to Rob for all his efforts he invested into our joint theoretical project and his patience at times when I was too busy to keep our scientific exchange going. The distance of 15880 kilometers between Coochiemudlo Island and Hamburg could not stop Rob from visiting [DESY](#) twice to work with us (and probably also to enjoy some German beers). He always was an appreciated guest and adviser and did not only teach me kinetic plasma theory but also how to approach physical problems in a rigorous way.

## DR. ALBERTO MARTINEZ DE LA OSSA

Alberto was a great colleague and a fun person to work with. I profited from the fruitful discussions about simulations with him. In addition, he was supporting me a lot with the amendments of [HiPACE](#). Alberto, to me the master of unix hacks and programming, was happily helping me with tips and hints for coding.

## THE PLASMA AND FLA TEAM

These acknowledgments cannot be written without mentioning the plasma and FLA team. I would like to thank Tobi, Lucas, Charlotte, Matt, Olena, Lars, Slava, John, Jan-Patrick, Halil, Alexander, Steffen, Eugen, Sebastian, Lena, Matthias and Violetta for being great colleagues and moreover good friends. The years at [DESY](#) would not have been so much fun without you guys!

## DR. CHRISTOPHER BEHRENS

I'd like to thank Chris for his ideas and comments on my work, which triggered me to do some of the studies which are now part of this thesis. He always was a great source of motivation and I appreciated the scientific email discussions with him, although they often turned out as fully automatic email bombardments I was defenselessly exposed to.

## DR. KLAUS FLÖTTMANN

I appreciate the good conversations I had with Klaus and was always astonished by his profound expertise in all facets of accelerator physics. Ideas and insights I had during or after such conversations helped a lot to improve this thesis.

## DR. JORGE VIEIRA, DR. RICARDO FONSECA, DR. FRANK S. TSUNG, PROF. DR. LUÍS O. SILVA

I would like to thank the [OSIRIS](#) consortium and most especially Jorge, Ricardo, Frank and Luís for their great support on questions regarding the code and for the invitation to Lisbon and the hospitality I experienced there. Despite being very busy, they were highly responsive when I was bugging them with queries.

## MARC WENSKAT, SEBASTIAN ADERHOLD, FELIX SCHLANDER, RICARDA LAASCH, YEGOR TAMASHEVICH

Marc, Sebastian, Felix, Ricarda and Yegor were my office mates during the PhD time at DESY. They had to tolerate my increasingly obsessive thesis writing habits, e.g. when I tended to be too absorbed by my work to notice what was happening around me. Luckily, they always found a way to distract me with fun conversations (which probably rescued me from turning into some physicist zombie). They are also great pals to enjoy the leisure time with, e.g. to go for frequent bouldering.

## SUSAN-KATRIN KETELS, URSULA DJUANDE, IRIS KERKHOFF

Susan, Uschi and Iris made work and life at DESY much more pleasant and were always happy to help PhD students with all the formalities they encounter during their studies and work. Not only did they give me all possible kind of support on struggles with DESY formalities but even supplied the FLA team with snacks from time to time (probably so as to keep some of us students alive).

## USERS OF HIPACE

I'd like to thank the users of [HiPACE](#) for prompting me with their comments and suggestions to implement improvements into the code.

## THE LAOLA COLLABORATION

Plasma-based accelerator efforts at DESY were bundled in the [LAOLA](#) collaboration. I would like to express my recognition for the support and interest for my work by members of the [LAOLA](#) collaboration.

## DESY FOOTBALL CREW

Thanks to all the guys who joined for the weekly football matches. It was great fun to play with you (almost on Champions League level) and will certainly miss the sports.

PROF. DR. STEFAN KARSCH AND DR. ANTONIA POPP

I shall not forget where I once started off in this scientific field as a master student and where I got my first inspirations and impulses. I would like to say thanks to the MPQ and LMU guys, specifically to Stefan and Antonia.

DR. ANDRÉ MIEDE

Designed the  $\LaTeX$  template which the layout of this thesis is based on.

MY PARENTS AND FAMILY

Last but not least, I'd like to thank my parents and family for strongly supporting me during my education and studies.



*Wissenschaft kann die letzten Rätsel der Natur nicht lösen. Sie kann es deswegen nicht, weil wir selbst ein Teil der Natur und damit auch ein Teil des Rätsels sind, das wir lösen wollen.*

— Max Planck

## CURICULUM VITÆ

---

### PERSONAL DATA

NAME: Timon Johannes Mehrling

BIRTH: March 17, 1985 in Interlaken-Unterseen, Switzerland

CITIZENSHIP: German

GENDER: Male

### EDUCATION AND ACADEMIC EXPERIENCE

#### Universität Hamburg and DESY, Germany

Jun 2011 -  
present

- Doctoral candidate
  - Dissertation title: *Theoretical and numerical studies on the transport of transverse beam quality in plasma-based accelerators*
  - Supervisors: Dr. Jens Osterhoff, Prof. Dr. Brian Foster

#### Technische Universität München, Germany

Apr 2008 -  
Mar 2011

- **Diplom in physics (M.Sc.)** awarded in March 2011
  - Title: *Studying laser wakefield acceleration of relativistic electron bunches in inhomogeneous plasma with PIC simulations*
  - Supervisors: Prof. Dr. Reinhard Kienberger (TUM), Prof. Dr. Stefan Karsch (LMU)

#### Albert-Ludwigs-Universität Freiburg, Germany

Oct 2005 -  
Mar 2008

- **Vordiplom in physics** awarded in June 2007
- Semester abroad at NTNU Trondheim, Norway 2007

#### Georg-Kerschensteiner Schule Müllheim, Germany

Aug 2001 -  
Jun 2004

- **Abitur** awarded in June 2004
- Advanced courses in mathematics and technical mechanics

## EMPLOYMENT AND TEACHING

- Universität Hamburg, Germany** Oct 2011 - Feb 2012
- Preparation of exercises for the Lecture "Physics of Plasma Accelerators" by Dr. Jens Osterhoff
- Universität Hamburg, Germany** Apr 2011 - May 2011
- Research assistant in the "Helmholtz Young Investigator Group" of Dr. Jens Osterhoff
- Ludwig-Maximilians-Universität München, Germany** Mar 2010 - May 2010
- Assistant in the laboratory for attosecond physics for Prof. Dr. Stefan Karsch
- Max-Planck-Institut für Physik in München, Germany** Aug 2009 - Oct 2009
- Laboratory assistant for Dr. Béla Majorovits in the GERDA project
- Technische Universität München, Germany** Jul 2008 - Aug 2008
- Vacation course - preparation of lectures and exercises on classical electrodynamics
- Max-Planck-Institut für Quantenoptik, Garching, Germany** Jun 2008 - Sep 2008
- Laboratory assistant for Prof. Dr. Karl Kompa

## ADDITIONAL EXPERIENCE

- Alternative social service abroad** Sep 2004 - Sep 2005
- Volunteer worker for the regional Evangelic Church Baden at the Youth Center in Kumbo, Cameroon

## PROFESSIONAL MEMBERSHIPS

DPG Deutsche Physikalische Gesellschaft (since 2009)

KFB Komitee für Beschleunigerphysik (since 2011)

## CONTACT

RESEARCHGATE [Profile: Timon Mehrling](#)

ORCID [Profile: Timon Mehrling](#)

## LIST OF PUBLICATIONS

---

Julia Grebenyuk, **Timon Mehrling**, Frank S. Tsung, Klaus Floettman, and Jens Osterhoff. Simulations of laser-wakefield acceleration with external electron-bunch injection for REGAE experiments at DESY. *AIP Conference Proceedings*, 1507(1):688–692, 2012. doi: <http://dx.doi.org/10.1063/1.4773781>. URL <http://scitation.aip.org/content/aip/proceeding/aipcp/10.1063/1.4773781>.

Julia Grebenyuk, Alberto Martinez de la Ossa, **Timon Mehrling**, and Jens Osterhoff. Beam-driven plasma-based acceleration of electrons with density down-ramp injection at FLASHForward. *Nuclear Instruments and Methods in Physics Research Section A: Accelerators, Spectrometers, Detectors and Associated Equipment*, 740(0):246 – 249, 2014. ISSN 0168-9002. doi: <http://dx.doi.org/10.1016/j.nima.2013.10.054>. URL <http://www.sciencedirect.com/science/article/pii/S0168900213014356>. Proceedings of the first European Advanced Accelerator Concepts Workshop 2013.

Alberto Martinez de la Ossa, Julia Grebenyuk, **Timon Mehrling**, Lucas Schaper, and Jens Osterhoff. High-quality electron beams from beam-driven plasma accelerators by wakefield-induced ionization injection. *Phys. Rev. Lett.*, 111:245003, Dec 2013. doi: [10.1103/PhysRevLett.111.245003](http://dx.doi.org/10.1103/PhysRevLett.111.245003). URL <http://link.aps.org/doi/10.1103/PhysRevLett.111.245003>.

Alberto Martinez de la Ossa, Christopher Behrens, Julia Grebenyuk, **Timon Mehrling**, Lucas Schaper, and Jens Osterhoff. High-quality electron beams from field-induced ionization injection in the strong blow-out regime of beam-driven plasma accelerators. *Nuclear Instruments and Methods in Physics Research Section A: Accelerators, Spectrometers, Detectors and Associated Equipment*, 740(0):231 – 235, 2014. ISSN 0168-9002. doi: <http://dx.doi.org/10.1016/j.nima.2013.10.016>. URL <http://www.sciencedirect.com/science/article/pii/S016890021301334X>. Proceedings of the first European Advanced Accelerator Concepts Workshop 2013.

**Timon Mehrling**. Studying laser wakefield acceleration of relativistic electron bunches in inhomogeneous plasma with PIC simulations. Diplomarbeit, Technische Universität München Arcisstraße 11, 80333 München, March 2011.

**Timon Mehrling**, Julia Grebenyuk, Frank S. Tsung, Klaus Floettmann, and Jens Osterhoff. Transverse emittance growth in staged laser-wakefield acceleration. *Phys. Rev. ST Accel. Beams*, 15:111303, Nov

2012. doi: 10.1103/PhysRevSTAB.15.111303. URL <http://link.aps.org/doi/10.1103/PhysRevSTAB.15.111303>.

**Timon Mehrling**, Carlo Benedetti, Carl B. Schroeder, and Jens Osterhoff. HiPACE: a quasi-static particle-in-cell code. *Plasma Physics and Controlled Fusion*, 56(8):084012, 2014. doi: 10.1088/0741-3335/56/8/084012. URL <http://stacks.iop.org/0741-3335/56/i=8/a=084012>.

## DECLARATION

---

### **Eidesstattliche Versicherung**

Hiermit erkläre ich an Eides statt, dass ich die vorliegende Dissertationsschrift selbst verfasst und keine anderen als die angegebenen Quellen und Hilfsmittel benutzt habe.

*Hamburg, August 2014*

---

Timon Johannes Mehrling